

ON THE PREVALENCE OF STARBURSTS IN DWARF GALAXIES

by

Janice Christine Lee

A dissertation submitted to the faculty of the
DEPARTMENT OF ASTRONOMY
in partial fulfillment of the requirements
for the degree of
DOCTOR OF PHILOSOPHY
in the Graduate College of
THE UNIVERSITY OF ARIZONA

2006

THE UNIVERSITY OF ARIZONA
GRADUATE COLLEGE

As members of the Dissertation Committee, we certify that we have read the dissertation
prepared by Janice Christine Lee
entitled On the Prevalence of Starbursts in Dwarf Galaxies
and recommend that it be accepted as fulfilling the dissertation requirement for the
Degree of Doctor of Philosophy

Robert Kennicutt

Date: September 5, 2006

Deidre Hunter

Date: September 5, 2006

Romeel Dave

Date: September 5, 2006

Xiaohui Fan

Date: September 5, 2006

Final approval and acceptance of this dissertation is contingent upon the candidate's
submission of the final copies of the dissertation to the Graduate College.

I hereby certify that I have read this dissertation prepared under my direction and
recommend that it be accepted as fulfilling the dissertation requirement.

Dissertation Director: Robert Kennicutt

Date: September 5, 2006

STATEMENT BY AUTHOR

This dissertation has been submitted in partial fulfillment of requirements for an advanced degree at The University of Arizona and is deposited in the University Library to be made available to borrowers under rules of the Library.

Brief quotations from this dissertation are allowable without special permission, provided that accurate acknowledgment of source is made. Requests for permission for extended quotation from or reproduction of this manuscript in whole or in part may be granted by the head of the major department or the Dean of the Graduate College when in his or her judgment the proposed use of the material is in the interests of scholarship. In all other instances, however, permission must be obtained from the author.

SIGNED: Janice Christine Lee

ACKNOWLEDGMENTS

I am extremely grateful for the strong scientific network that has supported my intellectual and professional development as an astronomer, and it is a sincere pleasure to acknowledge the folks that have been at its core.

First, special thanks are in order for my advisor Rob Kennicutt. Like any parent with high expectations for his children, Rob would *never, ever* allow me to short-change myself in terms of my career aspirations, and by example he has impressed upon me the critical importance of unyielding tenacity and continual growth. Rob's sage scientific guidance and support has been important in helping me to complete this thesis and to also lay the groundwork for ambitious future endeavors.

I would also like to thank my $H\alpha$ survey teammates who have labored to create the dataset on which this thesis is based. This includes Rob, who has led the project, data analyst extraordinaire Sanae Akiyama, who also manages the broader $H\alpha$ flux database, Jose Funes (Vatican Observatory) and Shoko Sakai (UCLA). Sanae, Jose and Shoko have also given me much advice and encouragement for which I am grateful.

Two others who have been absolutely integral to helping me survive in our intensely competitive field are John Salzer (Wesleyan) and Liese van Zee (Indiana). Salzer and the Wesleyan Astronomy Department (to whom I also owe my gratitude) opened the doors for me to a life in academic research when there were few other options for a person who had already left college on an alternate career path. van Zee took me under her wing early in my grad career when I was convinced my dissertation should focus on observationally constraining the inner profiles of dark matter haloes. For many years, both of these incredibly devoted teachers have not only been expert sounding boards for my ideas and questions on the nature of star formation in dwarf galaxies, but have also been generous dispensers of advice, comfort and friendship.

I also warmly thank my peers (both former and current grads and postdocs) at Steward for their camaraderie and for creating the supportive, fun and fertile scientific environment that I have grown in. Those who must be especially noted include Joannah Hinz, Chien Peng, Christian Drouet D'Aubigny, academic siblings John Moustakas and Moire Prescott, officemate Iva Momcheva, Christy Tremonti, Rose Finn, Casey Meakin, Marianne Vestergard, Audra Baleisis, Cathy Petry and all the members of the recently established Women's Science Forum.

Finally, fruitful discussions with committee member D. Hunter (Lowell), D. Garnett, D. Zaritsky, A. Zabludoff, former advisor C. Impey, A. Dolphin, D. McCarthy, J. Harris, M. Mac Low (AMNH), E. Skillman (Minnesota), S. Oey (Michigan), C. Martin (UCSB), and J. Gallagher (Wisconsin) are acknowledged. M. Haynes (Cornell) is thanked for providing access to the GALPHOT package and the Arecibo General Catalog of HI in local galaxies.

DEDICATION

They say that it takes a village to raise a child, and this must especially be true when mom is off writing a thesis. I thus dedicate this work to the small village of devoted family and friends who have helped me care for my children while I have worked countless days and nights trying to figure out what in the Universe is going on in these very complicated dwarf galaxies.

For my family — for my husband Ted, whose passions and life goals parallel my own — at the roots, it is our true and equal partnership in marriage and parenthood that makes it possible for us to simultaneously fulfill our commitments to both our children and our chosen vocations. For my mom Evylin, my dad Ben, my sisters Jenny and Nin, and my brother Jun. For the teachers and staff and the Satori School. And for the good Lord, who has abundantly provided for and watched over all of us. I am extremely thankful for all of you – your precious efforts have been essential in enabling me to finally reach this milestone. Kobe and Kylie, of course, are very lucky to have you too, and it is my utmost hope that the examples that we set for them now will inspire and propel them to assiduously seek out their dreams in the future and live their lives to the very, very fullest.

TABLE OF CONTENTS

LIST OF FIGURES	9
LIST OF TABLES	11
ABSTRACT	12
CHAPTERS:	
1 INTRODUCTION	14
1.1 The Significance of Starbursts in Dwarf Galaxies	14
1.2 Methods for Constraining the Prevalence of Bursts	15
1.3 Our Current Understanding of the Evolutionary Status of Dwarf Irregular Galaxies	18
1.4 Overview of the Thesis	21
2 OBSERVATIONS OF THE CURRENT STAR FORMATION IN A COMPLETE SAMPLE OF DWARF GALAXIES	25
2.1 Introduction	25
2.2 The 11HUGS Sample	27
2.2.1 The Motivations for, and Challenges in Assembling a Volume-Limited Sample in the Local Neighborhood	27
2.2.2 Construction of the Sample	30
2.2.3 A Catalog of Star-Forming Galaxies within 11 Mpc	37
2.3 11HUGS: H α Imaging	52
2.3.1 Observations	52
2.3.2 Image Processing and Continuum Subtraction	54
2.3.3 Astrometry	55
2.3.4 Aperture Photometry	56
2.3.5 Absolute Flux Calibration	57
2.3.6 Integrated Flux and EW Error Analysis	58
2.3.7 Literature Comparison of Integrated Fluxes and EW	62
2.3.8 The 11HUGS Integrated H α Flux and EW Catalog	68
3 BASIC PROPERTIES OF THE 11HUGS SAMPLE	85
3.1 Selection Properties	85
3.2 Completeness	85
3.2.1 The Rauzy T_C Completeness Statistic	86
3.2.2 Luminosity and Mass Functions Comparisons	89
3.2.3 Comparison with Local Volume Galaxies found in HIPASS	91
3.3 Non-detections	92

TABLE OF CONTENTS — CONTINUED

4	GLOBAL STAR FORMATION PROPERTIES OF GALAXIES IN THE 11 MPC VOLUME: GENERAL OBSERVATIONAL PATTERNS	100
4.1	ABSTRACT	100
4.2	The $H\alpha$ EW as a Relative Star Formation Indicator	101
4.3	The Local Galaxy Sequence in the M_B -EW and V_{max} -EW Planes	102
4.3.1	Sources of Data	103
4.3.2	Qualitative Features	104
4.3.3	Quantitative Features	107
4.3.4	Physical Underpinnings of the Observed Sequence	110
5	DWARF GALAXY STARBURST STATISTICS	122
5.1	ABSTRACT	122
5.2	Adopted Definitions	122
5.2.1	What is a dwarf galaxy?	122
5.2.2	What is a starburst?	123
5.3	The Fraction of Starbursts Systems among Dwarf Irregulars	125
5.4	The Fraction of Star Formation Occurring in Starbursting Dwarfs	127
5.5	Comparison with Previous Work	129
6	CONSTRAINTS ON THE DWARF GALAXY STARBURST DUTY CYCLE	137
6.1	ABSTRACT	137
6.2	Evolutionary Synthesis Models	138
6.2.1	Calculation of the Model Grid	139
6.2.2	Comparison with Models of KTC94	141
6.3	Birthrates of Dwarf Galaxies in the 11HUGS Sample	143
6.4	The Viability of Continuous SFR Models	143
6.4.1	Checks for Possible Systematics in the 11HUGS EWs	145
6.4.2	Possible Escape of Ionizing Photons into the IGM?	150
6.4.3	Lower Maximal Stellar Masses in the IMF?	151
6.4.4	Summary Assessment of the Discrepancy between Predictions of Continuous Models and Observations	153
6.5	The Viability of Cyclical Burst Models	154
6.5.1	Implied Duty Cycle Parameters	158
6.5.2	Additional Duty Cycle Parameters Constraints under the Equal Probability Assumptions	158
6.6	Discussion	162
6.6.1	Comparison with Previous Results on the SFHs of Dwarfs	162

TABLE OF CONTENTS — CONTINUED

APPENDICES:

A	EMISSION-LINE FLUX CALIBRATION	178
A.1	Unit Response	178
A.2	Transmission Corrections	179
A.3	The Final Calibrated Emission Line Flux	182
B	CORRECTIONS TO THE OBSERVED $H\alpha$ + $[NII]$ FLUXES AND EW'S	184
B.1	$[NII]/H\alpha$ Estimation	184
B.2	Estimation of the Extinction in the $H\alpha$ Flux and EW	185
B.3	Comments on the Resultant Correction	187
REFERENCES	192

LIST OF FIGURES

2.1	Fractional Errors in the 11HUGS Integrated $H\alpha$ Fluxes and EWs . .	61
2.2	Comparison to Integrated Spectral $H\alpha$ Flux and EW Measurements	65
2.3	Comparison to Additional $H\alpha$ Flux and EW Measurements in the Literature	66
3.1	Histograms of the T-type, B Magnitude, Galactic Latitude and Distance for the 11HUGS Sample	94
3.2	Rauzy (2001) T_C Statistical Test for Completeness in M_B	95
3.3	Rauzy (2001) T_C Statistical Test for Completeness in M_{HI}	96
3.4	Rauzy (2001) T_C Statistical Test for Completeness in $L_{H\alpha}$	97
3.5	Comparison with B-band Luminosity Functions	98
3.6	Comparison with HI Mass Functions	99
4.1	The Local Galaxy Sequence in the M_B -EW Plane	117
4.2	The Local Galaxy Sequence in the V_{max} -EW Plane: The 11HUGS Sample	118
4.3	The Local Galaxy Sequence in the V_{max} -EW Plane: The Composite 11HUGS + $H\alpha$ GS Sample	119
4.4	Logarithmic EW Frequency Distributions	120
4.5	$L_{H\alpha}$ vs. M_B	121
5.1	$H\alpha$ EW Cumulative Frequency Distribution	135
5.2	Cumulative Distribution of $L_{H\alpha}$ as a Function of EW($H\alpha$)	136
6.1	Model Predicted Relationships between Stellar Birthrate and the $H\alpha$ EW	169
6.2	Continuous τ Models in the $H\alpha$ EW-Color Plane	170
6.3	Stellar Birthrates in the $L_{H\alpha}$ - M_B Plane	171
6.4	Burst Models in the $H\alpha$ EW-Color Plane	172
6.5	Time Evolution of $U-B$, $B-V$ and $H\alpha$ EW Following the Onset of a Burst: 10 & 100 Myr Duration Bursts	173

LIST OF FIGURES — CONTINUED

6.6	Time Evolution of Burst Models in the $H\alpha$ EW-Color Plane	174
6.7	Evolutionary Tracks of τ Models in the UBV Plane	175
6.8	Evolutionary Tracks of Burst Models in the UBV Plane	176
6.9	Time Evolution of $U-B$, $B-V$ and $H\alpha$ EW Following the Onset of a Burst: 50 Myr Duration Bursts	177
A.1	Filter Response Functions and Transmission Corrections	183
B.1	$NII\ \lambda 6583/H\alpha$ vs. M_B from Integrated Spectral Measurements . . .	189
B.2	$A_{H\alpha}$ vs. M_B from Integrated Spectral Measurements	190
B.3	Effects of the Combined NII and Internal Extinction Correction . .	191

LIST OF TABLES

2.1	The 11HUGS Target Catalog	40
2.2	Reference Codes for Table 2.1	51
2.3	Observational Set-Ups Used in the $H\alpha$ Imaging Survey	52
2.4	The 11HUGS Integrated $H\alpha$ + $[NII]$ Flux and EW Catalog	73
4.1	$H\alpha$ EW Distribution Statistics	116
5.1	$H\alpha$ EW Distribution Statistics	134
6.1	Synthetic $H\alpha$ EWs: Exponential Decay Models	165
6.2	Synthetic $H\alpha$ EWs: Burst Models	166
6.3	SFR Conversion Factors	167
6.4	Synthetic Colors and Mass-to-Light Ratios	168

ABSTRACT

An outstanding question in galaxy evolution research is whether the star formation histories of low mass systems are dominated by global starbursts or modes that are more quiescent and continuous. In this thesis, we quantify the prevalence of global starbursts in dwarf galaxies at the present epoch, and attempt to infer their characteristic durations, frequencies and amplitudes in the past. Our approach is to directly tally the number of bursting dwarfs in a complete local sample, and to compute the fraction of star formation that is concentrated in these systems. The resulting starburst number and mass fractions are then combined with $B - V$ colors from the literature, the $H\alpha$ EWs presented here, and stellar evolutionary synthesis models in order to place constraints on the average starburst duty cycle. The primary dataset used has been put together by the 11 Mpc $H\alpha$ UV Galaxy Survey, who have collected data on an approximately volume-limited, statistical sample of star-forming galaxies within 11 Mpc of the Milky Way.

Our main observational results, along with the accumulation of star formation studies of dwarf galaxies over the past three decades, paint a consistent picture where systems that are currently experiencing a massive global burst are just the $6 \pm 3\%$ tip of a low-mass galaxy iceberg. Moreover, bursts are responsible for $22 \pm 10\%$ of the total star formation in the overall dwarf galaxy population, so the majority of stars in low-mass systems do not appear to be formed in this mode today.

Over their lifetimes, however, a greater fraction of the stellar mass of a dwarf may be formed in the burst mode. Synthesis modeling suggests that bursts cycles appear to be necessary in order to simultaneously explain the present-day

observed blue $B - V$ colors and modest $H\alpha$ EWs of *typical, currently non-bursting* dIrrs, unless non-standard assumptions concerning the IMF and the escape fractions of Lyman continuum photons are made. The starburst cycle that we converge upon involves burst durations of 50-100 Myrs, cycle frequencies of $\lesssim 1 - 3$ per Gyr, and elevated burst SFRs that are a factor of 6-10 higher than the rate in the quiescent state. Galaxies characterized by such a SFH would spend $\sim 10\%$ of their lives in the burst state, and form $\sim 50\%$ of their stellar mass during this time.

CHAPTER 1

INTRODUCTION

1.1 The Significance of Starbursts in Dwarf Galaxies

Do cycles of violent, intense, but short-lived global bursts represent a significant mode of star formation in low-mass galaxies? This question was originally raised over thirty years ago, in connection with the discoveries of dwarf galaxies that resembled “isolated extragalactic HII regions” (Sargent & Searle 1970). These systems, now commonly referred to as the blue compact dwarfs (BCDs) or HII galaxies, were first identified in Zwicky’s (1966, 1971) catalogs of “compact” and “eruptive” galaxies, and in Markarian’s (1967, 1969a,b) survey for objects with large ultraviolet excesses. Star formation histories punctuated by strong “flashes” were then eventually proposed as the most likely solution to the puzzle presented by the anomalously blue colors and low gas-phase metal abundances observed in the lowest luminosity members of these samples (Searle & Sargent 1972; Searle, Sargent & Bagnuolo 1973, hereafter SSB73; Huchra 1977b).

Since then, the study of starbursts in dwarf galaxies has been greatly amplified due to the gradual recognition that these events may have a profound impact on systems with such shallow potential wells. The consequences can be far-reaching. Starburst episodes have been invoked, although with much ensuing debate, as an agent which transforms gas-rich dwarf irregulars¹ (dIrrs) to gas poor dwarf ellip-

¹Throughout this thesis I will use the term dwarf irregular to broadly refer to the full suite of low-mass star-forming galaxies. This will include the Sm class, where spiral structure is just barely apparent, the Im class, where there is a clear lack of organized structure, and the BCDs. I will also note here that the term BCD has historically been somewhat vaguely defined — Thuan & Martin (1981) introduced the classification to encompass galaxies with $M_B \gtrsim -18$, an optical

ticals (dEs) through gas consumption and expulsion (Vader 1986; Dekel & Silk 1986; Skillman & Bender 1995 and references therein, Marlowe et al. 1999). The stellar winds and supernovae produced by starbursts are argued to drive metal-enriched winds which may escape the haloes of low-mass galaxies and pollute the intergalactic medium (IGM) (e.g., Mac Low & Ferrara 1999; Martin 1999; Garnett 2002). Starbursts, therefore, are also implicated in the potentially related phenomenon of the observed decrease of the effective yield and metallicity with decreasing luminosity (e.g., Skillman et al. 1989; Lee, Salzer & Melbourne 2004), rotational velocity (Garnett 2002) and stellar mass (Tremonti et al. 2004).

An outstanding issue of basic importance to all these matters deals with the prevalence of starbursts in dwarfs. We must ask: What are the characteristic durations, frequencies and amplitudes of the starburst cycles which determine their efficacy as critical sinks of fuel and impulsive sources of disruptive energy? What is the mass fraction of stars formed during the burst phases? How do these parameters vary over cosmic time? Moreover, are all low mass galaxies are equally prone to bursting episodes, or rather does the starburst mode only operate in a particular sub-set of the population? These are the open questions that have motivated this thesis.

1.2 Methods for Constraining the Prevalence of Bursts

A generic description of the information needed to fully answer these questions is as follows. We would require a statistically complete sample of dwarf galaxies that span the total range of star formation activities, from those systems which are

spectrum exhibiting “strong sharp narrow emission lines superposed on a blue continuum,” and optical sizes $\lesssim 1$ kpc in diameter — and this has led to class of objects that is quite heterogeneous in their physical properties (see Gil de Paz et al. 2003 for a more comprehensive review). However, one of the intentions of these criteria is to isolate low-mass systems which are in a burst phase, and accordingly, the I will use the term BCD to refer to starbursting dwarfs.

presently undergoing a starburst event, to those which are in a period of relative quiescence. Star formation histories (SFHs) would be needed for each of galaxies in the sample, and the temporal sampling of the SFHs must be fine enough to resolve a burst cycle. The typical modes of global star formation can then be characterized. If violent fluctuations in the star formation rate (SFR) are evident for only some galaxies, then one can search for commonalities in the physical properties among those objects that may distinguish them from non-bursting systems.

Of course, it is often not possible to gather the ideal dataset which will yield all the bits of information needed to entirely constrain a problem. This is certainly true for the motivating questions of this thesis, and for galaxy evolution studies in general. The trouble is that we typically cannot follow the SFHs of individual systems back through cosmic time. The exception is for the galaxies in and around the Local Group. The stellar populations of these galaxies can be resolved and observed to sufficient depth such that color-magnitude diagrams (CMDs) can be used to reconstruct detailed SFHs. The results of these investigations for nearby dIrrs have shown that many of them have had only modest fluctuations in their star formation rates (e.g., Tosi et al. 1991; Greggio et al. 1993; Marconi et al. 1995; Aparicio et al. 1997a, b; Dohm-Palmer et al 1998; Gallagher et al. 1998; Dolphin et al. 2005). In particular, Dohm-Palmer et al. (1998) derived the SFH of four Local Group dIrrs (Sextans A, Pegasus DIG, Leo A and GR 8) over the recent past using main sequence and blue helium burning (supergiant) stars, and found that there were no bursts (no star formation episodes that deviated from the average activity by more than a factor of ~ 3) in these systems over the past 500 Myrs. Assuming a burst duration of 100 Myr, they then inferred that the total time spent in the burst state must be less than $\sim 5\%$, since there was the potential of observing 20 burst episodes in their data, but none were encountered. Clearly,

the conclusions of this study are weakened by the very small sample examined. However, by increasing the number of galaxies observed, extending the analysis to include earlier times, and capturing systems in which bursts *have* played a role, CMDs can indeed be used to robustly constrain the duty cycle and the prevalence of starbursts in the evolution of dwarfs. This should be possible for a large, statistical sample of dwarfs with the next generation of very large 30-m class telescopes such as the Giant Magellan Telescope, but in the meantime, we require an alternate strategy.

One reasonable approach is to use the present-day *integrated* properties of dwarfs to trace their SFHs. Although this method is coarser in its temporal resolving power, it allows for the analysis of the larger sample that is needed, and so, is complementary to the CMD studies. Certainly, the use of global properties, in particular the UBV colors and $H\alpha$ -based SFRs, to infer SFHs has long been the staple of galaxy evolution studies (e.g., Tinsley 1968, 1972; SSB73; Kennicutt 1998 and references therein; Bruzual & Charlot 2003 and references therein). However, a robust analysis based on a dwarf sample which is not only statistical and complete, but also spans the full range of activities and includes all BCDs/HII galaxies as well as the more difficult to observe quiescent, low surface brightness systems in a given volume, has not yet been carried out. The work in this thesis aims to fill the need for such an analysis. We will give an overview of our particular strategy at the end of the chapter, but first we complete this discussion by providing a more general background on our current understanding of the SFHs of dIrr galaxies.

1.3 Our Current Understanding of the Evolutionary Status of Dwarf Irregular Galaxies

Over the past three decades, dIrrs have been shown to be the most gas-rich, metal-poor and the bluest of all galaxies on the Hubble sequence. There have been many studies which have concluded that the present-day properties of most dIrrs reflect SFHs that are characterized by constant, but relatively low SFRs over the galaxies' lifetimes. This result has been primarily based on (1) the comparison of observed global colors with those synthesized by stellar population modeling (e.g., SSB73; Huchra 1977b; van Zee 2001), (2) the calculation of current SFRs from $H\alpha$ emission line fluxes (e.g., Gallagher, Hunter & Tutukov 1984; van Zee 2001; Hunter & Elmegreen 2004), and (3) the estimation of gas consumption timescales (e.g., Hunter, Gallagher & Rautenkranz 1982; van Zee 2001; Lee et al. 2002). More recently, studies of the resolved stellar population of the nearest dwarfs have provided additional evidence for this picture, as described above.

This picture, however, does not yet entirely exclude the possibility that the SFHs, which appear constant when averaged over a Hubble time, are actually composed of short burst cycles when examined with a finer temporal resolution. Clearly, a direct consequence of such variability is that we should be able to observe dIrrs in a range of star formation states. As already discussed, this is in fact where the idea of burst cycles originated – with the first observations of BCDs/HII galaxies. Using UBV photometry and the earliest generation of stellar synthesis models, SSB73 and Huchra (1977b) found that the extremely blue colors ($B-V \sim 0.0$) of these systems could be fit by models where there was a much elevated episode of star formation (“a flash”) superimposed on a older stellar population. Ever since then, the objectives at the forefront of research on low-mass galaxies have included the need to elucidate the relationship between the

BCDs and the quiescent dIrrs — i.e., to establish whether the typical dIrr can be a post-burst BCD, and if not, to identify the population which does represent the BCDs in their off-state — and to characterize the short term variability in the SFHs.

Matters can be substantially simplified by assuming that the bursts observed in BCDs can occur with equal probability in any dwarf galaxy with gas, and that all dIrrs share a common SFH. That is, the large ranges in properties exhibited by dwarfs are merely a consequence of observing them at different points in their star formation cycles. *If* these “equal probability” assumptions are true (the subject of which we will return to in Chapter 6), then the frequency distribution of galaxies in the various phases will correspond to the time spent in those phases, for a complete sampling of the population.

Perhaps the most quantitative analysis along these lines was carried out early on by Sargent (1972), who tentatively estimated that these hyperactive systems make up $\sim 10\%$ of the overall dwarf galaxy population. He reached this conclusion by comparing the space densities of low luminosity systems ($M_p \gtrsim -17$) in Markarian’s UV-selected survey and van den Bergh’s (1961) normal field galaxy sample. Although rigorous completeness tests were carried out, the result was emphasized as preliminary since the analysis suffered from small number statistics and large incompleteness corrections; both of Sargent’s starbursting and normal dwarf samples contained only about a dozen objects. Nevertheless, the rough estimate was used in SSB73 to infer that dIrrs undergo 5 to 10 short starbursts, each with a duration of $\sim 10^8$ yrs, over their lifetimes of 10^{10} years (i.e., dwarfs spent $\sim 10\%$ of their lives in the burst state). Note that this is roughly consistent with the Dohm-Palmer et al. (1998) 5% estimate based on resolved stellar populations.

Surprisingly however, there have been a dearth of studies in the intervening years that have tried to produce a robust confirmation of Sargent's initial estimates. Huchra (1977a) repeated the exercise, but his space densities were also based on the Markarian samples and thus share the same uncertainties due to small numbers and incompleteness. In the following decade, work on the SFHs of dwarf galaxies was focused on similarly sized samples that were simply chosen to be representative of the parameter space that dwarfs are thought to occupy (e.g., Hunter, Gallagher & Rautenkranz 1982), or selected to probe the properties of a particular subclass of them (e.g., Bohuski, Fairall & Weedman 1978, emission-line galaxies; Thuan 1983, BCDs; Hunter & Gallagher 1985, isolated dIrrs). More recent analyses have built upon this foundation by increasing the number of dwarfs studied by factors of a few, but the samples are still not complete in nature (e.g., van Zee 2000, 2001; Parodi et al. 2002; Gil de Paz, Madore & Pevunova 2003; Hunter & Elmegreen 2004, 2006). The exceptions among these studies have involved the emission-line and color-selected surveys which have produced the most homogenous and best characterized samples containing large number of dwarf galaxies. However, programs such as the Haro (1956), Markarian (1967, 1969a,b), UCM (Zamorano et al 1994.) and KISS (Salzer et al. 2000) surveys, preferentially have selected the most strongly star-forming systems by design and become severely incomplete for galaxies in which the current star formation rate is not elevated relative to the average past activity. In sum, there has been no robust follow-up statistical analyses which have focused on uniting the disparate types of dwarfs to our knowledge.

And so, this overview brings us to our present-day understanding of bursts in dwarf galaxies. The current situation is, admittedly, a bit odd. The first and essentially last rigorous statistical studies were done over 30 years ago, and have

already tentatively shown that dwarfs spend a small minority of their time in the burst state (given the assumptions stated above). Yet these results seem to have been perhaps largely forgotten and/or overshadowed by discoveries of the most extreme members of the low-mass galaxy population, and this has led to the development of a “common wisdom” that the recent SFHs dwarfs are typically *dominated* by bursts. I refer to the conception that “dwarfs are bursty” as common wisdom because although this idea is often referred to in conversation, and anecdotally-supported allusions to it are sometimes found in the literature (e.g., Dong, Lin & Murray 2003; Elmegreen & Scalo 2006), well-substantiated statements of it are difficult to find in print.

It is in this context that we revisit this problem.

1.4 Overview of the Thesis

In this thesis, we quantify the prevalence of global starbursts in dwarf galaxies at the present epoch, and attempt to infer their characteristic durations, frequencies and amplitudes. Our approach is to directly tally the number of bursting dwarfs in a statistically complete local sample, and to compute the fraction of star formation that is concentrated in these systems. The resulting starburst number and mass fractions are then combined with $B - V$ colors from the literature, the $H\alpha$ EWs presented here, and stellar evolutionary synthesis models in order to place constraints on the average duty cycle. The primary dataset that we use has been put together by the 11 Mpc $H\alpha$ UV Galaxy Survey (11HUGS) team, who have constructed an approximately volume-limited, statistical sample of star-forming galaxies within 11 Mpc of the Milky Way. The $H\alpha$ -imaging component of the survey (Kennicutt et al. 2006, in preparation) yields measurements of the SFRs and birthrates (normalized SFRs) over the past $\sim 10^7$ yrs which are

needed for our analyses. We describe the survey and its completeness properties in Chapters 2 and 3, respectively.

Before focusing on solely on dwarf galaxies however, we take a step back and give a more general overview of the connections between the current star formation activity and the mass, luminosity and morphology of galaxies across the full extent of the 11HUGS sample in Chapter 4. To do this, we examine the parameter spaces defined by (i) M_B and the $H\alpha$ EW, and (ii) the disk rotational velocity V_{max} and the $H\alpha$ EW. Galaxies form sequences in these planes which exhibit two characteristic transitions. One occurs at $M_B \sim -19$ and $V_{max} \sim 120 \text{ km s}^{-1}$, where the more luminous and massive galaxies tend to have Sa–Sb bulge-dominated morphologies and EWs that turn-off toward lower values. The EW distribution of galaxies in this regime also has a dispersion that is larger by 50% as compared with the intermediate mass systems below the transition. The systematic drop of the EW indicates that star formation is shutting off above this particular mass threshold. This transition is another manifestation of the recently uncovered bimodality of the galaxy population, i.e., the general division at a stellar mass of $\sim 3 \times 10^{10} M_\odot$ over which the stellar populations in galaxies are predominantly red and old, and under which galaxies are blue and more actively star-forming (e.g., Kauffmann et al. 2003b, Blanton et al. 2005). The second transition occurs at $M_B \sim -15$ and $V_{max} \sim 50 \text{ km s}^{-1}$, where the least luminous and lowest mass galaxies in the sequence have predominantly irregular morphologies, and an EW distribution that is broader by a factor of 2. The region between these two transition, which is mostly populated by late-type spirals, thus has the tightest EW distribution. Possible explanation for the lower-mass feature include (i) burstier star formation due to negative feedback in physically small systems (e.g., as explored by Gerola et al. 1980), and/or the absence of the stabilizing effect of spiral

structure, and (ii) star formation “flickering,” statistical effects due to the very low average SFRs in these dwarfs (e.g., Hunter & Gallagher 1986).

Our main *observational* results on the prevalence of starbursts in dwarf galaxies are presented in Chapter 5. We first specify and justify our criteria for identifying starbursts as those systems with integrated $H\alpha$ EW larger than the 3σ limit of the logarithmic EW distribution (i.e $EW > 100\text{\AA}$). We then calculate the starburst number fraction, and the fraction of the dwarf galaxy $H\alpha$ luminosity density produced by these systems. The findings of this thesis, along with the accumulation of work on the star formation properties of dIrrs over the past three decades, paint a consistent picture in which dwarfs that are currently experiencing a massive global burst are just the $6 \pm 3\%$ tip of a low-mass galaxy iceberg. Moreover, bursts are responsible for $22 \pm 10\%$ of the total star formation in the overall dwarf galaxy population, so the majority of stars in low-mass systems are not formed in this mode *today*. This consistency is quite notable since the aggregate of these studies cover a broad range of independent approaches to the problem.

The *model-dependent* results of this thesis, however, are at odds with previous conclusions that the SFHs of typical dIrr galaxies are characterized by constant SFRs. We instead find that the majority of dIrrs are currently forming stars at rates that are depressed by $\sim 50\%$ relative to their lifetime averages. This disagreement can generally be traced back to changes over the past 30 years in the base assumptions that stellar evolutionary synthesis models are predicated on, which specifically can affect dwarf galaxies. We elaborate on these issues, and describe the model grid we have constructed and use here in Chapter 6.

Finally, the latter half of Chapter 6, we present and discuss the finding that bursts cycles appear to be necessary in order to simultaneously explain the present-day observed blue $B - V$ colors and modest $H\alpha$ EWs of *typical, currently non-*

bursting dIrrs, unless non-standard assumptions concerning the IMF and the escape fractions of Lyman continuum photons are made. The starburst cycle that we converge upon involves burst durations of 50-100 Myrs, cycle frequencies of $1-3 \text{ Gyr}^{-1}$, and elevated burst SFRs that are a factor of 6-10 higher than the rate in the quiescent state. Galaxies characterized by such a SFH would spend $\sim 10\%$ of their lives in the burst state, and form $\sim 50\%$ of their stellar mass during this time. We note that it is quite remarkable that such a SFH was predicted by the first back-of-the-envelope calculations of SSB73. This 10% duty cycle is in agreement with the observed starburst number fraction of 0.06 ± 0.03 . However, the $\sim 50\%$ mass fraction is only nominally consistent with the $22 \pm 10\%$ inferred using the “equal probability” assumptions, in which all dIrr galaxies are similarly able to burst and the observed starburst star formation fraction has been constant over cosmic time. If all of the inputs to our burst cycle solution are robust, then this nominal consistency indicates that the equal probability assumptions may not be entirely correct. We speculate that the most likely explanation may be that starbursts in low-mass systems have occurred at a different rate in the past.

CHAPTER 2

OBSERVATIONS OF THE CURRENT STAR FORMATION IN A COMPLETE SAMPLE OF DWARF GALAXIES

2.1 Introduction

The work in this thesis is primarily based upon data from an $H\alpha$ imaging survey of the 11 Mpc local volume, which is the result of a collaborative effort led by Robert Kennicutt and a team that includes data analyst Sanae Akiyama (Steward), Jose Funes (Vatican), Shoko Sakai (UCLA) and myself. The objectives of the survey extend far beyond those that are pursued in this thesis. Broadly, the goals are to characterize, using a complete sample, the star formation demographics of the local volume and to provide a foundation for follow-up studies of the HII region populations, star formation, chemical abundance, and ISM properties of the nearest galaxies. The program has obtained $H\alpha$ + $[NII]$ and R -band imaging for all known spiral and irregular galaxies which are within a distance of 11 Mpc, outside of the plane of the Milky Way ($|b| > 20^\circ$), and brighter than 15 B magnitudes. These bounds define the ranges over which the parent catalogs that we have used to build our sample are relatively complete, but observations have also been made for a number of other local galaxies that fall outside these limits. A UV imaging component was added to the survey subsequent to its essential completion, and the composite project was named 11HUGS, the 11 Mpc $H\alpha$ UV Galaxy Survey. The UV data is being obtained through two bands at 1500 Å and 2300 Å for a complete subset of the $H\alpha$ catalog galaxies through an ongoing GALEX Cycle 1 Legacy program, for which the collaboration has been extended to in-

clude Christy Tremonti (Steward) and Liese van Zee (Indiana). The combination of $H\alpha$ imaging, which provides snapshots of the ongoing star formation, and UV imaging, which traces star formation over a much longer $\sim 10^8$ yr timescale, will yield powerful constraints on the systematic errors in the inferred star formation related quantities.

The design and execution of the $H\alpha$ imaging program is described in this chapter to provide background for the analyses of the prevalence of global starbursts in low-mass systems. For more details the reader is referred to Kennicutt et al. (2006, in preparation). In Section 2.2, we describe the sample selection strategy with an emphasis on the dwarf galaxies of primary interest in this thesis. We also document the sample construction and compilation of ancillary literature data, and provide the final target catalog. In Section 2.3, we describe the observations and data reduction, and compare our integrated fluxes and EWs with measurements available in the literature. The 11HUGS catalog of integrated (galaxy-wide) $H\alpha + [\text{NII}]$ fluxes and EWs can be found at the end of this chapter.

The contributions of the team members to the project are as follows. The sample selection was carried out by Kennicutt and Sakai, the bulk of the observation by Kennicutt, Funes and Akiyama, and the image processing primarily by Akiyama. My roles mainly dealt with the flux calibration and measurements of the images, wrap-up observations for these purposes, and the compilation of ancillary data. I also subsequently refined and updated the sample, to ensure completeness for the calculation of the dwarf galaxy starburst statistics presented in Chapter 5. Note that all distance dependent quantities assume $H_0 = 75 \text{ km s}^{-1} \text{ Mpc}^{-1}$ throughout this entire work.

2.2 The 11HUGS Sample

2.2.1 The Motivations for, and Challenges in Assembling a Volume-Limited Sample in the Local Neighborhood

The definition of our sample was driven by two primary scientific objectives: to characterize the full range of star formation properties among local galaxies, and to constrain the starburst duty cycle in low-mass systems. Ideally, the dataset used for tackling these issues would be one that truly gives a complete inventory of the current star formation in *all* galaxies within a local volume, and further, one that is large enough to ensure decent number statistics. However, the ability to assemble such a dataset rests upon having a total census of the galaxy population within the given volume, and this is an impractical, if not unachievable, goal. After all, faint nearby galaxies are continually discovered, and the number of known galaxies within ~ 10 Mpc has doubled from ~ 200 to over 450 in the past ten years alone (e.g. Karachentsev et al 2004). Although these new additions most often have magnitudes which fall below the limits of the older, large, homogeneous catalogs such as Zwicky's CGCG ($B < 15.5$) and the UGC ($B_J < 14.5$), they are not all necessarily typical of the dead, gas poor dwarf spheroidals that most recent Local Group discoveries bring to mind (e.g. Canes Venatici dSph, Zucker 2006; Belokurov et al. 2006 and references therein). Some of the newly cataloged galaxies have been shown to have $H\alpha$ -derived star formation rates (SFRs) of $\sim 0.01 M_{\odot} \text{ yr}^{-1}$ (e.g. Karachentsev et al. 2005), which is common of the average system studied in the seminal work by Gallagher, Hunter and others on the star formation histories of dwarf irregular (dIrr) galaxies (e.g. Gallagher & Hunter 1984; Hunter & Gallagher 1986 and references therein). Thus, it appears that we might not yet be at the point of diminishing returns in an inventory of star formation of a statistical sample of nearby dwarf galaxies, even if this tally were based

on the most up-to-date and comprehensive of galaxy databases available today.

Nevertheless, we must begin somewhere, and as with other scientific endeavors, this somewhere is determined by the adequacy of the datasets available to address the objective at hand, and the outstanding issues surrounding that objective. Here we will focus most of our attention on the subject of this thesis, which concerns the star formation histories of dwarf galaxies.

To repeat some of the background given in the introductory chapter, solid groundwork has been laid over the past three decades in terms of revealing the nature of dIrrs as gas-rich, metal-poor, but not-necessarily-young galaxies which have enough fuel to sustain star formation at their current rates for another Hubble time. The aggregate of this work has also shown that dIrrs (which I will generically use to refer to the full suite of Im, Sm and BCD – star-forming dwarf – galaxies) have the most expansive range of star formation properties among late-type systems on the Hubble sequence. Galaxies with otherwise similar characteristics in the dIrr morphological class encompass those which are observed to be relatively quiescent and forming stars at rates which are a only few percent of their past average rate, to the spectacular instances of starbursting systems in which the current rate is enhanced by several times over the past average. This immediately brings to the forefront the outstanding issue of the possible evolutionary connections between the various star formation states of dwarfs. Progress in our understanding of this issue depends on our ability to constrain the starburst duty cycle in low-mass systems; that is, to quantify the characteristic frequencies and durations of starbursts and the mass fraction of stars formed in these episodes. However, work on astrophysical questions which demand samples of dwarf galaxies which are not only representative, but statistically complete, has been notoriously difficult simply because of the general challenges associated

with observing such faint objects.

Though the advent of large-format, high quantum efficiency CCDs and the ever-increasing size of telescope apertures has greatly ameliorated the difficulties involved with collecting data on large samples of faint, nearby galaxies, statistically complete samples of dwarf galaxies which span the full range of star formation properties had not yet materialized at the time of the inception of this project.

In light of this, we were motivated to carry out an observational program which would move us one step closer toward filling the need for a complete dataset on the star formation properties of the overall dwarf galaxy population. We have produced an approximation of an ideal total galactic star formation inventory of the local volume based on existing galaxy catalogs. Our program generally concentrates on obtaining $H\alpha$ imaging for all known spiral and irregular galaxies which are within a distance of 11 Mpc, outside of the plane of the Milky Way ($|b| > 20$), and brighter than 15 B magnitudes on the RC3 system. These constraints have been chosen as a compromise between two necessities: one to avoid the severe incompleteness that is known to set in at larger distances, fainter apparent magnitudes and lower Galactic latitudes, and another to try to keep the sample large enough such that an analysis of the dwarf galaxy starburst cycle based on this dataset is not entirely dominated by Poisson statistics. Within our imposed limits on B -band brightness and Galactic latitude, the current census of the inhabitants of the local volume should be fairly complete, and any incompleteness that does occur should be statistically correctable. The morphological selection was applied to avoid spending large amounts of observing time imaging elliptical, dwarf spheroidal, or gas-poor S0 galaxies, which are known to contain few if any detectable HII regions (Pogge & Eskridge 1987, 1993, Kennicutt

1998a). However, to address the more general scientific objective of characterizing the star formation properties over the full mass-spectrum of local volume galaxies, we include peculiar or unusually gas-rich early-type objects which are already known to contain significant amounts of star formation (e.g., Cen A = NGC 5128).

Even armed with a clear framework for constructing such a sample, the task of compiling a list of targets is still a non-trivial exercise. Although ambiguities can arise in determining which galaxies actually belong in a sample with a specified distance limit in *any* volume, they are more problematic within several Mpc of the Milky Way. Observed heliocentric recessional velocities of galaxies in the local neighborhood cannot be directly used to compute distances for the galaxies in our sample since they can be dominated by peculiar motions. Instead, a model must be used which at least corrects velocities for the motion of the Local Group and for infall onto the Virgo cluster. The computed flow-corrected velocities can vary by $\sim 15\%$ depending upon the precise model adopted, however, and even these cannot be employed blindly – attention must be paid to possible membership in less massive groups (e.g., Coma I, Leo and Fornax) whose gravitational effects have not been included in most models, but can also have a $\sim 15\%$ effect on the distances. Fortunately, we can think of no cosmological bias that would cause this uncertainty to systematically vary as a function of star formation properties, so we have proceeded in the following way, where we have tried to be practical but as comprehensive as possible.

2.2.2 Construction of the Sample

We have chosen to use the Nearby Galaxies Catalog (NBG) of Tully (1988) to build the foundation of our sample, since its completeness properties with distance are well understood and documented (Tully 1988c, Shaya et al. 1992). The NBG

lists 2367 galaxies that were known in 1978 to have $v_{\odot} \leq 3000 \text{ km s}^{-1}$. The contents of the NBG are mainly a combination of galaxies in the magnitude-limited Shapley-Ames sample ($B < 12$) and an all-sky HI survey based on a homogeneous re-inspection of photographic atlases by Tully, Fisher and collaborators. For each entry, the NBG provides a distance which is based on the Virgocentric flow model of Tully & Shaya (1984) and assumes $H_0 = 75 \text{ km s}^{-1} \text{ Mpc}^{-1}$. In the direction toward the Virgo cluster, model-based velocities are triple-valued, so Tully et al. have used independent distance estimators to identify the most probable velocity for galaxies within 28° of the Virgo core. In addition, galaxies with probable membership in 13 other massive clusters are identified and given distances consistent with the mean flow-corrected velocity of the cluster. One of the many other contributions of the NBG is that it also gives affiliations for over 98% of its entries with gravitationally bound groups and looser associations, or “clouds.” These cluster, group and cloud assignments are particularly important for the treacherous fine-tuning of our initial sample, as will be discussed in a moment.

From the NBG, a list of 315 candidates was generated by selecting galaxies with NBG reported morphological types later than S0/a (i.e. with non-negative Hubble type codes) and distances less than 11 Mpc. *There were no Galactic latitude or apparent magnitude restrictions applied to this list.* However, the following modifications were made based on more recently published direct distances and group membership. The Coma I group (NBG cloud 14 group -1), which was previously assigned a distance of 9.7 Mpc in the NBG, was subsequently placed far beyond 11 Mpc (e.g. at 16.4 Mpc, by Trentham & Tully 2002). Further, it has a cepheid measurement to one of its members, NGC 4414, of 17.70 Mpc (Freedman et al. 2001). Thus, the 17 spiral and irregular galaxies associated with this struc-

ture were removed from our candidate list. In addition, 4 galaxies associated with the NGC 3184 group (NBG cloud 15 group +7) by Ferrarese et al. (2000b) were excluded since cepheid distances to two of its members, NGC 3319 and NGC 3198, show that the group is at a distance of ~ 13.6 Mpc (Freedman et al. 2001). Three other galaxies with new cepheid distances were also removed. NGC 2090 and NGC 2541, have distances of 11.75 and 11.22, respectively, as reported by Freedman et al. 2001, while Leonard et al. (2002) places NGC 1637 at a distance of 11.7 Mpc. Another galaxy, NGC 3985, with $d(\text{NBG})=8.3$ Mpc, was later identified to be a member of the Ursa Major cluster which is at 18.6 Mpc (Tully & Pierce 2000), and was omitted as well. NGC 4517, with $d(\text{NBG})=10.4$ Mpc, was also excluded as it was identified to be associated with the Virgo cluster by Gavazzi et al. (2002). Finally, a cross check of recessional velocities given in the NBG with measurements collected by NED for the remaining candidates showed that five galaxies have updated redshifts which place them well outside the local volume. These galaxies, NGC 4687, NGC 4941, NGC 7518, CGCG 413-002 and ESO347-IG007, were not retained in the candidate list either. This leaves us with 284 galaxies from the NBG.

Of course, there have been many new redshifts measured and additional galaxies identified since the compilation of the NBG. To account for these objects, a second list of candidates was generated by first searching NED for all galaxies with $|b| > 20^\circ$, $B < 15$ and $v_\odot \leq 3000 \text{ km s}^{-1}$. Applying these restrictions on this search produces a sample which approximately replicates the overall characteristics of the NBG catalog. Heliocentric velocities were corrected using a flow-field model and galaxies with distances greater than 11 Mpc (where a Hubble constant of $75 \text{ km s}^{-1} \text{ Mpc}^{-1}$ is used to maintain consistency with the NBG) were eliminated. We use a linear velocity field model which includes a single attractor, the Virgo

Cluster, based on the algorithm outlined by the H_o HST Key Project (Mould et al. 2000). The model used to calculate distances for the NBG is not straightforward to precisely reproduce, particularly in the large volumes toward Virgo and Coma I, so we have simply opted to use this alternate model. The overall differences between NBG flow model and the one employed here are relatively generic — they involve the choice of the correction to the Local Group centroid (e.g., the prescription of Yahil, Tammann & Sandage (1977) vs. the IAU adopted $300 \sin l \cos b$) and in the parameters describing the correction for Virgocentric flow (e.g. infall velocity, position and extent of the cluster). After the distance limit was applied, elliptical and lenticular galaxies were removed from the NED candidate list.

At this point, it would appear as if the process of identifying galaxies based on our previously established criteria has been completed. However, we have yet to fold in the wealth of information on galaxies with primary and secondary distance measurements or group membership. The latter issue of a galaxy’s affiliation with structures which may perturb the flow velocities by more than $\sim 15\%$ is not an entirely straightforward one to deal with since ambiguities in group/cluster assignments will arise for dynamically complex regions, as well as for objects at the peripheries of the structures. This is another reason we chose to use the NBG as a starting point for constructing our sample – much of this work has already been done for the galaxies tabulated there. Thus, the strategy applied to fine-tune the NED candidate list is one that is: (1) based on the membership assignments given by the NBG and supplemented by those discussed in the appendix of Ferrarese et al. 2000b, and (2) tied to cepheid and SBF derived distances to central members of the groups/clusters (Ferrarese et al. 2000b, Freedman et al. 2001, Tonry et al. 2001). We now proceed to document the details of the modifi-

cations made to the candidate list in this last step.

The main structures that contaminate our sample with distant galaxies are the Coma I group (16.4; Trentham & Tully 2002), the Ursa Major cluster (18.6 Mpc; Tully & Pierce 2000), and the Virgo Cluster (17.0 Mpc; Trentham & Tully 2002) and its satellite groups. All NBG galaxies affiliated with cloud 14 group -1 (Coma I) or cloud 11 group -1 (Virgo) were removed. Ursa Major cluster (cloud 12 group -1) members were eliminated based on the more recent Ursa Major catalog of Tully et al. (1996). Galaxies associated with several smaller groups were also omitted. These groups are: the N3184 group (15 +7; $\langle D(\text{cepheid}) \rangle \sim 13.6$ Mpc, Freedman et al. 2001), the Leo Cloud (cloud 21; $\langle D(\text{SBF}) \rangle \sim 20$ Mpc, Tonry et al. 2001), the Fornax cluster (51 -1; $\langle D(\text{cepheid}) \rangle = 19.0$ Mpc, Freedman et al. 2001), and the Dorado or NGC 1566 cluster (53 -1; $\langle D(\text{Fundamental Plane}) \rangle = 13.8$ Mpc, Freedman et al. 2001). Galaxies in our NED candidate list that were not originally included in the NBG were removed if they were found to lie within the velocity, RA, or DEC ranges formed by one of these NBG assemblages. On the other hand, galaxies with flow-corrected velocities greater than 11 Mpc, but within two groups near the boundary of the volume with cepheid distances less than 11 Mpc were retained. These are the NGC 1023 group (cloud 17 group -1) with a distance to NGC 925 of 9.16 Mpc, and the Leo I group (cloud 15 group -1) with an average distance to NGC 3351 and NGC 3368 of 10.0 Mpc (Freedman et al. 2001). When completed this process leaves us with 58 spiral and irregular galaxies with $|b| > 20^\circ$ and brighter than 15 NED “indicative optical magnitudes” that are not in our first sample of 284 NBG galaxies.

Clearly, the use of NED magnitudes to identify galaxies brighter than our chosen limit may be problematic. Although the NED “Basic Data” compilation uses *B*-band measurements from the RC3 (de Vaucouleurs, et al. 1991) whenever pos-

sible, it also compiles photometry from other smaller studies when RC3 magnitudes are not available. Most frequently, the tabulated data from other sources in the literature correspond to B -band photometry (although these have not been reduced to a homogeneous system with the RC3 magnitudes), but data in other filters are also collected as necessary to provide an “indicative optical magnitude.” In spite of this, the combination of the NBG and NED target lists should still yield a sample which represents virtually all known spiral and irregular galaxies brighter than 15 RC3 B_T magnitudes, within our given distance and Galactic latitude limits. This is because we have found that the NED non-RC3 magnitudes tend to be systematically brighter than measurements that we have subsequently compiled which *have* been homogenized to the RC3 system (i.e. B magnitudes from the Hyperleda database).¹ Thus, the sample as currently defined will contain some galaxies fainter than $B(\text{RC3})=15$, but should be fairly complete to that brightness. More rigorous tests of the sample’s completeness properties have been performed and a thorough discussion of both its completeness and other general properties will be given in the following chapter.

As will be described in detail in the next section, calibrated $H\alpha$ images have been obtained by our group for the majority of the NBG and NED final candidate lists over a four year campaign, using three different telescopes in both northern and southern hemispheres. Further, $H\alpha$ measurements have been compiled from the literature for those galaxies which were not observed. The resulting dataset presented here helps fill a critical need for statistical studies of the star formation properties of dwarf galaxies, but again, it is still only an approximation of an ideal total star formation inventory of the local volume. Although we would expect that our sample is relatively complete to the specified limits, there remains

¹We note that although this is true at the time of the final revision of our sample (June 2005), it may not be true at some later date since NED is of course a dynamic repository of data.

the population of galaxies within 11 Mpc that may have on-going star formation, but which lies outside the boundaries that we have imposed on Galactic latitude, B -band brightness and morphology. During the course of our observational campaign, we have used gaps in our program to obtain data for some of these objects. $H\alpha$ images, fluxes and EWs are also available in the literature for several other of these galaxies. The aggregate of those measurements from the literature and the ones accumulated by our group for galaxies at low Galactic latitudes $|b| < 20^\circ$, fainter than 15 B magnitudes, and/or with elliptical or lenticular morphologies can be thought of as the beginning of a sample which represents a 1st (or 2nd) order correction to our approximation of the wholly complete star formation inventory. A justification for or against conducting another $H\alpha$ survey for a deeper statistical sample of local galaxies is not clear at the time of the writing of this chapter, but will be revisited later after the analysis of the dwarf galaxy starburst duty cycle in Chapter 6.

In Table 2.1, we tabulate the galaxies, along with the properties relevant for their selection, in our final candidate lists of 284 NBG galaxies and 58 galaxies compiled from NED. We also include an additional 57 galaxies with existing $H\alpha$ measurements that are within 11 Mpc (based on our flow field model) but are not within the bounds of the initial NBG or NED samples. Taken altogether, the 399 galaxies listed in Table 2.1 and the $H\alpha$ measurements that we have collected for them, both from the literature and from our own observations, comprise the $H\alpha$ dataset of 11HUGS, and embody an exhaustive synthesis of our present state of knowledge of the star formation currently occurring in galaxies within 11 Mpc as inferred through this nebular recombination line.

2.2.3 A Catalog of Star-Forming Galaxies within 11 Mpc

The 399 galaxies in the resultant $H\alpha$ sample described above constitute the general 11HUGS catalog. Sub-samples for subsequent studies (including the UV component of the survey) are derived from this parent set of galaxies. The galaxies and the general properties relevant for their selection are given in Table 2.1.

The information listed in the columns there are as follows:

Column (1) – The running index number in this table.

Column (2) – Internal 11HUGS reference ID number.

Column (3) – Galaxy name.

Columns (4-5) – J2000 equatorial coordinates.

As reported in NED.

Column (6) – Galactic latitude.

Column (7) – Heliocentric recessional velocity.

As reported in NED. *In $km\ s^{-1}$.*

Column (8) – Flow-field corrected recessional velocity.

A linear velocity field model is employed which includes a single attractor (the Virgo Cluster) and a correction to the Local Group centroid as specified by Yahil, Tammann & Sandage (1977). The algorithm used is based on the prescription in Mould et al. 2000 by the H_o HST Key Project. *In $km\ s^{-1}$.*

Column (9) – NBG distance.

Distance as reported in the Nearby Galaxies Catalog (NBG, Tully 1988). The NBG provides a distance which is based on the Virgocentric flow model of Tully & Shaya (1984) and assumes $H_o = 75\ km\ s^{-1}\ Mpc^{-1}$. In the volume surrounding the Virgo cluster, model-based velocities are triple-valued, so Tully et al. have used independent distance estimators to identify the most probable velocity for galaxies within 28° of

the Virgo core. In addition, galaxies with probable membership in 13 other massive clusters are identified and given distances consistent with the mean flow-corrected velocity of the cluster. *In Mpc.*

Column (10-11) – Adopted distance & distance determination method.

Direct measurements from the literature, such as those based on standard candles, are adopted when available. The majority of these measurements for galaxies in our 11 Mpc sample has also been compiled and recently published by Karachentsev et al. (2004) in their *Catalog of Neighboring Galaxies* (hereafter, KKHM). We have simply chosen to adopt the direct measurements listed in KKHM, unless updated values are given by Freedman et al. (2001) or Mould et al. (2005). If direct measurements are not available, distances are computed from the flow corrected velocities listed in column 8, using $H_0 = 75 \text{ km s}^{-1} \text{ Mpc}^{-1}$. *In Mpc.*

The methods used to determine the tabulated distances are: the luminosity of cepheids “ceph,” the luminosity of the tip of the red giant branch “trgb,” surface brightness fluctuations “sbf,” membership in known groups “mem,” the luminosity of the brightest stars “bs,” and the Tully-Fisher relation “tf.” Flow model derived distances are indicated with “v(flow).”

Column (12) – Morphological type & classification error.

Revised de Vaucouleurs morphological types were taken from the HyperLeda database. The numerical codes follow those established in the RC2. A dozen objects without types in Hyperleda, all of which are dwarf galaxies, were assigned codes based on the classification listed by NED. Further, since starbursting dwarf galaxies, a.k.a blue compact dwarfs (BCDs) or HII galaxies, are often misclassified as ellipticals, the

morphological codes for 17 galaxies which appear in the Palomar/Las Campanas Atlas of BCDs (Gil de Paz et al. 2003) were checked. Nearly all of these galaxies were either indeed classified as ellipticals, had large errors ($\text{err}(T) \leq 3$) or were not classified at all. These dwarfs were (re-)assigned a code of 11 (compact irregular). All galaxies with classifications given by us have $\text{err}(T)$ set to -999.

Column (13) – Apparent *B*-band magnitude & error.

B-band photometry has been compiled from the literature, and adopted from the following large, homogeneous, catalogs in the following order of preference, when available: (1) B_T from the collection of dwarf galaxy observations obtained by van Zee, Haynes & Salzer (e.g. van Zee, Haynes & Salzer 1997), and Binggeli, Barazza, Bremnes, Parodi & Prugniel (e.g. Parodi, Barazza & Binggeli 2002), (2) B_T as reported in the RC3 (de Vaucouleurs et al 1991), and (3) B_T as compiled and reduced to the RC3 system by HyperLeda. For a small number of objects (18 galaxies), a measurement is not available from one of these sources. In these cases, the literature is searched and a *B* magnitude taken from smaller datasets of photometry given in individual papers. As a last resort, the “indicative optical magnitude” listed on NED is adopted in 8 cases.

Column (14) – Reference codes for photometry and distances.

The key to the reference codes are given in Table 2.2. Numerals give distance references, while letters give those for the photometry. Negative numerals indicate distances adopted from KKH, where the original distance reference cited in their compilation has been repeated here for completeness and convenience.

TABLE 2.1 – The 11HUGS Sample

#	ID	Galaxy Name	RA(J2000)	DEC(J2000)	b	cz	v(flow)	D(NBG)	D	method	T	err(T)	B	err(B)	References
(1)	(2)	(3)	(4)	(5)	(6)	(7)	(8)	(9)	(10)	(11)	(12)	(13)	(13)	(14)	
1	2000	UGC12894	000022.5	392944	-22.32	335	619	...	8.3	v(flow)	10	1	16.55	0.2	0 k
2	1	WLM	000158.1	-152739	-73.63	-116	-5	1	0.92	trgb	10	2	11.03	0.08	-5 a
3	2	ESO349-G031	000813.3	-343442	-78.12	207	190	2.4	4.1	tf	10	1	15.56	0.2	-25 b
4	3	N00024	000956.7	-245744	-80.43	554	544	6.8	7.3	v(flow)	5	1	12.19	0.13	0 a
5	4	N00045	001404.0	-231055	-80.67	471	473	5.9	6.3	v(flow)	8	1	11.32	0.08	0 a
6	5	N00055	001454.0	-391149	-75.74	129	101	1.3	1.8	tf	9	1	8.42	0.05	-25 a
7	6	NGC0059	001525.4	-212642	-80.02	382	398	...	5.3	sbf	-3	1	13.12	0.14	-15 a
8	7	MCG-04-02-003	001911.4	-224006	-81.44	669	658	...	8.8	v(flow)	9	3	15.57	0.32	0 b
9	8	U00192	002023.1	591735	-3.34	-348	-58	0.7	0.66	ceph	10	1	11.8	0.2	-11 a
10	9	N00224	004244.3	411609	-21.57	-300	-14	0.7	0.79	ceph	3	1	4.36	0.02	3 a
11	10	IC1574	004303.8	-221449	-84.76	361	368	4.5	4.92	trgb	10	1	14.50	0.08	-25 k
12	11	N00247	004708.3	-204538	-83.56	160	194	2.1	4.1	tf	7	1	9.67	0.07	-25 a
13	12	N00253	004733.1	-251718	-87.96	241	247	3	3.94	trgb	5	1	8.04	0.05	-25 a
14	13	UGC A015	004949.2	-210054	-83.88	301	317	3.7	3.34	trgb	10	1	15.38	0.11	-25 k
15	2002	UGC00521	005112.2	120131	-50.85	659	793	...	10.6	v(flow)	10	1	15.31	0.02	0 m
16	14	SMC	005244.8	-724943	-44.33	158	-29	0.1	0.06	ceph	9	1	2.7	0.1	-11 a
17	15	N00300	005453.5	-374100	-79.42	144	110	1.2	2.00	ceph	7	1	8.72	0.05	3 a
18	2003	LGS3	010355.0	215306	-40.89	-287	-45	...	0.62	trgb	13	-999	16.18	-999	-39 g
19	16	U00668	010447.8	020704	-60.56	-234	-54	0.7	0.65	ceph	10	1	9.88	0.09	3 a
20	17	UGC00685	010722.4	164102	-46.02	157	341	...	4.79	trgb	9	1	14.20	0.08	-32 k
21	18	UGC00695	010746.4	010349	-61.53	664	741	...	9.9	v(flow)	6	2	15.28	0.39	0 b
22	19	U00891	012118.9	122443	-49.80	643	770	9.4	10.3	v(flow)	9	1	14.72	0.04	0 k
23	20	UGC01056	012847.3	164119	-45.26	595	742	...	9.9	v(flow)	10	2	14.87	0.41	0 b
24	2004	UGC01104	013242.5	181902	-43.47	686	836	...	7.5	bs	9	3	14.41	0.03	-47 k
25	21	N00598	013350.9	303937	-31.33	-179	69	0.7	0.84	ceph	6	1	6.27	0.03	3 a
26	22	N00625	013504.2	-412615	-73.12	405	324	3.9	4.07	trgb	9	1	11.71	0.13	-29 a
27	23	N00628	013641.7	154659	-45.71	657	794	9.7	7.3	bs	5	1	9.95	0.1	-47 a
28	24	U01176	014009.9	155417	-45.37	633	772	9.3	9	bs	10	1	14.4	0.2	-47 a
29	25	U01195	014227.0	135837	-47.07	774	895	10.8	11.9	v(flow)	10	2	14.2	0.6	0 b
30	27	UGC A020	014314.7	195832	-41.25	498	662	8	8.8	v(flow)	10	1	15.78	0.02	0 l
31	28	ESO245-G005	014503.7	-433553	-70.29	395	305	3.6	4.43	trgb	10	1	12.7	0.2	-25 a
32	29	U01249	014730.6	271952	-33.90	338	544	6.4	7.2	bs	9	1	12.07	0.19	-14 a
33	30	N00672	014754.3	272559	-33.78	421	622	7.5	7.2	bs	6	1	11.47	0.1	-14 a
34	31	U01281	014931.4	323519	-28.71	156	392	4.6	4.2	trgb	8	1	13.61	0.04	4 k
35	2005	ESO245-G007	015106.3	-442641	-68.95	56	-17	...	0.44	trgb	10	1	13.33	0.175	-13 b
36	33	N00784	020117.0	285015	-31.59	198	414	4.7	3	trgb	8	1	12.23	0.08	4 a
37	34	U01561	020405.1	241230	-35.75	610	782	9.3	10.4	v(flow)	10	1	16.23	0.34	0 b
38	1001	NGC0855	021403.6	275238	-31.53	595	785	...	9.73	sbf	-5	2	13.3	0.13	-52 a

TABLE 2.1 – Continued

#	ID	Galaxy Name	RA(J2000)	DEC(J2000)	b	cz	v(flow)	D(NBG)	D	method	T	err(T)	B	err(B)	References
(1)	(2)	(3)	(4)	(5)	(6)	(7)	(8)	(9)	(10)	(11)	(12)	(13)	(14)	(15)	(16)
39	35	U01807	022113.4	424546	-17.12	629	879	10.9	9.16	mem	10	1	16.5	-999	2 z
40	36	N00891	022233.4	422057	-17.41	528	781	9.6	9.16	mem	3	1	10.81	0.18	2 a
41	37	U01865	022500.2	360216	-23.10	580	803	9.8	9.16	mem	9	1	14.37	0.3	2 b
42	38	N00925	022716.9	333445	-25.17	553	766	9.4	9.16	ceph	7	1	10.69	0.11	3 a
43	2006	UGC01924	022749.8	314336	-26.82	598	803	...	10.7	v(flow)	6	1	15.23	0.10	0 k
44	39	N00949	023048.6	370814	-21.63	609	835	10.3	9.16	mem	4	2	12.4	0.14	2 a
45	40	N00959	023224.0	352942	-23.00	597	816	10.1	9.16	mem	8	1	12.95	0.14	2 a
46	41	U02014	023254.0	384050	-20.05	565	799	9.9	9.16	mem	10	1	15.65	0.18	2 a
47	42	U02023	023318.2	332928	-24.74	603	812	10.1	9.16	mem	10	1	13.88	0.12	2 k
48	43	U02034	023342.9	403141	-18.29	578	819	10.2	9.16	mem	10	2	13.7	0.2	2 a
49	44	U02082	023616.1	252527	-31.70	707	874	10.7	11.7	v(flow)	6	1	13.69	0.12	0 a
50	45	ESO115-G021	023748.1	-612018	-51.43	513	357	4.5	4.66	trgb	8	1	13.34	0.1	-26 j
51	46	N01003	023916.6	405221	-17.54	626	866	10.7	9.16	mem	6	1	12	0.08	2 a
52	47	Maffei2	024154.9	593615	-0.33	-17	279	3.4	2.8	tf	4	1	14.77	0.29	-27 f
53	48	N01058	024329.9	372027	-20.37	518	746	9.1	9.16	mem	5	1	11.82	0.15	2 a
54	49	U02259	024755.4	373218	-19.80	583	809	10	9.16	mem	8	1	15.16	0.26	2 b
55	50	ESO154-G023	025650.4	-543417	-54.31	578	432	5.4	5.8	v(flow)	8	2	12.69	0.1	0 j
56	51	N01156	025942.6	251417	-29.20	375	553	6.4	7.8	bs	10	1	12.75	0.1	-20 j
57	52	ESO300-G014	030937.8	-410150	-58.46	951	824	10.1	11	v(flow)	9	1	13	0.3	0 a
58	53	N01249	031001.3	-532009	-53.41	1074	912	10.7	12.2	v(flow)	6	1	12.19	0.14	0 a
59	54	N01291	031718.3	-410628	-57.05	839	715	8.6	9.5	v(flow)	0	1	9.39	0.04	0 a
60	55	N01313	031815.8	-662953	-44.64	475	300	3.7	4.15	trgb	7	1	9.2	0.2	-38 a
61	56	N01311	032007.4	-521107	-52.66	571	427	5.2	5.7	v(flow)	9	1	13.18	0.1	0 j
62	57	U02684	032023.7	171745	-32.75	350	488	5.5	6.5	bs	10	1	16.30	0.02	-47 m
63	58	UGC02689	032127.7	404806	-13.68	277	519	...	6.9	v(flow)	-2	1	14.95	0.1	0 c
64	59	UGC02716	032407.2	174512	-31.82	379	517	...	6.9	v(flow)	8	1	14.64	0.1	0 j
65	60	IC1959	033311.8	-502438	-51.54	640	496	6	6.6	v(flow)	9	1	13.26	0.1	0 j
66	61	U02847	034648.9	680546	10.58	31	327	3.9	3.28	ceph	6	1	9.1	0.14	-45 a
67	62	IC2000	034907.3	-485131	-49.60	980	827	10.3	11	v(flow)	6	1	12.8	0.6	0 b
68	63	ESO302-G014	035140.9	-382708	-50.88	881	758	9.3	10.1	v(flow)	10	1	15.5	0.5	0 b
69	64	N01487	035546.1	-422205	-49.76	848	715	8.9	9.5	v(flow)	7	3	12.34	0.07	0 a
70	65	ESO249-G036	035915.6	-455221	-48.61	901	756	9.4	10.1	v(flow)	10	1	15.75	0.31	0 b
71	66	UGCA086	035950.1	670837	10.65	67	363	4.4	2.65	bs	10	1	13.5	-999	-21 z
72	1003	NGC1510	040332.6	-432400	-48.23	913	771	10.3	10.3	v(flow)	-2	1	13.47	0.11	0 a
73	67	N01512	040354.3	-432057	-48.16	896	758	9.5	10.1	v(flow)	1	1	11.13	0.1	0 a
74	68	N01507	040427.2	-021118	-37.56	863	882	10.6	11.8	v(flow)	8	2	12.89	0.15	0 a
75	69	NGC1522	040607.7	-524009	-45.97	905	744	...	9.9	v(flow)	10	-999	13.93	0.13	0 a
76	70	N01518	040649.6	-211029	-45.31	927	862	10.5	11.5	v(flow)	8	1	12.28	0.13	0 a

TABLE 2.1 – Continued

#	ID	Galaxy Name	RA(J2000)	DEC(J2000)	b	cz	v(flow)	D(NBG)	D	method	T	err(T)	B	err(B)	References
(1)	(2)	(3)	(4)	(5)	(6)	(7)	(8)	(9)	(10)	(11)	(12)	(13)	(13)	(14)	
77	71	IC2049	041204.3	-583325	-43.35	869	697	...	9.3	v(flow)	7	1	15.19	0.49	0 b
78	72	ESO483-G013	041241.3	-230936	-44.58	823	753	...	10	v(flow)	-3	1	14.18	0.36	0 b
79	73	NGC1556	041744.5	-500952	-44.78	982	823	...	11.0	v(flow)	2	1	13.47	0.13	0 a
80	74	UGCA090	042113.5	-215044	-42.31	906	838	10.1	11.2	v(flow)	7	1	12.67	0.18	0 a
81	75	N01569	043049.0	645053	11.24	-104	148	1.6	1.95	bs	10	2	11.86	0.09	-34 a
82	76	UGCA092	043204.9	633649	10.52	-99	151	1.5	1.8	bs	10	1	15.22	-999	-21 g
83	77	N01560	043247.7	715246	16.02	-36	241	3	3.45	trgb	7	1	12.16	0.14	-27 a
84	2007	ESO158-G003	044616.7	-572035	-39.30	975	799	13.3	10.7	v(flow)	9	1	14.006	0.09	0 b
85	79	U03174	044834.5	001430	-26.91	670	702	8.2	9.4	v(flow)	10	1	15.02	0.02	0 m
86	80	ESO119-G016	045129.2	-613903	-37.77	969	788	10.4	10.5	v(flow)	10	1	14.79	0.2	0 b
87	81	N01705	045413.7	-532141	-38.74	628	462	6	5.1	trgb	10	-999	12.77	0.13	-53 a
88	82	N01744	045957.6	-260119	-35.02	748	664	7.8	8.8	v(flow)	7	2	11.6	0.3	0 a
89	83	N01796	050242.8	-610823	-36.55	987	806	10.6	10.7	v(flow)	5	1	12.86	0.13	0 a
90	84	ESO486-G021	050319.7	-252523	-34.13	865	781	...	10.4	v(flow)	2	2	14.47	0.2	0 b
91	85	MCG-05-13-004	050624.1	-315711	-35.12	686	579	...	7.7	v(flow)	9	3	13.22	0.43	0 b
92	86	N01800	050625.4	-315715	-35.12	803	696	7.4	9.3	v(flow)	9	3	13.07	0.1	0 j
93	87	N01808	050742.3	-373046	-35.90	1000	871	10.8	11.6	v(flow)	1	1	10.76	0.1	0 a
94	88	UGCA103	051047.0	-313550	-34.14	981	872	10.8	11.6	v(flow)	9	1	13.13	0.15	0 a
95	89	UGCA106	051159.3	-325821	-34.20	933	820	10.2	10.9	v(flow)	9	1	13.05	0.23	0 b
96	90	UGCA105	051415.0	623431	13.66	111	380	4.5	3.15	trgb	10	1	14.46	0.22	-24 b
97	91	LMC	052334.5	-694522	-32.89	278	48	0.1	0.05	ceph	9	1	0.91	0.05	-55 a
98	92	U03303	052459.5	043018	-16.92	522	568	6.6	7.2	bs	10	1	13.95	0.1	-33 j
99	2008	ESO553-G046	052705.7	-204041	-27.42	543	472	...	6.3	v(flow)	1	3	14.528	0.146	0 b
100	93	UGCA114	055054.3	-144645	-19.94	902	859	10.7	11.5	v(flow)	7	1	12.97	0.1	0 b
101	94	UGCA116	055542.6	032330	-10.77	789	831	10.3	11.1	v(flow)	5	2	15.48	0.13	0 a
102	95	ESO364-G7029	060545.2	-330451	-23.37	787	669	8.3	8.9	v(flow)	10	1	14	0.21	0 b
103	96	AM0605-341	060719.3	-341217	-23.40	772	650	...	8.7	v(flow)	10	2	15.52	0.42	0 b
104	97	N02188	061009.5	-340622	-22.81	749	626	7.9	8.3	v(flow)	9	2	12.14	0.13	0 a
105	98	UGCA120	061116.3	-213557	-18.19	854	781	9.7	10.4	v(flow)	10	1	14.08	0.16	0 b
106	99	UGCA127	062055.5	-082942	-10.61	734	714	8.7	9.5	v(flow)	6	1	14.16	0.1	0 b
107	100	U03475	063028.8	393014	13.14	487	689	8.6	9.2	v(flow)	9	1	15	0.14	0 b
108	101	UGC03600	065540.0	390543	17.48	412	592	...	7.3	bs	10	1	16.19	0.1	-33 j
109	102	AM0704-582	070518.8	-583113	-21.15	554	343	...	4.9	trgb	9	1	14.95	0.1	-26 j
110	103	N02337	071013.5	442726	21.80	436	642	8.2	7.9	bs	10	1	13.48	0.1	-33 j
111	104	U03817	072244.5	450631	24.11	438	643	8.3	8.6	bs	10	1	15.96	-999	-33 i
112	105	U03860	072817.2	404612	23.93	354	514	7.2	7.81	trgb	10	2	15.07	0.14	-29 a
113	106	N02366	072854.6	691257	28.53	100	344	2.9	3.19	trgb	10	1	11.43	0.1	-26 a
114	107	ESO059-G001	073118.2	-681117	-21.48	528	303	4.4	4	v(flow)	10	1	13.98	0.1	0 j

TABLE 2.1 – Continued

#	ID	Galaxy Name	RA(J2000)	DEC(J2000)	b	cz	v(flow)	D(NBG)	D	method	T	err(T)	B	err(B)	References
(1)	(2)	(3)	(4)	(5)	(6)	(7)	(8)	(9)	(10)	(11)	(12)	(13)	(14)	(15)	(16)
115	108	N02427	073627.9	-473805	-12.70	972	811	10.9	10.8	v(flow)	8	1	12.33	0.1	0 a
116	109	N02403	073651.4	653609	29.18	131	364	4.2	3.22	ceph	6	1	8.93	0.07	3 a
117	110	U03966	074126.0	400644	26.17	361	511	7.4	6.8	bs	10	1	13.9	0.3	-12 a
118	111	U03974	074155.4	164809	18.54	272	264	2.1	5.18	trgb	10	1	13.6	0.3	-26 a
119	112	CGCG262-028	074732.1	511129	29.37	454	685	...	9.1	v(flow)	5	3	14.93	0.41	0 b
120	113	U04115	075701.8	142327	20.90	338	318	3.2	5.49	trgb	10	1	15.23	0.1	-26 j
121	114	N02500	080153.3	504415	31.56	514	751	10.1	10	v(flow)	7	1	12.2	0.13	0 a
122	115	N02537	081314.7	455926	32.96	447	636	9	6.9	bs	9	2	12.82	0.1	-47 j
123	117	U04278	081358.9	454434	33.06	565	781	10.6	10.4	v(flow)	7	1	13.07	0.15	0 a
124	119	U04305	081904.0	704309	32.69	157	408	4.5	3.39	trgb	10	1	11.1	0.15	-26 a
125	120	N02552	081920.1	500025	34.29	524	753	10	10	v(flow)	9	1	12.56	0.15	0 a
126	121	M81dwA	082356.0	710145	33.01	113	354	4.3	3.55	trgb	10	-999	18.69	0.1	-26 d
127	122	U0426	082828.4	415124	35.21	397	537	6.3	5.7	bs	10	1	15	0.2	-33 a
128	123	U04459	083407.2	661054	34.95	19	210	2	3.56	trgb	10	1	14.78	0.1	-26 j
129	124	ESO495-G021	083615.4	-262434	8.58	873	759	10.5	10.1	v(flow)	10	-999	12.46	0.09	0 b
130	125	U4483	083703.0	694631	34.38	178	425	...	3.21	trgb	10	1	15.27	0.1	-6 j
131	126	N02683	085241.4	332514	38.76	411	478	5.7	7.7	sb	3	1	10.64	0.07	-52 a
132	127	U04704	085900.3	391236	40.74	596	759	8.7	10.1	v(flow)	8	1	15.33	0.41	0 b
133	209	LSBCD564-08	090253.8	200432	37.60	483	469	...	6.3	v(flow)	10	-999	16.9	-999	0 g
134	128	U04787	090734.9	331636	41.81	552	650	7.8	8.7	v(flow)	8	1	15.41	0.32	0 b
135	2010	LSBCD634-03	090853.5	143455	36.94	318	230	...	3.1	v(flow)	10	-999	17.5	-999	0 z
136	129	UGC A148	090946.5	-230033	16.66	725	572	7	9.8	mem	10	1	15.32	0.19	-40 a
137	1007	NGC2784	091219.5	-241021	16.35	691	523	7.1	9.82	sb	-2	1	11.30	0.13	-52 a
138	130	UGC A153	091312.1	-192431	19.59	765	633	8	8.4	v(flow)	10	1	15.4	0.1	0 j
139	131	N02835	091752.9	-222118	18.51	888	778	10.8	10.4	v(flow)	5	1	11.01	0.17	0 a
140	2011	LSBCD565-06	091930.0	213612	41.76	498	479	...	6.4	v(flow)	10	-999	16.95	-999	0 g
141	132	UGC A162	092128.1	-223007	19.03	850	727	9.9	9.7	v(flow)	9	2	15.24	0.18	0 b
142	133	UGC04998	092512.1	682259	38.89	623	956	...	10.5	sb	10	1	14.72	0.1	0 j
143	134	N02915	092611.5	-763736	-18.36	468	227	3.3	3.78	trgb	1	2	13.2	0.1	-26 j
144	135	N02903	093210.1	213004	44.54	556	539	6.3	8.9	bs	4	1	9.68	0.1	-8 a
145	1009	UGC05076	093236.4	515219	45.57	571	798	...	10.6	v(flow)	10	1	15.21	0.41	0 b
146	2012	UGC A168	093321.5	-330201	13.64	925	785	11.1	10.5	v(flow)	6	1	12.80	0.20	0 a
147	136	CGCG035-007	093444.9	062532	38.99	574	467	...	6.2	v(flow)	5	3	15.46	0.19	0 b
148	137	UGC0151	094027.1	482015	47.60	773	1040	6.9	13.9	v(flow)	10	2	13.78	0.45	0 b
149	138	U05139	094032.3	711056	38.66	143	376	4.4	3.84	trgb	10	1	14.17	0.1	-26 j
150	140	IC0559	094443.9	093655	42.70	513	395	...	5.3	v(flow)	5	3	14.82	0.41	0 b
151	2013	UGC05209	094504.2	321418	49.51	538	581	...	7.7	v(flow)	10	1	16.06	-999	0 g
152	141	N02976	094715.3	675500	40.90	3	184	2.1	3.56	trgb	5	1	11.24	0.1	-26 j

TABLE 2.1 – Continued

#	ID	Galaxy Name	RA(J2000)	DEC(J2000)	b	cz	v(flow)	D(NBG)	D	method	T	err(T)	B	err(B)	References
(1)	(2)	(3)	(4)	(5)	(6)	(7)	(8)	(9)	(10)	(11)	(12)	(13)	(14)	(15)	(16)
153	1011	UGC05272b	095019.4	312721	50.55	539	569	...	7.1	mem	10	2	17.76	0.1	-54 b
154	142	U05272	095022.4	312916	50.56	520	545	6.5	7.1	bs	10	1	15.41	0.1	-33 j
155	143	U5288	095117.0	074939	43.25	557	431	5.2	6.8	bs	8	1	14.32	0.08	-47 k
156	144	NGC3037	095123.5	-270036	20.70	889	750	...	10	v(flow)	9	2	13.71	0.2	0 b
157	145	N03031	095533.2	690355	40.90	-34	146	1.4	3.63	ceph	2	1	7.89	0.03	3 a
158	146	N03034	095552.2	694047	40.57	203	440	5.2	3.53	trgb	7	4	9.3	0.09	-46 a
159	147	U05340	095645.7	284935	51.62	503	493	5.9	5.9	bs	10	1	14.76	0.14	-33 a
160	1012	KDG061	095703.1	683531	41.28	-135	26	...	3.6	trgb	8	3	15.17	0.1	-22 d
161	148	U5336	095732.0	690245	41.06	46	241	...	3.7	mem	10	1	14.3	0.3	-30 a
162	149	ESO435-IG020	095920.7	-280754	21.03	710	510	...	6.8	v(flow)	10	-999	14.39	0.31	0 b
163	150	U05364	095926.4	304447	52.42	20	-14	1	0.69	trgb	10	1	12.92	0.18	-51 a
164	151	U05373	100000.1	051956	43.78	301	134	1.6	1.36	trgb	10	1	11.85	0.14	-24 a
165	152	UGC1193	100236.0	-060049	37.43	662	492	6.2	9.7	mem	7	1	14.84	0.1	-41 j
166	153	N03109	100306.6	-260932	23.07	403	140	1.8	1.33	trgb	9	1	10.39	0.07	-24 a
167	154	N03077	100320.6	684404	41.66	14	199	2.1	3.82	trgb	6	5	10.61	0.13	-26 a
168	156	UGC05427	100441.0	292155	53.40	498	481	...	7.1	bs	8	1	15.95	0.22	-33 b
169	1013	UGC05428	100506.4	663332	43.09	-129	22	...	3.5	trgb	10	1	15.95	0.1	-22 d
170	1014	NGC3115	100514.0	-074307	36.78	720	560	6.7	9.68	sb	-3	1	9.87	0.04	-52 a
171	157	U05423	100530.6	702152	40.81	350	630	9	5.3	bs	10	1	15.2	0.1	-47 j
172	158	NGC3125	100633.6	-295609	20.64	865	706	...	9.4	v(flow)	10	-999	13.5	0.13	0 a
173	160	UGC05451	100719.0	470022	52.31	629	827	...	11.0	v(flow)	10	1	14.36	0.12	0 b
174	161	U5456	100719.6	102146	47.94	544	405	...	3.8	trgb	5	2	13.72	0.13	-32 a
175	162	KUG1004+392	100723.0	385810	53.99	580	679	...	9.1	v(flow)	10	2	15.96	0.15	0 b
176	163	SextansA	101100.8	-044134	39.88	324	114	1.3	1.32	ceph	10	1	11.86	0.07	-7 a
177	165	N03239	102505.6	170937	54.82	753	688	8.1	9.2	v(flow)	9	2	11.73	0.13	0 a
178	166	UGC05672	102820.9	223417	57.33	531	432	...	6.3	bs	5	3	15.14	0.14	-47 b
179	167	U05666	102821.2	682443	43.61	57	246	2.7	4.02	trgb	9	1	10.8	0.19	-26 a
180	168	UGC05692	103035.0	703707	42.18	180	413	...	4	trgb	9	1	13.71	0.1	-26 j
181	169	N03274	103217.1	274007	59.21	537	476	5.9	6.5	bs	7	1	13.21	0.13	-33 a
182	2014	ESO375-G071	103609.4	-371416	18.22	956	805	11.6	10.7	v(flow)	10	1	13.26	0.2	0 b
183	170	N03299	103623.8	124227	55.29	641	478	5.4	10.4	mem	8	1	14.11	0.12	-28 b
184	171	U05764	103643.3	313248	60.43	586	571	6.9	7.6	v(flow)	10	1	15.21	0.19	0 a
185	172	UGC05797	103925.2	014305	49.44	713	518	...	6.9	v(flow)	10	1	15	0.12	0 b
186	173	U05829	104242.2	342656	61.53	629	657	8	8.8	v(flow)	10	1	13.73	0.18	0 a
187	174	N03344	104330.9	245522	61.26	586	490	6.1	6.5	v(flow)	4	1	10.45	0.13	0 a
188	175	N03351	104357.8	114214	56.37	778	631	8.1	10	ceph	3	1	10.53	0.1	3 a
189	176	N03365	104612.6	014848	50.75	986	940	10.7	12.5	v(flow)	6	1	13.17	0.15	0 a
190	177	N03368	104645.7	114912	57.01	897	827	8.1	10.52	ceph	2	1	10.11	0.13	3 a

TABLE 2.1 – Continued

#	ID	Galaxy Name	RA(J2000)	DEC(J2000)	b	cz	v(flow)	D(NBG)	D	method	T	err(T)	B	err(B)	References
(1)	(2)	(3)	(4)	(5)	(6)	(7)	(8)	(9)	(10)	(11)	(12)	(13)	(14)	(15)	(16)
191	178	U05889	104722.3	140410	58.29	572	391	5.1	9.3	bs	9	1	14.22	0.16	-28 a
192	180	UGC05923	104907.6	065502	54.64	712	508	...	6.8	v(flow)	0	1	14.03	0.37	0 b
193	181	U05918	104936.5	653150	47.12	340	580	7.1	7.4	bs	10	2	15.22	0.1	-47 j
194	1019	NGC3412	105053.3	132444	58.70	841	719	8.1	10.4	mem	-2	1	11.45	0.13	-28 a
195	182	N03423	105114.3	055024	54.37	1013	1010	10.9	13.5	v(flow)	6	1	11.59	0.1	0 a
196	184	N03432	105231.3	363711	63.16	616	654	7.8	8.7	v(flow)	9	1	11.67	0.11	0 a
197	185	KDG073	105257.1	693258	44.23	-132	32	...	3.7	trgb	10	-999	17.28	0.1	-26 j
198	1021	NGC3489	110018.6	135404	60.91	677	465	6.4	10.4	mem	-1	1	11.12	0.13	-28 a
199	186	N03486	110023.9	285830	65.49	681	627	7.4	8.4	v(flow)	5	1	11.05	0.1	0 a
200	187	UGC06102	110148.4	284121	65.78	702	651	...	8.7	v(flow)	10	1	15.53	0.41	0 b
201	188	N03510	110343.4	285313	66.21	705	654	7.9	8.7	v(flow)	8	2	14.3	0.8	0 b
202	189	MRK36	110458.5	290822	66.49	646	571	6.9	7.6	v(flow)	10	-999	15.7	0.2	0 a
203	190	N03521	110548.6	-000209	52.83	805	573	7.2	7.6	v(flow)	4	1	9.83	0.1	0 a
204	191	N03593	111437.0	124904	63.21	628	383	5.5	5.1	v(flow)	0	1	11.86	0.08	0 a
205	192	NGC3599	111527.0	180637	66.14	835	647	...	8.6	v(flow)	-2	1	12.82	0.14	0 a
206	193	N03600	111552.1	413532	65.68	719	868	10.5	11.6	v(flow)	1	1	13.96	0.44	0 b
207	194	N03621	111816.0	-324842	26.10	727	499	7.1	6.64	ceph	7	1	10.18	0.15	3 a
208	195	N03623	111855.9	130537	64.22	807	533	7.3	7.1	v(flow)	1	1	10.25	0.05	0 a
209	196	N03627	112015.0	125930	64.42	727	446	6.6	10.05	ceph	3	1	9.65	0.13	3 a
210	197	N03628	112016.9	133520	64.78	843	577	7.7	7.7	v(flow)	3	1	10.28	0.05	0 a
211	198	IC2787	112319.1	133747	65.40	742	449	...	6	v(flow)	6	1	16.05	0.2	0 b
212	199	UGC06457	112712.2	-005941	55.34	963	770	...	10.3	v(flow)	10	1	15	0.6	0 b
213	200	U06456	112759.9	785939	37.33	-100	120	1.4	4.34	trgb	10	-999	15.9	0.38	-38 b
214	201	U06541	113328.9	491414	63.28	249	316	4	3.89	trgb	11	-999	14.4	0.1	-26 j
215	202	N03738	113548.8	543126	59.31	229	340	4.3	4.9	trgb	10	1	11.97	0.1	-26 j
216	203	N3741	113606.2	451701	66.45	229	261	...	3.03	trgb	10	1	14.49	0.1	-26 j
217	204	U06782	114857.2	235016	75.53	525	329	5	4.4	v(flow)	9	2	15.07	0.1	0 c
218	205	U06817	115053.0	385249	72.74	242	224	3.1	2.64	trgb	10	1	13.56	0.1	-24 j
219	206	U06900	115539.4	313110	77.08	590	464	5.9	6.2	v(flow)	10	1	14.8	0.19	0 a
220	207	N04020	115856.6	302444	78.05	760	655	8	8.7	v(flow)	7	1	13.82	0.21	0 b
221	209	U07007	120133.1	332029	77.58	774	766	8.9	10.2	v(flow)	9	1	16.3	-999	0 z
222	210	N04068	120400.8	523518	63.04	210	302	3.8	5.2	bs	10	1	13.02	0.1	-35 j
223	211	NGC4080	120451.8	265933	79.63	567	373	...	5	v(flow)	10	1	14.28	0.13	0 b
224	213	N04096	120601.0	472840	67.79	566	698	8.8	9.3	v(flow)	5	1	11.48	0.1	0 a
225	214	N04144	120958.4	462727	69.01	265	308	4.1	9.8	bs	6	1	12.05	0.13	-18 a
226	215	N04163	121209.1	361009	77.70	165	141	2.1	3.6	bs	10	1	13.75	0.1	-50 j
227	216	N04190	121344.7	363803	77.59	228	197	2.8	3.5	bs	10	1	13.9	0.3	-50 a
228	2015	UGC07242	121408.4	660541	50.60	68	244	...	4.3	mem	6	1	14.657	0.41	-42 b

TABLE 2.1 – Continued

#	ID	Galaxy Name	RA(J2000)	DEC(J2000)	b	cz	v(flow)	D(NBG)	D	method	T	err(T)	B	err(B)	References
(1)	(2)	(3)	(4)	(5)	(6)	(7)	(8)	(9)	(10)	(11)	(12)	(13)	(13)	(14)	
229	217	UGCA276	121457.9	361308	78.06	284	242	...	2.86	trgb	10	1	15.7	0.1	-24 d
230	218	N04204	121514.5	203931	79.50	861	957	7.9	12.8	v(flow)	8	1	14.01	0.41	0 b
231	219	U07267	121523.6	512058	64.84	472	617	7.8	8.2	v(flow)	8	2	15.29	0.19	0 b
232	220	U07271	121533.3	432606	72.15	546	607	7.5	8.1	v(flow)	7	1	15.53	0.1	0 b
233	221	N04214	121538.9	361940	78.07	291	249	3.5	2.94	trgb	10	1	10.24	0.14	-32 a
234	222	U7298	121630.1	521339	64.06	172	259	...	4.21	trgb	10	1	16.06	0.1	-26 j
235	223	N04236	121642.1	692746	47.36	0	186	2.2	4.45	trgb	8	1	10.05	0.17	-22 a
236	224	N04244	121729.9	374829	77.16	244	219	3.1	4.49	trgb	6	1	10.88	0.16	-26 a
237	225	N04242	121730.1	453708	70.32	517	601	7.5	8	v(flow)	8	1	11.37	0.16	0 a
238	226	U07321	121733.8	223226	81.05	408	243	3.8	3.2	v(flow)	7	1	14.15	0.15	0 a
239	227	N04248	121750.3	472431	68.68	484	581	7.3	7.8	v(flow)	3	3	13.21	0.1	0 j
240	228	IC3104	121846.0	-794334	-16.95	430	191	3.1	2.27	trgb	10	1	13.49	0.2	-24 b
241	229	N04258	121857.5	471814	68.84	448	532	6.8	7.98	ceph	4	1	9.1	0.07	3 a
242	1084	UGC07356	121909.1	470523	69.05	272	322	...	6.7	sb	10	1	15.58	0.1	-17 e
243	2016	ISZ399	121959.5	-172331	44.83	900	707	...	9.4	v(flow)	13	-999	14.716	0.177	0 b
244	230	N04288	122038.1	461733	69.89	535	637	8	8.5	v(flow)	7	1	13.26	0.13	0 a
245	231	U07408	122115.0	454841	70.38	462	531	6.7	7.1	v(flow)	9	3	13.35	0.15	0 a
246	232	UGC07490	122425.3	702001	46.62	465	780	11.1	10.4	v(flow)	9	1	13.05	0.16	0 a
247	233	N04395	122548.9	333248	81.53	319	253	3.6	4.61	trgb	9	1	10.64	0.15	-26 a
248	234	UGCA281	122616.0	482937	68.08	281	347	4.7	5.7	bs	10	-999	15.36	0.34	-35 b
249	235	U07559	122705.1	370833	78.74	218	194	2.8	4.87	trgb	10	1	14.2	0.2	-26 a
250	236	U07577	122740.9	432944	72.94	196	218	3	2.54	trgb	10	1	12.84	0.18	-24 a
251	237	N04449	122811.2	440536	72.40	207	234	3	4.21	trgb	10	1	9.99	0.13	-26 a
252	238	U07599	122828.5	371401	78.79	278	247	3.5	6.9	bs	8	3	14.88	0.1	-36 j
253	239	U07605	122838.7	354303	80.14	309	262	3.7	4.43	trgb	10	1	14.79	0.15	-26 b
254	240	N04455	122844.1	224921	83.29	637	344	6.2	4.6	v(flow)	7	1	13.8	0.8	0 b
255	241	U07608	122845.3	431335	73.26	538	596	7.6	7.9	v(flow)	10	1	13.67	0.19	0 a
256	1089	NGC4460	122845.5	445151	71.69	490	554	8.1	9.59	sb	-1	2	12.779	0.239	-52 b
257	1090	MC+07-26-011	122852.2	421041	74.26	408	419	...	5.6	v(flow)	8	2	16.33	0.1	0 b
258	242	U07639	122953.4	473152	69.17	382	455	5.8	8	bs	10	1	13.99	0.1	-36 j
259	1091	MC+07-26-012	123023.8	425406	73.66	436	461	...	6.1	v(flow)	6	2	16.47	0.1	0 b
260	243	N04485	123031.1	414201	74.81	493	514	9.3	6.9	v(flow)	10	1	12.32	0.05	0 a
261	244	N04490	123036.1	413834	74.87	565	608	7.8	8.1	v(flow)	7	1	10.22	0.06	0 a
262	245	UGC07678	123200.7	394959	76.67	666	730	...	9.7	v(flow)	6	2	16.1	0.5	0 b
263	246	U07690	123226.8	424218	73.95	537	588	7.5	7.8	v(flow)	10	1	13.1	0.4	0 a
264	247	U07699	123248.0	373718	78.80	496	458	6.2	6.1	v(flow)	6	1	13.6	0.13	0 b
265	248	U07698	123254.4	313228	84.02	331	250	3.8	6.1	bs	10	1	13	0.3	-36 a
266	249	U07719	123400.6	390110	77.57	678	734	8.9	9.8	v(flow)	8	1	15.33	0.41	0 b

TABLE 2.1 – Continued

#	ID	Galaxy Name	RA(J2000)	DEC(J2000)	b	cz	v(flow)	D(NBG)	D	method	T	err(T)	B	err(B)	References
(1)	(2)	(3)	(4)	(5)	(6)	(7)	(8)	(9)	(10)	(11)	(12)	(13)	(14)	(15)	(16)
267	250	N04534	123405.4	353108	80.83	802	890	9.8	11.9	v(flow)	8	1	13.04	0.41	0 b
268	251	U07774	123622.5	400019	76.75	526	531	6.8	7.1	v(flow)	7	1	15.02	0.1	0 b
269	1093	UGCA290	123721.8	384438	78.02	458	433	...	6.7	trgb	10	-999	15.74	0.1	-3 b
270	252	UGCA292	123840.0	324601	83.72	307	241	3.6	3.1	bs	10	1	16.10	0.05	-36 k
271	253	N04592	123919.0	-003154	62.19	1072	979	9.6	13.1	v(flow)	8	1	12.9	0.26	0 b
272	2017	MESSIER104	123959.4	-113723	51.15	1024	916	20	9.33	bsf	1	1	8.98	0.06	-11 a
273	254	N04605	124000.3	613629	55.47	143	305	4	5.2	bs	5	1	10.89	0.09	-19 a
274	255	N04618	124132.7	410904	75.83	544	576	7.3	7.7	v(flow)	8	1	11.22	0.04	0 a
275	256	N04625	124152.6	411626	75.72	609	672	8.2	9	v(flow)	9	1	12.92	0.04	0 a
276	257	N04631	124208.0	323226	84.22	606	497	6.9	6.6	v(flow)	7	1	9.75	0.16	0 a
277	258	U07866	124215.1	383012	78.46	354	330	4.5	4.57	trgb	10	1	13.71	0.19	-26 a
278	259	N04656	124357.7	321005	84.70	646	536	7.2	7.2	v(flow)	9	2	10.96	0.09	0 a
279	260	U07916	124425.1	342312	82.59	607	536	7.2	7.2	v(flow)	10	1	15	1	0 b
280	261	N04670	124517.1	270732	88.63	1069	1511	11.0	20.1	v(flow)	1	3	13.09	0.13	0 a
281	262	ESO381-G020	124600.4	-335017	29.02	585	337	5.1	4.5	v(flow)	10	1	14.7	0.28	0 b
282	1096	UGCA298	124655.4	263351	88.85	801	585	8.9	7.8	v(flow)	-3	2	15.579	0.256	0 b
283	263	U07950	124656.4	513646	65.50	502	673	8.9	9	v(flow)	10	1	15.1	0.3	0 a
284	264	U07949	124659.8	362835	80.60	333	295	4.2	9.9	bs	10	1	15.12	0.1	-36 b
285	265	N04707	124822.9	510953	65.96	468	619	8	8.3	v(flow)	9	1	13.4	0.2	0 a
286	266	N04736	125053.0	410714	76.01	308	314	4.3	4.66	trgb	2	1	8.99	0.13	-26 a
287	267	U08024	125405.2	270855	89.41	374	259	4	4.3	bs	10	1	13.94	0.18	-36 a
288	2018	UGC08055	125604.3	034843	66.66	618	314	...	4.2	v(flow)	10	1	17	0.1	0 b
289	2019	UGCA309	125617.8	343917	82.40	717	721	15.6	9.6	v(flow)	10	1	15.5	-999	0 z
290	268	N04826	125643.7	214052	84.42	408	250	4.1	7.5	bsf	2	1	9.36	0.1	-52 a
291	269	U08091	125840.4	141303	76.98	214	957	1.7	2.1	trgb	10	1	14.68	0.06	-4 a
292	270	UGCA319	130214.4	-171415	45.56	747	519	7.1	6.9	v(flow)	9	2	14.96	0.38	0 b
293	271	UGCA320	130316.8	-172523	45.36	744	517	7.1	6.9	v(flow)	9	3	13.52	0.14	0 a
294	2020	LEDA170228	130412.1	-045328	57.83	920	692	...	9.2	v(flow)	-2	3	14.843	0.407	0 b
295	272	N04945	130527.5	-492806	13.34	560	319	5.2	3.6	mem	6	1	9.3	0.2	-2 a
296	273	U08188	130549.5	373618	79.09	321	304	4.4	4.49	ceph	9	1	12.4	0.7	3 b
297	274	U08201	130624.8	674225	49.36	37	228	2.8	4.57	trgb	10	1	12.8	0.2	-26 a
298	2021	MC03-34-002	130756.6	-164121	46.00	922	782	...	10.4	v(flow)	4	4	14.79	0.131	0 b
299	275	U08215	130803.6	464941	70.03	218	280	3.9	5.6	bs	10	1	16.08	0.1	-35 j
300	276	UGC08245	130834.2	785613	38.16	70	333	...	4.4	v(flow)	10	1	15.22	0.33	0 b
301	277	N05023	131212.1	440220	72.58	407	466	6	5.4	bs	6	1	12.85	0.15	-47 a
302	278	CGCG217-018	131251.8	403235	75.87	570	632	...	8.4	v(flow)	10	-999	15.1	0.41	0 b
303	279	U08308	131322.7	461913	70.32	164	224	3.2	4.19	trgb	10	1	15.54	0.1	-26 j
304	280	U08313	131354.1	421236	74.24	625	745	9.2	9.9	v(flow)	5	1	14.775	0.1	0 b

TABLE 2.1 – Continued

#	ID	Galaxy Name	RA(J2000)	DEC(J2000)	b	cz	v(flow)	D(NBG)	D	method	T	err(T)	B	err(B)	References
(1)	(2)	(3)	(4)	(5)	(6)	(7)	(8)	(9)	(10)	(11)	(12)	(13)	(14)	(15)	(16)
305	281	U08320	131427.9	455509	70.66	192	250	3.6	4.33	trgb	10	1	13.11	0.1	-26 j
306	282	U08331	131530.3	472956	69.09	260	335	4.6	8.2	bs	10	1	14.31	0.1	-18 j
307	283	N05055	131549.2	420149	74.29	504	566	7.2	7.5	v(flow)	4	1	9.31	0.1	0 a
308	284	N05068	131854.6	-210220	41.38	673	454	6.7	6.1	v(flow)	6	1	10.7	0.2	0 a
309	285	N05102	132157.6	-363749	25.84	467	218	3.5	3.4	trgb	-3	1	10.35	0.1	-23 a
310	286	N05128	132527.6	-430109	19.42	547	312	4.9	3.66	trgb	-2	1	7.84	0.06	-48 a
311	287	IC4247	132644.4	-302145	31.89	274	23	...	4.6	mem	2	4	14.57	0.11	-31 b
312	288	ESO324-G024	132737.3	-412850	20.88	513	272	4.6	3.73	trgb	10	1	12.91	0.2	-23 b
313	289	N05204	132936.2	582506	58.00	201	366	4.8	4.65	trgb	9	1	11.73	0.13	-26 a
314	290	N05194	132952.7	471143	68.56	463	593	7.7	8	mem	4	1	8.96	0.06	-44 a
315	291	N05195	132958.7	471605	68.49	465	596	9.3	8	sb	2	5	10.45	0.07	-52 a
316	292	U08508	133044.4	545436	61.31	62	183	2.7	2.56	trgb	10	1	13.94	0.1	-24 j
317	293	SBS1331+493	133322.9	490606	66.58	599	818	...	10.9	v(flow)	4	6	16.54	0.42	0 b
318	294	N5206	133343.8	-480904	14.12	571	345	...	3.6	mem	-3	1	12	0.6	-2 b
319	295	N05229	133402.7	475455	67.61	364	474	6.4	5.1	bs	7	1	14.18	0.1	-47 j
320	296	N05238	133442.7	513651	64.19	235	354	4.9	5.2	bs	8	1	13.6	0.1	-19 j
321	297	ESO270-G017	133447.3	-453251	16.66	826	668	10.8	8.9	v(flow)	9	1	11.8	0.8	0 b
322	298	[KK98] 208	133635.5	-293417	32.28	381	140	...	4.68	trgb	10	2	14.3	-999	-23 z
323	299	N05236	133700.8	-295159	31.97	516	288	4.7	4.47	ceph	5	1	8.2	0.03	-49 a
324	300	ESO444-G084	133720.1	-280246	33.74	587	371	5.6	4.61	trgb	10	1	15.48	0.23	-23 b
325	301	UGC08638	133919.4	244632	78.98	274	203	...	3.4	v(flow)	10	1	15.1	0.6	-37 b
326	302	U08651	133953.8	404421	73.12	201	236	3.4	3.01	trgb	10	1	14.45	0.05	-24 k
327	303	N05253	133955.9	-313824	30.10	404	163	3.2	3.15	ceph	-3	5	10.87	0.12	3 a
328	304	N05264	134136.9	-295450	31.71	478	248	4.2	4.53	trgb	9	3	12.6	0.15	-23 a
329	305	U08683	134232.4	393930	73.58	661	806	10.2	10.7	v(flow)	10	1	15.64	0.41	0 b
330	306	ESO325-G011	134500.5	-415140	19.91	541	316	5.3	3.4	trgb	10	1	14.01	0.2	-23 b
331	308	ESO383-G087	134917.8	-360342	25.36	326	78	1.9	1	v(flow)	8	1	11.68	0.32	0 b
332	309	ESO383-G091	135032.3	-371720	24.10	141	-118	...	3.6	mem	7	1	14.43	0.1	1 b
333	310	U08760	135050.6	380109	73.45	193	219	3.3	5.1	bs	10	2	14.45	0.05	-36 k
334	312	U08837	135445.7	535403	60.80	144	278	3.9	8.3	bs	10	1	13.71	0.1	-19 j
335	313	U08833	135448.7	355015	73.96	228	241	3.6	3.19	trgb	10	1	15.15	0.05	-26 k
336	314	ESO384-G016	135701.5	-352002	25.65	561	353	...	3.7	sb	10	-999	14.99	0.13	-16 b
337	315	N05457	140312.5	542055	59.77	241	402	5.4	4.81	ceph	6	1	8.31	0.09	3 a
338	316	N05408	140321.0	-412244	19.50	509	290	4.9	4.81	trgb	10	1	12.2	0.2	-23 a
339	317	N05474	140501.5	533945	60.19	273	438	6	7.2	bs	6	1	11.82	0.1	-19 j
340	318	N05477	140533.1	542739	59.49	304	485	6.4	7.7	bs	9	1	14.24	0.1	-19 j
341	319	Circinus	141309.3	-652021	-3.81	449	214	4.2	2.9	v(flow)	3	2	12.1	0.3	0 a
342	320	U09128	141556.5	230319	70.46	154	123	2.2	2.5	trgb	10	1	14.46	0.06	-1 k

TABLE 2.1 – Continued

#	ID	Galaxy Name	RA(J2000)	DEC(J2000)	b	cz	v(flow)	D(NBG)	D	method	T	err(T)	B	err(B)	References
(1)	(2)	(3)	(4)	(5)	(6)	(7)	(8)	(9)	(10)	(11)	(12)	(13)	(14)	(15)	(16)
343	1103	SBS1415+437	141701.4	433005	66.20	609	818	...	10.9	v(flow)	10	-999	17.815	0.604	0 b
344	321	N05585	141948.2	564346	56.48	305	515	7	5.7	bs	7	1	11.2	0.14	-19 a
345	322	U09240	142443.4	443133	64.48	150	243	3.7	2.79	trgb	10	1	13.31	0.04	-24 k
346	323	UKS1424-460	142803.7	-461806	13.38	397	167	3.1	3.58	trgb	10	1	16.5	-999	-23 z
347	324	U09405	143524.4	571519	54.71	222	423	5.7	8	bs	10	1	14.57	0.1	-33 j
348	325	MRK475	143905.4	364821	65.31	583	749	9.6	10	v(flow)	10	-999	15.46	0.18	0 a
349	326	NGC 5832	145745.7	714056	42.16	447	796	11.5	10.6	v(flow)	3	1	14.09	0.42	0 b
350	327	ESO223-G009	150108.7	-481726	9.17	586	416	7.7	5.6	v(flow)	10	1	13	1	0 b
351	328	ESO274-G001	151413.6	-464836	9.34	522	349	7.2	4.7	v(flow)	7	1	11.7	0.4	0 a
352	329	NGC5949	152800.7	644547	44.97	435	769	11.2	10.2	v(flow)	4	1	13.37	0.23	0 b
353	330	UGC09992	154147.8	671515	42.37	427	771	11.2	10.3	v(flow)	10	1	14.86	0.1	0 k
354	1109	LEDA100404	160858.9	173025	43.60	418	542	...	7.2	v(flow)	9	2	17.435	0.431	0 b
355	332	ESO137-G018	162059.2	-602916	-7.43	606	454	7.2	6.1	v(flow)	5	1	12.17	0.21	0 b
356	333	ESO179-IG013	164720.0	-572628	-7.90	775	659	10.9	8.8	v(flow)	9	1	15	2	0 b
357	2022	UGC10669	170025.3	701724	34.68	442	812	11.6	10.8	v(flow)	10	1	16.31	0.14	0 k
358	335	IC4662	174706.4	-643825	-17.85	308	128	3	1.7	v(flow)	10	1	11.74	0.14	0 a
359	336	N06503	174927.1	700840	30.64	60	370	6.1	5.27	trgb	6	1	10.91	0.09	-26 a
360	337	IC4710	182838.1	-665854	-22.65	741	607	8.9	8.1	v(flow)	9	1	12.5	0.2	0 a
361	339	ESO104-G022	185541.2	-644839	-24.81	795	671	9.7	8.9	v(flow)	10	1	15.52	0.2	0 b
362	340	N06744	190946.2	-635125	-26.14	841	720	10.4	9.6	v(flow)	4	1	9.14	0.17	0 a
363	341	ESO104-G044	191123.1	-641309	-26.38	779	657	...	8.8	v(flow)	9	1	14.91	0.2	0 b
364	2023	ESO141-G042	191612.0	-622142	-26.65	909	792	11.1	10.6	v(flow)	9	1	15.448	0.414	0 b
365	342	NGC6789	191641.9	635818	21.52	-141	153	...	3.6	trgb	10	1	14.4	0.6	-9 b
366	343	ESO594-G004	192959.0	-174041	-16.29	-77	-42	0.7	1.04	trgb	10	1	13.99	-999	-24 h
367	2024	IC4870	193737.6	-654843	-29.27	879	751	...	10.0	v(flow)	10	1	14.397	0.417	0 b
368	344	N06822	194456.6	-144721	-18.40	-57	8	0.7	0.5	ceph	10	1	9.31	0.06	-55 a
369	345	IC4951	200931.2	-615047	-32.84	794	679	9.9	9.1	v(flow)	8	1	13.91	0.2	0 b
370	2025	UGC11583	203015.3	602625	12.31	127	483	...	5.9	bs	10	1	15.7	0.1	-43 b
371	2026	LEDA166192	203032.9	602117	12.23	126	482	...	5.9	bs	9	2	16.5	0.1	-43 b
372	2027	LEDA166193	203132.0	604844	12.39	139	497	...	5.9	bs	10	2	16.7	0.1	-43 b
373	346	N06946	203452.3	600914	11.67	48	395	5.5	5.9	bs	6	1	9.61	0.1	-43 a
374	2028	KKR55	204520.8	602440	10.78	32	379	...	5.9	bs	10	1	17.59	0.594	-43 b
375	347	DDO210	204651.8	-125053	-31.34	-137	-35	0.7	0.94	trgb	10	1	14.14	0.32	-24 k
376	2029	KKR56	204824.1	583706	9.37	-43	293	...	5.9	bs	10	1	17.6	0.1	-43 b
377	2030	CEPHEUS1	205110.6	565325	8.01	58	406	...	5.9	mem	10	-999	15.4	-999	-43 g
378	348	IC5052	205206.3	-691213	-35.81	598	458	6.7	6.1	v(flow)	7	1	11.79	0.15	0 a
379	2031	KKR59	210324.2	571714	6.99	-3	340	...	5.9	bs	10	1	15.7	0.1	-43 b
380	2032	KKR60	210551.3	571232	6.69	-14	328	...	5.9	mem	10	1	18	-999	-43 g

TABLE 2.1 – Continued

#	ID	Galaxy Name	RA(J2000)	DEC(J2000)	b	cz	v(flow)	D(NBG)	D	method	T	err(T)	B	err(B)	References
(1)	(2)	(3)	(4)	(5)	(6)	(7)	(8)	(9)	(10)	(11)	(12)	(13)	(14)	(15)	(16)
381	349	N07064	212903.0	-524603	-44.82	797	707	10.6	9.4	v(flow)	5	1	13.1	0.2	0 a
382	350	N07090	213628.6	-543324	-45.38	857	757	10.4	10.1	v(flow)	5	1	11.33	0.16	0 a
383	351	IC5152	220241.9	-511744	-50.19	124	52	1	2.07	trgb	10	1	10.68	0.48	-24 b
384	352	U11891	220333.9	434457	-9.36	462	784	10.5	10.5	v(flow)	10	1	15.35	0.41	0 b
385	353	ESO238-G005	222230.0	-482418	-54.24	706	625	8.4	8.3	v(flow)	10	1	19.8	-999	0 z
386	2033	IC5256	224945.8	-684126	-44.73	950	796	...	10.6	v(flow)	8	1	14.582	0.149	0 b
387	355	N07640	232206.6	405043	-18.94	369	665	8.6	8.9	v(flow)	5	1	11.86	0.15	0 a
388	356	U12588	232442.4	412048	-18.64	415	710	9.3	9.5	v(flow)	8	1	14.42	0.15	0 b
389	357	UGCA438	232627.5	-322320	-70.86	62	79	1	2.23	trgb	10	1	14.67	0.28	-24 b
390	358	ESO347-G017	232656.0	-372049	-69.49	690	636	8.2	8.5	v(flow)	9	1	15	0.9	0 b
391	359	U12613	232836.2	144435	-43.55	-183	54	1	0.76	trgb	10	1	12.50	0.15	-55 k
392	360	U12632	232958.7	405925	-19.31	422	714	9.2	9.5	v(flow)	9	1	12.78	0.17	0 a
393	361	IC5332	233427.4	-360605	-71.37	706	653	8.4	8.7	v(flow)	7	1	11.21	0.15	0 b
394	362	N07713	233615.4	-375619	-70.88	689	630	8.2	8.4	v(flow)	7	1	11.51	0.15	0 a
395	363	U12713	233814.4	304229	-29.58	299	557	6.9	7.4	v(flow)	0	1	14.91	0.03	0 k
396	364	UGCA442	234345.5	-315722	-74.53	267	260	3.3	4.27	trgb	9	1	13.6	0.15	-25 a
397	365	ESO348-G009	234923.5	-374619	-73.17	657	597	7.7	8	v(flow)	10	1	16.7	0.7	0 b
398	366	ESO149-G003	235202.8	-523440	-62.24	594	488	6.1	6.4	tf	10	1	15.04	0.14	-25 b
399	367	N07793	235749.7	-323530	-77.17	230	221	2.8	3.91	trgb	7	1	9.63	0.05	-25 a

TABLE 2.2 – Reference Codes for Table 2.1

Distance References		Photometry References
1 Cote et al. 1997: Cen A group	-27 KKH: Karachentsev et al. 2003c	a RC3
2 Ferrarese et al. 2000: N1023 group (N925 cep)	-28 KKH: Leo group	b LEDA
3 Freedman et al. 2001	-29 KKH: M. E. Sharina 2004, private com.	c Barazza, Binggeli & Prugniel 2001
4 Mould 2005	-30 KKH: M81 group	d Brennes, Binggeli & Prugniel 1998
-1 KKH: Aparicio et al. 2000	-31 KKH: M83 group	e Brennes, Binggeli & Prugniel 2000
-2 KKH: Cen A group	-32 KKH: Maiz-Apellaniz et al. 2002	f Buta & McCall 1999
-3 KKH: Crone et al. 2002	-33 KKH: Makarova & Karachentsev 1998	g KKH
-4 KKH: Dohm-Palmer et al. 1998	-34 KKH: Makarova & Karachentsev 2003	h Lee and Kim 2000
-5 KKH: Dolphin 2000	-35 KKH: Makarova et al. 1997	i Makarova & Karachentsev 1998
-6 KKH: Dolphin et al. 2001b	-36 KKH: Makarova et al. 1998	j Parodi, Barazza & Binggeli 2002
-7 KKH: Dolphin et al. 2003	-37 KKH: Makarova et al. 1998. 2.3 Mpc is a lower limit	k van Zee 2000
-8 KKH: Drozdovsky & Karachentsev 2000	-38 KKH: Mendez et al. 2002	z NEID
-9 KKH: Drozdovsky et al. 2001	-39 KKH: Miller et al. 2002	
-10 KKH: Evans et al. 2000	-40 KKH: N2784 group	
-11 KKH: Ferrarese et al. 2000	-41 KKH: N3115 group	
-12 KKH: Georgiev et al. 1997	-42 KKH: N4236 group	
-13 KKH: Held et al. 1999	-43 KKH: N6946 group	
-14 KKH: I. O. Drozdovsky 1999, private com.	-44 KKH: Pair with N5195	
-15 KKH: Jerjen et al. 1998, +0.9 Mpc correction	-45 KKH: Saha et al. 2002	
-16 KKH: Jerjen et al. 2000b, -0.5 Mpc correction	-46 KKH: Sakai & Madore 1999	
-17 KKH: Jerjen et al. 2001	-47 KKH: Sharina et al. 1996	
-18 KKH: Karachentsev & Drozdovsky 1998	-48 KKH: Sofia et al. 1996	
-19 KKH: Karachentsev et al. 1994	-49 KKH: Tim et al. 2003	
-20 KKH: Karachentsev et al. 1996	-50 KKH: Tikhonov & Karachentsev 1998	
-21 KKH: Karachentsev et al. 1997	-51 KKH: Tolstoy et al. 1998	
-22 KKH: Karachentsev et al. 2000a	-52 KKH: Tosi et al. 2001	
-23 KKH: Karachentsev et al. 2002b	-53 KKH: Tosi et al. 2001	
-24 KKH: Karachentsev et al. 2002c	-54 KKH: U5272	
-25 KKH: Karachentsev et al. 2003a	-55 KKH: van den Bergh 2000	
-26 KKH: Karachentsev et al. 2003b		

TABLE 2.3 – Observational Set-Ups Used in the $H\alpha$ Imaging Survey

Telescope	Detector	CCD Scale	FOV	Continuum Filter	Line Filter(s)	Exp Times
(1)	(2)	(3)	(4)	(5)	(6)	(7)
Bok 2.3 m	Loral 2K \times 2K	0''/43	4'9	6451/1473	6585/66	1000/200
VATT 1.8m	Loral 2K \times 2K	0''/40	6'4	6338/1186	6585/66	1800/360
					6600/69	
CTIO 0.9m	Tek 2K \times 2K	0''/79	13'5	6425/1500	6563/75	2700/360
					6600/75	

Col(1): Telescope.

Col(2): CCD detector.

Col(3): CCD scale (arcsec pixel $^{-1}$).

Col(4): Detector field of view (arcminutes).

Col(5): Continuum filter (R -band) central wavelength and FWHM bandwidth (\AA).

Col(6): Narrowband $H\alpha$ + $[\text{NII}]$ filter central wavelength and FWHM bandwidth (\AA).

Col(7): Standard exposure times in narrowband and continuum filters (sec).

2.3 11HUGS: $H\alpha$ Imaging

2.3.1 Observations

Over a four year period between 2000 to 2004, narrowband $H\alpha$ and R -band imaging was obtained for the majority of galaxies in Table 2.1 using CCD imagers on the Steward Observatory Bok 2.3 m telescope on Kitt Peak (Bok), the Lennon 1.8 m Vatican Advanced Technology Telescope (VATT) on Mount Graham, and the 0.9 m telescope at Cerro Tololo Interamerican Observatory (CTIO). Table 2.3 summarizes the parameters for the instrumentation and filters used. Similar observing procedures were followed for all of the observations except as noted below.

Data for most of the northern galaxies in the survey were obtained with the now retired 2K CCD imager at the Bok telescope, primarily over 17 nights dur-

ing 2001 March to 2002 March. A customized 88 mm Andover 3-cavity interference filter, with an unusually high peak transmission of 90%, was obtained for the project. When combined with the 94% quantum efficiency of the 2K Loral CCD detector at $\sim 6500 \text{ \AA}$, this produced a fast system that enabled us to reach relatively deep emission-line flux and surface brightness limits ($\sim 2 \times 10^{-16} \text{ ergs cm}^{-2} \text{ s}^{-1}$ and $\sim 4 \times 10^{-18} \text{ ergs cm}^{-2} \text{ s}^{-1} \text{ arcsec}^{-2}$, respectively) in exposure times of only 1000 s. To subtract the continua from the narrowband images, we observed the same fields using a Kron-Cousins R filter, with standard integration times of 200 s. Using broadband R as the continuum filter complicates the process of continuum removal, due to the significant mean bandpass shift relative to the narrowband filter (see Table 2.3), and the presence of [N II], [S II], as well as $H\alpha$ itself in the continuum band. However, as will be discussed in Section 2.3.6, we were able to subtract and calibrate the narrowband images to requisite accuracy using the R -band data, and this enabled us to nearly double the size of the sample relative to what would have been possible had we used narrowband continuum filters instead.

The majority of observations on the VATT telescope used the same Andover narrowband filter, while a similar filter centered at 6600 \AA was used for a few objects. Longer total integration times of 1800 s (narrowband) and 360 s (R) were used to compensate for the smaller telescope aperture and the somewhat lower quantum efficiency of the CCD detector, to achieve the same signal/noise limits as the Bok observations to within 10%.

Data for galaxies lying too far south to reach from the Arizona telescopes were obtained using the Cassegrain Focus CCD Imager (CFCCD) on the CTIO 0.9 m telescope over 3 observing runs between 2001 and 2002. A 75 \AA bandpass $H\alpha$ interference filter from CTIO was used for the observations. Because of the much

smaller telescope aperture, it was not practical to reach the depth of the Bok and VATT observations, so exposure times were chosen (2700 s narrowband, 300 – 600 s *R*) to provide approximately 1/3 of the effective exposure time. The wide field of view of the CFCCD camera (13'5), however, allowed many of the most extended galaxies in the project to be imaged efficiently.

Whenever possible, galaxies were observed with imagers that encompassed the full extent of the $H\alpha$ -emitting disk, or else were covered with multiple pointings. Calibration exposures included zero, dome flatfield, twilight sky flatfield, and dark exposures following standard practice. During photometric conditions, observations of galaxies were interspersed with measurements of spectrophotometric standard stars from the catalogs of Massey et al. (1988), Oke et al. (1990), and Hamuy et al. (1992, 1994) several times per night to calibrate the flux zero-points. Although the majority of observations were made under photometric conditions, some data were taken through thin clouds, and these were subsequently calibrated using short (300 – 600 s) bootstrap exposures in the narrowband. This process provided a measurement of the transparency at the time of the first observations, and only those taken through transparencies higher than 50% were kept (although in most cases the transparency was $>80\%$), while the remainder were re-observed using the full exposure times.

2.3.2 Image Processing and Continuum Subtraction

Raw images were reduced following standard procedures using IRAF². The data were bias-subtracted and flat-fielded using the IRAF task CCDPROC. Multiple images, if taken, were medianed using IMCOMBINE. Cosmic rays were excised using JCRREJ2 (Rhoads 2000).

²The Image Reduction and Analysis Facility (IRAF) is distributed by the National Optical Astronomy Observatories, which are operated by AURA, Inc. under cooperative agreement with the National Science Foundation.

The processed narrowband images contain both $H\alpha$ and $[N\ II]$ line emission as well as underlying stellar continuum and Balmer absorption. Net emission-line-only images were produced by subtracting a scaled R image from the narrowband image, after the two were aligned using foreground stars. The R -band scaling factor for each instrumental set-up was established using the following strategy. For a number of galaxies with strong continua that were observed under photometric conditions, the subtractions were iteratively performed using a range of scalings, until the surface brightness of the continuum-dominated regions of the galaxy agreed with level of the background, and the stellar residuals reached an image-wide minimum. The average of the scaling factors that produced the best global subtractions was then adopted and primarily used for all galaxies observed with the same set-up. Scaling factors adopted in this way provided the optimal continuum subtraction for the majority of galaxies observed during clear nights, although slight adjustments were applied occasionally when they produced an obvious improvement in the images. Underlying stellar $H\alpha$ absorption is automatically corrected for, on average, in this process. For galaxies taken under non-photometric conditions, the scaling factor was adjusted manually to account for changes in transparency between the R and narrowband exposures.

2.3.3 Astrometry

An astrometric solution for each pair of narrow-band/ R -band images was calculated using the MCSZERO and MSCCMATCH tasks in the MSCRED package. These routines performed cross-correlation between the positions of stars in the R -band image and equatorial sky position of matching stars in the USNO-A2 catalog. The same calibration is assumed for the corresponding narrow-band image, which was previously aligned to the R -band image for the purposes of contin-

uum subtraction. The solutions are described using the standard WCS keywords and have rms deviations $<0''.5$ in both RA and DEC for all images.

2.3.4 Aperture Photometry

Aperture photometry was performed with the aid of the GALPHOT package³ for IRAF as follows.

First, the boundaries of the galaxies in the continuum and line-only images were individually marked by eye, and foreground stars and background galaxies (or in the case of the continuum-subtracted line images, the residuals of these objects) were automatically masked outside of this region, using the GALPHOT MCLEAN routine. Masking of objects or residuals within the galaxy boundaries was carefully done by hand to ensure that HII regions were not inadvertently removed.

Three different “aperture configurations” were used measure count rates, each of which seeks to minimize the contribution of the sky. The method applied most frequently employs a curve-of-growth analysis with a set of 10 concentric elliptical apertures which extend from the outer regions of the galaxies to the sky. The flux at which the growth curve begins to level off was adopted as the total integrated instrumental flux. Typically, the variation of the enclosed flux among at least three consecutive apertures at this point was less than 2%. This procedure is effective when the radial extent of the emission is substantially less than the field of view of the image, so that there is ample blank sky available for determination the background level. A different procedure was used when a galaxy filled the field of view, or when the sky background region was affected by vignetting. In those cases, an average background level was estimated from regions in the im-

³GALPHOT is a collection of scripts in the IRAF/STSDAS environment first developed by W. Freudling and J.J. Salzer. The current version has been further enhanced by members of the Cornell Extragalactic Group and is maintained by M.P. Haynes.

age that were the least affected by galaxy emission and/or vignetting, and the count rate was measured from the entire frame. Finally, there were a few galaxies where the nebular emission was confined to a handful of widely-separated faint H II regions, with little apparent diffuse emission between them. In such cases, a single large aperture curve-of-growth measurement yielded unacceptably large uncertainties ($>20\%$), so instead, smaller apertures were used to measure the individual H II regions and the results summed to estimate the integrated flux.

2.3.5 Absolute Flux Calibration

Since the methods that are used to convert observed narrowband count rates to absolute fluxes vary from study to study (and is partly dependent on the characteristics of the continuum filter used), we document the details of our calibration procedure in Appendix A. Here, we give a brief discussion of the steps that are involved.

Magnitudes of the observed spectrophotometric standards stars on the standard system were obtained by integrating their spectral energy distributions over the filter response functions. Zero points (ZPs) were then calculated by comparing these values with the instrumental magnitudes measured through aperture photometry. ZPs were averaged and the mean value adopted over periods of time in each run where σ_{ZP} was less than ~ 0.02 mag. These ZPs are used to set the absolute flux scale using the equations given in Appendix A. Galaxy images originally taken during nights which showed ZP variations larger than 0.02 mag, or taken during non-photometric nights when no standards were observed, were instead calibrated with short bootstrap calibration observations, or by tying the integrated measurements of the images to published fluxes based on the literature compilation of Kennicutt et al. (2006, in preparation). A standard atmospheric extinction coefficient of $0.08 \text{ mag airmass}^{-1}$ was adopted throughout.

Corrections for the filter transmission at the redshifted wavelengths of $H\alpha$ and [NII] were also applied (Appendix A), where the variation of the [NII]/ $H\alpha$ ratio between galaxies was approximately accounted for (Appendix B.1). When a broadband filter such as R is used as a proxy for the continuum band an additional series of corrections are needed to compensate for the presence of emission lines in the continuum bandpass, as well as for mean bandpass shifts between the narrowband and R filters (Appendix A). These latter corrections can be significant, and are typically 4–5% for the observational set-ups used.

2.3.6 Integrated Flux and EW Error Analysis

In this section, we discuss uncertainties in the integrated $H\alpha$ + [NII] fluxes which have been independently calibrated through our own observations, and the uncertainties in the EWs. For the small number of images that are tied to fluxes from the literature compilation of Kennicutt et al. (2006, in preparation), we are effectively citing those measurements, and the flux uncertainty in those cases is simply the one adopted from the original study, or is based on the differences in reported values if multiple measurements exist. Although these latter data do not offer an independent measurement of the integrated flux, they still provide us with measurements of the EWs.

For the data that have been taken under photometric conditions, the accuracy of our calibrated fluxes is primarily limited by the usual three factors: 1) errors in determination of the sky background level, 2) errors in the photometric zero-points, as dictated by the observing conditions, and 3) errors in the continuum subtraction. For the data initially taken through thin cirrus which were calibrated using shorter subsequent narrowband exposures of the same field, there is also the uncertainty associated with the bootstrapping procedure. Finally, for galaxies close to the Galactic plane ($b \lesssim 20^\circ$) there are significant uncertainties introduced

by the multitude of foreground stars that pepper the fields. The dominant error in the majority of our measurements is found to be due to uncertainties in the determination of the continuum level. All of these sources of error are incorporated into our quoted uncertainties, which will be presented alongside our measurements in Table 2.4. We now discuss these issues in more detail.

Standard flatfielding corrections using a combination of dome and twilight sky exposures generally produced images that are usually flat to $\pm 1\text{--}3\%$. However all three imagers showed systematic structure in the sky background arising from a combination of imperfect baffling, vignetting, and scattered light in various combinations. We were able to reduce some of these residual instrumental features through use of dark sky flats and some of the object exposures themselves. The effects of these signatures on the integrated photometry is minimal for most objects, but special care was taken to quantify their effects in galaxies with low surface brightness extended line emission. In the majority of images, however, where the sky background has been adequately sampled, flux errors due to the determination of the sky level are mostly between $1\text{--}4\%$.

As already discussed, zeropoint uncertainties for over 80% of our data are effectively limited to be no greater than 2%, since measurements of data that were originally taken during periods where the ZP showed variations larger than this were bootstrap calibrated with subsequent photometric observations. In this process, the count rates of galaxies measured from non-photometric data are scaled by the average ratio of the count rates of unsaturated stars common to the non-photometric and bootstrap images. The ratio of stellar count rates typically showed variations between $2\text{--}3\%$ within a given field. Overall, errors in the photometric zeropoint therefore vary between $1\text{--}5\%$, with the majority of these being smaller than 2%.

The reliability of the continuum scaling and subtraction is the dominant source of uncertainty in most of our measurements. The accuracy with which continuum levels can be determined from the R -band images was estimated in two ways. First, for a dozen galaxies spanning a range of fluxes, EWs and nebular emission spatial distributions in our sample, the narrowband images were subtracted with a range of continuum levels to identify the points at which the resultant line-only image begin to appear over- or under-subtracted. From this exercise, the continuum scaling was found to be determined to within $\sim 3\%$ for galaxies such as bright spirals with strong $H\alpha$ emission and ample area within the star-forming disk that are dominated by continuum. In the most difficult cases, as in some dwarf galaxies where it is not clear whether what is being subtracted away is continuum or actually diffuse ionized emission, this range increased to a level of 15–20%. Nevertheless, for the majority of galaxies, the range of acceptable subtractions corresponds to variations between 4–7% in the R -band scaling factor. As a check on these estimated uncertainties, we examined the distribution of the differences between the average scaling factor determined for each observational set-up and the actual scaling factors used to subtract the photometric data. The dispersion in the differences was 5%, which is consistent with the results of the first exercise. Thus, we have used the fractional difference between the actual and average scale factor, or a minimum uncertainty of 5%, to calculate the corresponding fractional error in the emission-line flux due to uncertainties in the continuum level within the apertures used to measure the narrowband images. This results in a median flux error of 12%, with lower ($\sim 10\%$) uncertainties for higher EW ($>20\text{\AA}$) systems and larger ones ($\sim 20\%$) for lower EW ($<20\text{\AA}$) systems (see Fig. 2.1). These are also indicative of the typical *total* flux errors since those caused by calibration of the photometric zeropoint or determination of sky

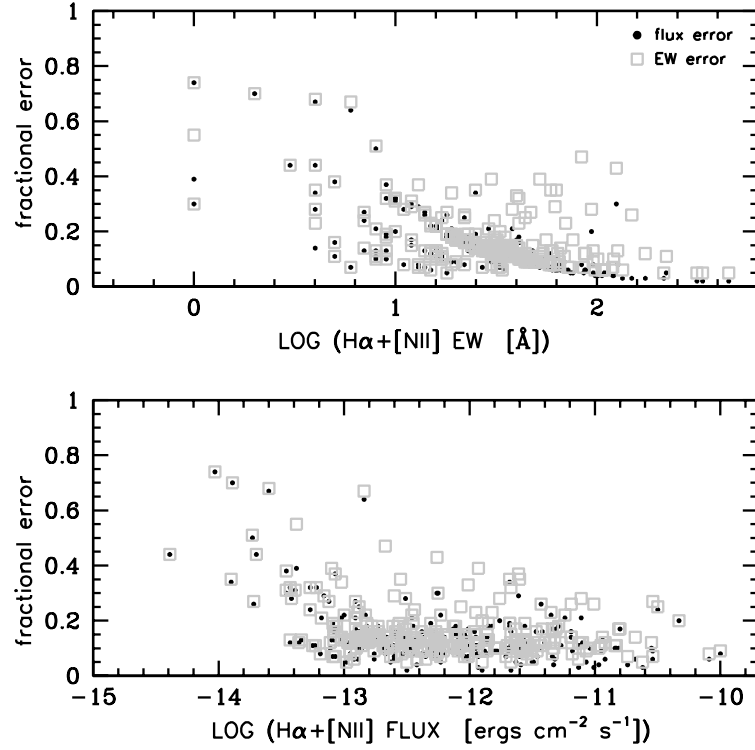


Figure 2.1: Total flux and EW errors plotted against the measurements themselves. Gray squares represent EW errors while points represent flux errors. The errors generally increase with decreasing EW, due to the dominance of the continuum subtraction errors in the total uncertainty. The 11HUGS fluxes and EWs have median uncertainties of $\sim 12\%$.

background are much smaller on average, as described above.

Uncertainties in the EW measurements are generally driven by the same factors as in the flux measurements. However, errors in the absolute flux calibration do not come into play since the EW is a ratio of the emission-line flux to the underlying continuum flux density, and calibrations are not required for the measurements in the first place. Also, since the uncertainties in the continuum levels usually translate into much larger fractional errors in the emission-line flux than in the continuum flux density itself, the errors in the EW follow the errors in the fluxes to within a few percent in most cases. The exceptions involve galaxies that

are faint, extended low surface brightness systems whose integrated continuum fluxes cannot be determined to better than a few tenths of a magnitude because of bright foreground stars either in the vicinity of, or superimposed on the galaxy, and/or limitations imposed by imperfections in the flat-fielding. We illustrate the distributions of the total uncertainties in our measurements by plotting the fractional errors in our fluxes and EWs as functions of the measurements themselves in Fig. 2.1.

2.3.7 Literature Comparison of Integrated Fluxes and EW

Many of the galaxies that we have observed have independent $H\alpha + [N II]$ and/or $H\alpha$ flux measurements in the literature, and these provide a valuable external check on our photometry and calibrations. The best comparison data set for this purpose is the integrated spectrophotometric atlas of nearby galaxies of Moustakas & Kennicutt (2006; hereafter MK06). This atlas is based on 8 Å resolution spectra with a wavelength range of 3650 – 6950 Å which were obtained by drift-scanning the spectrograph slit over as much of the optical extents of the galaxies as practical. Thus, spectral measurements extracted from this dataset represent the averaged, integrated properties of the galaxies, rather than local ones derived from the more usual single-position spectral observations of individual HII regions or the nuclear regions of galaxies. Emission-line fluxes were extracted from these spectra after fitting a stellar synthesis model to the underlying continuum. This process provides high S/N measurements even for relatively low emission-line EWs, and includes explicit correction for underlying stellar $H\alpha$ absorption.

There are 77 galaxies in common between 11HUGS and MK06, with 61 of these having independently calibrated fluxes from our observations. The left panel of Figure 2.2a compares the respective $H\alpha + [NII]$ fluxes. Galactic foreground extinction corrections have not been applied to either data set in this

comparison. The filled gray circles denote galaxies where the full extent of the $H\alpha$ emission was thought to be sampled by the spectral scan, while the open gray circles denote galaxies in which the scan misses outlying low surface brightness regions such as extended tidal features or the outer portions of spiral arms. Particularly in these latter cases, the drift scan apertures are generally smaller than the ones used in the photometry of our imaging data. Thus, we have also re-measured our imaging using the MK06 spectral apertures for the majority of galaxies in common between the samples, and have overplotted the resulting fluxes using black symbols.

Considering that the fluxes from these two datasets have been measured using entirely different techniques, the correspondence between the 11HUGS and MK06 results is quite reassuring. For the galaxies which have been fully covered by the spectral drift scans, the mean offset between the original 11HUGS measurements and the MK fluxes is only 0.007 dex (MK06 spectra 1–2% brighter) with an rms dispersion about the mean of 0.086 dex. The expected systematic difference for galaxies that suffer from spectral aperture undersampling is also seen, with the MK05 fluxes being 15% fainter on average. Using the re-measured 11HUGS fluxes instead confirms that most of this difference is indeed due to aperture effects, as the mean offset is reduced to 0.012 dex (MK spectra fainter by $< 3\%$) as shown in the residual plot in the left panel of Figure 2.2. The rms dispersion about a mean difference of zero is 0.083 dex, and is reduced by $\sim 5\%$ to 0.066 dex when it is calculated about the best fit line to the residuals. These dispersions are consistent with the average flux uncertainties of 10–15% in both datasets.

We compare the EWs in right panel of Figure 2.2. Although the correspondence between the measurements is still good, the MK06 EWs are higher on av-

erage whether the galaxies that are compared have been limited by the aperture sizes in the MK06 observations or not. The mean offsets between the original 11HUGS EWs and the MK06 values for the fully covered and aperture limited galaxies are 10% and 20% respectively. It may seem odd that galaxies which are completely enclosed by the spectral scans should exhibit such an offset, but since the resultant spectral apertures are generally set by the extents of the nebular regions, they often do not contain all of the continuum emission, which is more extended in galaxies on average. On the other hand, the apertures used to measure the continuum light in our imaging include the entire stellar disk (when not restricted by the FOV of the detector), and are larger than the narrowband apertures on average. Thus, the spectral continuum flux densities are typically lower than those measured from the imaging, leading to comparatively higher spectral EWs. However, these differences can only be partly explained by aperture differences. When we use the spectral apertures to re-measure our scaled R -band images, the relative mean offset of the MK EWs decrease, but are still 7% higher than the 11HUGS EWs. It is possible that the method we use to scale the R -band images, systematically overestimates the continuum flux density, but this would also result in systematically fainter fluxes, which are not seen. Another plausible explanation is that the sky background levels are overestimated in some of the spectral data where the spectrograph slit ($\sim 3''/3$) cannot adequately sample the sky. The rms dispersion about the mean difference between the re-measured 11HUGS and MK EWs is $\sim 20\%$, which is consistent with the dispersion seen in the flux comparison.

In addition to comparisons with the MK06 measurements, we have also taken advantage of a comprehensive compilation of integrated $H\alpha$ (and $H\alpha + [\text{NII}]$) fluxes and EWs by Kennicutt et al. (2006, in preparation; hereafter KAL06) to

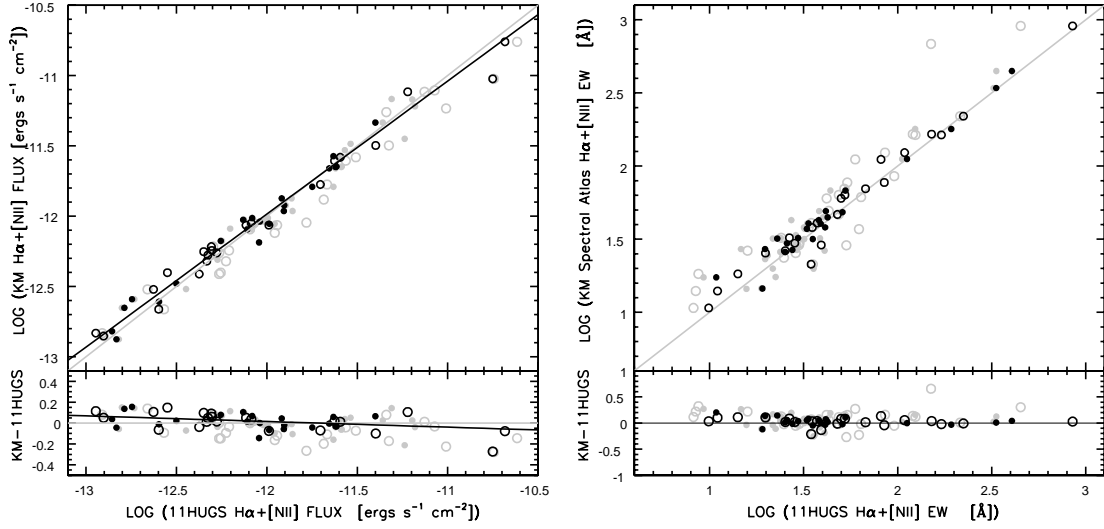


Figure 2.2: (*left*) Integrated H α + [NII] fluxes based on 11HUGS observations plotted against measurements from the integrated spectral atlas of Moustakas & Kennicutt (2006, MK06). Black symbols represent a comparison with imaging fluxes re-measured using the drift scan spectral apertures, while gray symbols represent a comparison that uses the original 11HUGS photometry. Open and filled circles denote galaxies where the extents of the nebular emission are limited by the MK06 apertures and those that are fully covered respectively. The line of one-to-one correspondence is shown by the gray line. The best fit line to the black symbols is indicated in black. A residual plot is shown in the bottom panel. (*right*) Same as the left panel, but for a comparison of the integrated H α + [NII] EWs.

carry out a more general comparison of our measurements with those already published in the literature. Measurements gathered by KAL06 were reduced to a uniform system by (1) standardizing corrections for Galactic extinction and [NII] contamination (where applicable), (2) inter-comparing common measurements among different studies to (a) determine if zeropoint corrections are necessary for the individual datasets, and (b) identify and remove highly discrepant measurements.⁴ After the flux scales of the studies are homogenized in this way,

⁴Note that although both the 11HUGS and MK06 measurements are included in the KAL06 compilation, they have been excluded from homogenization procedure for the purposes of this

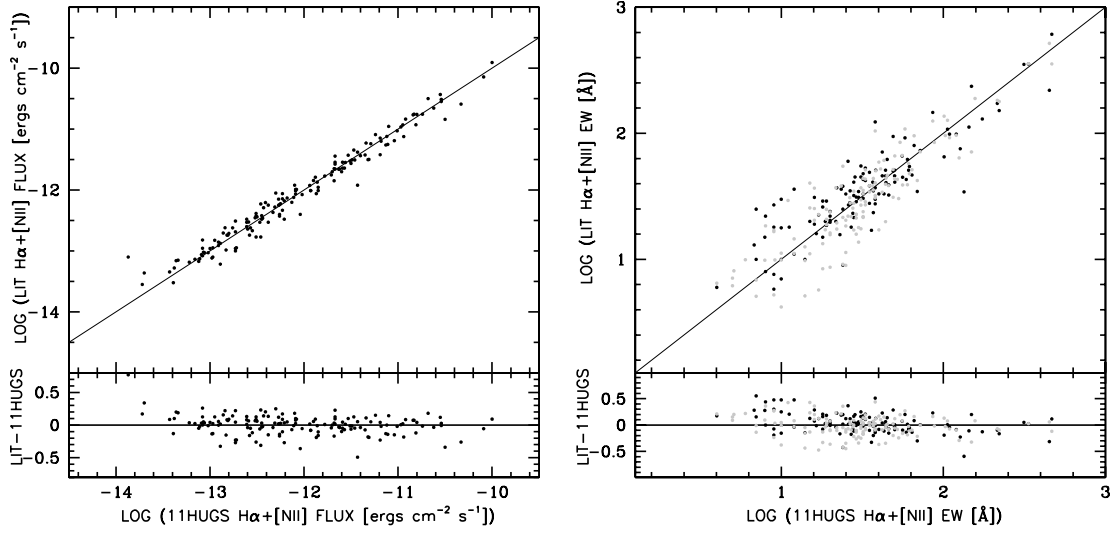


Figure 2.3: (*left*) Integrated H α + [NII] fluxes based on 11HUGS observations plotted against measurements from the homogenized flux compilation of Kennicutt et al. (in prep). (*right*) Same as the previous panel except for the EWs.

common measurements are averaged. Fluxes from the KAL06 compilation are available for $\sim 60\%$ of the galaxies that we have observed and calibrated independently, and we compare our measurements to those data in the left panel of Figure 2.3. The agreement is excellent with essentially no mean offset (11HUGS $\sim 1\%$ fainter), although there is a quite a large 0.15 dex (40%) rms dispersion about the mean.

As for the EWs, measurements from KAL06 are available for 40% of the galaxies that we have observed, and a comparison between the datasets is shown in the right panel of Figure 2.3. Again, there is good overall correspondence between the measurements. For the higher EW systems ($\text{EW} \gtrsim 15\text{\AA}$), there is a small mean offset of 0.013 dex (11HUGS 3% lower) and a rms dispersion of 0.164 dex (46%). However, our measurements of the lowest EW systems ($\text{EW} \lesssim 15\text{\AA}$) appear

analysis.

to be systematically lower by 30%. The literature EW values of these galaxies are primarily from the H α Galaxy Survey of James et al. (2004), who themselves have reported that their EWs are 30% larger on average than other measurements in literature. Since the EWs, unlike the fluxes in KAL06, have not been homogenized in any way, this discrepancy persists in the comparison presented here. Thus, we attribute the 30% offset as a systematic error in the James et al. (2004) measurements.

In summary, based on both the comparisons against the integrated spectral data of MK06 and the literature compilation of KAL06, we conclude that the methods we have used to flux calibrate, continuum subtract and measure our narrowband imaging result in measurements that are on an overall flux scale that is accurate to within $\pm 3\%$. Our reported EWs are also generally consistent with other measurements in the literature, although the possibility remains they may be underestimated by up to 7% on average.

2.3.8 The 11HUGS Integrated $H\alpha$ Flux and EW Catalog

We conclude this chapter with a presentation of the 11HUGS integrated $H\alpha$ flux and EW catalog. We have obtained narrowband $H\alpha+[NII]$ and R -band images for 307 of the 399 galaxies identified in Table 2.1, where 282 of these have been independently calibrated through our own observations. Integrated measurements from the literature are available for the majority of the remaining galaxies. We report both our measurements and those from the literature in Table 2.4 below. Overall, $\sim 95\%$ of the galaxies in the sample have fluxes, and $\sim 92\%$ have both fluxes and EWs.

Only 18 galaxies ($<5\%$ of the sample) lack measurements, and many of these have not been observed due to bright foreground stars which make obtaining adequate imaging difficult, if not impossible. As will be discussed in the following chapter, the physical properties of this subset of galaxies are not biased in any particular way, so the absence of these measurements should not affect conclusions regarding the star formation properties of the greater sample. Upper-limits corresponding to a 5σ point source detection have been listed for another 16 galaxies that have not been detected.

Column (1) – The running index number in this table.

Column (2) – Internal 11HUGS reference ID number.

Column (3) – Galaxy name.

Column (4) – Integrated $H\alpha+[NII]$ flux & error.

In LOG (ergs cm⁻² s⁻¹).

Column (5) – Integrated $H\alpha+[NII]$ EW & error.

In Å.

Column (6) – Source of flux & EW measurements.

The sources of the integrated $H\alpha+[NII]$ fluxes and EWs listed in the previous columns are coded as follows.

Galaxies with 11HUGS imaging

1.1 : (N=230) Measurements and errors are based on 11HUGS observations which were carried out under photometric conditions.

1.2 : (N= 51) Measurements and errors are based on 11HUGS observations which were initially carried out under thin cirrus, and are calibrated with bootstrap observations obtained under subsequent photometric conditions.

1.3 : (N= 25) 11HUGS observations for these galaxies were initially carried out under non-photometric conditions, but no subsequent bootstrap observations were obtained, generally because fluxes were known to already exist in the literature. Thus, EWs are based on 11HUGS observations, while fluxes are adopted from the compilation of KAL05.

1.4: For one galaxy, UGCA298, 11HUGS observations were carried out under non-photometric conditions and no bootstrap calibration exposures were obtained. There is no previously published $H\alpha$ flux measurement. The reported flux should thus be considered a lower-limit.

Galaxies without 11HUGS imaging

2.1 : (N= 46) Both flux and EW measurements are available in the literature, and have been adopted from the compilation of KAL06. Fluxes gathered by KAL05 were reduced to a uniform system by (1) standardizing corrections for Galactic extinction and [NII] contamination (where applicable), and (2) inter-comparing common measurements among different studies to determine if zeropoint corrections are necessary for the individual datasets, and to also identify and remove

highly discrepant measurements. After the flux scales of the various studies are homogenized in this way, common measurements are averaged.

Errors are adopted in the following order of preference. For galaxies with multiple measurements in the literature, the quoted errors correspond to half the range of non-rejected measurements. For galaxies with only single measurements, 1σ errors from the original paper are listed. If no errors are given by the reporting author, and an EW can be estimated by KAL05 (see description for code 2.2 below), then half the fractional difference between the predicted EW and the measured EW is adopted as the error for both the flux and EW. In all cases a minimum error of 0.01 dex is assigned to the fluxes. If an error cannot be estimated in one of these ways, a 10% uncertainty is quoted.

2.2 : (N= 15) Flux values have been adopted from the compilation of KAL05. However, no previous measurements of the EW are available in the literature, so the estimated values given by KAL05 have been adopted. KAL05 have computed EWs for galaxies for which both fluxes are available in their compilation and published *R*-band photometry exist elsewhere in the literature. Continuum flux densities are calculated from the *R*-band magnitudes and an approximate correction for the contribution of the $H\alpha + [NII]$ flux to the *R*-band light that scales with the EW itself is applied. The relation used is given by:

$$EW = f(H\alpha + [NII]) 10^{0.4(R+21.801)} \quad (2.1)$$

When the estimated values from this relation are compared with measured values from the literature, there is a rms dispersion of $\sim 35\%$

about a mean difference of zero. Thus, a fractional error of 35% is adopted for the estimated EWs given in the table.

2.3 : (N= 13) Flux values have been adopted from the compilation of KAL05. EWs are not available in the literature, and cannot be estimated because the relevant photometry does not exist.

0 : (N= 18) No measurements are available.

Column (7) – Telescope Used for 11HUGS Observations.

The telescopes and parameters of the detectors and filters used at each facility are given in Table 2.3.

Column (8) – Spatial Coverage Code for 11HUGS Observations.

The integer part of the code in this column indicates if the nebular emission in a galaxy has been adequately covered by the 11HUGS observations. For galaxies with large angular extents, observations using two different pointings were sometimes needed to more completely image the entire star-forming region. Decimal codes of “X.2” indicate when this has been done.

1 : (N=263) The boundaries of the star-forming regions/disk are clearly seen and the nebular emission in the galaxy has been completely sampled.

2 : (N= 28) The boundaries of the star-forming regions appear to be coincident with the edge of the FOV. The nebular regions are thought to be completely sampled, but there may be outer low surface brightness components of the galaxy which are not contained within the images.

3 : (N= 16) The fluxes for these galaxies should be considered lower limits since the imaging does not fully cover the high surface brightness nebular regions.

Column (9) – *B*-band Galactic extinction.

The Galactic extinctions listed represent an average of values based on the maps of Burstein & Heiles (1978) and Schlegel, Finkbeiner & Davis (1998), when both are available. We adopt independently measured foreground extinctions from the literature for the three galaxies in our sample which are closest to the Galactic plane (IC 10, Maffei 2, Circinus), since the SFD98 extinctions in these regions of the sky (i.e. $b < 5^\circ$) are known to be highly overestimated. Whereas the SFD98 A_B values are 6.6, 10.0 and 6.3 magnitudes for IC 10, Maffei 2, and Circinus, the adopted measurements are only 3.15 (based on $E(B-V)=0.77$ from Richer et al. 200), 6.12 (based on A_B for Maffei 1 from Fingerhut et al. 2003) and 2 magnitudes (based on $A_V=1.5+/-0.15$ from Freeman et al. 1977), respectively.

Column (10) – Absolute *B*-band magnitude.

Absolute *B*-band magnitudes are calculated using the distances and apparent magnitudes tabulated in Table 2.1, and the Galactic extinctions listed in the previous column.

Column (11) – The total $[NII]_{\lambda\lambda 6548,6583}/H\alpha$ ratio.

$[NII]_{\lambda 6584}$ to $H\alpha$ emission-line flux ratios are taken from (1) the integrated spectral observations of Moustakas & Kennicutt (2006) and Jansen et al. (2000), and (2) the spectra of individual HII regions from the various dwarf galaxy datasets of van Zee (van Zee & Haynes 2006 and references therein) where the average is adopted for those galaxies with multiple HII region observations. If measurements are not available from one of these sources, then the ratio is estimated using an empirical scaling relation between $[NII]_{\lambda 6584}/H\alpha$ and M_B , derived using data from MK06 (see Appendix B.1). The relation used is

given by:

$$\begin{aligned} \log([\text{NII}]\lambda 6584/\text{H}\alpha) &= (-0.173 \pm 0.007) M_B - (3.903 \pm -0.137) \quad \text{if } M_B > -21 \\ [\text{NII}]\lambda 6584/\text{H}\alpha &= 0.54 \quad \text{if } M_B \leq -21 \end{aligned} \quad (2.2)$$

$[\text{NII}]\lambda 6548$ is computed in the usual way, as 1/3 of $[\text{NII}]\lambda 6584$, which is set by the electron transition probabilities between energy levels in $[\text{NII}]$.

Column (12) – Integrated $\text{H}\alpha$ luminosity.

$L_{\text{H}\alpha}$ is calculated using the fluxes given in this table and the distances compiled in Table 2.1. A correction for foreground extinction is made using $A_{\text{H}\alpha} = 0.6 A_B$, but no correction has been applied for extinction internal to the galaxies themselves. Luminosities have been computed to exclude $[\text{NII}]$ emission, by using the $[\text{NII}]/\text{H}\alpha$ using the ratios in this table. *In ergs s^{-1} .*

TABLE 2.4 – The 11HUGS Integrated $H\alpha$ + $[\text{NII}]$ Flux and EW Catalog

#	ID	Galaxy Name	log f	err(log f)	EW	err(EW)	Source	Telescope	Coverage	Ab	M_B	$[\text{NII}]/H\alpha$	Ref.	L($H\alpha$)
(1)	(2)	(3)	(4)	(5)	(6)	(7)	(8)	(9)	(10)	(11)	(12)	(13)	(14)	(15)
1	2000	UGC12894	-13.41	0.02	2.3	0.45	-13.48	0.03	...	38.56
2	1	WLM	-11.68	0.13	25	9	1.1	KPNO	2.2	0.13	-13.91	0.04	...	38.34
3	2	ESO349-G031	<-15.1	...	0	...	2.2	0.05	-12.56	0.02	...	<36.2
4	3	N00024	-11.87	0.04	19	1	2.1	0.07	-17.20	0.15	...	39.89
5	4	N00045	-11.20	0.04	36	13	2.2	0.07	-17.75	0.18	...	40.42
6	5	N00055	-10.12	0.02	38	13	2.2	0.06	-17.91	0.20	...	40.41
7	6	NGC0059	-12.36	0.06	38	5	1.2	KPNO	1	0.07	-15.58	0.08	...	39.15
8	7	MCG-04-02-003	-13.01	0.05	18	2	2.1	0.07	-14.22	0.05	...	38.96
9	8	U00192	-10.95	0.04	69	7	1.1	KPNO	3	3.16	-15.45	0.07	...	39.49
10	9	N00224	-9.30	0.12	4	1	2.2	0.18	-20.31	0.51	...	40.44
11	10	IC1574	-13.19	0.12	6	2	2.1	0.06	-14.02	0.04	...	38.27
12	11	N00247	-10.79	0.08	25	9	2.2	0.07	-18.47	0.24	...	40.44
13	12	N00253	-10.12	0.02	16	5	2.2	0.07	-20.00	0.45	...	41.00
14	13	UGCA015	<-15.5	...	0	...	1.1	KPNO	1	0.07	-12.31	0.02	...	<35.6
15	2002	UGC00521	0	0.22	-15.03	0.06
16	14	SMC	-7.96	0.04	24	5	2.1	0.17	-16.36	0.11	...	39.68
17	15	N00300	-10.44	0.01	23	8	2.2	0.06	-17.84	0.19	...	40.18
18	2003	LGS3	<-15.5	...	0	...	2.1	0.16	-7.94	0.00	...	<34.2
19	16	U00668	-11.11	0.08	38	11	1.2	CTIO	3.2	0.06	-14.25	0.05	...	38.59
20	17	UGC00685	-12.57	0.07	31	6	1.1	KPNO	1	0.18	-14.38	0.10	MK05	38.87
21	18	UGC00695	-13.02	0.05	27	4	1.1	KPNO	1	0.08	-14.78	0.06	...	39.05
22	19	U00891	-13.12	0.10	14	4	1.2	KPNO	1	0.11	-15.46	0.12	Vetal97	38.96
23	20	UGC01056	-12.76	0.03	35	5	1.2	KPNO	1	0.22	-15.33	0.07	...	39.33
24	2004	UGC01104	-12.80	0.01	23.9	8	2.2	0.19	-15.16	0.07	...	39.01
25	21	N00598	-9.37	0.10	29	10	2.2	0.18	-18.53	0.25	...	40.50
26	22	N00625	-11.40	0.05	31	4	1.1	CTIO	1	0.07	-16.41	0.11	...	39.87
27	23	N00628	-10.84	0.04	35	4	1.1	VATT	3	0.21	-19.58	0.38	...	40.88
28	24	U01176	-12.81	0.05	32	5	1.2	VATT	1	0.21	-15.58	0.08	...	39.20
29	25	U01195	-12.51	0.06	27	4	1.2	KPNO	1	0.21	-16.39	0.11	...	39.73
30	27	UGCA020	-12.89	0.03	70	17	1.1	KPNO	1	0.18	-14.12	0.03	Vetal97	39.11
31	28	ESO245-G005	-11.96	0.03	42	3	2.1	0.07	-15.60	0.08	...	39.40
32	29	U01249	-11.96	0.06	22	4	1.1	KPNO	2	0.30	-17.51	0.05	MK05	39.89
33	30	N00672	-11.49	0.06	28	5	1.3	KPNO	3	0.29	-18.11	0.21	...	40.29
34	31	U01281	-12.45	0.07	22	4	1.2	KPNO	1	0.17	-14.68	0.07	MK05	38.89
35	2005	ESO245-G007	0	0.07	-9.96	0.01
36	33	N00784	-11.78	0.04	53	5	1.2	KPNO	2	0.24	-15.39	0.06	MK05	39.28
37	34	U01561	-12.90	0.04	17	2	1.1	KPNO	1	0.33	-14.18	0.14	MK05	39.24
38	1001	N855	-12.23	0.04	40	4	1.2	KPNO	1	0.26	-16.90	0.13	...	39.83

TABLE 2.4 – Continued

#	ID	Galaxy Name	log f	err(log f)	EW	err(EW)	Source	Telescope	Coverage	Ab	M_B	[NII]/Ha	Ref.	L(Ha)
(1)	(2)	(3)	(4)	(5)	(6)	(7)	(8)	(9)	(10)	(11)	(12)	(13)	(14)	(15)
39	35	U01807	-12.85	0.05	28	4	1.2	KPNO	1	0.32	-13.63	0.04	...	39.21
40	36	N00891	-11.35	0.09	15	3	1.1	VATT	3	0.29	-19.29	0.34	...	40.60
41	37	U01865	-12.73	0.06	30	5	1.1	KPNO	1	0.25	-15.69	0.08	...	39.30
42	38	N00925	-11.10	0.70	27	2	2.1	0.29	-19.41	0.36	...	40.84
43	2006	UGC01924	-13.41	0.05	2.3	0.31	-15.23	0.07	...	38.74
44	39	N00949	-11.78	0.04	26	5	1.3	KPNO	1	0.21	-17.62	0.17	...	40.20
45	40	N00959	-12.09	0.05	38	5	1.2	KPNO	1	0.23	-17.09	0.28	MK05	39.86
46	41	U02014	-13.34	0.05	16	2	1.2	KPNO	1	0.19	-14.35	0.05	...	38.69
47	42	U02023	-12.41	0.05	32	4	1.1	KPNO	1	0.38	-16.30	0.10	VH05	39.64
48	43	U02034	-12.51	0.11	11	3	1.1	KPNO	1	0.21	-16.32	0.10	...	39.50
49	44	U02082	-12.46	0.08	16	3	1.1	KPNO	1	0.57	-17.22	0.15	...	39.83
50	45	ESO115-G021	-12.11	0.06	31	5	1.1	CTIO	1	0.06	-15.06	0.06	...	39.29
51	46	N01003	-11.60	0.04	42	4	1.1	KPNO	2	0.27	-18.08	0.18	MK05	40.40
52	47	Maffet2	-11.95	0.06	4	1	1.2	VATT	2	6.12	-18.59	0.26	...	40.39
53	48	N01058	-11.63	0.05	29	4	1.1	KPNO	2	0.25	-18.24	0.49	MK05	40.26
54	49	U02259	-12.28	0.05	28	4	1.1	KPNO	1	0.27	-14.92	0.06	...	39.76
55	50	ESO154-G023	-11.93	0.04	40	3	2.1	0.04	-16.16	0.10	...	39.65
56	51	N01156	-11.51	0.03	49	4	1.1	KPNO	1	0.82	-17.53	0.18	MK05	40.48
57	52	ESO300-G014	-12.17	0.07	13	2	2.1	0.04	-17.24	0.15	...	39.94
58	53	N01249	-11.62	0.04	37	4	1.1	CTIO	1	0.04	-18.28	0.23	...	40.55
59	54	N01291	-11.66	0.01	8	3	2.2	0.03	-20.53	0.56	...	40.19
60	55	N01313	-10.63	0.14	35	4	2.1	0.25	-19.14	0.32	...	40.63
61	56	N01311	-12.04	0.03	33	2	1.1	CTIO	1	0.05	-15.64	0.08	...	39.53
62	57	U02684	-13.72	0.10	18	5	1.2	KPNO	1	0.50	-13.26	0.05	Vetal97	38.08
63	58	UGC02689	<-15.5	...	0	...	1.1	VATT	1	0.69	-14.94	0.06	...	<36.4
64	59	UGC02716	-12.95	0.03	13	1	1.2	KPNO	1	0.51	-15.06	0.06	...	38.90
65	60	IC1959	-12.04	0.03	47	4	2.1	0.02	-15.86	0.09	...	39.64
66	61	U02847	-10.81	0.04	56	10	1.2	VATT	3	2.88	-21.36	0.72	...	40.74
67	62	IC2000	-12.10	0.06	17	3	2.1	0.02	-17.43	0.16	...	40.00
68	63	ESO302-G014	-12.75	0.03	49	3	2.1	0.02	-14.54	0.05	...	39.32
69	64	NGC1487	-11.57	0.04	46	5	2.1	0.03	-17.57	0.17	...	40.40
70	65	ESO249-G036	-12.57	0.04	36	3	2.1	0.02	-14.29	0.05	...	39.50
71	66	UGCA086	-12.01	0.07	40	13	1.1	KPNO	3.2	3.55	-17.17	0.15	...	39.71
72	1003	N1510	-12.17	0.05	35	4	1.1	CTIO	1	0.02	-16.61	0.12	...	39.89
73	67	N01512	-11.43	0.10	14	4	1.1	CTIO	2	0.02	-18.91	0.29	...	40.55
74	68	N01507	-11.94	0.05	32	4	1.1	KPNO	1	0.54	-18.01	0.20	...	40.33
75	69	NGC1522	-12.26	0.03	61	5	1.1	CTIO	1	0.03	-16.08	0.09	...	39.78
76	70	N01518	-11.70	0.04	35	4	1.1	KPNO	1	0.12	-18.14	0.22	...	40.44

TABLE 2.4 – Continued

#	ID	Galaxy Name	log f	err(log f)	EW	err(EW)	Source	Telescope	Coverage	Ab	M_B	[NII]/Ha	Ref.	L(Ha)
(1)	(2)	(3)	(4)	(5)	(6)	(7)	(8)	(9)	(10)	(11)	(12)	(13)	(14)	(15)
77	71	IC2049	0	0.05	-14.70	0.05
78	72	ESO483-G013	-12.35	0.03	34	2	1.2	KPNO	1	0.14	-15.96	0.09	...	39.73
79	73	NGC1556	-12.01	0.03	59	5	1.1	CTIO	1	0.05	-16.78	0.13	...	40.11
80	74	UGCA090	-12.04	0.06	24	4	1.1	KPNO	2	0.07	-17.64	0.22	MK05	40.07
81	75	N01569	-10.62	0.01	215	12	1.1	KPNO	1	2.53	-17.12	0.07	MK05	40.61
82	76	UGCA092	-12.53	0.03	96	12	1.2	KPNO	1	2.84	-13.90	0.04	...	38.72
83	77	N01560	-11.54	0.05	36	4	1.1	VATT	2.2	0.72	-16.25	0.10	MK05	39.74
84	2007	ESO158-G003	0	0.02	-16.15	0.10
85	79	U03174	-12.82	0.03	24	8	2.2	0.36	-15.20	0.08	Vetal97	39.25
86	80	ESO119-G016	-12.60	0.04	46	5	1.1	CTIO	1	0.06	-15.38	0.07	...	39.51
87	81	N01705	-11.50	0.02	109	7	1.1	CTIO	1	0.11	-15.88	0.09	...	39.98
88	82	N01744	-11.67	0.05	31	4	1.1	KPNO	2	0.09	-18.21	0.22	...	40.23
89	83	N01796	-11.80	0.04	45	4	1.1	CTIO	1	0.05	-17.34	0.16	...	40.29
90	84	ESO486-G021	-12.49	0.04	43	4	1.2	KPNO	1	0.07	-15.69	0.08	...	39.61
91	85	MCG-05-13-004	-12.01	0.03	32	2	1.1	CTIO	1	0.03	-16.24	0.10	...	39.81
92	86	N01800	-12.09	0.05	32	4	1.1	KPNO	1	0.03	-16.80	0.21	MK05	39.85
93	87	N01808	-10.94	0.05	29	4	1.1	CTIO	1	0.10	-19.66	0.39	...	41.15
94	88	UGCA103	-11.93	0.03	52	20	1.1	KPNO	1	0.03	-17.22	0.15	...	40.22
95	89	UGCA106	-11.95	0.04	37	5	1.1	KPNO	1	0.05	-17.18	0.15	...	40.16
96	90	UGCA105	-11.60	0.03	59	20	1.1	VATT	2	1.36	-14.39	0.05	...	39.78
97	91	LMC	-6.97	0.05	36	8	2.1	0.29	-17.87	0.19	...	40.50
98	92	UGC3303	0	VATT	1	0.57	-15.91	0.09
99	2008	ESO553-G046	0	0.15	-14.62	0.05
100	93	UGCA114	-11.86	0.05	32	5	1.1	KPNO	1	0.60	-17.93	0.19	MK05	40.41
101	94	UGCA116	-11.67	0.01	451	23	1.1	KPNO	1	2.90	-17.65	0.06	MK05	41.17
102	95	ESO364-G7029	-12.31	0.04	37	5	1.1	CTIO	1	0.11	-15.86	0.09	...	39.66
103	96	AM0605-341	-12.66	0.06	29	4	1.1	CTIO	1	0.10	-14.27	0.05	...	39.30
104	97	N02188	-11.72	0.04	36	13	2.2	0.08	-17.54	0.20	...	40.15
105	98	UGCA120	-12.78	0.06	35	6	1.1	KPNO	1	0.36	-16.37	0.11	...	39.38
106	99	UGCA127	-11.67	0.05	48	7	1.1	VATT	1	2.95	-18.68	0.27	...	40.97
107	100	U03475	-12.83	0.09	16	4	1.1	VATT	1	0.97	-15.79	0.08	...	39.37
108	101	UGC03600	-13.90	0.13	4	2	1.1	VATT	1	0.49	-13.61	0.04	...	38.01
109	102	AM0704-582	-12.67	0.03	84	39	1.1	CTIO	1	0.43	-13.93	0.04	...	38.87
110	103	N02337	-11.86	0.03	44	4	1.1	KPNO	1	0.38	-16.39	0.10	MK05	40.06
111	104	U03817	-12.97	0.05	59	8	1.2	VATT	1	0.39	-14.10	0.04	...	39.05
112	105	U03860	-12.97	0.05	33	4	1.1	KPNO	1	0.24	-14.63	0.05	...	38.93
113	106	N02366	-11.01	0.01	149	38	1.1	KPNO	1	0.16	-16.25	0.03	MK05	40.10
114	107	ESO059-G001	-12.61	0.07	20	4	1.1	CTIO	1	0.63	-14.66	0.05	...	38.80

TABLE 2.4 – Continued

#	ID	Galaxy Name	log f	err(log f)	EW	err(EW)	Source	Telescope	Coverage	Ab	M_B	[NII]/Ha	Ref.	L(Ha)
(1)	(2)	(3)	(4)	(5)	(6)	(7)	(8)	(9)	(10)	(11)	(12)	(13)	(14)	(15)
115	108	N02427	-11.66	0.04	27	10	2.2	0.83	-18.67	0.27	...	40.58
116	109	N02403	-10.25	0.04	26	3	2.1	0.17	-18.78	0.28	...	40.78
117	110	U03966	-13.06	0.07	20	4	1.1	KPNO	...	0.21	-15.48	0.07	...	38.70
118	111	U03974	-12.51	0.06	32	5	1.2	KPNO	1	0.12	-15.09	0.06	...	39.00
119	112	CGCG262-028	-12.42	0.02	98	6	1.1	KPNO	1	0.25	-15.11	0.06	...	39.61
120	113	U04115	-12.61	0.05	37	4	1.2	VATT	1	0.11	-13.58	0.03	...	38.96
121	114	N02500	-11.60	0.04	38	4	1.1	VATT	1	0.15	-17.95	0.24	MK05	40.42
122	115	N02537	-11.65	0.01	37	5	1.3	KPNO	1	0.19	-16.57	0.26	MK05	40.05
123	117	U04278	-12.07	0.04	37	4	1.1	KPNO	1	0.19	-17.20	0.15	...	40.03
124	119	U04305	-11.27	0.04	51	4	2.1	0.11	-16.67	0.12	...	39.84
125	120	N02552	-12.02	0.05	32	4	1.1	VATT	...	0.19	-17.63	0.31	MK05	39.99
126	121	M81dwA	<-15.3	...	0	...	1.1	KPNO	1	0.09	-9.15	0.01	...	<35.9
127	122	U04426	-13.43	0.12	10	3	1.1	VATT	1	0.14	-13.92	0.04	...	38.18
128	123	U04459	-12.26	0.12	125	54	1.1	KPNO	1	0.13	-13.11	0.02	MK05	38.94
129	124	ESO495-G021	-11.13	0.01	134	8	1.1	KPNO	1	0.48	-18.04	0.21	...	40.99
130	125	U4483	-12.46	0.05	144	11	1.3	KPNO	1	0.14	-12.41	0.02	MK05	38.66
131	126	N02683	-11.34	0.07	12	2	1.2	KPNO	3	0.11	-18.90	0.29	...	40.43
132	127	U04704	-12.88	0.06	25	4	1.2	VATT	1	0.09	-14.78	0.06	...	39.21
133	2009	LSBCD564-08	<-15.3	...	0	...	2.1	0.10	-12.18	0.02	...	<36.4
134	128	U04787	-12.82	0.07	19	4	1.1	VATT	1	0.07	-14.36	0.09	MK05	39.12
135	2010	LSBCD634-03	<-15.4	...	0	...	2.1	0.14	-10.08	0.01	...	<35.7
136	129	UGCA148	-13.24	0.09	18	4	1.1	CTIO	1	0.75	-15.39	0.07	...	38.97
137	1007	N2784	-12.22	0.10	2	0.4	1.1	CTIO	1	0.82	-19.48	0.37	...	39.91
138	130	UGCA153	-13.18	0.08	29	6	1.2	VATT	1	0.34	-14.56	0.05	...	38.81
139	131	N02835	-10.92	0.03	88	10	1.2	CTIO	1	0.42	-19.50	0.37	...	41.16
140	2011	LSBCD565-06	<-15.7	...	0	...	2.1	0.13	-12.20	0.02	...	<36.0
141	132	UGCA162	-12.77	0.05	32	4	1.1	CTIO	1	0.28	-14.97	0.06	...	39.32
142	133	UGC04998	-13.27	0.09	7	2	1.1	KPNO	1	0.21	-15.59	0.08	...	38.87
143	134	N02915	-11.85	0.05	38	5	1.1	CTIO	1	0.85	-15.54	0.08	...	39.56
144	135	N02903	-10.73	0.06	20	5	2.1	0.10	-20.17	0.56	MK05	41.08
145	1009	U5076	-13.71	0.20	4	3	1.1	KPNO	1	0.04	-14.96	0.06	...	38.40
146	2012	UGCA168	0	0.62	-17.92	0.20
147	136	CGCG035-007	-13.23	0.05	16	2	1.1	KPNO	1	0.15	-13.65	0.04	...	38.46
148	137	U05151	-12.30	0.04	42	4	1.1	KPNO	1	0.06	-17.00	0.13	MK05	40.03
149	138	U05139	-12.44	0.05	31	7	1.1	KPNO	1	0.13	-13.88	0.04	...	38.82
150	140	IC0559	-13.07	0.03	13	1	1.1	KPNO	1	0.07	-13.87	0.04	...	38.46
151	2013	UGC05209	-13.97	0.07	2.3	0.04	-13.42	0.03	...	37.89
152	141	N02976	-11.19	0.06	28	4	1.1	KPNO	1	0.21	-16.72	0.12	...	39.99

TABLE 2.4 – Continued

#	ID	Galaxy Name	log f	err(log f)	EW	err(EW)	Source	Telescope	Coverage	Ab	M_B	[NII]/Ha	Ref.	L(Ha)
(1)	(2)	(3)	(4)	(5)	(6)	(7)	(8)	(9)	(10)	(11)	(12)	(13)	(14)	(15)
153	1011	LEDA 086265	-13.84	0.05	55	7	1.1	KPNO	1	0.06	-11.56	0.02	...	37.95
154	142	U05272	-12.38	0.03	45	4	1.1	KPNO	1	0.06	-13.91	0.04	...	39.40
155	143	U5288	-12.47	0.04	46	5	1.2	VATT	1	0.08	-14.93	0.08	VH05	39.26
156	144	NGC3037	-12.16	0.04	41	4	1.1	CTIO	1	0.27	-16.56	0.11	...	39.94
157	145	N03031	-10.32	0.05	9	1	2.1	0.24	-20.15	0.48	...	40.77
158	146	N03034	-10.09	0.03	64	5	1.1	KPNO	2	0.40	-18.84	0.28	...	41.07
159	147	U05340	-12.72	0.06	33	5	1.2	KPNO	1	0.05	-14.15	0.04	...	38.90
160	1012	KDG61	-13.41	0.05	36	5	1.1	KPNO	1	0.24	-12.85	0.03	...	37.83
161	148	U5336	-13.07	0.14	9	3	1.1	KPNO	1	0.25	-13.79	0.04	...	38.19
162	149	ESO435-IG020	-11.93	0.01	174	21	1.1	CTIO	1	0.29	-15.06	0.06	...	39.86
163	150	U05364	-12.84	0.22	6	4	1.2	KPNO	1	0.08	-11.35	0.02	VH05	36.93
164	151	U05373	-12.20	0.01	5	4	1.3	KPNO	1	0.09	-13.91	0.04	...	38.15
165	152	UGCA193	-12.80	0.06	30	4	1.2	VATT	1	0.11	-15.21	0.07	...	39.25
166	153	N03109	-11.10	0.05	30	4	1.1	CTIO	1.2	0.22	-15.45	0.07	...	39.25
167	154	N03077	-11.18	0.04	30	2	1.2	KPNO	1	0.25	-17.55	0.38	MK05	39.98
168	156	UGC05427	-13.09	0.08	18	4	1.1	VATT	1	0.07	-13.37	0.03	...	38.69
169	1013	U5428	-14.71	0.25	1	1	1.1	VATT	1	0.27	-12.04	0.02	...	36.52
170	1014	N3115	-11.46	0.03	10	1	1.3	CTIO	1	0.15	-20.21	0.49	...	40.45
171	157	U05423	-12.86	0.05	27	4	1.1	KPNO	1	0.26	-13.68	0.05	MK05	38.71
172	158	NGC3125	-11.49	0.02	221	25	1.1	KPNO	1	0.29	-16.65	0.12	...	40.56
173	160	UGC05451	-12.72	0.05	14	2	1.1	KPNO	1	0.03	-15.87	0.16	NFGS	39.38
174	161	U5456	-12.32	0.01	46	6	1.3	KPNO	1	0.11	-14.29	0.05	...	38.93
175	162	KUG1004+392	-12.63	0.02	74	5	1.1	VATT	1	0.03	-13.86	0.04	...	39.36
176	163	SextansA	-11.67	0.07	41	13	1.1	KPNO	1	0.13	-13.87	0.04	...	38.66
177	165	N03239	-11.32	0.03	60	8	1.1	VATT	1	0.12	-18.21	0.10	MK05	40.68
178	166	UGC05672	-13.08	0.05	8	1	1.1	KPNO	1	0.05	-13.91	0.04	...	38.59
179	167	U05666	-11.23	0.07	28	4	2.1	0.11	-17.33	0.16	...	40.02
180	168	UGC05692	-12.82	0.05	7	1	1.1	KPNO	1	0.13	-14.43	0.05	...	38.47
181	169	N03274	-11.91	0.06	50	6	1.3	KPNO	1	0.08	-15.93	0.13	MK05	39.76
182	2014	ESO375-G071	0	0.26	-17.15	0.14
183	170	N03299	-12.48	0.10	7	2	1.3	VATT	1	0.07	-16.04	0.09	...	39.61
184	171	U05764	-12.95	0.03	44	4	1.1	KPNO	1	0.06	-14.25	0.03	Vetal97	38.89
185	172	UGC05797	-13.19	0.03	11	1	1.1	KPNO	1	0.09	-14.28	0.05	...	38.57
186	173	U05829	-12.08	0.04	38	4	1.1	VATT	1	0.07	-16.06	0.08	Vetal97	39.87
187	174	N03344	-11.19	0.07	41	6	1.2	KPNO	3	0.09	-18.70	0.52	MK05	40.35
188	175	N03351	-11.24	0.08	16	3	1.1	KPNO	3	0.08	-19.55	0.68	MK05	40.63
189	176	N03365	-12.27	0.06	22	4	1.1	KPNO	1	0.14	-17.45	0.30	MK05	39.92
190	177	N03368	-11.47	0.06	5	1	1.1	VATT	2	0.08	-20.08	0.47	...	40.51

TABLE 2.4 – Continued

#	ID	Galaxy Name	log f	err(log f)	EW	err(EW)	Source	Telescope	Coverage	Ab	M_B	[NII]/Ha	Ref.	L(Ha)
(1)	(2)	(3)	(4)	(5)	(6)	(7)	(8)	(9)	(10)	(11)	(12)	(13)	(14)	(15)
191	178	U05889	-13.01	0.04	8	4	1.3	VATT	1	0.09	-15.72	0.08	...	38.99
192	180	UGC05923	-12.92	0.03	15	1	1.1	KPNO	1	0.08	-15.21	0.15	NFGS	38.78
193	181	U05918	-13.16	0.04	19	5	1.3	VATT	1	0.02	-14.15	0.04	...	38.64
194	1019	N3412	-12.55	0.10	2	0.4	1.1	CTIO	1	0.09	-18.73	0.27	...	39.48
195	182	N03423	-11.43	0.04	37	4	1.1	KPNO	1	0.10	-19.17	0.32	...	40.81
196	184	N03432	-11.34	0.03	64	5	1.2	KPNO	3	0.03	-18.06	0.18	MK05	40.55
197	185	KDG073	<-15.6	...	0	...	1.1	VATT	1	0.07	-10.63	0.01	...	<35.6
198	1021	N3489	-12.92	0.23	1	1	1.1	VATT	1	0.05	-19.02	0.30	...	39.09
199	186	N03486	-11.12	0.05	44	6	1.3	KPNO	2.2	0.05	-18.62	0.26	...	40.72
200	187	UGC06102	-13.43	0.05	15	2	1.1	KPNO	1	0.06	-14.23	0.05	...	38.52
201	188	N03510	-12.10	0.04	42	4	1.1	KPNO	1	0.07	-15.46	0.17	MK05	39.81
202	189	MRK36	-12.21	0.05	467	33	1.3	KPNO	1	0.07	-13.77	0.03	MK05	39.63
203	190	N03521	-10.85	0.04	16	1	2.1	0.16	-19.73	0.57	MK05	40.84
204	191	N03593	-11.71	0.03	14	1	1.1	KPNO	1	0.04	-16.72	0.12	...	39.74
205	192	NGC3599	-13.67	0.07	1	0.2	1.1	VATT	1	0.04	-16.90	0.13	...	38.23
206	193	N03600	-12.13	0.04	38	4	1.1	KPNO	1	0.04	-16.40	0.21	MK05	40.01
207	194	N03621	-10.55	0.04	54	7	1.1	CTIO	2	0.37	-19.30	0.34	...	41.13
208	195	N03623	-11.53	0.04	5	1	1.1	KPNO	2	0.06	-19.07	0.31	...	40.15
209	196	N03627	-10.74	0.05	19	1	2.1	0.08	-20.44	0.54	...	41.17
210	197	N03628	-11.49	0.05	8	1	2.1	0.07	-19.22	0.39	MK05	40.23
211	198	IC2787	<-15.6	...	0	...	1.1	KPNO	1	0.09	-12.93	0.03	...	<36.0
212	199	UGC06457	-12.85	0.05	27	4	1.1	VATT	1	0.09	-15.16	0.07	...	39.25
213	200	U06456	-12.25	0.03	127	17	1.1	KPNO	1	0.12	-12.41	0.06	MK05	39.11
214	201	U06541	-12.23	0.02	86	6	1.1	KPNO	1	0.04	-13.59	0.04	MK05	39.02
215	202	N03738	-11.84	0.02	27	5	1.3	KPNO	1	0.02	-16.50	0.13	MK05	39.57
216	203	N3741	-12.41	0.04	56	6	1.3	KPNO	1	0.06	-12.97	0.02	MK05	38.63
217	204	U06782	-13.27	0.07	49	19	2.1	KPNO	1	0.08	-13.23	0.03	...	38.10
218	205	U06817	-12.49	0.01	26	5	1.3	VATT	1	0.06	-13.60	0.04	...	38.43
219	206	U06900	-13.22	0.12	10	3	1.1	KPNO	1	0.06	-14.22	0.05	...	38.44
220	207	N04020	-12.20	0.06	29	4	1.2	KPNO	1	0.04	-15.92	0.27	MK05	39.66
221	209	U07007	-13.39	0.12	10	3	1.1	VATT	1	0.04	-13.78	0.04	...	38.70
222	210	N04068	-12.10	0.04	28	5	1.3	KPNO	1	0.05	-15.61	0.07	MK05	39.39
223	211	NGC4080	-12.63	0.04	17	2	1.1	KPNO	1	0.07	-14.28	0.05	...	38.84
224	213	N04096	-11.57	0.04	20	2	1.1	KPNO	1	0.04	-18.40	0.42	MK05	40.30
225	214	N04144	-11.68	0.04	23	5	1.3	KPNO	1	0.03	-17.94	0.19	MK05	40.31
226	215	N04163	-12.91	0.08	8	2	1.1	KPNO	1	0.04	-14.07	0.18	MK05	38.22
227	216	N04190	-12.37	0.04	22	5	1.3	KPNO	1	0.06	-13.88	0.11	MK05	38.77
228	2015	UGC07242	0	0.05	-13.56	0.03

TABLE 2.4 – Continued

#	ID	Galaxy Name	log f _{err} (log f)	EW	err(EW)	Source	Telescope	Coverage	Ab	M_B	[NII]/Ha	Ref.	L(Ha)
(1)	(2)	(3)	(4)	(5)	(6)	(7)	(8)	(9)	(10)	(11)	(12)	(13)	(14)
229	217	UGCA276	<-15.6	0	...	1.1	KPNO	1	0.05	-11.63	0.02	...	<35.4
230	218	N04204	-11.88	42	4	1.1	VATT	1	0.11	-16.63	0.12	...	40.39
231	219	U07267	-12.97	11	4	1.3	VATT	1	0.08	-14.36	0.05	...	38.93
232	220	U07271	-13.00	16	2	1.2	VATT	1	0.03	-14.04	0.04	...	38.89
233	221	N04214	-10.79	62	7	1.3	KPNO	3	0.05	-17.15	0.16	MK05	40.17
234	222	U7298	<-15.4	0	...	1.1	KPNO	1	0.07	-12.13	0.02	...	<35.9
235	223	N04236	-10.96	26	3	2.1	0.06	-18.25	0.22	...	40.34
236	224	N04244	-11.31	20	4	1.1	KPNO	2	0.05	-17.43	0.23	MK05	40.00
237	225	N04242	-11.85	18	3	1.1	KPNO	1	0.03	-18.17	0.22	...	39.96
238	226	U07321	-12.56	18	3	1.1	KPNO	2	0.08	-13.46	0.03	...	38.53
239	227	N04248	-12.66	8	1	1.1	KPNO	1	0.04	-16.29	0.26	MK05	39.11
240	228	IC3104	-12.43	9	1	1.1	CTIO	1	1.11	-14.40	0.05	...	38.61
241	229	N04258	-10.50	11	1	2.1	0.03	-20.44	0.54	...	41.21
242	1084	U7356	<-15.5	0	...	1.1	KPNO	1	0.05	-13.60	0.04	...	<36.2
243	2016	ISZ399	-12.46	27	2.7	2.1	0.17	-15.32	0.07	...	39.58
244	230	N04288	-12.09	49	4	1.1	KPNO	1	0.03	-16.42	0.21	MK05	39.77
245	231	U07408	-14.85	0	0.2	1.2	VATT	1	0.03	-15.93	0.09	...	36.90
246	232	UGC07490	-12.46	16	2	1.1	KPNO	1	0.05	-17.09	0.14	...	39.61
247	233	N04395	-11.28	24	2	2.1	0.04	-17.72	0.18	...	40.06
248	234	UGCA281	-11.90	335	17	1.1	KPNO	1	0.03	-13.45	0.03	MK05	39.69
249	235	U07559	-12.45	38	5	1.3	KPNO	1	0.03	-14.27	0.05	...	38.99
250	236	U07577	-12.50	9	2	1.3	KPNO	1	0.04	-14.23	0.05	...	38.38
251	237	N04449	-10.54	72	5	1.1	KPNO	1	0.04	-18.17	0.22	...	40.71
252	238	U07599	-13.46	12	4	1.2	KPNO	1	0.04	-14.35	0.05	...	38.29
253	239	U07605	-12.95	31	4	1.1	KPNO	1	0.04	-13.48	0.03	...	38.42
254	240	N04455	-12.07	35	4	1.1	VATT	1	0.07	-14.58	0.14	MK05	39.30
255	241	U07608	-12.36	54	5	1.2	VATT	1	0.04	-15.85	0.09	...	39.49
256	1089	N4460	-11.77	35	3	1.2	KPNO	1	0.04	-17.17	0.15	...	40.22
257	1090	MCG07-26-011	-13.29	19	3	1.1	KPNO	1	0.05	-12.46	0.02	...	38.28
258	242	U07639	-13.42	4	1	1.2	VATT	1	0.03	-15.55	0.08	...	38.44
259	1091	MCG07-26-012	-13.66	9	2	1.1	KPNO	1	0.04	-12.51	0.02	...	37.99
260	243	N04485	-11.63	76	13	1.1	KPNO	3	0.05	-16.92	0.13	...	40.08
261	244	N04490	-10.68	66	9	1.1	KPNO	3	0.05	-19.37	0.35	...	41.10
262	245	UGC07678	-12.60	27	2	1.1	KPNO	1	0.03	-13.87	0.05	NFGS	39.44
263	246	U07690	-12.31	24	4	1.1	KPNO	1	0.07	-16.43	0.13	MK05	39.52
264	247	U07699	-12.27	26	4	1.1	KPNO	1	0.03	-15.35	0.16	NFGS	39.32
265	248	U07698	-12.23	44	5	1.1	KPNO	2	0.05	-15.98	0.09	...	39.39
266	249	U07719	-12.69	52	6	1.2	KPNO	1	0.03	-14.66	0.05	...	39.36

TABLE 2.4 – Continued

#	ID	Galaxy Name	log f	err(log f)	EW	err(EW)	Source	Telescope	Coverage	Ab	M_B	[NII]/Ha	Ref.	L(Ha)
(1)	(2)	(3)	(4)	(5)	(6)	(7)	(8)	(9)	(10)	(11)	(12)	(13)	(14)	(15)
267	250	N04534	-11.95	0.05	64	7	1.2	KPNO	1	0.03	-17.36	0.15	MK05	40.23
268	251	U07774	-12.88	0.10	22	6	1.2	KPNO	1	0.04	-14.27	0.05	...	38.89
269	1093	UA290	-13.18	0.03	46	4	1.1	KPNO	1	0.03	-13.42	0.03	...	38.54
270	252	UGCA292	-12.77	0.01	157	12	1.3	KPNO	1	0.04	-11.40	0.02	VH05	38.22
271	253	N04592	-11.69	0.04	41	4	1.1	VATT	2	0.09	-17.77	0.19	...	40.57
272	2017	MESSIER104	-12.10	0.35	0.4	1	2.1	0.17	-21.04	0.72	...	39.74
273	254	N04605	-11.13	0.05	34	4	1.1	VATT	1	0.03	-17.72	0.27	MK05	40.28
274	255	N04618	-11.36	0.04	33	4	1.1	KPNO	1	0.05	-18.26	0.29	MK05	40.39
275	256	N04625	-12.03	0.06	25	4	1.1	KPNO	1	0.04	-16.89	0.55	MK05	39.78
276	257	N04631	-10.55	0.06	45	1	2.1	0.05	-19.40	0.35	...	41.05
277	258	U07866	-12.21	0.03	49	4	1.1	VATT	1	0.04	-14.63	0.05	...	39.18
278	259	N04656	-11.07	0.02	96	9	1.1	KPNO	2.2	0.04	-18.37	0.07	MK05	40.71
279	260	U07916	-12.55	0.03	63	22	1.1	VATT	1	0.05	-14.33	0.05	...	39.23
280	261	N04670	-11.59	0.02	106	6	1.1	VATT	1	0.05	-18.48	0.16	MK05	41.04
281	262	ESO381-G020	-12.27	0.03	65	6	1.2	CTIO	1	0.27	-13.84	0.04	...	39.16
282	1096	UGCA298	>-12.74	0.05	39	5	1.4	VATT	1	0.05	-13.93	0.04	...	>39.1
283	263	N07950	-12.80	0.05	15	2	1.1	KPNO	1	0.03	-14.70	0.11	MK05	39.15
284	264	U07949	-13.10	0.05	30	12	1.1	KPNO	1	0.05	-14.91	0.06	...	38.96
285	265	N04707	-12.52	0.06	25	4	1.1	VATT	1	0.03	-16.23	0.10	...	39.36
286	266	N04736	-10.72	0.06	10	1	2.1	0.04	-19.39	0.71	MK05	40.47
287	267	U08024	-12.73	0.05	27	4	1.1	KPNO	1	0.03	-14.26	0.04	Vetal97	38.61
288	2018	UGC08055	-13.46	0.04	2.3	0.08	-11.19	0.01	...	37.87
289	2019	UGCA309	0	0.02	-14.43	0.05
290	268	N04826	-11.04	0.04	9	1	1.1	KPNO	1	0.16	-20.18	0.48	...	40.66
291	269	U08091	-12.35	0.01	103	9	1.3	KPNO	1	0.08	-12.01	0.05	VH05	38.37
292	270	UGCA319	-13.89	0.23	2	1	1.1	CTIO	1	0.23	-14.47	0.05	...	37.90
293	271	UGCA320	-11.94	0.03	52	5	1.1	CTIO	1	0.24	-15.91	0.04	MK05	39.86
294	2020	LED170228	0	0.11	-15.09	0.06
295	272	N04945	-10.50	0.09	17	4	1.1	CTIO	1.2	0.78	-19.26	0.34	...	40.75
296	273	U08188	-11.87	0.05	28	4	1.1	KPNO	2	0.03	-15.89	0.09	...	39.48
297	274	U08201	-12.91	0.10	7	2	1.1	KPNO	1	0.07	-15.57	0.08	...	38.47
298	2021	MCG-03-34+002	0	0.22	-15.52	0.08
299	275	U08215	-14.39	0.16	3	1	1.1	KPNO	1	0.02	-12.68	0.02	...	37.18
300	276	UGC08245	-13.46	0.14	5	2	1.2	KPNO	1	0.11	-13.11	0.03	...	37.92
301	277	N05023	-12.13	0.07	19	3	1.1	KPNO	1	0.04	-15.85	0.09	...	39.39
302	278	CGCG217-018	-12.91	0.07	21	4	1.1	KPNO	1	0.03	-14.55	0.05	...	39.00
303	279	U08308	-13.11	0.04	36	4	1.1	KPNO	1	0.02	-12.59	0.02	...	38.21
304	280	U08313	-12.45	0.03	46	4	1.1	VATT	1	0.03	-15.23	0.07	...	39.60

TABLE 2.4 – Continued

#	ID	Galaxy Name	log f _{err} (log f)	EW _{err} (EW)	Source	Telescope	Coverage	Ab	M_B	[NII]/Ha	Ref.	L(Ha)
(1)	(2)	(3)	(4)	(5)	(6)	(7)	(8)	(9)	(10)	(11)		(12)
305	281	U08320	-12.38	22	4	1.1	1	0.03	-15.10	0.06	...	38.95
306	282	U08331	-12.98	18	1	1.1	1	0.02	-15.28	0.07	...	38.90
307	283	N05055	-10.80	20	4	1.1	2	0.04	-20.10	0.47	...	40.87
308	284	N05068	-10.83	43	5	1.1	1	0.37	-18.60	0.26	...	40.81
309	285	N05102	-12.25	1	0.4	1.1	1	0.22	-17.53	0.17	...	38.88
310	286	N05128	-10.33	10	2	1.1	1	0.49	-20.47	0.54	...	40.80
311	287	IC4247	-13.25	8	1	1.1	1	0.20	-13.95	0.04	...	38.19
312	288	ESO324-G024	-12.07	44	11	1.2	1	0.43	-15.38	0.07	...	39.23
313	289	N05204	-11.46	56	5	1.1	2	0.03	-16.64	0.12	...	39.91
314	290	N05194	-10.27	23	3	2.1	...	0.08	-20.63	0.60	MK05	41.43
315	291	N05195	-12.10	4	1	2.1	...	0.08	-19.14	0.32	...	39.69
316	292	U08508	-12.59	06	24	4	1	0.03	-13.13	0.06	MK05	38.29
317	293	SBS1331+493	-12.76	0.03	50	4	1	0.02	-13.67	0.04	...	39.38
318	294	N5206	<-14.5	...	0	...	1	0.53	-16.31	0.10	...	<36.8
319	295	N05229	-12.54	0.03	22	2	1	0.04	-14.40	0.05	...	38.94
320	296	N05238	-12.26	0.06	54	6	1	0.02	-15.00	0.10	MK05	39.21
321	297	ESO270-G017	-11.68	0.07	23	4	1	0.43	-18.38	0.24	...	40.31
322	298	PGC166170	0	...	0.17	-14.22	0.05
323	299	N05236	-10.00	0.04	33	3	1	0.21	-20.26	0.50	...	41.25
324	300	ESO444-G084	-12.90	0.07	32	5	1	0.26	-13.10	0.03	...	38.56
325	301	UGC08638	-12.60	0.03	62	18	1	0.03	-12.59	0.02	...	38.54
326	302	U08651	-12.61	0.05	33	4	1	0.01	-12.96	0.03	VH05	38.42
327	303	N05253	-10.74	0.02	120	9	1	0.21	-16.83	0.12	MK05	40.34
328	304	N05264	-12.31	0.08	9	2	1	0.20	-15.88	0.18	MK05	39.06
329	305	U08683	-13.00	0.08	16	3	1	0.02	-14.52	0.05	...	39.12
330	306	ESO325-G011	-12.01	0.03	87	11	1	0.32	-13.97	0.04	...	39.19
331	308	ESO383-G087	-11.54	0.04	19	2	1	0.25	-13.57	0.03	...	38.58
332	309	ESO383-G091	-13.27	0.12	9	3	1	0.29	-13.65	0.04	...	37.98
333	310	U08760	-13.16	0.11	12	3	1	0.04	-14.12	0.04	...	38.33
334	312	U08837	-12.33	0.04	37	4	1	0.03	-15.92	0.09	...	39.56
335	313	U08833	-13.36	0.05	17	2	1	0.03	-12.39	0.02	...	37.73
336	314	ESO384-G016	<-15.0	...	0	...	1	0.27	-13.12	0.03	...	<36.3
337	315	N05457	-10.24	0.15	27	9	2	0.02	-20.84	0.63	...	41.28
338	316	N05408	-11.33	0.02	121	12	1	0.28	-16.49	0.11	...	40.14
339	317	N05474	-11.57	0.05	28	4	1	0.02	-17.49	0.17	...	40.16
340	318	N05477	-12.27	0.03	58	5	1	0.02	-15.22	0.07	...	39.56
341	319	Circinus	-11.19	0.06	22	6	1	2.00	-17.21	0.15	...	40.23
342	320	U09128	-13.70	0.16	4	2	1	0.05	-12.58	0.02	Vetal97	37.18

TABLE 2.4 – Continued

#	ID	Galaxy Name	log f	err(log f)	EW	err(EW)	Source	Telescope	Coverage	Ab	M_B	[NII]/Ha	Ref.	L(Ha)
(1)	(2)	(3)	(4)	(5)	(6)	(7)	(8)	(9)	(10)	(11)	(12)	(13)	(14)	(15)
343	1103	SBS 1415+437	-12.89	0.40	205	25	2.1	0.02	-12.39	0.02	...	39.37
344	321	N05585	-11.62	0.05	29	4	1.1	KPNO	2	0.03	-17.61	0.17	...	39.91
345	322	U09240	-12.73	0.07	9	2	1.1	KPNO	1	0.03	-13.94	0.09	MK05	38.21
346	323	PGC051659	0	0.56	-11.82	0.02
347	324	U09405	-13.87	0.35	2	2	1.2	VATT	1	0.03	-14.97	0.06	...	38.00
348	325	MRK475	-12.50	0.01	314	16	1.1	KPNO	1	0.03	-14.57	0.04	MK05	39.57
349	326	NGC 5832	-12.23	0.08	15	3	1.1	KPNO	1	0.09	-16.13	0.10	...	39.88
350	327	ESO223-G009	-11.82	0.07	41	10	1.1	CTIO	1	1.12	-16.86	0.13	...	39.97
351	328	ESO274-G001	-11.61	0.11	13	5	1.2	CTIO	1	1.11	-17.77	0.19	...	40.01
352	329	NGC5949	-12.09	0.04	17	2	1.1	KPNO	1	0.09	-16.76	0.12	...	39.98
353	330	UGC09992	-13.08	0.07	20	4	1.1	VATT	1	0.12	-15.32	0.09	VH05	39.02
354	1109	LEDA100404	<-15.6	...	0	...	1.1	KPNO	1	0.17	-12.03	0.02	...	<36.2
355	332	ESO137-G018	-11.76	0.08	94	26	1.1	CTIO	1	1.05	-17.81	0.19	...	40.07
356	333	ESO179-IG013	0	CTIO	1	1.18	-15.90	0.09
357	2022	UGC10669	-14.44	0.19	2.3	0.14	-14.00	0.04	...	37.69
358	335	IC4662	-10.97	0.02	101	10	1.1	CTIO	1	0.28	-14.69	0.05	...	39.61
359	336	N06503	-11.29	0.07	20	4	1.1	KPNO	2	0.14	-17.84	0.19	...	40.19
360	337	IC4710	-11.67	0.04	40	4	1.1	CTIO	1	0.38	-17.42	0.16	...	40.25
361	339	ESO104-G022	-12.73	0.05	36	4	1.1	CTIO	1	0.29	-14.51	0.05	...	39.30
362	340	N06744	-10.67	0.04	70	24	2.2	0.16	-20.93	0.65	...	41.19
363	341	ESO104-G044	-13.60	0.22	4	3	1.1	CTIO	1	0.16	-14.97	0.06	...	38.38
364	2023	ESO141-G042	0	0.21	-14.88	0.06
365	342	NGC6789	-12.58	0.05	23	3	1.1	VATT	1	0.32	-13.70	0.04	...	38.67
366	343	ESO594-G004	-13.02	0.08	19	7	1.1	KPNO	1	0.54	-11.63	0.02	...	37.21
367	2024	IC4870	-12.22	0.05	12	1.2	2.1	0.41	-16.02	0.09	...	39.92
368	344	N06822	-10.54	0.04	47	12	1.1	CTIO	3	0.94	-15.12	0.06	...	39.14
369	345	IC4951	-12.45	0.05	33	4	1.1	CTIO	1	0.12	-16.00	0.09	...	39.54
370	2025	UGC11583	-13.54	0.06	2.3	1.34	-14.49	0.05	...	38.38
371	2026	LEDA166192	-13.51	0.22	2.3	1.29	-13.64	0.04	...	38.41
372	2027	LEDA166193	-13.80	0.07	2.3	1.80	-13.95	0.04	...	38.24
373	346	N06946	-10.42	0.06	34	4	2.1	1.54	-20.79	0.62	...	41.36
374	2028	KKR55	-13.32	0.03	2.3	2.67	-13.93	0.04	...	38.92
375	347	DDO210	-14.35	0.11	1	0.2	1.1	CTIO	1	0.18	-10.91	0.00	Vetal97	35.72
376	2029	KKR56	-14.00	0.28	2.3	3.15	-14.40	0.05	...	38.36
377	2030	CEPHEUS1	-13.18	0.10	2.3	4.05	-17.50	0.17	...	39.35
378	348	IC5052	-11.46	0.04	46	4	2.1	0.19	-17.33	0.16	...	40.18
379	2031	KKR59	-12.76	0.05	2.3	3.79	-16.94	0.13	...	39.72
380	2032	KKR60	-13.08	0.12	2.3	4.48	-15.33	0.07	...	39.59

TABLE 2.4 – Continued

#	ID	Galaxy Name	log f	err(log f)	EW	err(EW)	Source	Telescope	Coverage	Ab	M_B	[NII]/Ha	Ref.	L(Ha)
(1)	(2)	(3)	(4)	(5)	(6)	(7)	(8)	(9)	(10)	(11)	(12)	(13)	(14)	(15)
381	349	NGC7064	0	0.03	-16.80	0.13
382	350	N07090	-11.42	0.07	23	4	CTIO	1	0.05	-18.74	0.27	40.57
383	351	IC5152	-11.27	0.04	32	4	CTIO	1	0.05	-15.95	0.09	39.42
384	352	U11891	-11.90	0.04	33	7	KPNO	1	1.52	-16.27	0.10	40.54
385	353	ESO238-G005	-13.08	0.06	28	4	CTIO	1	0.03	-9.82	0.01	38.84
386	2033	IC5256	0	0.08	-15.63	0.08
387	355	N07640	-11.56	0.05	30	4	KPNO	3	0.45	-18.34	0.24	MK05	MK05	40.43
388	356	U12588	-12.26	0.05	29	4	KPNO	1	0.52	-15.99	0.25	MK05	MK05	39.80
389	357	UGCA438	-14.03	0.24	1	1	CTIO	1	0.06	-12.14	0.02	36.75
390	358	ESO347-G017	-12.53	0.05	34	4	CTIO	1	0.07	-14.72	0.05	39.40
391	359	U12613	-13.38	0.14	1	1	KPNO	1	0.19	-12.09	0.02	36.50
392	360	U12632	-12.18	0.04	40	6	KPNO	2	0.56	-17.67	0.18	39.92
393	361	IC5332	-11.27	0.06	28	4	0.07	-18.56	0.25	40.61
394	362	NGC7713	-11.41	0.04	40	4	0.07	-18.18	0.15	MK05	MK05	40.48
395	363	U12713	-12.83	0.05	29	4	KPNO	1	0.25	-14.69	0.04	VH05	VH05	39.03
396	364	UGCA442	-12.46	0.05	25	4	CTIO	1	0.07	-14.62	0.05	38.87
397	365	ESO348-G009	-13.08	0.05	18	2	0.06	-12.87	0.03	38.81
398	366	ESO149-G003	-12.78	0.03	53	3	0.06	-14.05	0.04	38.91
399	367	N07793	-10.60	0.08	31	5	0.08	-18.41	0.24	40.59

CHAPTER 3

BASIC PROPERTIES OF THE 11HUGS SAMPLE

3.1 Selection Properties

To begin, we present distributions of the 11HUGS galaxies in T-type, B magnitude, Galactic latitude and distance in Figure 3.1. These are the properties relevant for the selection of the targets for the survey. Histograms for the entire target catalog (Table 2.1) are shaded in gray. Histograms for the core sample for which we have tried to be complete as possible in our compilation of currently known galaxies (i.e. for $|b| > 20^\circ$, $B < 15$, $T \geq 0$ and $D < 11$ Mpc) are outlined in black. The samples are clearly dominated by dwarf irregular systems, as would be expected for a dataset on star-forming galaxies that is thought to be approximately distance-limited. The 18 galaxies which lack $H\alpha$ flux measurements are also separately indicated. About half are in the core sample (shaded in black) and half are not (cross-hatched). As mentioned at the end of the last chapter, most of these galaxies have either not been observed or fluxed due to excessively bright foreground stars.

3.2 Completeness

Ultimately, the 11HUGS sample is a composite of numerous catalogs with diverse selection criteria, so its selection function would not be straightforward to derive analytically. Rather we estimate the completeness limits of our sample by performing a statistical test similar to the widely applied V/V_{max} test (Schmidt 1968). We also qualitatively compare our number density distributions with indepen-

dently established B-band luminosity and HI mass functions. Finally, we check our target sample against the contents of the HIPASS (HI Parkes All Sky Survey, Meyer et al. 2004) catalog.

3.2.1 The Rauzy T_C Completeness Statistic

The Rauzy (2001) T_C completeness statistic is analogous to the V/V_{max} test (Schmidt 1968), but does not rely on any assumptions about the spatial homogeneity of the sample. The method is based on the estimation of the uniform variate ζ , which is a ratio of space number densities. More specifically, if $F(x)$ is the normalized integral of the luminosity function from $-\infty$ to x , and Z is the distance modulus $m - M$, then

$$\zeta = \frac{F(M)}{F[M_{lim}(Z)]}. \quad (3.1)$$

An estimate of ζ is given by

$$\zeta \sim \frac{r_i}{n_i + 1}, \quad (3.2)$$

where r_i is the number of galaxies with $M \leq M_i$ and $Z \leq Z_i$, and n_i is the number of galaxies with $M_i < M \leq M_{lim}^i$ and $Z \leq Z_i$. The expectation value of ζ is 0.5 and its variance is given by

$$V_i = \frac{1}{12} \frac{n_i - 1}{n_i + 1}, \quad (3.3)$$

The T_C completeness statistic is then defined as

$$T_C = \frac{\sum_{i=1}^{N_{gal}} (\zeta_i - \frac{1}{2})}{\sqrt{\sum_{i=1}^{N_{gal}} V_i}}, \quad (3.4)$$

To test for completeness, T_C is computed for sub-samples truncated to increasing apparent magnitude limits. For complete samples T_C has an expectation value of 0 and variance of order unity, while systematically negative values of T_C indicate that the sample is becoming incomplete. The confidence levels for rejection of the hypothesis that the sample is complete up to a particular limit are 84.1%, 99.7% and 99.4% when $T_C < -1$, $T_C < -2$ and $T_C < -3$ respectively. In his paper describing the T_C estimator, Rauzy uses a 2σ , $T_C < -2$ criterion for rejection of the completeness hypothesis. In what follows, we will opt to be more conservative and use the point at which T_C begins to fall consistently below zero to indicate the limit to which the sample is 100% complete.

We first calculate T_C as a function of B (corrected for Galactic extinction) and plot the results in the top panel of Figure 3.2. Three different subsets of the overall target sample, as described in the figure, are examined. By construction, the 11HUGS sample is limited at $B \sim 15$ (prior to Galactic extinction corrections) in order to avoid the severe incompleteness that is known to set in at fainter magnitudes in the existing parent catalogs (e.g. Zwicky et al. 1961; Tully 1988c). Thus, it is not surprising that T_C drops precipitously for $B \gtrsim 15.5$ in all three subsets. This limit of $B=15.5$ for the 11HUGS core sample (thin solid line) corresponds to a 100% completeness in M_B to -14.7 at 11 Mpc. In the bottom panel, a plot of M_B with distance is shown to illustrate the depth of the sample throughout the studied volume.

We also check the completeness of the 11HUGS sample with respect to the HI mass. To do this, we have compiled HI single dish fluxes from the literature. Measurements are available for 97% of the galaxies in the overall 11HUGS target catalog. The data are primarily taken from the following three sources, in the following order of preference: the digital archive of Springob et al. (2005)

(N=110), the HI Parkes All Sky Survey (HIPASS) catalog as published in Meyer et al. (2004) (N=61), and the homogenized HI compilation of Paturel et al. (2003) as made available through the Hyperleda database (N=208). Finally, data for 9 galaxies are supplemented from the compilation accompanying the Catalog of Neighboring Galaxies of Karachentsev et al. (2004) and other individual papers.

We evaluate T_C as a function of the HI flux and plot the results in the top panel of Figure 3.3. Here, the T_C statistic begins to become systematically negative at integrated fluxes $< 9 \text{ Jy km s}^{-1}$. To find the corresponding completeness in the HI mass, we apply the standard relation $M_{HI}[M_\odot] = 2.36 \times 10^5 D^2 F$, where D is the distance in Mpc and F is the 21-cm line flux in Jy km s^{-1} . The gas is assumed to be optically thin, and corrections for the presumably small ($\lesssim 10\%$, Haynes & Giovanelli 1984, Zwaan et al. 2003) amount of HI self absorption are not applied. The HI mass is plotted against the distance in the bottom panel of Figure 3.3. At the edge of the 11 Mpc target volume, a limit of 9 Jy km s^{-1} corresponds completeness in M_{HI} down to $3 \times 10^8 M_\odot$.

Finally, we also compute T_C as a function of the $H\alpha$ flux and plot the results in Figure 3.4. At fluxes below $6 \times 10^{-14} \text{ ergs s}^{-1} \text{ cm}^{-2}$, T_C becomes systematically negative. This corresponds to a completeness down to a $H\alpha$ luminosity of $10^{39} \text{ ergs s}^{-1}$ at 11 Mpc, or a SFR of $0.008 M_\odot \text{ yr}^{-1}$, using the conversion of Kennicutt (1998). Since the Kennicutt calibration is based on expectations for a solar metallicity population, using this conversion for metal-poor ($\sim Z_\odot/5$) dwarf galaxies results in an overestimate of the SFR — a relative deficiency of metals will cause a greater number of ionizing photons to be produced per unit stellar mass formed. Applying a calibration that is based on a $Z_\odot/5$ population (see Table 6.3 and Section 6.2) instead yields a limiting SFR that is $\sim 70\%$ lower at $0.006 M_\odot \text{ yr}^{-1}$.

3.2.2 Luminosity and Mass Functions Comparisons

Another perhaps more intuitive way of checking the completeness of the sample is to compare the 11HUGS number density distributions to previously calculated luminosity and mass functions that are based on survey samples which have well-determined selection functions.

In Figure 3.5, we show the Schechter function fits to two independent luminosity functions (LFs) of datasets that have morphological make-ups which should be similar to the 11HUGS sample. The blue curve is based on the B-band follow-up of the Arecibo HI Strip Survey (AHISS, Zwaan, Briggs & Sprayberry 2001), a optically blind survey for galaxies based on 21-cm emission alone. The red curve is based on spiral and irregular galaxies in the Second Southern Sky Redshift Survey (SSRS2, da Costa et al. 1988; Marzke et al. 1998), which has generated its targets using the STScI Guide Star Catalog (Lasker et al. 1990). The SSRS2 LF is a composite of two separate Schechter function fits to the spiral and irregular populations. Clearly the SSRS2 and AHISS LFs are quite different in their determinations for the densities of dwarf galaxies. This difference emphasizes the uncertainties and illustrates the probable ranges of such measurements for low luminosity populations. The SSRS2 exhibits a much steeper rise at the faint end, with a slope of -1.8, while the slope of the AHISS LF is much flatter at -1.0.

The gray curves in Figure 3.5 show the number densities of the 11HUGS core sample ($|b| > 20^\circ$, $B < 15$, $T \geq 0$, $D < 11\text{Mpc}$). Subsets truncated at distances of 7, 8, 9, and 10 Mpc are also plotted. The densities based on the 11HUGS sample are systematically higher by a factor of ~ 2 . This is likely due to cosmic variance. Since (i) the characteristic correlation length, the scale on which the density of galaxies exceeds the average by a factor of two, has been well-measured to

be $r_o = 5h^{-1}$ Mpc, (ii) the power-law slope of the function $\xi = (r_o/r)^\gamma$, which parameterizes the excess probability over random of finding two galaxies separated by a distance r , has also been established to be 1.8 (Longair 1998 and references therein), and (iii) our volume is not centered on a void, it is not surprising that the densities we compute are higher relative to those based on surveys which probe much larger volumes. We note that Karachentsev et al. (2004) have also reported finding that the integrated luminosity densities of galaxies within 8 Mpc are larger by factors of 1.7 to 2 than other previous measurements based on their Catalog of Neighboring Galaxies.

Because of these differences in the overall normalizations, we will limit this analysis to qualitative comparisons and examine the relative shapes of the LFs. First, we shift the 11HUGS distributions by a factor of 2 to force approximate agreement with the LF densities at M^* (~ -20.0) and plot these in black. The 11HUGS distributions are not flat at the faint end and show increasing densities for dwarfs that are more consistent with the SSRS2 LF (blue) than the AHISS LF (red). However, the densities do not continue to rise and abruptly drop for $M_B > -14$. This is consistent with the determination based on the T_C statistic that 11HUGS is complete throughout its entire target volume to $M_B = -14.7$.

We also perform a comparison of the 11HUGS number densities as a function of the HI mass with HI mass functions (HIMFs) based on the optically blind searches of the Arecibo Dual Beam Survey (Rosenberg & Schneider 2002) and the HIPASS Bright Galaxy Catalog (Zwaan et al. 2003). The Schechter fits for these samples are plotted in along with the number densities of the 11HUGS galaxies. Again, the densities based on the 11HUGS samples (gray curves) are too high as compared with the mass functions from the literature, although the discrepancy is not as large as for the LFs. Karachentsev et al. (2004) find that the integrated

HI density with 8 Mpc is 1.4 times greater relative to other previous published values based on larger volumes. Shifting the 11HUGS densities down by this factor (black curves) results in better consistency with the HIPASS HIMF. The completeness of the 11HUGS core sample begins to drop at HI masses $\lesssim 10^8 M_\odot$, as the computed densities are systematically lower than the HIPASS HIMF past this point. This is consistent with the assessment based on the T_C statistic that 11HUGS is complete throughout its entire target volume to $M_{HI} = 3 \times 10^8 M_\odot$.

3.2.3 Comparison with Local Volume Galaxies found in HIPASS

Finally, we compare the contents of the 11HUGS target catalog with that of HIPASS as published in the optical counterpart analysis of Doyle et al. (2005). The HIPASS recession velocities were run through our flow model and cross-correlated with available direct distance measurements as in our examination of the nearby galaxies compiled by NED (Section 2.2.2). Out of the 4315 HI detections, there are 78 galaxies within 11 Mpc. (Note that HIPASS only surveys the southern sky up to a declination of $+2^\circ$, and has velocity coverage only beyond 300 km s^{-1} .) Of these 78 objects, 14 were not in the 11HUGS catalog. However, all of these objects were below our magnitude selection limit of $B=15$ and/or have $|b| < 20^\circ$. This provides another assurance that our core sample is relatively complete to its stated limits and not missing a large population of optically faint, but gas-rich systems.

In sum, the statistical tests we have performed on the 11HUGS sample, and the secondary checks against the contents of the HIPASS catalog as well as with independently derived luminosity and mass functions, show that the core sample is complete out to 11 Mpc for $M_B < -14.7$ and $M_{HI} > 3 \times 10^8 M_\odot$. In the analysis of starburst statistics performed in the following chapters, star formation properties will be examined as a function of M_B , and we will chose to be conservative by basing our primary conclusions only on galaxies in this core sample with

$M_B < -14.7$ (i.e. we will not try to expand the sample beyond this by applying incompleteness corrections). Before we proceed onward however, we conclude this chapter with a short discussion regarding the objects which were observed but had no detectable $H\alpha$ emission.

3.3 Non-detections

Only 16 galaxies (out of 383 which have been observed) have not been detected in $H\alpha$. 11 of these have been observed by 11HUGS. Two of the 16, NGC 5206 and UGC 2689 are low-luminosity early-type galaxies, so a lack of $H\alpha$ emission is not unexpected. The remaining 14 galaxies are classified as irregulars, and are all extremely low-luminosity systems with $-13.6 \geq M_B \geq -7.9$. Moreover, HI measurements are available for 13 of these systems, and show that they all have very low gas masses. For all other galaxies besides the most luminous non-detection (U7356; $M_B = -13.6$), which has a HI mass of $5 \times 10^8 M_\odot$, the values range from 2×10^5 to $5 \times 10^7 M_\odot$. The non-detections are indicated with the green symbols in bottom panels of Figures 3.2, 3.3 and 3.4, where the upper limits listed in the $L_{H\alpha}$ vs. distance plot correspond to 5σ point source detections. Thus, a lack of $H\alpha$ emission either reflects the lack of sufficient fuel for star formation, or SFRs that are so low that the probability of forming an ionizing star and/or of observing an HII region at any given time are small (e.g. LGS3; Aparicio, Gallart & Bertelli 1997). This would be a very interesting sample to follow-up, particularly in the UV, which probes SF on a timescale that is about 10 times longer than the 10^7 yr temporal sensitivity of $H\alpha$, and would be more likely to detect recent star-formation in “flickering” systems.

The fact that we see $H\alpha$ in over 95% of the galaxies in the 11HUGS sample may not be surprising given our morphological restriction to spiral and irreg-

ular galaxies in the selection of targets. After all, spirals are classified as such precisely because of the presence of star formation due to spiral density waves; i.e. visible spiral patterns are due concentrations of young stars and HII regions and not concentrations of slightly older populations unaccompanied by recent star formation. The same can thus be said for the dwarf irregulars, whose lumpy structure must be indicative of current star-formation. The interesting implication however is that if the SFHs of dIrrs follow burst cycles and remain dIrrs in the inter-burst state (i.e. rather than becoming dwarf ellipticals), then ‘off’ modes rarely occur and the inter-burst state must be characterized by low-levels of star formation rather than by its complete cessation. We will look at the properties of potential inter-burst states as well as of the overall burst cycles in detail in Chapter 6.

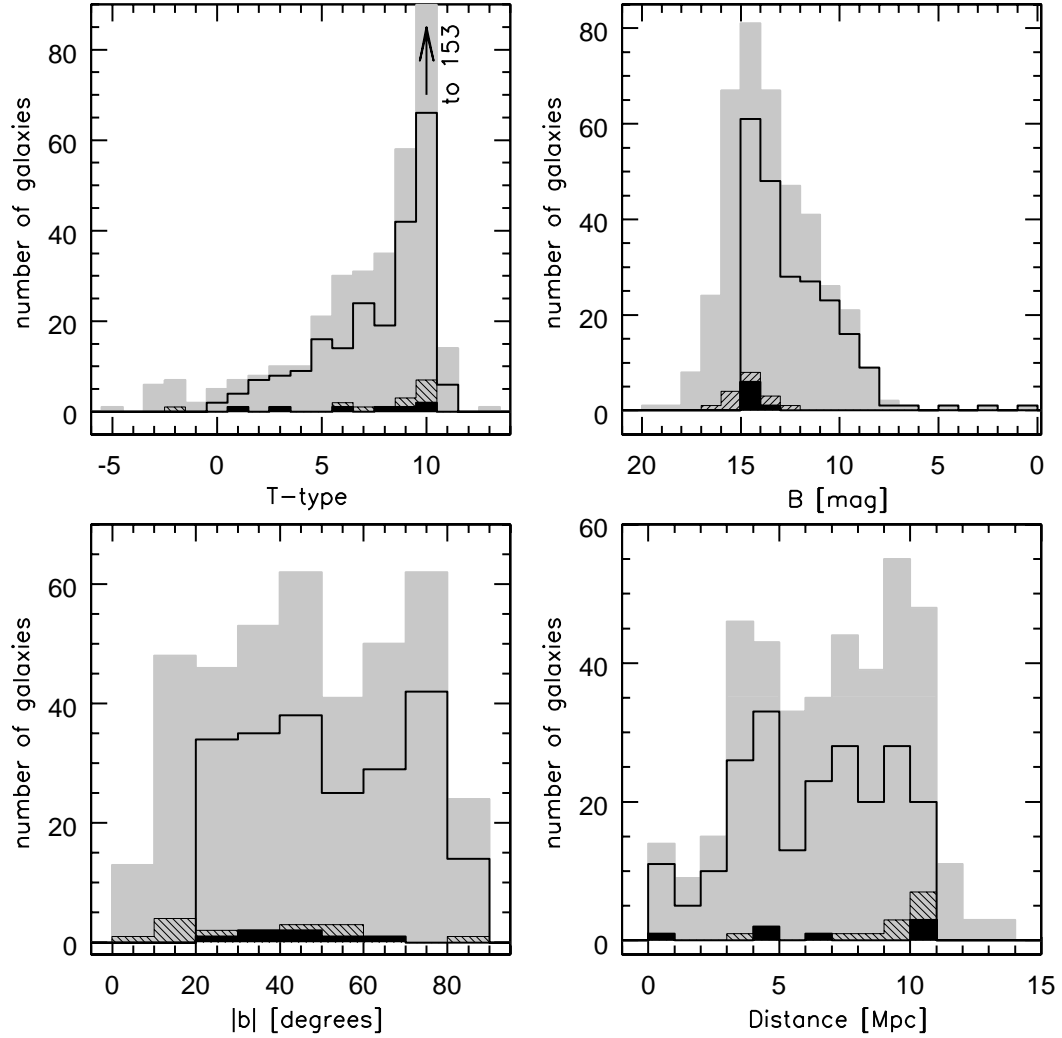


Figure 3.1: Histograms of properties relevant to the selection of the 11HUGS galaxies. The gray shaded histogram shown in the background of each panel illustrates the distributions of the total target sample listed in Table 2.1. The histograms outlined in black indicate the distributions for the core sample with $|b| > 20^\circ$, $B < 15$, $D < 11$ Mpc, and $T \geq 0$, for which we have tried to be as complete as possible in our compilation of currently known galaxies. The 18 galaxies which lack $H\alpha$ data are shaded in black if they are in the core sample and cross-hatched if they are not.

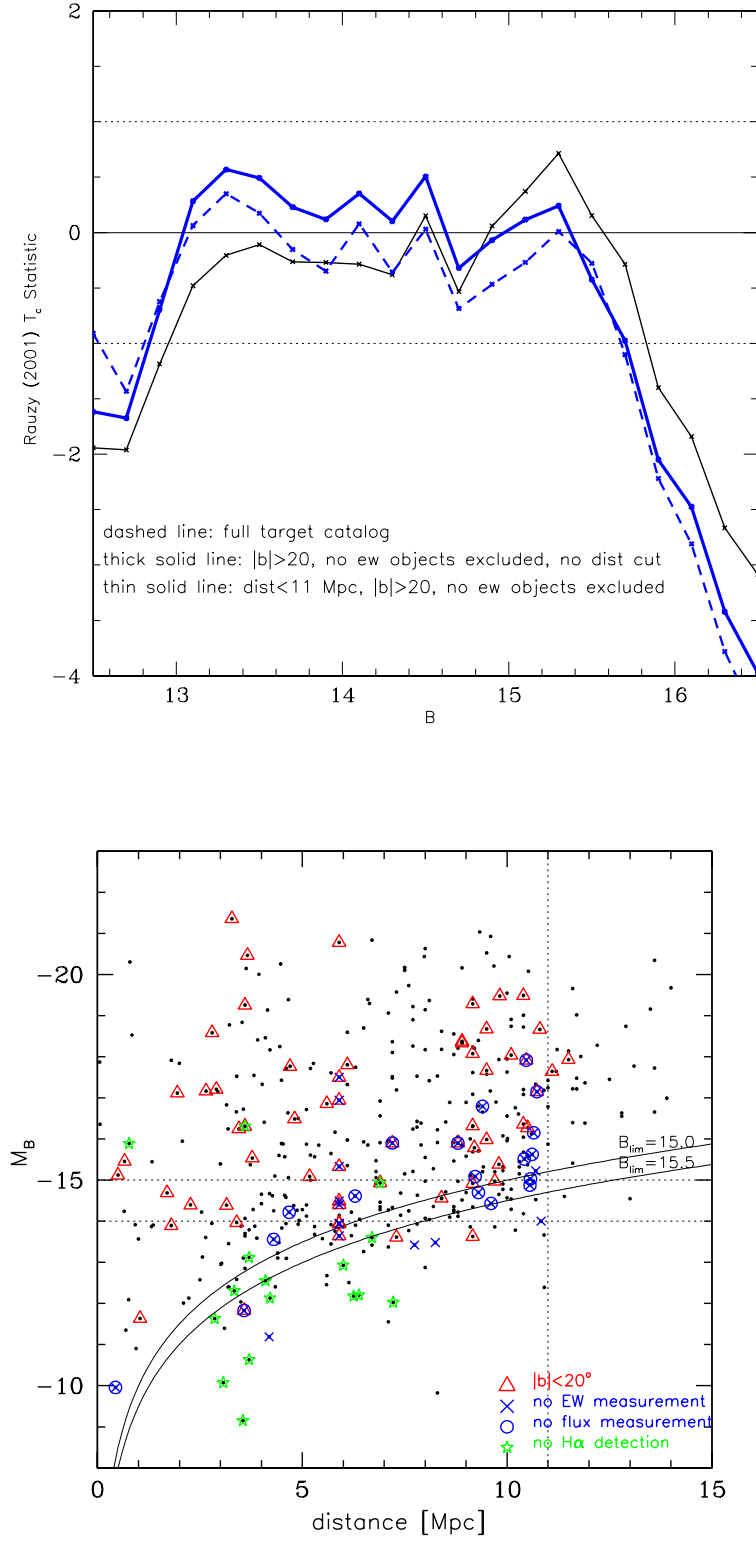


Figure 3.2: Rauzy (2001) T_C Statistical Test for Completeness in M_B . See section 3.2.1 for more details.

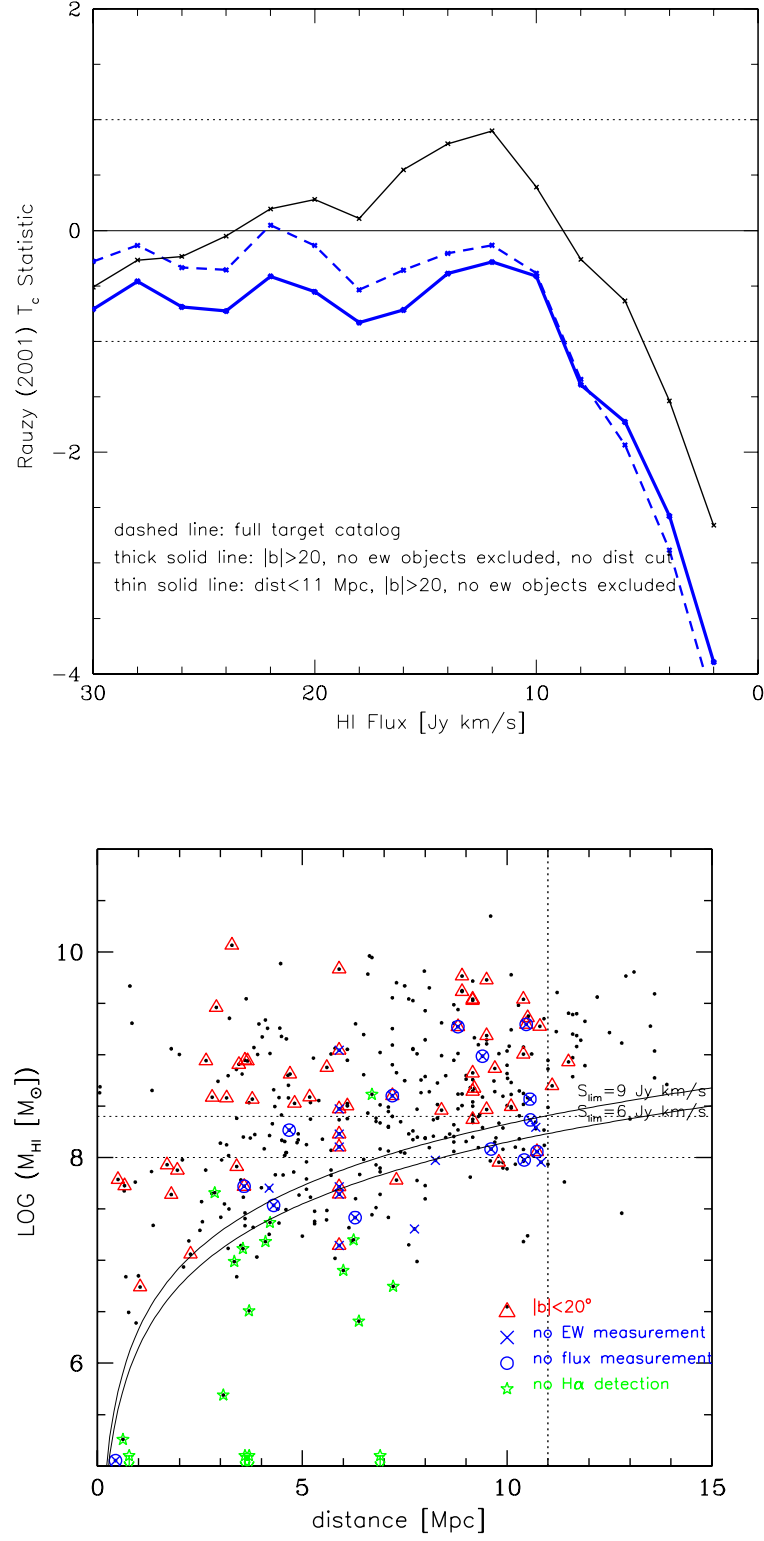


Figure 3.3: Rauzy (2001) T_C Statistical Test for Completeness in M_{HI} . See section 3.2.1 for more details.

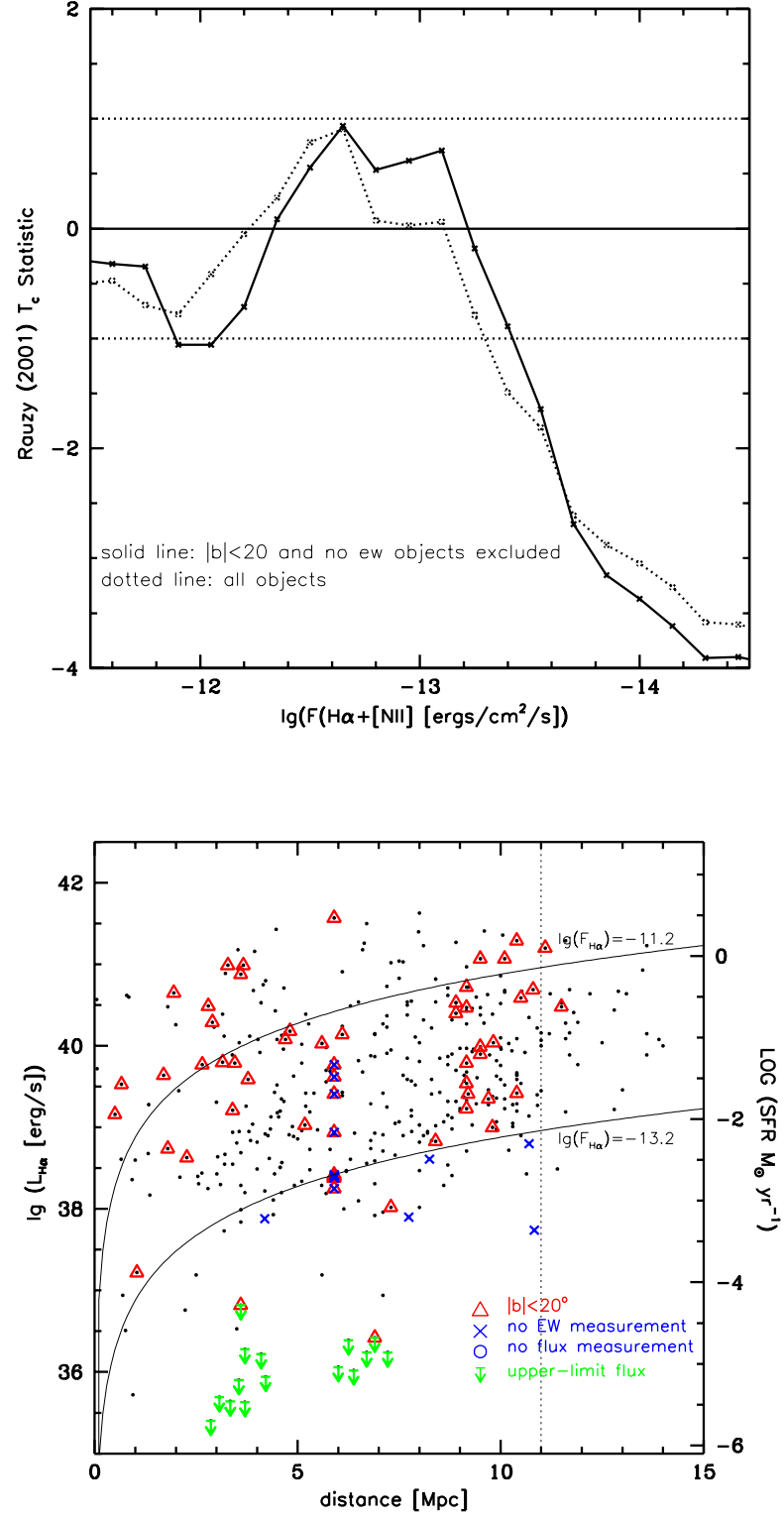


Figure 3.4: Rauzy (2001) T_C Statistical Test for Completeness in $L_{H\alpha}$. See section 3.2.1 for more details.

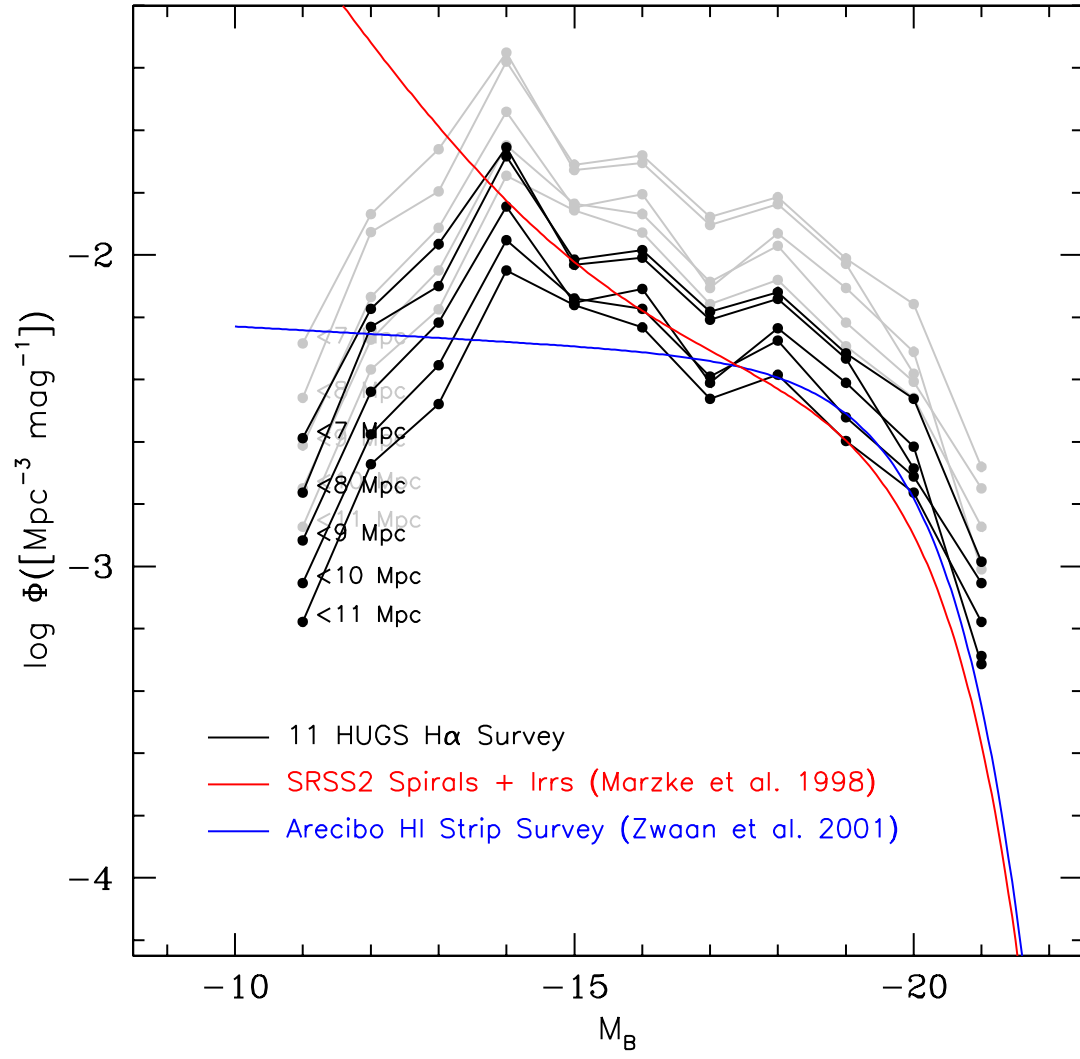


Figure 3.5: Comparison with B-band Luminosity Functions

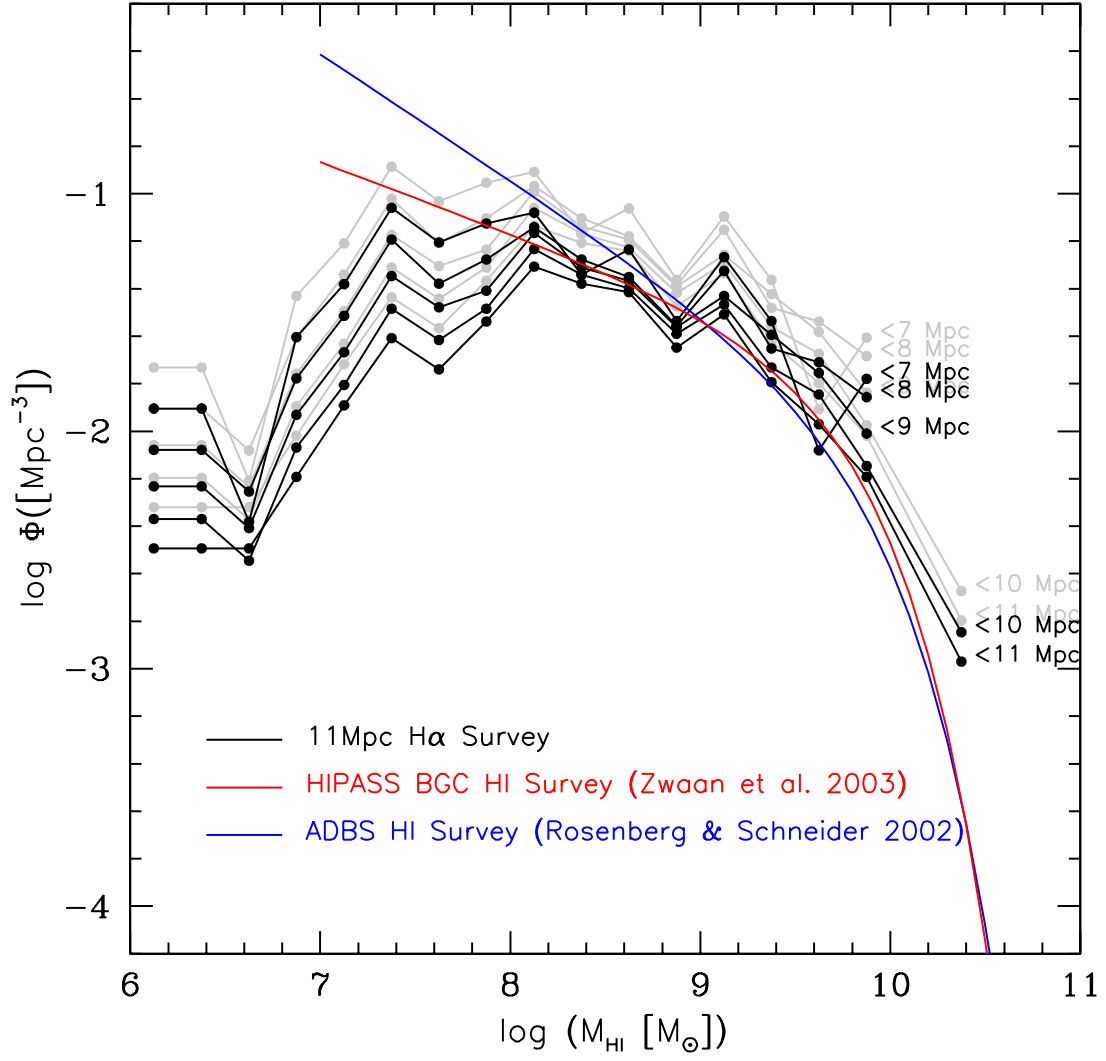


Figure 3.6: Comparison with HI Mass Functions

CHAPTER 4

GLOBAL STAR FORMATION PROPERTIES OF GALAXIES IN THE 11 MPC VOLUME: GENERAL OBSERVATIONAL PATTERNS

4.1 ABSTRACT

Before we begin our analysis of the incidence of global starbursts in dwarf galaxies, we broaden our focus and give a more general overview of the connections between the current star formation activity and the mass, luminosity and morphology of galaxies across the full extent of the 11HUGS sample. To do this, we examine trends in the $H\alpha$ EW with two tracers of the galaxy mass, M_B and V_{max} , the maximum circular rotational velocity of the disk.

To summarize our results, we find that galaxies form sequences in the M_B -EW and V_{max} -EW planes which exhibit two characteristic transitions. One occurs at $M_B \sim -19$ and $V_{max} \sim 120 \text{ km s}^{-1}$, where the more luminous, massive galaxies tend to have Sa–Sb bulge-dominated morphologies and EWs that turn-off toward lower values. The EW distribution of galaxies in this regime has a dispersion that is larger by 50% relative to that for the intermediate mass systems below the transition. The systematic drop of the EW indicates that the relative star formation activity in galaxies above this particular mass threshold is depressed. This transition is another manifestation of the recently uncovered bi-modality in the present-day galaxy population — the general division at $M_* \sim 3 \times 10^{10} M_\odot$ between massive galaxies that are predominantly red and old, and those that are less massive, blue and more actively star-forming (e.g. Kauffmann et al. 2003b, Blanton et al. 2005). The second transition occurs at $M_B \sim -15$ and $V_{max} \sim 50$

km s^{-1} , where the least luminous and lowest mass objects in the sequence tend to have irregular morphologies, and an EW distribution that is broader by a factor of 2. The region between these two transitions, which is mostly populated by late-type spirals, thus has the tightest EW distribution. Possible explanations for the lower-mass broadening include (i) burstier star formation due to negative feedback in physically small systems (e.g. as explored by Gerola et al. 1980), and/or the absence of the stabilizing effect of spiral structure, and (ii) star formation “flickering,” statistical effects due to the very low average SFRs in these dwarfs (e.g. Hunter & Gallagher 1986). In all regimes, the EWs are well characterized by log-normal distributions. However, for dwarf galaxies in our sample, we find excesses in the tails of the logarithmic EW distribution above what would be predicted for a normal function. These features will be used in the next chapter to develop a means of statistically identifying starbursts.

4.2 The $\text{H}\alpha$ EW as a Relative Star Formation Indicator

In all of the subsequent analyses in this thesis, we will make extensive use of the integrated $\text{H}\alpha$ emission-line EW as a measure of the normalized star formation activity in a galaxy. Recall that thermal Balmer emission results from the photoionization of nebular gas by young, short-lived O & B stars. Thus, the EW, which is given by the $\text{H}\alpha$ flux divided by the red continuum flux density, indicates the strength of the current SFR relative to the total mass of stars (i.e. the specific SFR). A closely related physical quantity is the stellar birthrate b , which is the current SFR relative to the average lifetime rate. This latter parameter is more intuitive as it is dimensionless and can easily be interpreted as a measure of “burstiness.” Galaxies with birthrates much greater than unity are in a bursting mode, experiencing episodes of elevated activity, while anomalously low birthrates in-

indicate that star formation has somehow been globally suppressed.

Transforming the observed EW to the physical properties that it represents requires the help of stellar population synthesis models. For example, the EW can be related to b given: (i) a set of stellar evolution tracks, (ii) assumptions about the stellar initial mass function (IMF) and the general form of the SFH, and (iii) a method to calculate the photoionization rate of the gas (e.g. Kennicutt 1983; Kennicutt, Tamblyn & Congdon 1994, hereafter KTC94). Such transformations will be discussed further in the next chapter and carried out in detail in Chapter 6. For now however, simply noting that the EW can be used as a relative SFR indicator is sufficient, since we will aim to keep this exposition of the issues primarily based on observables. This will allow our conclusions here to be as model-independent as possible. Finally, we note that the following analysis will consistently be carried out with respect to the *logarithm* of the EW, although we will not repeatedly re-state this. This is done because the EWs have a distribution that is generally log-normal, as will be shown below.

4.3 The Local Galaxy Sequence in the M_B -EW and V_{max} -EW Planes

To visualize trends in star formation activity across the 11HUGS sample, we examine the relationship of the EW with two indicators of the mass, M_B and V_{max} , the maximum circular rotational velocity. We have chosen to use M_B since B -band photometry is widely available in the literature and can be approximately reduced to a common (RC3) system for all of the galaxies in the sample. A drawback with using the B -band light to trace the stellar mass is however, that the mass-to-light ratio in the blue has strong systematic dependencies on the recent star formation history itself (e.g. Bell & deJong 2001). Thus, we have also looked at the variation of the EW with V_{max} , which traces mass gravitationally,

and should in principle be independent of the recent star formation activity in individual galaxies. The existence of the baryonic Tully-Fisher relation for low-mass galaxies (McGaugh 2005 and references therein) supports the use of V_{max} as a mass indicator for our dwarf dominated sample. Of course, using V_{max} is not without its own weaknesses. For example, one issue is that the maximal rotation velocity for low-mass systems is somewhat ill-defined since dwarfs are generally known to be solid body rotators (e.g. Skillman 1996). Another issue is that previous measurements of V_{max} are limited, and are not available for the complete sample. Therefore, the two tracers have complimentary strengths and weaknesses, such that general consistency checks on mass-dependent trends in the EW are provided by examining the distribution of galaxies in both V_{max} -EW and M_B -EW planes.

4.3.1 Sources of Data

The M_B 's used in this analysis have been compiled from the literature as described in Chapter 2 and given in Table 2.1. The EWs are from the 11HUGS survey as also described in Chapter 2 and reported in Table 2.4. We adopt V_{max} 's from the HyperLeda database (Paturel et al. 2003). These measurements of the rotational velocity are extrapolated from single-dish 21-cm line widths using a scaling relationship between the two quantities, which Paturel et al. have derived using galaxies for which line widths and rotation curves have both been previously measured.

V_{max} measurements are available for only $\sim 80\%$ of the 11HUGS sample, so to better assess trends in the V_{max} -EW plane, we include additional data from the $H\alpha$ Galaxy Survey ($H\alpha$ GS, James et al. 2004) in our analysis. The $H\alpha$ GS has also collected narrowband $H\alpha$ + $[NII]$ and R -band imaging for a comparably sized sample of nearby galaxies ($N=334$) in the northern sky. Specifically, it includes S0/a to

Im galaxies in the UGC (Nilson 1973) with recessional velocities between 0 and 3000 km s^{-1} and with D_{25} diameters between $1'.7$ to $6'.0$. There is a $\sim 25\%$ overlap between 11HUGS and the H α GS samples, but the selection methods used in the two surveys are complementary. 11HUGS provides a distance-limited sample over essentially the entire sky and maximizes the number statistics for the least luminous objects in the sample, while the H α GS probes a larger volume and thus includes a larger fraction of massive spiral galaxies.

4.3.2 Qualitative Features

In Figures 4.1 and 4.2, we show the distribution of 11HUGS galaxies in the M_B -EW and V_{max} -EW planes. Corrections for internal extinction and the [NII] contribution to the EW (see appendix B) have been applied to the symbols shown in gray, while the symbols shown in color represent the data prior to these corrections. No internal extinction corrections have been made to the M_B . We show only those galaxies in the sample that are (i) on the late Hubble sequence beginning with the S0a morphological type ($T \geq 0$), (ii) outside the galactic plane ($|b| > 20^\circ$), and (iii) within 11 Mpc. This is the subset of 11HUGS that is complete, as discussed in the previous chapter. We have used different symbols to represent different morphological types as indicated in the plot. Galaxies without EW measurements are plotted to the immediate right of the vertical axis, with the Sm and dIrr types slightly shifted from the earlier spiral types for clarity. Similarly, galaxies without V_{max} measurements are plotted immediately above the horizontal axis in Figure 4.2. Upper-limit symbols are overplotted on the non-detections.

Star-forming galaxies in the local Universe outline particular sequences in these diagrams. The average progression of increasing mass (as traced by luminosity and rotational velocity) with earlier morphological type (Roberts & Haynes 1994 and references therein) is one of the more obvious features in the plots.

We begin with a description of the distinguishing features of the sequence, and then discuss the underlying physical correlations that they are thought to reflect. We note that although many of the star formation trends that will be discussed are well-known, it is instructive to see how they are manifested in a parameter space defined by the relative SFR and mass, using a sample that is approximately volume-limited and dominated by dwarf galaxies.

Looking first at the distribution of points in the M_B -EW plane (Figure 4.1), qualitatively, we see that the mean EW and its dispersion systematically change as a function of both morphology and luminosity, with two characteristic transitions. Beginning at the bottom of the diagram, the largest range in the EW is exhibited by the lowest luminosity galaxies ($M_B \gtrsim -17$). Moving upwards in luminosity, the range narrows between $-17 \gtrsim M_B \gtrsim -19$. This transition from the 2.5 decades to the less than 1 decade span also correlates with morphology. The irregulars (light blue stars), which have both the highest and the lowest EWs, dominate the broad swath of points with $M_B \gtrsim -17$, but begin to diminish as the sequence tightens. The intermediate luminosity “waist” is then dominated by mid- to late-type spirals, which mostly lie between about 20Å and 40Å. There is then a second transition between the intermediate and highest luminosity galaxies in the sample. Above $M_B = -19$, the points gradually turn off toward lower EWs. The range and dispersion of the distribution again increases in this regime. The most luminous end of the sequence becomes primarily occupied by mid- to early-type bulge dominated spirals. Note that the extinction corrections that we have applied (gray symbols) do not affect the appearance of these general features.

Switching now to the V_{max} -EW plane (Figure 4.2), a sequence similar to the one exhibited in the M_B -EW plane, is also readily apparent. However, the char-

acteristic features are not quite as well delineated because there are fewer data points. Approximately 15% of the galaxies do not have V_{max} measurements in Hyperleda. Another $\sim 5\%$ that are nearly face-on ($i < 30^\circ$) are also excluded because the large inclination corrections applied to the observed rotational velocities make their V_{max} 's highly uncertain. Thus, we have suffered a data loss of $\sim 20\%$ in going from Figure 4.1 to Figure 4.2.

To better populate the V_{max} diagram, we momentarily sacrifice completeness and relax the constraints on the Galactic latitude, distance and apparent magnitude that have been applied to the 11HUGS sample. We also add galaxies from the H α GS. The composite dataset is plotted in Figure 4.3, where galaxies common to both samples appear only once, using the EWs measured by 11HUGS. The extinction corrected EWs, as represented by the gray symbols in the previous figures, have been omitted since the corrections have been shown to have a very limited impact on the distribution of points. Instead, we use the gray symbols in Figure 4.3 to indicate the positions of the excluded galaxies with $i < 30^\circ$. A handful of objects with low inclinations are outliers to the main distribution, likely because of large errors in V_{max} , but the majority of the gray points fall well within the general galaxy sequence.

It is clear that galaxies in the H α GS are concentrated in and avoid the same regions of parameter space as those in 11HUGS. With the addition of more data points, particularly in the high-luminosity, high- V_{max} regime, the distinguishing features of the galaxy sequence become more conspicuous. From this qualitative assessment, the two transitions at $M_B = -19$ and $M_B = -17$ appear to roughly occur at 50 km s^{-1} and 120 km s^{-1} . Note also that although the plume of high luminosity points appears to be stretched out in the V_{max} -EW plane, and the broad swath dominated by dwarf irregular galaxies appears compressed, this is just due to

the change of the ordinate from a logarithmic to a linear scale. In sum, the trends appear to be qualitatively consistent whether M_B or V_{max} is used as an indicator of the mass, and for two different, well-defined catalogs of spiral and irregular galaxies in the nearby Universe. This gives us some confidence that the features of the distribution are real, and not merely due to covariance between M_B and the EW, and/or to the peculiarities of the 11HUGS sample or the relatively limited local volume that it probes.

4.3.3 Quantitative Features

To quantify the trends along the sequence, we return to the M_B -EW plane. Here, measurements of both variables are available for essentially all galaxies within the 11HUGS complete sub-sample, so the density of points in Figure 4.1 is statistically representative of the local Universe, down to our completeness limit of -14.7 . We collapse the distribution along the M_B -axis in three coarse bins corresponding to the regimes defined by the two characteristic transitions. We also examine the EW distribution for the lowest luminosity galaxies in the sample which are fainter than our completeness limit. The resulting histograms are shown in Figure 4.4.

In Figure 4.4, the black histograms in each panel show the distribution of logarithmic EWs in the indicated magnitude range. The dotted lines outline those for the EWs that have been corrected for the contribution of [NII] and internal extinction, while the solid lines are for those of the data prior to the corrections. The EW histogram of the most luminous galaxies (gray area) is repeated in all panels for reference.

For each of the distributions plotted in Figure 4.4, we compute the means and the standard deviations in two ways. First, we simply use all of the EWs in a given luminosity bin, excluding the non-detection upper-limits. Gaussian

distributions with these means and standard deviations are over-plotted on the histograms (thin gray curves). For the two higher-luminosity bins (upper panels), these Gaussian functions appear to describe the data fairly well. However, the thin gray curves fit the data poorly for the two lower-luminosity bins (lower panels), implying that the full distributions of logarithmic EW in these luminosity ranges are not normal. This appears to be primarily caused by an excess of outliers, since the main bodies of the histograms do appear to have Gaussian profiles. Thus, to compute statistics that better characterize the majority of data, we find the best fitting Gaussian function for each histogram by minimizing χ^2 (yellow curves). We use the corresponding means and standard deviations in the remaining discussion below. The results of these calculations are summarized in Table 4.1. The integrated $H\alpha$ EW of local galaxies can thus be seen to form distributions that are primarily log-normal.

For the two intermediate luminosity bins which include galaxies with $-19 \lesssim M_B \lesssim -15$, the means and dispersions of the central body of logarithmic EWs are essentially the same, with values of $\sim 30\text{\AA}$, and 1- and 3- σ ranges from about 20–50 \AA , and 10–100 \AA respectively. The apparent narrowing of the sequence between $-19 \geq M_B \geq -17$ is thus due to the absence of outliers, rather than to a marked change in the central distributions. This lack of outliers may simply be caused by the decreasing number statistics with increasing luminosity, and does not necessarily mean that late-type galaxies cannot occupy these regions of parameter space; it only implies that galaxies with EW's lower than 10 \AA or higher than 100 \AA are very rare. Looking at this another way, we can use the Kolmogorov-Smirnov (KS) test to determine whether the EW samples in the two intermediate luminosity bins differ significantly. The result is that the probability that the two sample have been drawn from the same parent distribution is 35%, so we can-

not confidently conclude that the EWs have been drawn from two distinct parent populations.

However, significant differences do exist between the central EW distributions for galaxies in the highest and lowest luminosity bins relative to that for galaxies with $-19 \leq M_B \leq -15$. The turn-off to lower EWs of the highest luminosity, early-type galaxies corresponds to a drop in the mean EW by a factor of ~ 2 to 15\AA , and an increase in the dispersion by a factor of 1.5. At the opposite end of the sequence, the broadening at the lowest luminosities corresponds to a factor of two increase of the dispersion. There also appears to be a $\sim 25\%$ drop in the mean EW to 25\AA for these extreme dwarfs. Although the fractional errors in the EW do get larger with both decreasing EW and decreasing luminosity, changes in the average random uncertainty do not drive the variation of the dispersion along the sequence, except in the unlikely situation in which the 11HUGS errors have been substantially underestimated. The average measurement error changes by several percent at most between luminosity bins, and this can cause an increase in the dispersion of only a few hundredths dex. Thus, the transitions in the M_B -EW plane should be associated with $M_B \sim -19$ and $M_B \sim -15$, rather than $M_B \sim -19$ and $M_B \sim -17$ as identified above from a visual inspection of the diagram. Finally, we note that there is good correspondence between these revised characteristic M_B 's and the analogous V_{max} transition points implied by the Tully-Fisher relation. Based on the B -band Tully-Fisher relation derived by Kannappan, Fabricant & Franx (2002) using the full Nearby Galaxy Field Survey dataset (Jansen et al. 2000a), $M_B = -19$ and $M_B = -15$ map to maximal velocities of 120 km s^{-1} and 50 km s^{-1} respectively, when the appropriate velocity scale conversions given in their work are applied.

4.3.4 Physical Underpinnings of the Observed Sequence

As mentioned earlier, many of the general properties of the galaxy sequence in the M_B -EW and V_{max} -EW planes have been known for some time. The well-established, ordered variation of the old stellar content and the current star formation activity along the Hubble sequence (Kennicutt 1998 and references therein) underlies the changes in the distribution of EW with morphology. A large scatter and range of $H\alpha$ EWs for the dIrrs, a narrowing of the distribution for the Sb-Sc galaxies, and a tendency toward lower EWs for the earliest-type bulge-dominated spirals can also be identified in previous star formation studies which have been based on representative samples of galaxies (James et al. 2004; Kennicutt 1998; KTC94). What we have done a bit differently (aside from using an approximately volume-limited dataset) is to add a mass scale to the problem. It is the coupling of the trends in star formation with morphology, along with the fact that the Hubble sequence also represents a coarse progression in mass (Roberts & Haynes 1994 and references therein), that produce the M_B -EW and V_{max} -EW galaxy sequences described above. Thus, the M_B -EW and V_{max} -EW parameter spaces are valuable because they are constructed from simple observables and represent a concise synthesis of the systematic dependencies of the physical properties of star formation activity with mass and morphology.

While it is beyond the scope of this work to delve into the mechanisms that may drive and regulate global star formation, particularly those that operate outside the realm of dwarf galaxies, the characteristic features of the M_B -EW and V_{max} -EW galaxy sequences offer some insights into the nature of these mechanisms, so we briefly comment on such issues here.

First, we consider the transition at $M_B \sim -19$ and $V_{max} \sim 120 \text{ km s}^{-1}$, where the turn-off toward lower EWs for the most luminous and massive galaxies appears.

The average decrease of the mean EW can be nominally caused by the increasing contribution of continuum flux from the bulge component, as more massive galaxies tend to be early-type spirals. However, as argued by KTC94, a decrease in the SFR per unit mass of the stellar *disk* with earlier morphological type is more significant, and thus should be primarily responsible for the turn-off rather than the systematic increase of the bulge-to-disk ratio. As suggested previously, mechanisms associated with the growth of a dynamically hot, spheroidal component, such as the growth of supermassive blackholes and the resulting feedback from AGN, may also cause the relative, subsequent, long-term suppression of the overall star formation activity (Hopkins et al. 2006b and references therein).

Thus, the systematic drop in EW for the population indicates that star formation generally becomes depressed above a certain mass threshold in the present-day Universe. This can be due to an early epoch of highly efficient star-formation and subsequent gradual gas depletion, and/or mechanisms that suppress star formation which are uniquely associated with the transition mass identified in the diagrams. We note that this feature of the M_B -EW and V_{max} -EW galaxy sequences is another manifestation of the recently uncovered bimodality in galaxy properties — the general division at a stellar mass of $\sim 3 \times 10^{10} M_\odot$ over which the stellar populations in galaxies are red and dominated by old stellar populations (“the red sequence”), and under which galaxies are blue and more actively star-forming (“the blue sequence”) (e.g. Kauffmann et al. 2003b, Blanton et al. 2005).

Incidentally, we also note that another physical correlation, the mass-metallicity relationship, also undergoes a change at $M_B \sim -19$ and $V_{max} \sim 120 \text{ km s}^{-1}$ (Garnett 2002, Tremonti et al. 2004). Below this characteristic transition, O/H increases monotonically with increasing mass, while above it, the correlation significantly

flattens. The causes of this behavior are still being debated, but one favored explanation is that low-mass galaxies suffer the loss of metal-enriched material due to supernova-driven winds, whereas the most massive galaxies completely retain all of their metals due to their deep potential wells. This coincidence is interesting because supernova feedback is also thought to play a major role in regulating star formation in dwarf galaxies (e.g. Gerola, Seiden & Schulman 1980, Walter & Brinks 1999, Dekel & Woo 2003). Thus, $M_B \sim -19$ and $V_{max} \sim 120 \text{ km s}^{-1}$ transition may also indicate the mass scales for which supernova feedback may *globally* control star formation (Dekel & Woo 2003).

Finally, the transition at $M_B \sim -19$ and $V_{max} \sim 120 \text{ km s}^{-1}$ is also marked by a 50% increase in the dispersion of the EW for the more massive galaxies. Not all of this increase in the dispersion can be nominally attributed to rises in internal extinction variations (see Figure B.3 in Appendix B) and in the EW measurement error, which together can account for half of the increase in scatter at most. The remaining change may reflect a greater incidence of short-term fluctuations in the relative star formation activity for massive, early-type spirals as compared with the later-type spirals with $-19 \geq M_B \geq -17$.

Moving on to the lower-mass transition at $M_B \sim -15$ and $V_{max} \sim 50 \text{ km s}^{-1}$, we see that the trends in the EW for the most extreme dwarfs parallel those for the most massive galaxies. Below the transition there is a slight turn-off toward lower EWs (by $\sim 25\%$, from 30\AA to 24\AA) and a broadening of the distribution (by a factor of 2). In this case however, we suspect that the turn-off is not necessarily an indication of depressed star formation, but a reflection of the decreased probability of forming the highest-mass ionizing stars in systems where the average SFR is $\lesssim 0.01 M_\odot \text{ yr}^{-1}$ (see Figure 4.5). Calculations of the minimum SFR required to fully sample the stellar initial mass function (IMF) have been per-

formed by Kroupa & Weidner (2003) based on the assumption that the IMF acts like a probability distribution function. For a Salpeter IMF, and additional conservative assumptions on the IMF of cluster masses, Kroupa & Weidner (2003) predict that the upper-mass limit begins to dip below the standard value of $100 M_{\odot}$ at $\sim 0.03 M_{\odot} \text{ yr}^{-1}$ and reaches $50 M_{\odot}$ at $\sim 0.005 M_{\odot} \text{ yr}^{-1}$. From Figure 4.5, these SFRs respectively correspond to $M_B \sim -16$ and $M_B \sim -14$, which are values that approximately flank the transition. We calculate the reduction in the ionization rate for populations with $M_{up} = 50 M_{\odot}$ relative to that from a fully sampled IMF with $M_{up} = 100 M_{\odot}$ using Starburst99 (Leitherer et al. 1999) and find that it is 50%, which is enough to account for the drop in the typical EW. We note that while we only observe a 25% drop in the average EWs, this may be due to the coarse binning that is used, and the rapid incompleteness that sets in for galaxies with $M_B \gtrsim -14.7$. It thus would be interesting to obtain $H\alpha$ observations for a larger, complete sample of extreme star-forming dwarf galaxies to further investigate the extent of statistical effects on the IMF.

Statistical effects may also be responsible for the factor of ~ 2 broadening of the EW distribution below the transition at $M_B \sim -15$. The low average SFRs in the extreme dwarfs can also cause star formation “flickering,” since there are only a handful of HII regions in these systems at any given time. Figure 4.5 shows that the two magnitude average difference between the luminosity bins that flank the transition corresponds to a factor of ~ 6 difference between the typical SFRs. Thus, statistical effects will increase the scatter in the EW distribution by a factor of $\sqrt{6} = 2.5$, which can apparently fully account for the broadening.

This may seem to imply that statistics are all that are needed to explain the low mass transition in the M_B -EW plane. However, we note that the scatter does not continue to drop by another factor of two between the two intermediate lu-

minosity bins, so there must be other mechanisms at work. At issue is what can be considered a representative star formation “cell” in a galaxy, such that the summation of these cells can be used as a metric to discern whether mechanisms beyond statistics play a significant role in influencing star formation in galaxies of a given mass. If the galaxies in the lowest luminosity bin roughly approximate these cells, then there must be processes that act to increase the scatter in the EW for the intermediate luminosity galaxies above what would be expected from statistical effects alone. If not, then we must also consider other processes that would cause the scatter for the most extreme dwarfs to be larger than expected. One possibility is that feedback from massive stars (e.g. stellar winds, supernova shocks) on the ISM has a greater negative impact on the ISM of physically small, kiloparsec-sized systems, with the result that star formation is burstier in dwarf galaxies than in larger spirals. Gerola et al. (1980) originally explored such issues in their models of stochastic self-propagating star formation, which interestingly, show a characteristic stabilizing transition in fluctuations in the mean star formation rate for galaxies with $M_B \gtrsim -15$. This result, however, is again critically dependent on the assumed fundamental cell size and the refractory period (the time during which negative feedback inhibits the formation of new stars) which are both free parameters in their toy models. The more recent models of Mac Low & Ferrara (1999) are independent of such uncertainties and incorporate more realistic prescriptions for the density distributions of the gas, stellar and dark matter in dwarf galaxies. Again, they find that below a rotational velocity scale of ~ 30 km/s, feedback disrupts and blows out the ISM from the galaxy. While such sharp transition features in the models strongly suggest that the low-mass broadening of the EW distribution is not merely a result of statistical effects, a more careful comparison of the models and observations will be required to confirm

this. In particular, since the feedback energy is a key model input which depends on the characteristic SFRs, it will be important to check that the duty cycle results presented in the following two chapters are consistent with the model assumptions and lead to the trends in the relative SFR with mass as presented here.

Table 4.1: Logarithmic $H\alpha$ EW Distribution Statistics

EW($H\alpha$ + $[NII]$), no extinction correction					
Bin	N	<i>all EW</i>		<i>best-fit Gaussian</i>	
		$\langle \lg(EW) \rangle$	$\sigma[\lg(EW)]$	$\langle \lg(EW) \rangle$	$\sigma[\lg(EW)]$
$-22.0 \leq M_B < -19.0$	27	1.16	0.48	1.17	0.40
$-19.0 \leq M_B < -17.0$	53	1.51	0.18	1.52	0.16
$-17.0 \leq M_B < -14.7$	87	1.45	0.35	1.50	0.17
$-14.7 \leq M_B < -13.0$	102	1.37	0.48	1.40	0.33

EW($H\alpha$), extinction corrected					
Bin	N	<i>all EW</i>		<i>best-fit Gaussian</i>	
		$\langle \lg(EW) \rangle$	$\sigma[\lg(EW)]$	$\langle \lg(EW) \rangle$	$\sigma[\lg(EW)]$
$-22.0 \leq M_B < -19.0$	27	1.17	0.38	1.15	0.43
$-19.0 \leq M_B < -17.0$	53	1.49	0.18	1.48	0.17
$-17.0 \leq M_B < -14.7$	87	1.44	0.35	1.49	0.20
$-14.7 \leq M_B < -13.0$	102	1.38	0.46	1.39	0.35

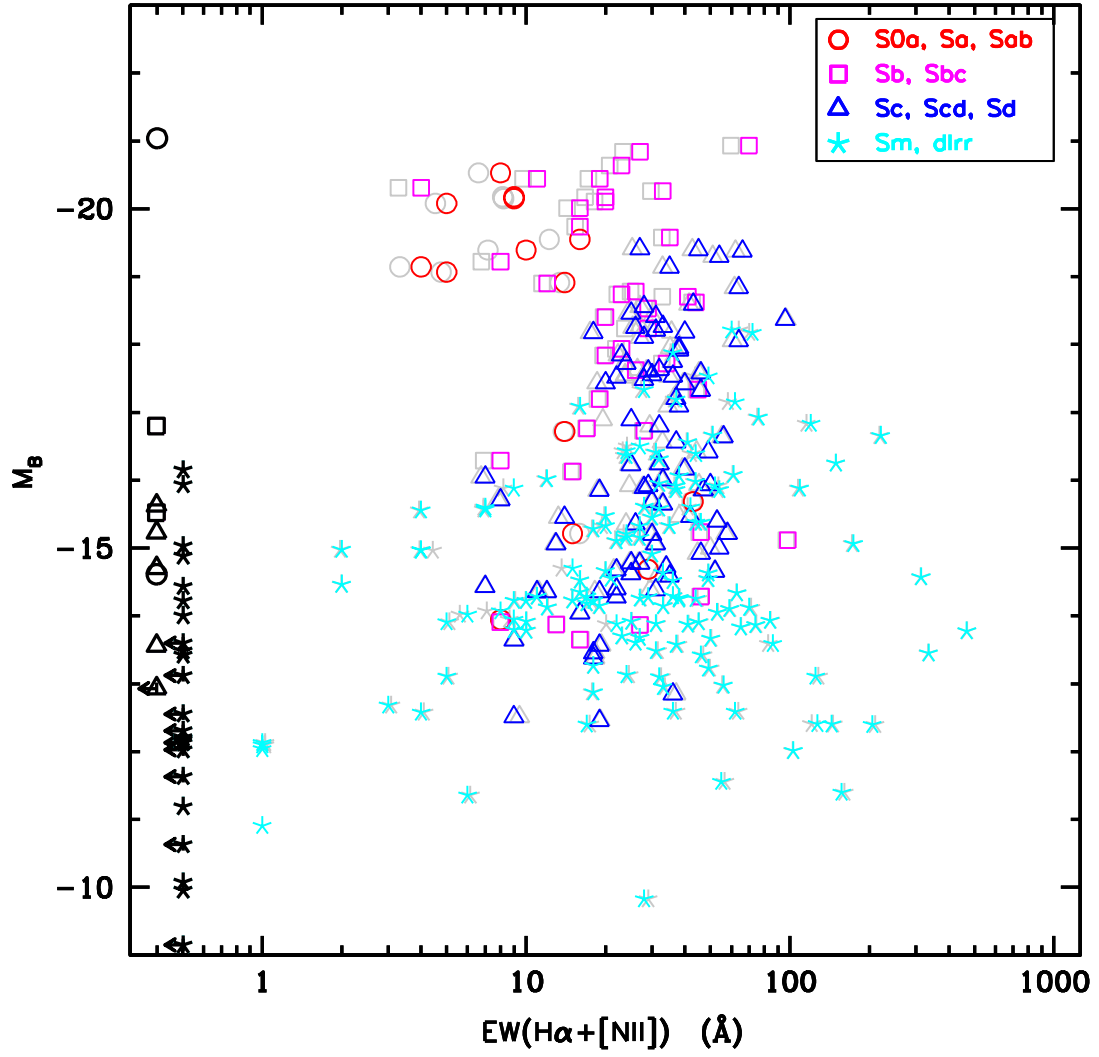


Figure 4.1: The Local Galaxy Sequence in the M_B -EW Plane – Galaxies from the complete subsample of 11HUGS are shown.

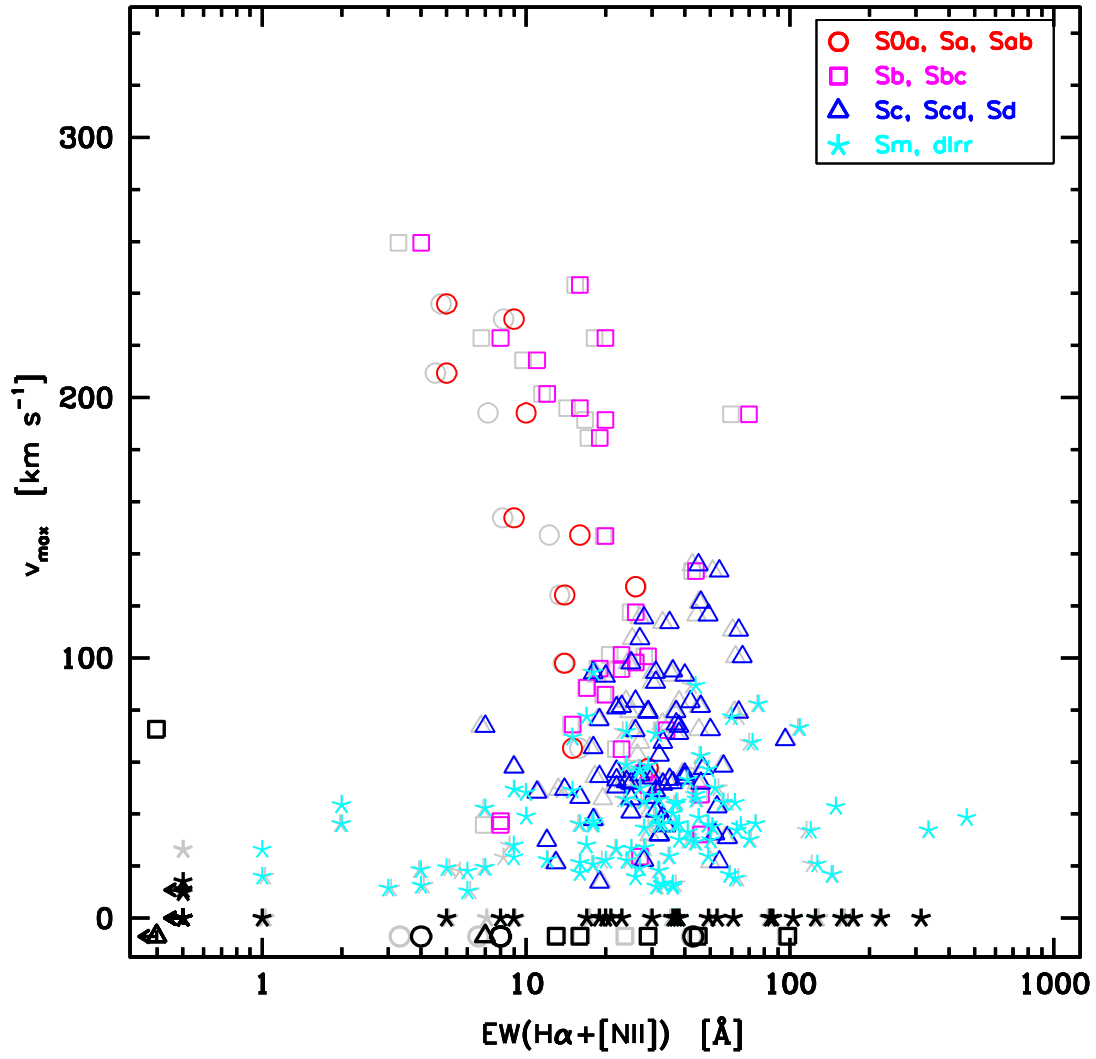


Figure 4.2: The Local Galaxy Sequence in the v_{\max} -EW Plane – Galaxies from the complete sub-sample of 11HUGS are shown.

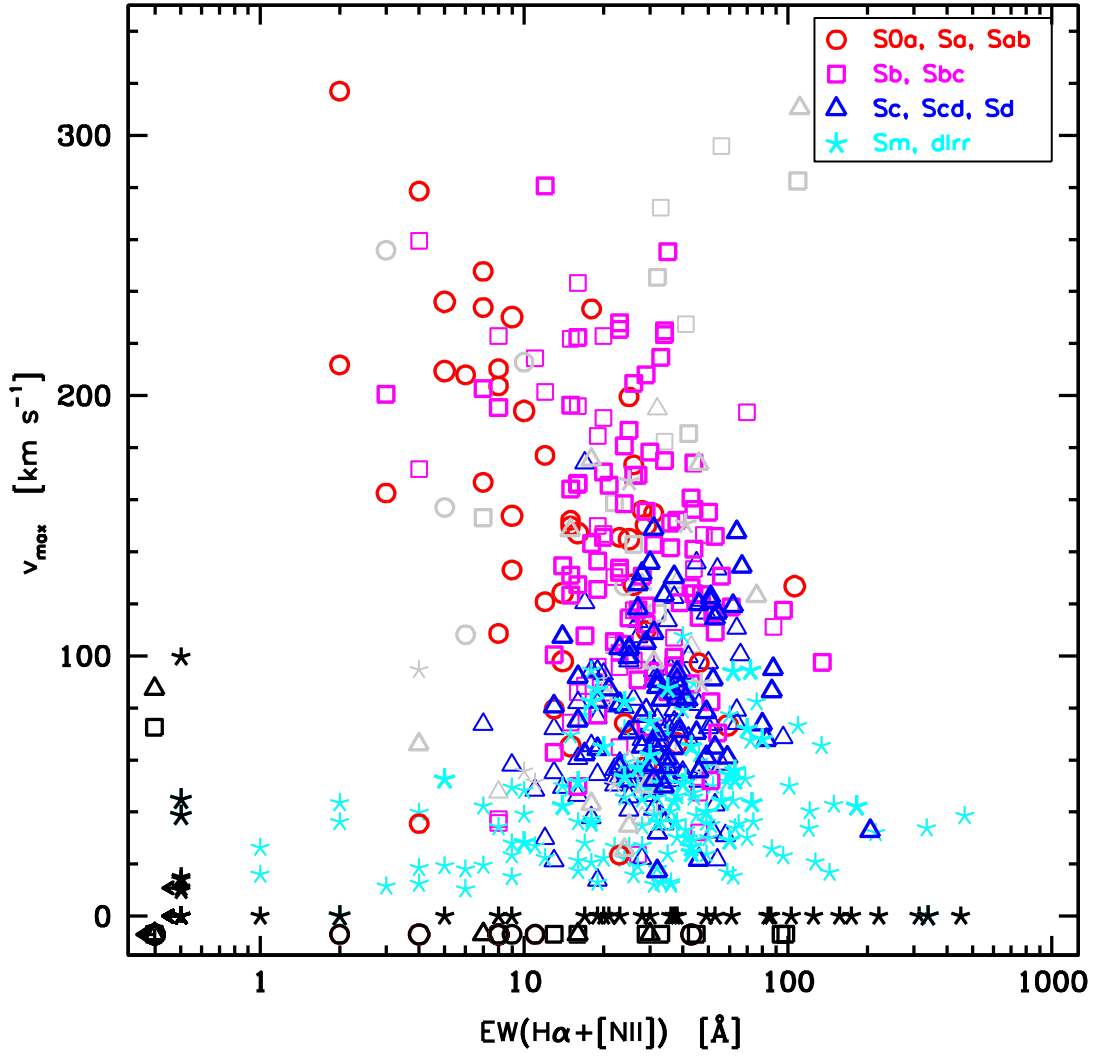


Figure 4.3: The Local Galaxy Sequence in the V_{\max} -EW Plane – All galaxies from 11HUGS and the H α GS with V_{\max} measurements available from Hyperleda are shown.

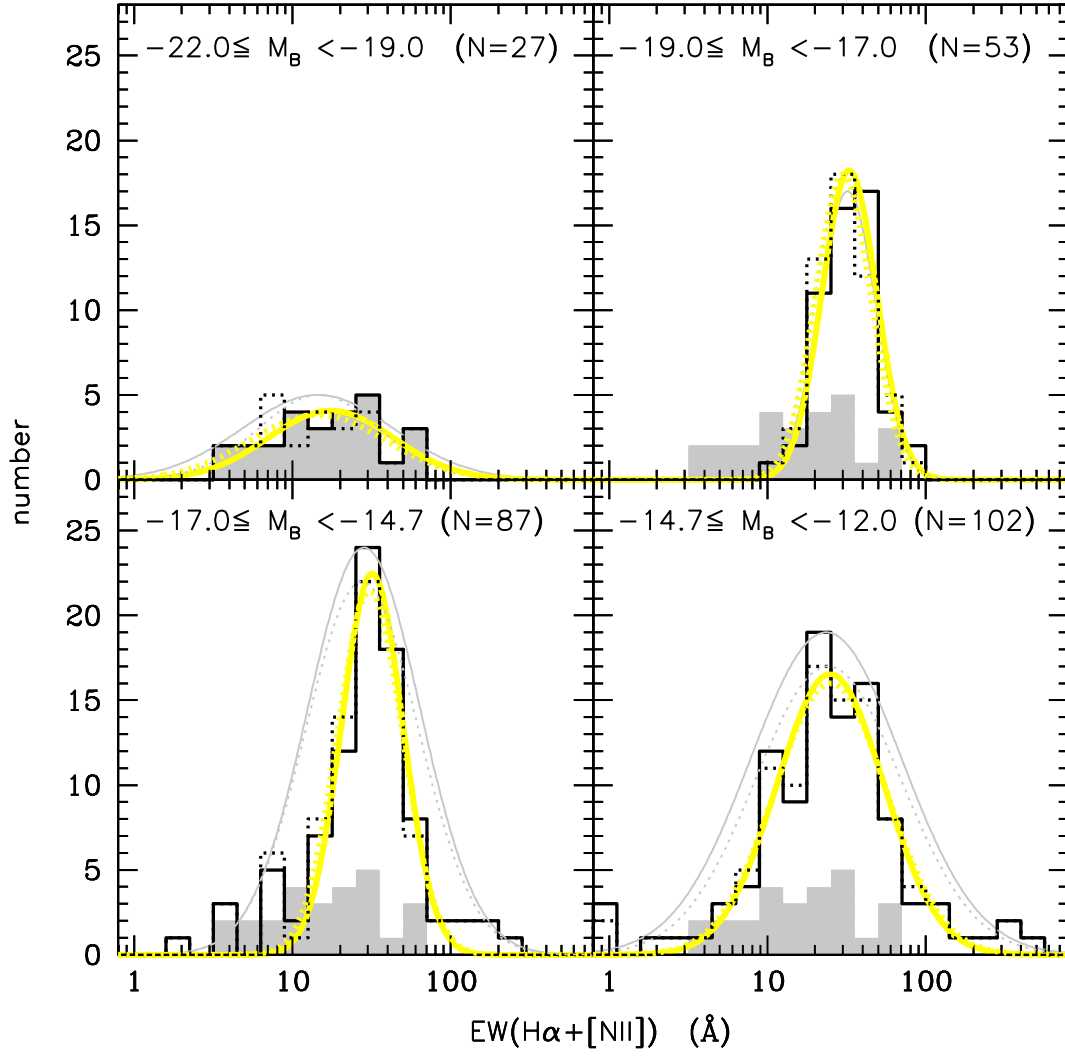


Figure 4.4: Logarithmic EW frequency distributions for galaxies in the complete sub-sample of 11HUGS.

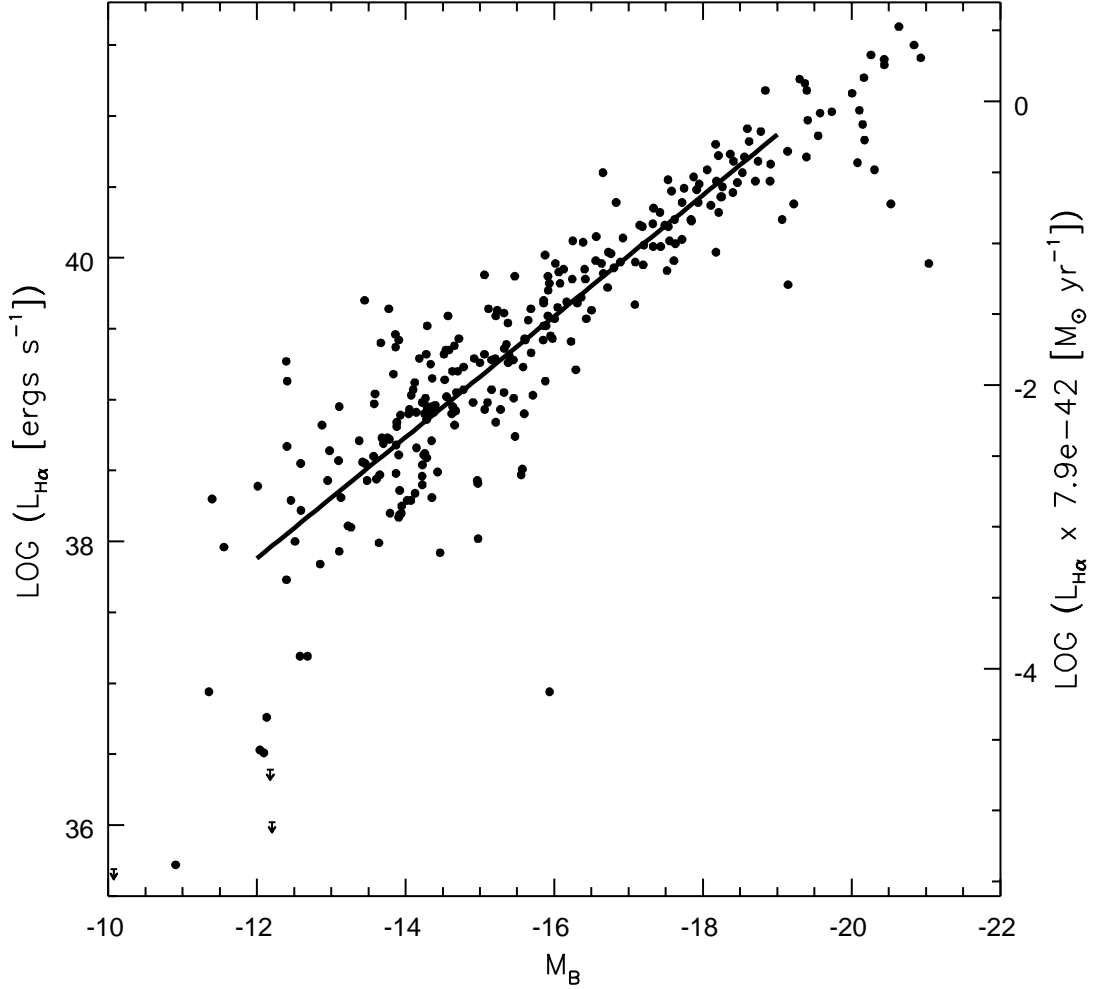


Figure 4.5: $L_{H\alpha}$ vs. M_B for the same 11HUGS galaxies plotted in Figure 4.1. Galactic, but no internal extinction corrections have been applied to the data. The line represents a fit to the data in the range $-19 \leq M_B \leq -12$ which is given by $\log(L_{H\alpha}) = -0.43M_B + 32.76$. Thus the $H\alpha$ and B -band luminosities roughly follow a one-to-one scaling. The right axis shows the corresponding SFR scale, based on the solar metallicity Kennicutt 1998 conversion, for approximate reference.

CHAPTER 5

DWARF GALAXY STARBURST STATISTICS

5.1 ABSTRACT

In this chapter, we focus on the first objective of the thesis, and quantify the prevalence of starbursts in present-day dwarf galaxies. To do this, we tally the number of high-EW($H\alpha$) dwarfs, and compute the fraction of on-going massive star formation that is concentrated in these systems. The volume-limited component of 11HUGS is used to perform the calculations. We find that global bursts are taking place in $6\pm3\%$ of local star-forming dwarfs and are responsible for $22\pm10\%$ of their total current star formation. We compare our numbers with previous estimates in the literature, and find that there is good consistency among the results. This is notable because the aggregate of these studies have been based upon a broad range of independent approaches to the problem. We will use these statistics in the next chapter to infer constraints on the dwarf galaxy starburst duty cycle.

5.2 Adopted Definitions

To begin, we address a couple rudimentary, but prerequisite issues regarding which systems can be considered to be dwarf galaxies, and which may qualify as starbursts.

5.2.1 What is a dwarf galaxy?

In general, the term *dwarf galaxy* is used to loosely refer to systems with luminosities that are about a couple of magnitudes fainter than M^* , the “knee” of the

luminosity function. As discussed in the previous chapter, this luminosity regime ($M_B \sim -18$) is significant because it is where the morphology of galaxies transition from being dominated by spiral structure to being irregular. Beyond this general criterion for identifying dwarfs however, there is little utility in establishing a more exact, single definition of the term. The standards used to decide what a dwarf is, whether is based on morphology, luminosity and/or mass, depend on the specific questions one is trying to answer. For our purposes here, we can use the natural division in the M_B -EW plane between massive galaxies with dwindling star formation, and those of smaller mass with higher birthrates, to identify a population to focus on. Accordingly, in our analysis below, we will examine burst statistics for galaxies fainter than the characteristic $M_B = -19$ transition in the M_B -EW sequence.

5.2.2 What is a starburst?

Deciding on the criteria for distinguishing bursting systems from the rest of the population is less trivial. Good reviews of this issue have already been given by Heckman (2005), Gallagher (2005) and Kennicutt et al. (2005), all in the proceedings of the 2004 Cambridge Starbursts conference (ed. de Grijs & Gonzalez Delgado). We consider only a few selected points here.

While there are many ways to define a starburst, perhaps the most physically compelling scheme is to identify them as the galaxies that are forming stars near the maximum possible rate set by causality — i.e. the rate that results when all of the gas in a system is consumed in one dynamical time (Heckman 2005). However, measurements of the total gas masses and global velocity dispersions that are required to compute the limiting SFRs are not available for all members of our sample, so we cannot carry out a complete analysis based on this parameterization of the burstiness. An alternate approach, as suggested by Gallagher

(2005) and Kennicutt et al. (2005) is to develop a characterization of normal star formation activity based on the overall population of galaxies, which can then be used to pinpoint unusual systems. A subset of these deviants should be the starbursts. This method is not only practical, given the data that we have in hand, but it is also particularly sensible, in light of the result that the distributions of the logarithmic $H\alpha$ EW (a measure of the burstiness as described in Chapter 4 and discussed in detail in Chapter 6), appear to be Gaussian in the regime where normal star-forming galaxies dominate. The Gaussian form of the distribution suggests a natural way to proceed — *define starbursts to be those galaxies with EWs that exceed the mean value by 3σ . Note that the fraction of starbursting galaxies based on this definition will not nominally be 0.3% since there are significant excesses in the tails of the EW distributions above what would be predicted by a Gaussian function.* The excesses are clearly illustrated in Figure 5.1 where the observed EW cumulative distribution functions are compared with those of the best fit Gaussian functions as given in Table 4.1.

As an initial check on the physical sensibility of this approach, let us see what the 3σ EW range roughly corresponds to in terms of the stellar birthrate. For galaxies with $M_B \gtrsim -19$ down to the 11HUGS completeness limit of -14.7 , the 3σ range (again based on the parameters of the best-fit Gaussian functions in Table 4.1) spans from 10\AA to 100\AA , with $\langle \lg(\text{EW}) \rangle \sim 30\text{\AA}$. Using the model grid from KTC94, these statistics imply that normal star-forming galaxies have birthrates approximately between 0.1 and 2 with an average value of ~ 0.5 . This is consistent with the general idea that starburst events must involve an increase in the SFR by a factor of about three within a short period, since normal disks commonly show factors of 2 to 3 fluctuations in their star formation activity, and these modest fluctuations are not associated with the starburst phenomenon (Hunter &

Gallagher 1986, Salzer 1989, Gallagher 2005). Therefore, it appears that the statistics of the EW distribution can be used to differentiate between galaxies with normal steady-state star formation and those with more intense episodic activity, and we will adopt the definition that galaxies with EW above the 3σ value of 100\AA are starbursts.

5.3 The Fraction of Starbursts Systems among Dwarf Irregulars

With the criteria established in the previous section, it is straightforward to determine the fraction of starbursting dIrrs in the local 11 Mpc volume. In Table 5.1, we list the fraction of galaxies above and below the 1, 2 and 3 σ ranges of EW values. The sample has been divided into the same luminosity bins as in our analysis of the features in the M_B -EW and V_{max} -EW planes in the previous chapter. All values in the table are based on measurements that have been corrected for internal extinction and the contribution of the [NII] lines to the observed flux as discussed in Appendix B.

We first focus on galaxies with $-17 \leq M_B < -14.7$, since this is the luminosity bin in which both the number statistics are tolerable and the sample is volume complete. The burst fractions based on the galaxies in this bin represent our most robust results, and we will choose to primarily quote these numbers in our subsequent analyses. Systems fitting the adopted definition of a starburst as one with $\text{EW} > 100\text{\AA}$ are rare in this luminosity range – there are only 5 galaxies with EWs this high, and this represents 6% of the population. Reassuringly, this result is not critically dependent on the exact EW threshold that is used. If we instead drop the threshold down to 2σ above the mean ($\text{EW} \geq 68\text{\AA}$), the number count only increases to 7 systems (8%). Corrections for the contribution of the [NII] lines to the flux and internal extinction also have a negligible impact. This is shown in Figure

5.1, where we plot the cumulative distributions as a function of the EW. The dotted histograms, which represent the distributions for the corrected EWs, and the solid histograms, which show those for the raw measurements, are marginally different. The dominant component of the uncertainty in the starburst number fraction is quite likely due to Poisson noise, so we will quote the primary result as $6^{+3.8}_{-2.5}\%$, where the errors span the 68.3% confidence interval.

For the higher luminosity galaxies ($-19 \leq M_B < -17$), there are no excesses in the tails of the EW distribution, and no observed starbursts according to the $\text{EW} > 100\text{\AA}$ criteria. This can be attributed to small number statistics, as there are $\sim 35\%$ fewer galaxies in this bin as compared with the $-17 \leq M_B < -14.7$ bin. Assuming for the moment that the starburst number fraction is also 6% here, then there should be $3^{+2.9}_{-1.6}$ galaxies with $\text{EW} > 100\text{\AA}$ for a sample of 53, so it is not unreasonable that there are not any galaxies with such high EWs observed. Of course, a fraction as high as $\sim 11\%$ would still be consistent with the observations. Thus, with this dataset alone, we can only conclude that the starburst number fraction is $\lesssim 11\%$ at the 99.7% confidence level.

The situation is more complicated for the lowest luminosity bin which includes galaxies with $-14.7 \leq M_B < -12$. First, the completeness drops precipitously at $M_B = -14.7$ (see Figure 3.2), so the statistics reported for these dwarfs must be interpreted with caution. The probable sense of the systematic incurred would be that the starburst mass and star-formation fractions would tend to be over-estimated since the low surface brightness normal dwarfs are more likely to be missing from the sample than the higher surface brightness starbursting systems. Second, the absolute EW starburst criteria changes. Since the EW distribution widens in this regime, the 3σ threshold is higher than for the more luminous dwarfs. The 2σ and 3σ values are 120\AA and 250\AA , and the number fractions of

galaxies above these thresholds are 7% and 3% respectively. Nevertheless, these numbers are consistent with the ones calculated for the other two bins, and do not significantly change even if we continue to use the prior EW criteria based on the distributions of the more luminous dwarfs. With the previous 2σ and 3σ values of 68\AA and 100\AA , the number fractions of galaxies are 12% ($N=12$) and 8% ($N=8$), respectively. Note that these results do not necessarily imply that the starburst number fraction does not change as a function of luminosity. There is a hint of decreasing burst number fraction with increasing luminosity, but we simply do not have the statistical power to definitively demonstrate any possible trends with the 11HUGS sample. What can be inferred though is that if there is such a trend with luminosity, it is likely to be very weak, changing by no more than 11% over 7 magnitudes in M_B .

5.4 The Fraction of Star Formation Occurring in Starbursting Dwarfs

Arguably however, the more important burst statistic is not the number fraction of starbursts, but the fraction of star formation that occurs in starburst episodes. If the star formation fraction is high, this would be evidence that the burst mode dominates the evolution of dwarfs, even if the number fraction is low. To estimate the star formation fraction, we sum the $H\alpha$ luminosities $L_{H\alpha}$ (which have been corrected for internal extinction and the contribution of [NII]) as a function of the EW. The percentage of $L_{H\alpha}$ contained in galaxies above and below the 1, 2 and 3 σ ranges of the EW are reported in Table 5.1. The cumulative $L_{H\alpha}$ distribution as a function of the EW are also plotted in Figure 5.2.

Again, we first examine the results for the $-17 \leq M_B < -14.7$ range. The 5 galaxies with $EW > 100\text{\AA}$ are responsible for 22% of all of the star formation occurring in this luminosity bin. A simple translation of the Poisson error in

the number fraction results in an error of $^{+15}_{-11}\%$ in the L_α fraction. From Figure 5.2, it can be seen that the starburst system that has the largest SFR contributes a bit less than 10%, so our simple-minded estimation of the error appears to be reasonable. This quantity is also not very sensitive to the exact criterion used to classify starbursts. A lower 2σ threshold only causes a small rise of the fraction to $27^{+15}_{-10}\%$.

For $-19 \leq M_B < -17$, no systems are observed with $\text{EW} > 100\text{\AA}$ as discussed above. However, the 2 galaxies with EWs higher than the 2σ threshold of 68\AA produce 6.7% of the $\text{H}\alpha$ luminosity, and this is consistent with the fact that the 7 galaxies with $-17 \leq M_B < -14.7$ and $\text{EW} > 68\text{\AA}$ produce 27% of the $\text{H}\alpha$ luminosity in that bin. Therefore, estimating that each starburst galaxy is on average responsible for $\sim 4\%$ of the total star formation occurring in the population, we infer that the fraction of star formation due to $\text{EW} > 100\text{\AA}$ galaxies in this luminosity range must be less than $\sim 25\%$ at the 99.7% confidence level.

Finally, as can be expected from the preceding discussion, the fraction of star formation occurring in the lowest luminosity starbursts is consistent with those computed for the two other bins. For the σ thresholds defined by the broader EW distribution for $-14.7 \leq M_B < -12$, galaxies with EW greater than 120\AA (2σ) and 250\AA (3σ) are responsible for 20% and 15% of the star formation respectively, while for the σ thresholds defined by the more luminous dwarfs it is 24% ($N=12$, $\text{EW} > 68\text{\AA}$) or 20% ($N=8$, $\text{EW} > 100\text{\AA}$).

From these calculations, it is clear that a significant amount of the overall star formation in present-day dwarf galaxies does take place in starbursts. However, the results also imply that a more continuous, steady state of star formation dominates in the present epoch, both in terms of being the mode that operates during the vast majority of the time and in which most of the stars are being created. The

average burst amplitude does not appear to vary strongly with luminosity, with 2-4% of the total star formation density in a given luminosity bin being concentrated in individual starbursting systems.

5.5 Comparison with Previous Work

Based on the 11HUGS sample, we have just shown that $6\% \pm 3\%$ of dIrrs are starbursting, and that $22\% \pm 10\%$ of the overall star formation in the dwarf population is due to these systems. How do these numbers compare with other estimates in the literature?

In terms of the starburst number fraction, there is good consistency between our result and previous estimates, which is notable because the aggregate of these studies cover a broad range of independent approaches to the problem. As discussed in the introductory chapter, the earliest investigations compared the space densities of low luminosity UV-selected Markarian galaxies to those of field galaxies (Sargent 1972, Huchra 1977) in order to constrain the fraction of “flashing” systems. This work produced tentative estimates of 7% at $M_p = -17$, and 10% at $M_p = -14$, based on very small samples containing about a dozen objects each, and large incompleteness corrections. A later study also focused on determining the space densities of active galaxies, but used the newer University of Michigan [OIII] λ 5007 emission-line selected survey (Salzer 1989). The comparison set of normal galaxies was based on the magnitude-selected catalogs of Zwicky (the Catalog of Galaxies and Clusters of Galaxies, 1961-1968) and Nilsson (the UGC, 1973). The number statistics of the Salzer (1989) samples were improved relative to the earlier Markarian studies, with $N \sim 40$ and $N \sim 30$ in the Michigan and general population samples respectively. Using the numbers reported there, we calculate that the low-luminosity Michigan emission-line

galaxies ($-17 \leq M_B < -15$) represent 5%-15% of the general population in that luminosity range.

More recently, in Lee et al. (2002), my collaborators and I attempted to constrain the number fraction of bursting dwarfs by comparing the HI mass functions/space densities of low HI mass, low-luminosity galaxies ($M_{HI} < 10^9 M_\odot$, $M_B > -18$) in the $H\alpha$ -selected KISS survey and in the HI blind surveys of Zwaan et al. (1997) and Rosenberg & Schneider (2002). A conclusion was that the dwarf galaxies found in KISS make up 25% of the overall population of low-mass galaxies. This was interpreted to mean that 1 out of every 4 dwarfs is bursting. However, this result was limited by small numbers and incompleteness in the HI blind survey samples at low masses (i.e the uncertainty in the faint end slope of the mass function). Further, the conclusion relies on the assumption that *all* dwarfs selected by KISS can be considered true starbursts although the sample includes many galaxies with $EW < 100 \text{ \AA}$. Thus, the 25% quoted in Lee et al. (2000) should be regarded as an upper-limit to the number fraction of starbursting dwarfs galaxies.

Kauffmann et al. (2003a,b) have used an entirely different method to calculate the fraction of bursty galaxies as a function of stellar mass in the Sloan Digital Sky Survey (SDSS). In this work, an extensive grid of stellar population synthesis models, spanning a range of metallicities and star formation histories, is constructed. A Bayesian technique is then used to compare the observed and modeled $H\delta$ absorption and 4000 \AA break to generate a likelihood distribution of the fraction of stellar mass formed in bursts for each galaxy in their sample. Two statistics are reported: (i) “ $F_{burst}(50 \text{ per cent}) > 0$,” the fraction of galaxies whose likelihood distribution of burst masses have *median* values greater than zero, and (ii) “ $F_{burst}(2.5 \text{ per cent}) > 0$,” the fraction of “high con-

fidence bursty galaxies” whose likelihood distributions have their lower 2.5 percentile point above zero. For galaxies with $8.0 < \log M_* < 8.5$ (which corresponds to $-16 \lesssim M_B \lesssim -14.5$ assuming an approximate $M/L_B = 1$ which is typical for dIrr galaxies; e.g. Miller & Hodge 1994; Chapter 6), Kauffman et al. find that the fraction with $F_{burst}(50 \text{ per cent}) > 0$ is over 50%, while $F_{burst}(2.5 \text{ per cent}) > 0$ is 9%. For higher mass dwarfs with $8.5 < \log M_* < 9.0$ ($-17 \lesssim M_B \lesssim -16$), the values instead are 36% and 4%, respectively. Clearly, the number fractions estimated using $F_{burst}(50 \text{ per cent}) > 0$ to discriminate whether a galaxy has undergone a burst in the recent past are far too large to be consistent with any of the other estimates discussed above. This is perhaps not too surprising since half of the models which are consistent with the observations for the $F_{burst}(50 \text{ per cent}) > 0$ galaxies have SFHs in which there have not been any bursts at all, and the burst number fractions computed in this way are probably overestimates. However, the fractions of “high confidence bursty galaxies” are in excellent agreement with the other measurements. Thus, it appears that the starburst number fraction for dwarf galaxies with $M_B \gtrsim -15$ is well determined, and moreover, relatively robust to the method used to pick out starbursts. Past estimates consistently lie between 4% and 10%, and our 11HUGS measurement of $6\% \pm 3\%$ is representative of these values.

With respect to the work of Kauffmann et al. (2003a,b), we also note that they have reported a very strong decrease of the burst number fraction with stellar mass, whereas we have concluded that any trend should be relatively weak, at least as a function of luminosity. In terms of the *absolute* change in the number fraction, examination of their Figure 5 reveals that it is indeed large, but only when the $F_{burst}(50 \text{ per cent}) > 0$ criterion is used to identify galaxies with recent bursts. The fraction of $F_{burst}(50 \text{ per cent}) > 0$ galaxies drops from 54% at $\sim 10^8$

M_{\odot} to $12\% \sim 10^{10}M_{\odot}$. However, when the analysis is restricted to the “high confidence bursty galaxies” the absolute decline is much smaller, changing from 9% to 1%. The latter result is more consistent with our inference that the number fraction should change by no more than 11% over 7 magnitudes in M_B .

As for the fraction of star formation which takes place in bursting systems, we know of few prior studies which have attempted to place constraints on this quantity for dwarf galaxies per se. Based on the SDSS, Brinchmann et al. (2003) have found that starbursts are responsible for 20% of the local star formation density. Although this is consistent with our 11HUGS estimate of $22\% \pm 10\%$, the Brinchmann measurement refers to the total galaxy population, and was not computed as a function of mass.

As another check on the starburst star formation fraction, we can perform a quick calculation using the KPNO International Spectroscopic Survey (KISS; Salzer et al. 2000), a 2nd generation CCD-based, emission-line selected, objective-prism survey. We use the sample of $H\alpha$ -selected galaxies cataloged in List 1 (Salzer et al. 2001), which contains 1128 candidates identified from the objective-prism images. Follow-up slit spectroscopy has been completed for all of these candidates and 907 of them are found to be star-forming galaxies. Completeness of the sample has been assessed through the standard V/V_{max} test (Schmidt 1968), and limiting volumes have been calculated for each object (Gronwall et al. in preparation; also see Lee et al. 2002). We use these volumes to calculate star formation rate densities as a function of the $H\alpha$ EW. We choose to use the $H\alpha$ fluxes and EWs that are measured from the objective-prism spectra, since they are less likely to suffer from aperture effects and will be closer to the integrated values than those measured from the slit spectra. For $-17 < M_B < -15$ (N=61), we find that galaxies with $EW > 100\text{\AA}$ (N=21) and $EW > 68\text{\AA}$ (N=34) are respon-

sible for 22% and 38% of the total $L_{H\alpha}$ output in this bin. We also can compute the starburst number fractions as a function of the EW by comparing the KISS number densities with a sample which better represents the overall population of dIrrs. Adopting the B-band luminosity function determined by Zwaan et al. (2001), which is based on the HI selected sample from the Arecibo HI Strip Survey (Zwaan et al. 1997), we find that the fraction of galaxies with $EW > 100\text{\AA}$ is 5% while it is 12% for the lower threshold of $EW > 68\text{\AA}$. These results, which are based on better number statistics for the high EW galaxies, are in good agreement with the fractions estimated from 11HUGs and elsewhere. Nevertheless, the KISS statistics just reported must be regarded as preliminary as we have not applied the necessary corrections for [NII] contamination, internal extinction and limited aperture, nor have we checked the correspondence between the objective-prism EWs with those that are truly integrated. Most of these second order corrections should be straightforward to carry out, and we leave these remaining tasks for future follow-up work.

Table 5.1: Logarithmic H α EW Distribution Statistics

	$-19.0 \leq M_B < -17.0$	$-17.0 \leq M_B < -14.7$	$-14.7 \leq M_B < -12.0$
Quantity	($N = 53$)	($N = 87$)	($N = 102$)
	$\langle \lg(\text{EW}) \rangle = 30\text{\AA}$	$\langle \lg(\text{EW}) \rangle = 31\text{\AA}$	$\langle \lg(\text{EW}) \rangle = 25\text{\AA}$
1σ range	20\AA, 45\AA	21\AA, 46\AA	12\AA, 55\AA
$N \leq 1\sigma, N \geq 1\sigma$	8, 8	23, 16	23, 17
$\% \leq 1\sigma, \% \geq 1\sigma$	15%, 15%	26%, 18%	23%, 17%
$\%L_{H\alpha} \leq 1\sigma, \%L_{H\alpha} \geq 1\sigma$	11%, 26%	15%, 38%	5.5%, 32%
2σ range	14\AA, 66\AA	14\AA, 68\AA	6\AA, 118\AA
$N \leq 2\sigma, N \geq 2\sigma$	2, 2	15, 7	8, 7
$\% \leq 2\sigma, \% \geq 2\sigma$	3.8%, 3.8%	17%, 8.0%	7.8%, 6.9%
$\%L_{H\alpha} \leq 2\sigma, \%L_{H\alpha} \geq 2\sigma$	5.1%, 6.7%	6.7%, 27%	<1%, 20%
3σ range	9\AA, 98\AA	10\AA, 100\AA	3\AA, 251\AA
$N \leq 3\sigma, N \geq 3\sigma$	0, 0	10, 5	3, 3
$\% \leq 3\sigma, \% \geq 3\sigma$	0%, 0%	11%, 5.7%	2.9%, 2.9%
$\%L_{H\alpha} \leq 3\sigma, \%L_{H\alpha} \geq 3\sigma$	0%, 0%	2.3%, 22%	<1%, 15%

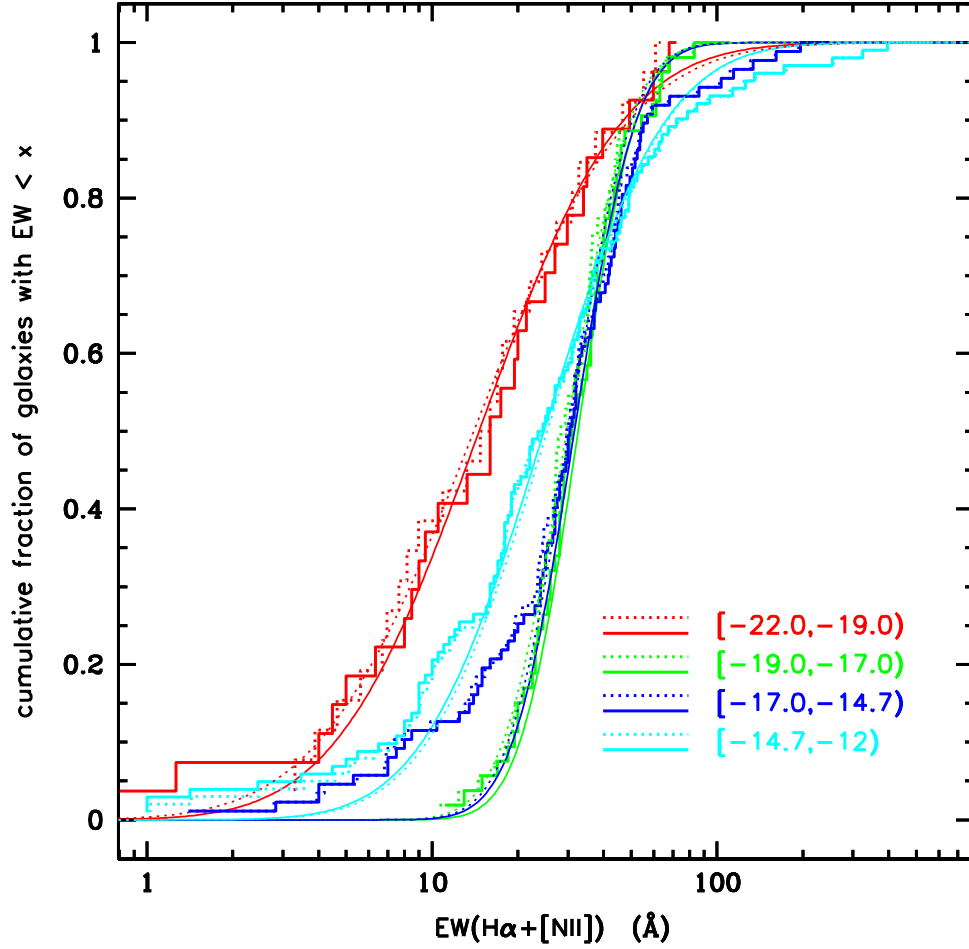


Figure 5.1: Cumulative $H\alpha$ EW distributions for galaxies in 11HUGS. The sample has been divided into 4 luminosity bins (color-coded as indicated in the figure) using the transitions in the M_B -EW and V_{max} -EW planes as a guide (see Chapter 4). The dotted histograms represent the distributions of the EWs which have been corrected for internal extinction and the contribution of the [NII] lines to the observed flux as described in Appendix B, while the solid histograms represent those of the uncorrected EWs. The smooth curves show the cumulative distributions of the best fit Gaussian functions as given in Table 4.1 and as over-plotted on the EW frequency distributions shown in Figure 4.4.

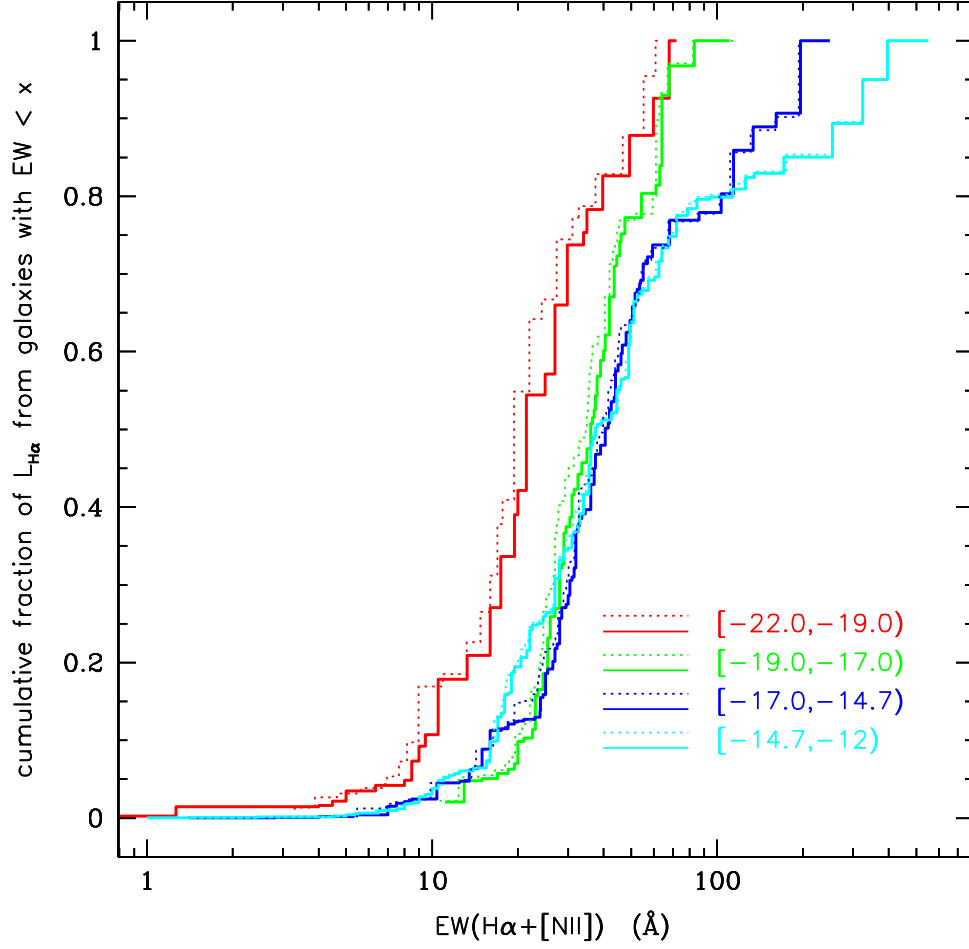


Figure 5.2: Cumulative distribution of $L_{H\alpha}$ as a function of $EW(H\alpha)$ for galaxies in 11HUGS. Again, the sample has been divided into 4 luminosity bins (color-coded as indicated in the figure) using the transitions in the M_B -EW and V_{max} -EW planes as a guide (see Chapter 4). The dotted histograms represent the distributions where the measurements have been corrected for internal extinction and the contribution of the [NII] lines to the observed flux as described in Appendix B, while the solid histograms represent those of the uncorrected measurements.

CHAPTER 6

CONSTRAINTS ON THE DWARF GALAXY STARBURST DUTY CYCLE

6.1 ABSTRACT

In this chapter, we focus on the second goal of the thesis and attempt to constrain the average starburst duty cycle in star-forming dwarf galaxies. We carry out our analysis by amassing clues from (i) the 11HUGS $H\alpha$ EW distribution (Chapters 3 & 4), (ii) the 11HUGS starburst number and star formation fractions (Chapter 4), (iii) UBV colors from the literature, and (iv) stellar evolutionary synthesis models.

First, we investigate whether invoking burst cycles are absolutely necessary for explaining the observed present-day properties of the *average, relatively quiescent* star-forming dwarf galaxy. We find that the blue UBV colors and modest EWs observed in typical dwarfs cannot be simultaneously matched by models which only include a continuous mode of star formation, unless the escape fraction of Lyman continuum photons is much higher than presently indicated by observations, or the currently favored IMFs have upper mass limits that are lower than the commonly adopted value of $100 M_{\odot}$. On the other hand, more standard models which include recent bursts with durations of 50-100 Myrs, birthrates of 6-10 (i.e. where 3-10% of the galaxy mass is formed in an episode), and cycle frequencies of $1-3 \text{ Gyr}^{-1}$, turn out to be consistent with both the observed $B-V$ and EW distributions. The burst models have 10 Gyr-old underlying populations formed according to exponentially declining SFRs with decay timescales of ~ 8 Gyrs, and current stellar birthrates $\lesssim 0.50$. Despite this success in simultaneously

matching the $B-V$ and EW data however, we have great difficulty modeling the $U-B$ colors correctly. The observed $U-B$ distribution can only be explained by the models if the majority of dwarfs are currently in the burst state, which is not only contrary to the result that the burst number fraction is $6\pm3\%$, but impossible since it is simply a contradiction in terms — the burst state is no longer the burst state if galaxies are perpetually in it. This perhaps can be attributed to problems with the stellar evolutionary tracks, and more work is needed here to clarify this issue. Finally, if the “equal probability” assumptions — that all star-forming dwarfs are similarly able to burst and the currently observed burst number and star formation fractions have been constant over cosmic history — are correct, then $22\pm10\%$ of the galaxy’s total mass must be formed in the burst mode. However, this estimate is just barely consistent with the $\sim 50\%$ mass fraction predicted by the models that best match the observations, which may be evidence that the equal probability assumptions are incorrect and that starbursts in dwarfs have occurred at a different pace in the past.

6.2 Evolutionary Synthesis Models

In this section we describe the evolutionary synthesis models which are used in conjunction with the observed $H\alpha$ EWs and UBV colors of star-forming dwarfs to gain insight into their SFHs.

First, we characterize the present evolutionary status of the population by finding the average stellar birthrate for dwarfs in the 11HUGS sample. In the last chapter, we have already used the model grid of KTC94 to estimate that the typical birthrate is ~ 0.5 ; i.e. that most dwarfs are now forming stars at rates that are lower by 50% compared to their past rates. However, the earlier models were calculated using solar metallicity stellar evolutionary tracks, which are not

appropriate for comparison to metal-deficient dwarf galaxies. Thus, we generate an updated set of models which cover a full range of metallicities, from $1/50 Z_{\odot}$ to $2.5 Z_{\odot}$. This will expand upon and provide an independent check of the KTC94 grid. More importantly however, this will provide the tools necessary to test whether invoking burst cycles are absolutely necessary for explaining the observed present-day properties of the *average, relatively quiescent* dwarf irregular galaxy, and if so, to constrain the frequencies, amplitudes and durations of the bursts.

6.2.1 Calculation of the Model Grid

Using the stellar population synthesis code of Bruzual & Charlot (2003), we create model galaxies which have both smooth and bursty SFHs. We follow the established convention in which exponentially declining SFRs are assumed to describe the continuous models, while bursty systems are formed by superimposing short episodes of enhanced star formation onto underlying components which are otherwise smooth (e.g. SSB73, LT78, KTC94, Kauffmann et al. 2003a).

Our synthetic galaxies are computed by summing the “standard” instantaneous burst populations provided in the BC03 default distribution, which are based on the Padova 1994 evolutionary tracks and the STELIB/BaSeL 3.1 spectral library. Our resulting grid contains models for (i) six metallicities between $1/200 Z_{\odot}$ to $2.5 Z_{\odot}$, (ii) two IMFs, that of Salpeter (1995) and Chabrier (2003) with mass limits of 0.1 and $100 M_{\odot}$, and (iii) 7 smooth SFHs, characterized by exponentially declining SFRs with decay timescales of 1, 2, 3, 4, 8, 12 Gyrs and ∞ (SFR=constant). We also generated a grid of 54 Salpeter IMF burst models which will be described further in the next section, and discussed at greater length in Section 6.5.

Birthrate parameters are straightforward to compute when the SFH is mod-

eled as an exponentially decaying function (a.k.a. “ τ models”). When $\text{SFR}(t) = \text{SFR}_0 e^{-t/\tau}$, a simple integration yields the total mass of stars formed over a time t :

$$M(t) = \text{SFR}_0 \frac{\tau}{t} (1 - e^{-t/\tau}). \quad (6.1)$$

The birthrate is then only dependent on the ratio of the age of the system to the decay timescale, t/τ :

$$b \equiv \frac{\text{SFR}(t)}{M(t)/t} = \frac{t}{\tau} \frac{e^{-t/\tau}}{(1 - e^{-t/\tau})}. \quad (6.2)$$

To compute present-day birthrates, it is assumed that stars have been forming according to this exponential law for a Hubble time, and we set t in the above equation to 10 Gyrs, as in KTC94.

After generating the model galaxies, the $\text{H}\alpha$ EW is determined as follows. First the rate of ionizing photons $N(\text{H}^0)$ produced at 10 Gyr is converted into the $\text{H}\alpha$ luminosity, assuming case B recombination, with nebular temperatures and densities of 10^4 K and 100 cm^{-3} respectively. Using the recombination coefficients from Osterbrock (1974) and assuming that the galaxies are radiation-bounded (i.e. there is no leakage of Lyman continuum photons),

$$\log L(\text{H}\alpha) [\text{ergs s}^{-1}] = \log N(\text{H}^0) [\text{s}^{-1}] - 11.87. \quad (6.3)$$

Second, the continuum luminosity density L_λ is computed from the model spectrum by performing simple first order fits to the local continuum around $\text{H}\alpha$. The EW then directly follows as $L(\text{H}\alpha)/L_\lambda$. The synthesized EWs for the continuous τ models are listed in Table 6.1 .

6.2.2 Comparison with Models of KTC94

We first compare the $b - EW$ mappings from KTC94 with those generated from our grid. In Figure 6.1, we plot the KTC94 models in gray. The open circles represent τ models while the filled circles represent those formed with a constant SFR and an instantaneous burst added at 10 Gyrs. We fit a line to the points, omitting the ones corresponding to the models where the SFR is exponentially increasing (i.e. when $\tau < 0$; the 4 topmost open circles for each IMF). These fits (also plotted in gray) approximate $b = f(EW(H\alpha))$ as a power law, $A [EW(H\alpha)]^n$, where

$$A, n = \begin{cases} 10^{-1.47}, 1.22 & : \text{Scalo} \\ 10^{-2.21}, 1.31 & : \text{Kennicutt} \\ 10^{-2.49}, 1.34 & : \text{Salpeter} \end{cases}$$

We overplot our models for four metallicities ($Z_{\odot}/50$, $Z_{\odot}/5$, $Z_{\odot}/2.5$, Z_{\odot}). The solar model is shown for comparison to the KTC94 results. The three sub-solar models plotted should cover the range of observed metallicities in the dwarf luminosity regime we have focused on, since according to the well-established local luminosity-metallicity relationship (e.g. Skillman et al. 1989; Richer & McCall 1995; Lee et al. 2003), $M_B = -19$ and $M_B = -12$ correspond to $\sim Z_{\odot}/2.5$ and $\sim Z_{\odot}/30$ respectively. The lowest and highest metallicity models are highlighted in blue and red, while the intermediate values are shown in black. The $b > 1$ models plotted in Figure 6.1 are constructed with an underlying 10 Gyr old population generated with a constant SFR as in KTC94, plus a burst component with star formation at an elevated but also constant rate for a duration of 10^7 years. The bursts turns on and off instantaneously, and the EW is taken at the end of the 10^7 yr period, where it reaches its maximum value. The EW for these burst models are given in the first 5 columns of Table 6.2.

The main ingredient that is different between the modeling done here and in KTC94 involves the adopted stellar libraries and evolutionary prescriptions. KTC94 is primarily based on the Schaller et al. (1992) Geneva tracks, while the present grid is based on the Padova 1994 tracks. Although the Geneva tracks are generally preferred for modeling young, ionizing populations, and the Padova tracks for populations dominated by old and intermediate-age stars, the differences between the two mainly involve convection in low and intermediate mass stars, and physics related to post main sequence evolution (see Charlot et al. 1996 and Vazquez & Leitherer 2005 for more details). This has a marginal impact on the hydrogen ionization output and the resulting EWs, as can be seen in Figure 6.1. As a result, we find that there is excellent agreement between the earlier and current $b - EW$ mappings — our solar metallicity Salpeter models (plotted in red in the top panel of Figure 6.1) and those of KTC94 produce EWs that differ by no more than 15% at any of the birthrates investigated.

What is also clear from Figure 6.1 is that the impact of the metallicity on the EW is fairly limited. For all four metallicities shown, the differences for the $b < 0.2$ ($\tau < 4$ Gyr) models are insignificant, as are the differences between the two intermediate metallicity models ($Z_{\odot}/2.5$, $Z_{\odot}/5$, plotted in black) for all of the SFHs computed. The effect of metallicity (lower metallicity stellar populations producing a greater number of ionizing photons per unit mass, and thus higher EWs) does become more apparent as the birthrates increase, and the O & B stellar populations become more dominant. The maximum difference, which occurs between $Z_{\odot}/50$ and Z_{\odot} for the highest birthrate models calculated ($b = 10$), is $\sim 50\%$. Nevertheless, variations in metallicity will not considerably impact the mapping between the EW and birthrate for our sample, especially since the vast majority of galaxies have EWs and metallicities in the range where the models tracks are

virtually identical.

6.3 Birthrates of Dwarf Galaxies in the 11HUGS Sample

It is now straightforward to find the typical birthrate of the dwarf galaxies in the 11HUGS sample by using our model grid and the observed 11HUGS $H\alpha$ EWs. However, note that the assumed IMF will have a critical effect on the predictions. In the lower panel of Figure 6.1, comparison of the models based on three currently viable IMFs, that of Kennicutt, Salpeter, and Chabrier, demonstrates that the EW is systematically offset by more than 50% from the model with the steepest fall-off for high mass stars ($\Gamma = -1.5$, Kennicutt) to the one with the flattest power-law slope ($\Gamma = -1.3$, Chabrier). Translating the 11HUGS EW distribution for galaxies with $-17 \leq M_B < -14.7$ to birthrates, we find that $\langle \log b \rangle$ is 0.55, 0.32 and 0.27, for the Kennicutt, Salpeter, and Chabrier IMFs respectively, which correspond to SFHs with decay timescales between 4 and 8 Gyrs. This confirms the estimates based on the KTC model grid which show that late-type dwarf galaxies are typically forming stars at a pace that is slower by $\gtrsim 50\%$ than their lifetime averaged rates.

6.4 The Viability of Continuous SFR Models

So far, we have used the synthesis models with the observed $H\alpha$ EWs to coarsely constrain the SFHs. In this calculation the SFR was measured (i.e. averaged) over the following two different timescales. Recall that hydrogen photoionization is due to massive O & B stars which are short-lived, so that thermal Balmer emission can only be observed if star formation has occurred over the past 10^7 yrs. Thus the numerator of the EW yields an essentially instantaneous measure of the SFR, and this was compared to the long-term, lifetime average SFR implied by the

red continuum flux density in the denominator. These two extremely long and extremely short timescale tracers provide insufficient constraints for constraining fluctuations that have occurred in the recent past. A third tracer is required that measures the SFR more nearly on the intermediate timescales that bursts are thought to occur. The UBV colors provide such a measure since they are dominated by intermediate mass A stars if they are present, and thus trace star formation that is averaged over a ~ 1 Gyr interval. This is the rationale for incorporating UBV colors in our analysis. The colors that we use are adopted from the dwarf galaxy studies of van Zee (2001) and Hunter & Elmegreen (2006).

With the combination of $H\alpha$ EWs and UBV colors, we first ask whether bursts are even necessary to explain the observed present-day properties of the *average, relatively quiescent* star-forming dwarf galaxy, since it is possible that the continuous models alone may be able to account for them. While bursting galaxies are undeniably found in our sample, it is not clear whether they are simply dIrrs in the “on” state, or whether they form an inherently different population that follows an evolutionary path distinct from the majority of dIrrs (e.g. Papaderos et al. 1996a,b; van Zee et al. 1998; van Zee 2001). If the latter scenario is true, then duty cycles should only be calculated for the subset of the population that suffer bursts, and a method for distinguishing those galaxies from the rest of the population would need to be developed. However, if continuous star formation models can be reasonably ruled out by the observed properties of typical dIrrs, *and* cyclical burst models can provide a more natural fit, this would be one argument against the burst/non-burst bimodality.

We assess the viability of continuous SFHs in Figure 6.2, where 10 Gyr-old τ models are plotted in the EW-color plane, along with data for galaxies in 11HUGS which have colors published in van Zee (2001) and Hunter & Elmegreen (2006).

In the plot, each curve represents a different metallicity family of exponential declining SFR models based on a Salpeter IMF. The blue and red curves indicate the most metal poor ($Z_{\odot}/200$) and metal rich ($2.5 Z_{\odot}$) models respectively, whereas the models highlighted in light blue ($Z_{\odot}/5$) represent those which best match the observed gas metallicities of the dwarfs considered here. The models with the shortest timescales ($\tau=1$ Gyr) have the reddest UBV colors, since they have formed most of their stars early-on, and occupy the lower right corner of the plot. Moving up the tracks, the models become bluer and the EWs increase as the decay timescale lengthens. The bluest UBV colors and highest EWs result from models with a constant SFR (i.e. $\tau = \infty$).

Clearly, the continuous models do not provide a good match to the observations. The models are too blue at a given EW to fit the majority of data, or conversely, the synthesized EWs are too low at a given color. However, the discrepancy is characterized by factor of two offsets, which is not extreme enough to definitively rule out continuous models, in and of itself — it is conceivable that systematics in the data or the models may produce such an offset. Therefore, we carefully evaluate the robustness of our data and the assumptions inherent in the calculations of the models that may have led to this discrepancy before drawing conclusions on the viability of the continuous models.

6.4.1 Checks for Possible Systematics in the 11HUGS EWs

Assuming first that there are no problems with the synthesis models, one issue that we must address is whether there could be an error in our measurements of the EW that would cause them to be systematically underestimated. The typical colors of the galaxies in Figure 6.2 are ~ 0.4 in $B-V$ and -0.2 in $U-B$ (as found in the van Zee 2000 study of isolated dwarf irregulars, and other previous dwarf observations such as that of Miller & Hodge 1994). From the grid of KTC94, these

colors correspond to an EW of 46 Å for a Kennicutt IMF, while from the grid computed here it would be 58 Å and 70 Å for the Salpeter and Chabrier IMFs respectively. Therefore, in order for a systematic offset to be the explanation, the EWs must be low by $\sim 50\%$ at the minimum. In Chapter 2, we already have checked our EWs against the integrated spectral measurements of MK06 and have found evidence that our image-based EWs may be underestimated. However, the size of the potential discrepancy was found to only be 7%, and moreover, it is not clear whether this is due to issues with the MK06 or 11HUGS continuum subtraction procedure. We have also checked if the systematic is larger for low-luminosity galaxies, and find that there is no apparent correlation with M_B . As for comparisons with other global EWs found elsewhere in the literature, James et al. (2004) do report a median observed EW which is $\sim 20\%$ higher (38 Å) for their nearby UGC irregular galaxies. However, James et al. also have noted that their measurements are on average $\sim 30\%$ higher than other previously reported values, whereas our EWs exhibit no such offset. Therefore, it is highly unlikely that a systematic error in the measurements alone could explain the inconsistency between the continuous models and the observations, although there may be some possibility that our data may be underestimated by up to 20%.

6.4.1.1 An Alternate Estimate of the Birthrate

Another way of looking at the discrepancy is that the UBV colors indicate that star-forming dwarfs should have typical birthrates of about unity, while the $H\alpha$ EWs suggests that the SFR of the population has slowed by a factor of two over time. Thus, we can further investigate possible systematics in the 11HUGS EWs by performing an alternate calculation of the birthrate which is based on the same model grid, but depends on observables other than the EW. If the low birthrates still persist, then this is indirect evidence that there is no severe systematic in the

11HUGS EW measurements. On the other hand, if the calculation produces a result which is more consistent with unity, we would need to critically reassess the 11HUGS EW scale.

To carry out this exercise, we use the fact that the stellar birthrate can also be expressed as:

$$b \equiv \frac{\text{SFR}(t) \cdot t}{M_*(t) \cdot (1 - R(t))}, \quad (6.4)$$

where M_* is the stellar mass, and R is the fraction of M_* that has been returned to the ISM through evolutionary processes. $L_{H\alpha}$ and M_B can be used to compute the SFR and the stellar mass by using the synthesis models to find the most appropriate, average conversion factors, i.e. $L_{H\alpha}/\text{SFR}$ and the mass-to-light ratio M_*/L_B . The value for R is also taken from the models. Thus, this is the same general method implicit in the conversion from EW to b , except that the continuum flux density at $H\alpha$ is replaced by M_B , and that the M_*/L_B must now be specified. We will choose a M_*/L_B which matches the blue colors observed, which is again $B - V \sim 0.4$. Thus, while this exercise is somewhat less sensitive to the systematics that could plague the EWs (e.g. the continuum subtraction procedure, which is the most uncertain step in the determination of image-based EWs), in truth, it is not completely independent of them since we are using the $H\alpha$ fluxes in the calculation. However, an advantage is that many more measurements of the $H\alpha$ flux have been made for dwarf galaxies than of the global EW in previous work, so there is a better basis for determining whether any potential inconsistencies are due to systematics in the 11HUGS data.

To apply this method to our sample, both $L_{H\alpha}$ (Table 2.4) and M_B (Table 2.1) are first corrected for internal extinction using the estimates computed in Appendix B and assuming that $E(B - V)_{\text{star}} = 0.44E(B - V)_{\text{gas}}$ (Calzetti 2001). We

then use the $Z = 0.004$ ($Z_{\odot}/5$) population models to find $L_{H\alpha}/\text{SFR}$ (Table 6.3) and M_*/L_B (Table 6.4), and calculate M_* and the SFR. We choose the $Z_{\odot}/5$ model since it is the best match for the metallicities of dIrrs in luminosity bin where the 11HUGS burst statistics are most robustly determined (i.e. $-17 \leq M_B \leq -14.7$). The recycled mass fractions are ~ 0.3 and ~ 0.5 for the Salpeter and Chabrier IMFs, which result in median birthrates of 0.42 and 0.34, respectively. Although we have not generated the appropriate metallicity models using a Kennicutt IMF, we have shown that the dependence on metallicity is limited, so the solar metallicity grid from KTC94 can be used to approximate the median b , which turns out to be 0.51.

Thus, these alternate calculations result in birthrates which agree with those based on the EWs, and reaffirm the discrepancy with the birthrates of ~ 1 predicted by the colors. Comparisons with other datasets in the literature (Chapter 2), have already shown that the 11HUGS $H\alpha$ fluxes are not offset on average from previous measurements, so it is unlikely that these low birthrates are due systematic errors in the data. However, van Zee (2001) has carried out the same birthrate calculation for a local sample of isolated dIrrs and has found that the median value, assuming a Salpeter IMF, is $0.7^{+0.5}_{-0.2}$. This result suggests that the continuous models alone are in fact consistent with observations of the SFR as traced by $H\alpha$ and the $B-V$ color, and is troubling as it could be an indication of a systematic error in the 11HUGS measurements. What could be going on?

The alternate birthrate calculation that we have just performed relies on $L_{H\alpha}$ and M_B , so we first compare the 11HUGS values for these quantities with those from van Zee (2001) as well as with additional measurements from Hunter & Elmegreen (2004, 2006). We homogenize the extinction corrections and distance scales of the datasets to follow van Zee (Galactic, but no internal extinction cor-

rections applied, $H_o=75 \text{ km s}^{-1} \text{ Mpc}^{-1}$) and plot the data in Figure 6.3.

In Figure 6.3, all three datasets sit on the same locus without any significant offsets, as illustrated by the linear fits to each of the datasets in the region that is commonly well-sampled ($-18 \lesssim M_B \lesssim -14$). There is a strong correlation between $L_{H\alpha}$ and M_B as would be expected for a sample of star-forming galaxies. We plot lines which correspond to van Zee’s result of $b = 0.7$ in the low-luminosity regime of interest, again using the $Z = 0.004$ ($Z_\odot/5$) Chabrier, Salpeter and Kennicutt IMF models computed earlier (red dashed lines from top to bottom). The tracks have been back-corrected for internal extinction using the same empirical correlation (Appendix B) used throughout this work. The red solid line corresponds to the median birthrates of 0.34 (Chabrier), 0.42 (Salpeter) and 0.51 (Kennicutt) as found for the 11HUGS dwarfs. It is clear that the $b = 0.7$ lines are significantly offset from all three datasets, and a median b of ~ 0.5 or lower is more consistent with all of the observations. This is strong evidence that the low median birthrates calculated based on the 11HUGS fluxes cannot be merely due to an offset in the data. The plot also indicates that the discrepancy is not likely caused by sample selection biases. Instead we suspect that the van Zee result may have been systematically overestimated. The values of M_*/L_B and $L_{H\alpha}/\text{SFR}$ that she used were based on models with two different metallicities. van Zee adopted the Kennicutt (1998) standard $H\alpha$ SFR conversion, which is for solar metallicity populations, while using mass-to-light ratios that are based on sub-solar models. This can lead to birthrates that are too high: a relative deficiency of metals will cause both lower mass-to-light ratios and a greater number of ionizing photons per unit mass to be produced, so that a systematic error will be incurred if only one of the effects is accounted for. From Table 6.3, it can be seen that the ratio between the Z_\odot and $Z_\odot/5$ SFR conversions is about 0.7. This would bring down the

van Zee birthrate from 0.7 to ~ 0.5 , which is more in-line with the results found here.

In sum, there is good evidence that the discrepancy between the predictions of the continuous models and the UBV and $H\alpha$ EW observations cannot be reconciled by a systematic in the 11HUGS measurements. Again, our EWs may be underestimated by up to 20%, if the EW scale of James et al. (2004) is correct, but more likely, the size of the potential offset is 7%. For a Salpeter IMF, the IMF assumed by most previous studies, these possible errors can inflate the birthrate to 0.4 at most. Next we consider whether assumptions in the models may have led to the discrepancy.

6.4.2 Possible Escape of Ionizing Photons into the IGM?

In calculating the $H\alpha$ luminosity from the ionizing flux produced by the models, we have simply assumed that galaxies are radiation bounded. If in reality there is leakage of the Lyman continuum photons into the IGM, and this is accounted for in the modeling, the synthesized $H\alpha$ fluxes and EW would decrease, while the UBV colors would change nominally, as needed for consistency with the observations. In order for leakage to completely solve the problem, the escape fraction for the average dIrr galaxy would have to be $\sim 50\%$ for a Kennicutt IMF to lower the predicted EWs to the observed typical value of 30 \AA while the majority of ionizing photons would have to be lost for the Salpeter and Chabrier IMF models. However, observations which have attempted to directly detect escaping Lyman continuum photons have all found upper-limits $< 10\%$ (e.g. Leitherer et al. 1995, Bergvall et al. 2005). Moreover, these detection experiments have been performed on starbursting galaxies where leakage is thought to most likely to occur, and the fractions in more typical dwarfs are probably a few percent at the most. A combination of a systematic underestimation of the 11HUGS EWs and an non-zero

escape fraction cannot plausibly bring the models and data into agreement either. Even if we suppose that the 11HUGS fluxes and EWs are underestimated by 20%, the escape fractions required are still $\gtrsim 30\%$. It thus seems unlikely that leakage can be the cause for the disagreement between the continuous models and the observations.

6.4.3 Lower Maximal Stellar Masses in the IMF?

Naturally, the b -EW mapping is very sensitive to the form of the adopted IMF. We have tested the consequences of using three different, but currently accepted, universal IMFs in the above analysis. None result in $B - V \sim 0.4$, $U - B \sim -0.2$ and $\text{EW} \sim 30 \text{ \AA}$ as observed. However, we have always made the standard assumption that the lower and upper mass limits are 0.1 and $100 M_{\odot}$ respectively. Lowering the maximal stellar mass included in the models would decrease the predicted EWs while not significantly altering the colors. For a Salpeter IMF, the predicted EW is 60 \AA for $M_{up}=100 M_{\odot}$, whereas it is $38, 34, 30$ and 24 \AA when M_{up} is $60, 55, 50$ and $45 M_{\odot}$ respectively. Thus, decreasing the upper mass limit to $\sim 50 M_{\odot}$ would reconcile the models and the data. But what would be the physical motivation for such a variation?

Recent work has debated whether, given an intrinsically invariant stellar IMF, the resultant IMF will depend on the SFR of a galaxy due to a combination of statistical effects and clustered star formation. As already discussed in Chapter 4, the sense of the effect would be such that galaxies with the lowest SFRs would be systematically deficient in the most massive stars and have observed IMFs with either lower maximal stellar masses or steeper slopes. The suggestion has been made primarily by Kroupa & Weidner (2003) and Weidner & Kroupa (2005, 2006), whose general argument is as follows. If stars are born primarily in clusters (whose formation itself is governed by some power law), the maximal stellar

mass formed in a cluster will necessarily scale with the cluster mass. Consequently, they contend that the summed stellar IMF will be deficient in high mass stars for those systems that form fewer clusters, since the probability of forming a massive cluster will be lower. In Weidner & Kroupa (2005), the upper stellar mass limit of the IMF as a function of the SFR (averaged over 10^7 yrs) is calculated under various assumptions of the power law slopes of the cluster and stellar IMFs. With the standard slope of 2.35 for both mass functions, they find that M_{up} begins to dip below $100 M_{\odot}$ at $\sim 0.03 M_{\odot} \text{ yr}^{-1}$ and reaches $50 M_{\odot}$ at $\sim 0.005 M_{\odot} \text{ yr}^{-1}$. They also explored the scenario which has the maximum plausible effect on the summed IMF, and in this case the limiting SFRs are instead greater by about an order of magnitude. Examination of Figure 6.3 shows that the corresponding approximate luminosity ranges over which M_{up} would vary between $100 M_{\odot}$ and $50 M_{\odot}$ are $-16 \gtrsim M_B \gtrsim -14$ for the standard scenario and $-18 \gtrsim M_B \gtrsim -16$ for the scenario with the maximum plausible effect. Although this is same luminosity regime in which we are attempting to reconcile the models with the observations, M_{up} must be on average $50 M_{\odot}$ to make an EW of 30\AA consistent with the blue colors observed whereas Weidner & Kroupa predict that M_{up} will only drop to this level for the lowest luminosity dwarfs. Therefore, a variable resultant IMF may possibly allow continuous models to fit the colors and EWs of the least luminous dwarfs simultaneously, but it does not appear that this would allow the continuous models viable for the intermediate luminosity systems.

We must also further note that the conclusions of Weidner & Kroupa are still being heavily debated. Systematic variations in the resultant IMF are strongly dependent on the form of the assumed cluster mass function, as they themselves note, and as discussed in detail in Elmegreen (2006). In particular, the differences in the intrinsic and resultant IMF are negligible if the cluster mass function slope

$\beta \lesssim 2$, and many studies appear to show that $\beta \sim 2$ (Zhang & Fall 1999), although these prior results have primarily been based on galaxies with much higher SFRs than the dwarfs we are interested in here. As for observations which constrain the stellar IMF itself in dwarf galaxies, there is tentative evidence that it may be steeper than Salpeter in some dwarfs (Annibali et al. 2003), although many other studies have shown a slope consistent with 2.35 (Greggio et al. 1993). These observations are reviewed in Elmegreen (2006) and the reader is referred there for more details.

6.4.4 Summary Assessment of the Discrepancy between Predictions of Continuous Models and Observations

To summarize, we have found that models characterized by continuous star formation cannot simultaneously match the blue colors and modest $H\alpha$ EWs of typical dIrr galaxies unless (i) the majority of Lyman continuum photons escape from the galaxy, or (ii) the currently favored IMFs have upper mass limits of about $50 M_{\odot}$ instead of the commonly adopted value of $100 M_{\odot}$. The first scenario seems unlikely to be plausible since observations indicate that the escape fraction of ionizing photons is $< 10\%$ (e.g. Bergvall et al. 2005). While the latter scenario might work for the lowest-SFR dwarf galaxies we are considering here, the plausibility of statistical effects leading to resultant IMFs that are different from an intrinsic, invariant IMF is still being heavily debated (e.g. Weidner & Kroupa 2005; Elmegreen 2006). Further, the potential statistical effects appear to be too small for the more luminous dwarfs ($M_B \lesssim -14$, $SFR \gtrsim 0.005 M_{\odot} \text{ yr}^{-1}$) to make the continuous models consistent with the observations for these systems. Therefore, it presently seems doubtful that continuous SFHs alone can account for the average properties of star-forming dwarf galaxies.

6.5 The Viability of Cyclical Burst Models

We now proceed to investigating whether burst models can provide a more natural match the data (i.e. *without* invoking variations in the IMF or large Lyman continuum photon escape fractions). The addition of bursts may result in models that better fit the data because they will cause the colors to be bluer than expected for a given EW, as predicted by continuous models alone. Bursts, of course, will also cause the $H\alpha$ EW to be elevated, but the EW will decay essentially instantaneously in its aftermath, whereas the colors will remain bluer than normal for a longer period of time. Moreover, in the post-burst state the $H\alpha$ EW will be lower than expected since the intermediate mass stars from the burst will continue to contribute to the continuum flux long after the $H\alpha$ emission from the burst has faded away.

To investigate whether bursts can account for the observations, we have generated a grid of 54 Salpeter IMF, $Z_{\odot}/5$ models which include (i) three different underlying populations characterized by decay timescales of $\tau=4$ Gyr, $\tau=8$ Gyr, and $SFR=\text{constant}$, chosen because they produce present-day EWs which flank the typical observed value of 30\AA , (ii) burst amplitudes from $b=2$ to $b=10$, and (iii) burst durations of 10 and 100 Myrs. The bursts are added at an age of 10 Gyrs, and we have only considered the simplest case where the bursts turn on and shut off instantaneously.

The effects of adding bursts to continuous models are illustrated in Figure 6.4 in the EW-color plane. In the top panel, the loci of the continuous models are repeated from the Figure 6.2, and eight selected burst models are overplotted. The yellow and black loops represent the 10^7 and 10^8 yr duration episodes respectively. As the burst evolves, the colors and EWs move around the loops in the counter-clockwise direction. The height of the loop is controlled by the am-

plitude of the burst and the SFH of the underlying population, while the width is controlled by the both burst duration and amplitude. The three innermost yellow loops are $b=2$, $b=5$ and $b=10$ bursts superimposed on a constant SFR model, while the two outermost loops represent $b=10$ bursts superimposed on $\tau=8$ Gyr and $\tau=4$ Gyr models. Qualitatively, this ensemble of models overlaps the data well. The blue galaxies with low EWs in the lower left of the diagrams do not seem to be fit by any of the models and merit further study. However, galaxies do not move along the loops at a constant rate, and we must also determine whether the distribution of data is consistent with the frequencies implied by the temporal evolution of the synthetic EWs and colors in order to establish the viability of the burst models.

To illustrate these post-burst timescale dependent effects, we plot the colors, EWs and birthrate as a function of time in Figure 6.5. Here, the $b=10$ models are shown, where the 10^7 and 10^8 yr duration bursts are plotted separately in the left and right hand panels. For reference, the evolution of the models which have not been through a burst are also plotted (dotted lines). A successful match to the observations (indicated by the gray shaded area) would require post-burst EWs which vary about an average value of 30\AA , $U-B$'s of ~ -0.2 and $B-V$'s of ~ 0.4 . For the $H\alpha$ EW, the shaded area corresponds to the $\pm 1\sigma$ range as determined from the 11HUGS sample. The gray areas in the $U-B$ and $B-V$ plots are based on the median, and upper and lower quartile values from van Zee (2000). From both this plot and Figure 6.4, it is clear that the shorter 10^7 yr bursts ($\lesssim 1\%$ of the galaxy's stellar mass formed in the episode) cannot reproduce the observations. However, the more substantial $b \sim 10$, 10^8 yr episodes ($\sim 10\%$ of the galaxy's stellar mass formed in the episode), superimposed on exponential decay models with $\tau \sim 8$ Gyr, do appear to have post-burst properties that match the typical $B-V$ colors

and EWs of star-forming dwarfs. The $U-B$ colors, on the other hand, cannot be fit unless the galaxies are perpetually bursting, which is simply impossible, and we will comment more on this problem in a moment.

We also illustrate the varying amounts of time spent along different sections of the looped tracks in the EW-color plane in Figure 6.6. In this figure, we now only show the 10^8 yr duration burst models and use the blue, yellow and pink curves to indicate periods of 10^8 yrs (i.e. altogether the first 3×10^8 yrs after the burst is initiated), and the red curve to indicate a 7×10^8 yr period, from 3×10^8 yrs to 1 Gyr after the burst. Thus, there should be a higher concentration of data points along the red portions of the tracks if the burst models are to be viable. Qualitatively (since we are limited in making more quantitative statements because the UBV data for the 11HUGS sample are not complete), this does appear to be true in the $EW-B-V$ plane. In the $EW-U-B$ plane, however, the data tend to sit on the pink/yellow portions of the tracks, and are too blue by ~ 0.1 mag to be consistent with the dominant post-burst state. This would seem to rule out the viability of the burst model since all of the observations that we have in hand cannot be matched simultaneously. Let us reserve judgment for the time being though, and investigate this further in the UBV plane, where more data is available.

In the UBV plane, we first plot the evolutionary tracks of the continuous models (Figure 6.7, top panel). As in the previous figures, the red and blue curves represent the $2.5 Z_{\odot}$ and $Z_{\odot}/200$ populations respectively, and the light blue curves show the models $Z_{\odot}/5$ which best match the metallicities of the dIrrs considered here. There is a clear problem with the synthesized $U-B$ colors since, quite oddly, the lower metallicity tracks tend to be systematically too red in comparison with the data, whereas the higher metallicity tracks actually provide a better match. We also plot the burst models in the UBV plane in Figure 6.8 to further illustrate

this point. The top panel shows the 10^8 yr duration, $b \sim 10$ bursts for the $2.5 Z_{\odot}$ tracks, while the bottom panel shows those for the $Z_{\odot}/5$ tracks. Again, the tracks have been color-coded to indicate increments of 10^8 yr of time (blue, yellow and pink) and 7×10^8 yrs (red). The data points do not converge upon the red portions of the tracks in either case because the synthesized $U - B$ colors are too red on average, although the super solar metallicity models at least bisect the observations. van Zee (2001) has also documented this problem, using continuous models generated with an earlier version of the BC03 code, which she attributed to problems with the evolutionary prescriptions for low-metallicity massive stars. Although we have not yet tracked down the exact source of the problem, it is reasonable to assume that uncertainties in the models will affect the predicted U -band flux to a much greater degree than the other observables that we are considering. The synthesized $B - V$ color and $H\alpha$ EW should be relatively robust since they are essentially dictated by stellar evolution along the main sequence, which is thought to be better understood. For example, it has recently become clear that the predictions for the temperatures and lifetimes of red supergiants at sub-solar metallicities do not match the observations (Origlia et al. 1999, Massey & Olsen 2003, Vazquez & Leitherer 2005). Despite this, Origlia et al. (1999) found that the $B - V$ colors of young LMC clusters and blue compact dwarf (starburst) galaxies could be modeled accurately. It is also relevant to note that the same study also found that the $U - B$ colors become bluer when the temperatures of the red supergiants are lowered, which is more consistent with spectral observations of these stars in the Magellanic Clouds (Massey & Olsen 2003), and would help reconcile the discrepancy in Figure 6.4. Another issue deals with nebular continuum emission, which we have not included in our models. The addition of nebular emission will make $U - B$ color bluer, but will nominally affect the $B - V$ colors and $H\alpha$ EWs

for composite population older than 1 Gyr (Leitherer & Heckman 1995). Clearly, the models must be scrutinized carefully to conclusively isolate the cause(s) of the discrepant U -band fluxes, and more work is needed here. Until then, we will choose to exclude the $U - B$ colors from the analysis and draw our conclusions using the $B-V$ colors and $H\alpha$ EW only.

6.5.1 Implied Duty Cycle Parameters

With this in mind, we return now to Figures 6.4 and 6.5, and only focus on the $B - V$ colors and $H\alpha$ EWs. Again, there is reasonable agreement between the post-burst properties of the models with 10^8 yr duration, $b \sim 10$ episodes that are superimposed on 10 Gyr old, $Z_{\odot}/5$ populations with exponentially declining SFR described by decay timescales of ~ 8 Gyr. Note however that the EWs and $B-V$ color return to the values given by the continuous models after about 1 Gyr following the burst. In order to keep the predictions within the window of observed values, these bursts must occur at least every Gyr.

Thus, the need to simultaneously match the typical $B - V$ colors and EWs yields constraints on the characteristic duty cycle for which we have just found one particular solution: that bursts on average occur every ~ 1 Gyr, with durations of $\sim 10^8$ yrs and amplitudes $b \sim 10$. Of course, the uniqueness of this solution has not yet been examined. To do this, we turn to the constraints provided by the burst number and mass fractions calculated in the previous chapter.

6.5.2 Additional Duty Cycle Parameters Constraints under the Equal Probability Assumptions

In the preceding chapter, we used the 11HUGS sample to determine both the fraction of late-type dwarf galaxies that are presently in the starburst phase, and the fraction of the overall current star formation that occurs in this subset of the

population. By making a number of simplifying assumptions, we can use these statistics to provide additional constraints on the characteristic frequencies and amplitudes of the average starburst duty cycle.

Let us first suppose that bursts can occur with equal probability in any dIrr, and that all dIrrs share a common average SFH. If this is approximately true, then the starburst number fraction corresponds to the fraction of total time an individual system spends in the burst mode, while the fraction of star formation observed to be taking place in the starburst population corresponds to the fraction of the total stellar mass formed in the burst mode. Let us also assume that these statistics have remained the same over the lifetimes of the galaxies, which is taken to be 10 Gyrs for simplicity.

Under these “equal probability” assumptions the durations of all burst episodes must sum to $6 \pm 3 \times 10^8$ yrs (i.e. 6% of 10 Gyrs). The synthesis models have shown that one duty cycle solution that maintains the $B - V$ colors and $H\alpha$ EWs at post-burst levels which are comparable to the typical observed values involves bursts with durations of 10^8 yrs which repeat at least every Gyr. The sum of the durations in this case would be about 1 Gyr, which agrees with the constraints implied by the burst number fraction. This consistency suggests that the temporal parameters are fairly well constrained. We have shown that bursts with short 10^7 yr durations and reasonable amplitudes do not produce post-burst effects significant enough to match the observations. Also, it is unlikely that a massive galaxy-wide burst can be coordinated on timescales much less than a dynamical time, which is $\sim 10^8$ yrs for dwarf galaxies. On the other hand, increasing the duration by a factor of two would require that the time between bursts also increases by a factor of 2 to keep consistency with the observed burst number fraction. However bursts that occur every ~ 2 Gyr are already too infrequent to keep the colors sufficiently

blue.

Turning now to issues of amplitude, in our one duty cycle solution, $\sim 50\%$ of the stars are formed in the burst mode. This is just nominally consistent with the observation that $22 \pm 10\%$ of the current star formation in dIrrs is concentrated in the starbursting systems. Although the amplitude of the bursts could be lowered to $b \sim 4$ to match this constraint, this would violate the $6 \pm 3\%$ starburst number fraction — the galaxies would have to burst at least twice as frequently to maintain the needed blue $B - V$ colors and consequently spend 20% of their time in the burst state. At this point, it may appear that a simple fix would be to halve the burst duration to 50 Myr for the $b \sim 4$ bursts. However, this would require that the episodes repeat even more frequently at 4 times per Gyr, which leads to the same disagreement with the number fraction. Finally, further fine tuning of the amplitude shows that models with slightly stronger $b \sim 6$ bursts and 50 Myr durations occurring 3 times per Gyr also achieve nominal consistency with both burst mass and number fractions, as a system with such a cycle will spend 15% of its time and form $\sim 50\%$ of its stars in the burst mode. Figure 6.9 illustrates the color and EW time evolution of these 50 Myr bursts. Thus, this exercise has yielded the approximate ranges of typical burst parameters: durations between 50 and 100 Myrs, birthrates between 6 and 10, and frequencies between 1 to 3 per Gyr.

The characteristic duty cycle parameters that we have converged upon appear to be viable but only in a delicate, or almost too delicate, balance with the observed constraints provided by the $B - V$ colors, the $H\alpha$ EWs, and the starburst number and mass fractions. This suggests that either (i) the problem is extremely well constrained, (ii) the model we have developed to explain the observations is far too contrived, or (iii) something is wrong with one of the pieces in this puz-

zle. As for this last possibility, we can think of at least two explanations for the tension between the model duty cycle parameters and observed starburst statistics. The first is mundane and involves our empirical extinction correction which scales as only as a function of luminosity. Since starbursts tend to be more heavily obscured, it may be that we have underestimated the $H\alpha$ luminosity being produced by these systems relative to the currently less active dIrrs. This may increase the starburst star formation fraction above the value that we have calculated and this needs to be followed-up, perhaps by examining the Balmer decrement as a function of EW for a large sample of starbursting dwarfs. The second explanation is that the "equal probability" assumption that the bursts number and mass fractions have remained constant over the lifetimes of the galaxies is incorrect. The direction of the tension is that viable burst models result in combinations of frequency and burst mass fractions that are although *nominally* consistent, are too large to be *comfortably* consistent with the present day observations. This could be a potential clue that bursts in dwarf galaxies occurred at a different pace in the past. In particular, we note that if dwarf galaxies have only been undergoing bursts in the most recent half of their lifetimes, the disagreement with the burst mass fraction would be resolved. Clearly however, this would require a mechanism to suppress the burst cycles in the early half of lifetimes, which seems a bit artificial. In any case, this characteristic starburst scenario should be easy to disprove if it is indeed tenuous. Additional tests, such as an examination of the distribution of a complete set of $B - V$ colors and an expansion of the $H\alpha$ -based analyses to larger volumes, provide avenues for future work. Clearly, our observational constraints do not really allow us to probe the SFHs farther back than about 1 Gyr ago, so eventually repeating the analyses carried out here with samples of dwarf galaxies at higher redshift would also be valuable. Finally, as

discussed earlier, the predicted EWs are quite sensitive to the assumed IMF. Since we have only performed the burst analyses using a Salpeter IMF, more work is needed to quantify the uncertainties in the duty cycle constraints due to reasonable variations in the high mass slope.

6.6 Discussion

6.6.1 Comparison with Previous Results on the SFHs of Dwarfs

As mentioned in the introductory chapter, there has been a great deal of work on the evolutionary histories of dIrr galaxies over the past three decades. Most studies, including the seminal work of Searle, Sargent & Bagnuolo (1973) and Hunter, Gallagher & Rautenkranz (1982), have included some combination of synthesis modeling, integrated UBV colors, and the $H\alpha$ SFRs of representative samples of dwarfs. This thesis can be considered the direct descendant of such studies, so we begin our comparison with previous results there.

The general consensus among this aggregate of work has been that most late-type dwarf galaxies have had approximately constant SFRs over their lifetimes (e.g. Searle, Sargent & Bagnuolo 1973; Hunter & Gallagher 1985; Huchra 1977b). Some have further concluded that global starbursts are probably not needed to account for the observed properties of typical systems (e.g. Gallagher, Hunter & Tutukov 1984; van Zee 2001). While this appears to directly contradict the findings presented here, we have found that the results can be reconciled as follows.

The UBV colors by themselves do suggest that $b \sim 1$ as discussed in Section 6.4.1.1, so it would be reasonable for analyses which only have included UBV photometry to come to this conclusion (e.g. SSB73). However, $H\alpha$ -based SFRs have also been considered in tandem with the colors in many other prior studies. In these cases, we have found that accounting for differences in the syn-

thesis modeling can explain the conflicting results. One difference is that most early models were based on solar metallicity stellar tracks, which were all that were available at the time, whereas we have interpreted our data using sub-solar metallicity tracks. For the estimation of *relative* SFR properties such as the birthrate, this should not matter, since the effect of metallicity will be roughly normalized out as demonstrated by our modeling of the EW. However, a systematic overestimation of such quantities can occur if standard solar-metallicity based SFR prescriptions are used in conjunction with other outputs from sub-solar models as in van Zee (2001). Another significant difference is that the earliest generation of models employed IMF upper mass limits which were much lower (30–50 M_{\odot}) compared with the standard 100 M_{\odot} adopted today (Searle, Sargent & Bagnuolo 1973; Huchra 1977b; Larson & Tinsley 1978; Hunter, Gallagher & Rautenkranz 1982), again because evolutionary tracks for higher stellar masses had not yet been developed. IMF upper-mass limits in this regime certainly would allow continuous star formation models to match the observations as discussed in Section 6.4.3. We note that it is an interesting irony that Huchra (1977b) was led to argue for a flatter IMF and test models with higher upper-mass limits (i.e. $M_{up} > 30 M_{\odot}$) in order to match the $H\beta$ EWs and colors of the exceptionally active Markarian galaxies, while we have been forced to argue for either a steeper IMF or lower upper-mass limits (i.e. $M_{up} < 100 M_{\odot}$) to match the observations for a more representative, and complete, sample of star-forming dwarfs. This clearly underscores the sensitivity of results about the viability of continuous SFR models which incorporate high-mass SFR tracers such as Balmer-line emission on the form of the IMF. Nevertheless, it is quite remarkable that the first back-of-the-envelope duty cycle calculations from the UBV color analysis of SSB73 had resulted in burst parameters similar to those we have found here.

Critically analyzing the consistency between our inferred duty cycle and the SFHs computed from resolved stellar populations will require more careful work. As discussed in the introduction, such studies have generally found that most dIrrs have had only modest, factor of 2-3 fluctuations in their SFRs over their lifetimes, whereas the starbursts in our best-fit model must have birthrates between 5 and 10. The temporal resolution of the CMD-based SFHs, however, only allows for the identification of a ~ 100 Myr episode over the past ~ 0.5 Gyrs. Thus, given a sample of N galaxies we would expect to see $\sim N/2 \pm (N/2)^{1/2}$ bursts. From the preliminary work of Dolphin et al. (2006) on the SFHs of galaxies in the Local Group, a cursory check shows that only 2 out of 18 dIrr galaxies have recent bursts with the high amplitudes suggested by our burst cycle solution, and this presents a serious discrepancy that must be resolved. In particular, a detailed comparison between the results will involve ensuring that (i) the time averaging of the SFHs are done in a consistent way, (ii) there are no significant differences in the stellar evolutionary models used, and (iii) that SFRs based on the counting of individual stars are consistent with the SFRs based on the integrated $H\alpha$ fluxes. Fortunately, these issues can be taken up in the near future in collaboration with a group led by Evan Skillman which has recently obtained new deep HST-ACS data which resolves the stellar populations of the M81 dwarfs.

Table 6.1: Synthetic $H\alpha$ EWs: Exponential Decay Models

SALPETER IMF									
SFH	b	EW(emission); EW(absorption)							
		Z=0.0004		Z=0.004		Z=0.008		Z=0.02	
$\tau = 1$	4.5e-04	1.3	-2.5	1.3	-2.1	1.4	-2.2	1.5	-2.0
$\tau = 2$	3.4e-02	5.6	-2.6	5.7	-2.3	6.1	-2.4	6.0	-2.2
$\tau = 3$	0.12	15.1	-2.8	15.0	-2.5	15.8	-2.7	15.5	-2.5
$\tau = 4$	0.22	23.8	-2.9	23.2	-2.7	24.1	-2.8	23.6	-2.6
$\tau = 8$	0.50	42.5	-3.2	39.5	-2.9	40.5	-3.2	38.9	-2.9
$\tau = 12$	0.64	49.9	-3.3	45.6	-3.0	46.6	-3.3	44.5	-3.0
const. SFR	1.00	65.8	-3.4	58.2	-3.2	58.9	-3.5	55.5	-3.2
CHABRIER IMF									
SFH	b	EW(emission); EW(absorption)							
		Z=0.0004		Z=0.004		Z=0.008		Z=0.02	
$\tau = 1$	4.5e-04	1.4	-2.5	1.4	-2.1	1.5	-2.2	1.6	-2.1
$\tau = 2$	3.4e-02	7.0	-2.7	7.1	-2.3	7.4	-2.5	7.2	-2.2
$\tau = 3$	0.12	19.0	-2.9	18.6	-2.6	19.4	-2.7	18.8	-2.5
$\tau = 4$	0.22	29.8	-3.0	28.6	-2.7	29.5	-2.9	28.3	-2.7
$\tau = 8$	0.50	52.3	-3.2	47.9	-3.0	48.8	-3.2	46.2	-3.0
$\tau = 12$	0.64	61.0	-3.3	55.0	-3.1	55.9	-3.3	52.6	-3.1
const. SFR	1.00	79.5	-3.5	69.4	-3.2	69.9	-3.5	65.1	-3.2

Table 6.2: Synthetic $H\alpha$ EWs: Burst Models

SALPETER IMF												
b	const. SFR population @ 10^7 yr +			const. SFR population @ 10^7 yr +			const. SFR population @ 10^7 yr +			const. SFR population @ 10^7 yr +		
	const. SFR population @ 10 Gyr			$\tau=8$ Gyr population @ 10 Gyr			$\tau=8$ Gyr population @ 10 Gyr			$\tau=4$ Gyr population @ 10 Gyr		
	$Z=0.0004$	0.004	0.008	0.02	$Z=0.0004$	0.004	0.008	0.02	$Z=0.0004$	0.004	0.008	0.02
2	126	110	112	104	119	110	112	106	119	113	118	113
3	184	159	160	148	192	172	176	165	208	192	198	187
4	239	203	204	188	261	229	233	216	291	262	268	249
5	292	245	246	224	326	281	284	260	369	323	330	302
6	343	283	284	257	388	328	331	300	442	378	384	348
7	392	319	319	287	446	371	373	336	510	427	432	388
8	438	353	352	315	502	410	412	368	575	472	476	423
9	483	384	382	340	555	447	447	397	636	512	515	454
10	526	414	411	364	606	481	480	423	694	549	550	482

CHABRIER IMF												
b	const. SFR population @ 10^7 yr +			const. SFR population @ 10^7 yr +			const. SFR population @ 10^7 yr +			const. SFR population @ 10^7 yr +		
	const. SFR population @ 10 Gyr			$\tau=8$ Gyr population @ 10 Gyr			$\tau=8$ Gyr population @ 10 Gyr			$\tau=4$ Gyr population @ 10 Gyr		
	$Z=0.0004$	0.004	0.008	0.02	$Z=0.0004$	0.004	0.008	0.02	$Z=0.0004$	0.004	0.008	0.02
2	152	131	132	122	147	132	134	125	149	139	142	134
3	221	187	188	172	235	206	209	192	258	232	237	220
4	286	238	239	216	318	272	274	250	358	313	318	290
5	348	285	285	257	395	331	333	300	451	382	387	348
6	407	329	328	293	468	384	385	343	537	444	448	398
7	463	369	367	326	536	432	432	382	616	498	500	440
8	517	406	404	356	600	475	474	416	691	547	547	477
9	568	440	437	383	661	515	513	447	760	590	589	510
10	617	473	468	408	719	551	548	474	825	629	626	538

Table 6.3: SFR Conversion Factors

Z	$L(H\alpha)/\text{SFR} \quad [(\text{M}_\odot \text{yr}^{-1})/(10^{41} \text{ergs s}^{-1})]$		
	Kennicutt (1993)	Salpeter (1955)	Chabrier (2003)
0.05	—	11.37	6.83
0.02	7.35 ¹	8.22	4.90
0.008	—	6.61	3.93
0.004	—	5.98	3.56
0.0004	—	5.16	3.10
0.0001	—	4.05	2.44

¹ from models of KTC94.

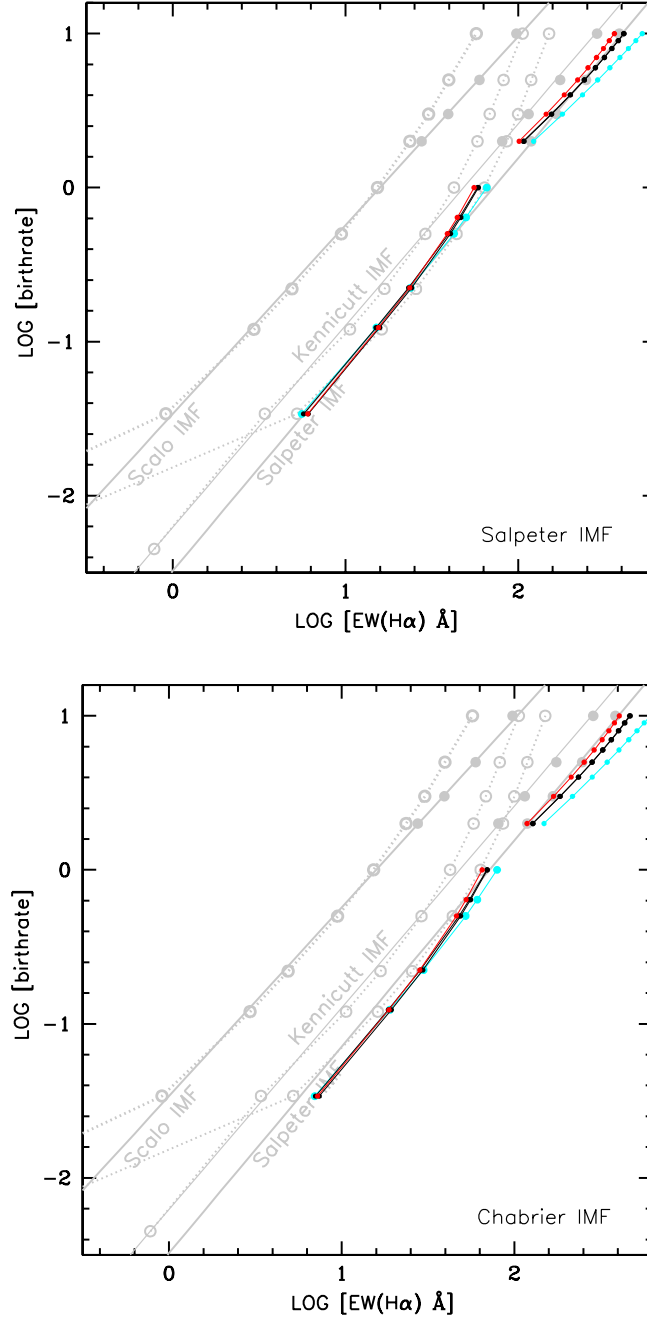


Figure 6.1: Relationship between stellar birthrate and the H α EW as predicted by the evolutionary synthesis models computed in this work. The colored curves in the top panel show the predicted mapping assuming a Salpeter IMF, while those in the bottom panel are based on a Chabrier IMF. Four different metallicity models are shown. The blue and red curves respectively represent the lowest ($Z_{\odot}/50$) and highest (Z_{\odot}) metallicity models, and the black curves represent models of intermediate metallicity ($Z_{\odot}/2.5$ and $Z_{\odot}/5$). For comparison, the results from KTC94 are plotted in gray in both panels. See text for more details.

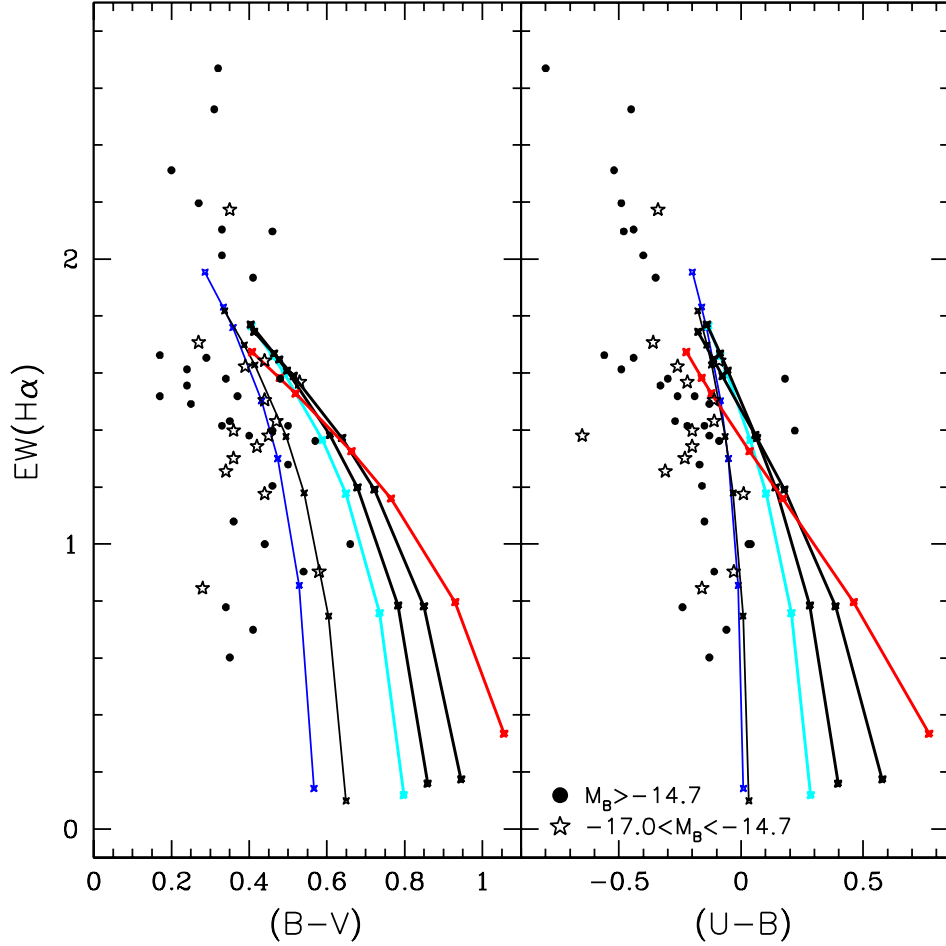


Figure 6.2: Continuous τ models in the $H\alpha$ EW-Color plane. Color data is taken from Hunter & Elmegreen (2006) and van Zee (2001). Galactic, but no internal extinction corrections have been applied to the colors. $H\alpha$ EWs are from 11HUGs. Six sets of different metallicity, Salpeter IMF models are plotted at an age of 10 Gyrs. The blue and red tracks indicate the most metal poor ($Z_{\odot}/200$) and metal rich ($2.5 Z_{\odot}$) models respectively, whereas the models which best match the observed gas metallicities of dwarf galaxies are highlighted in light blue ($Z_{\odot}/5$). The models with the shortest exponential decay timescales ($\tau=1$ Gyr) have the reddest UBV colors, since they have formed most of their stars early-on, and occupy the lower right corner of the plot. Moving up the tracks, the models become bluer and the EWs increase as the timescale lengthens. The bluest UBV colors and highest EWs result from models with a constant SFR (i.e. $\tau = \infty$).

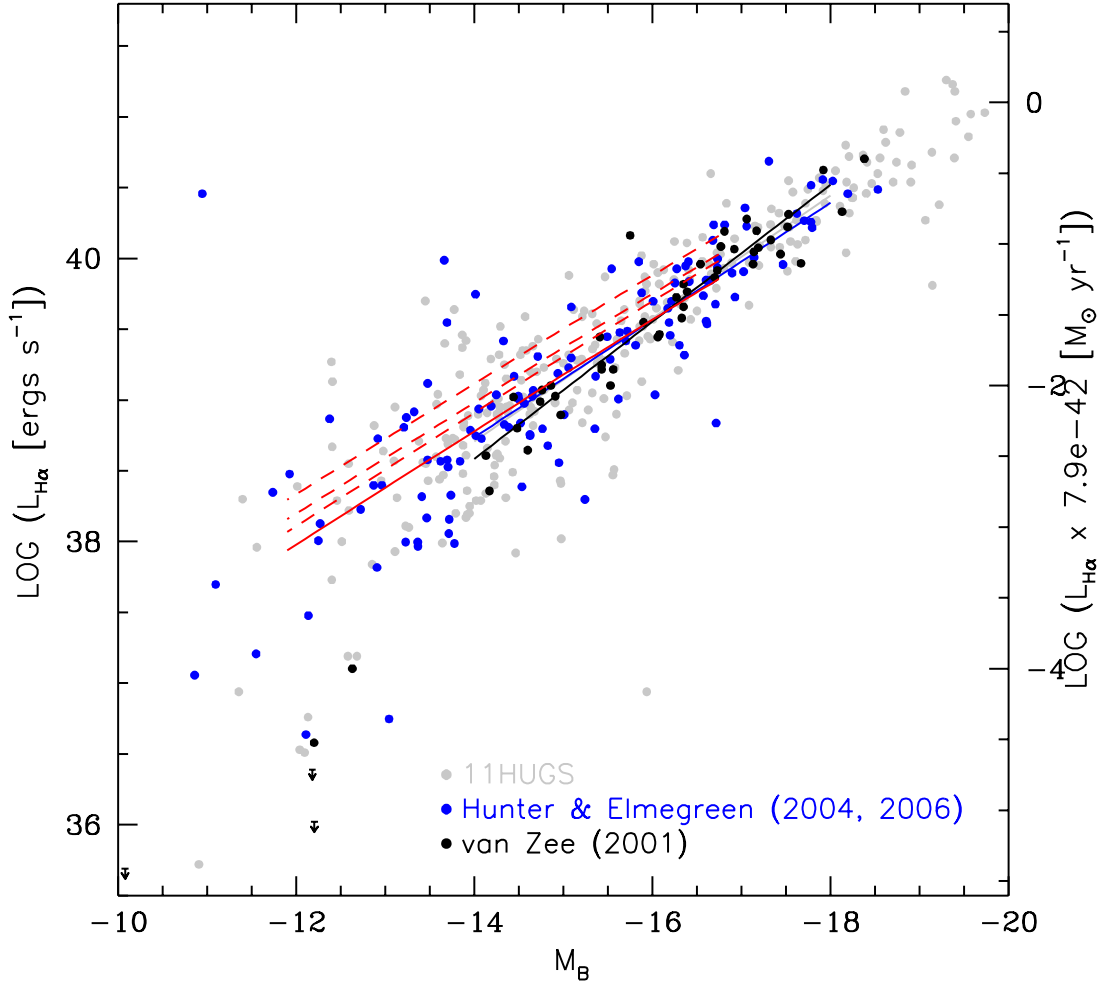


Figure 6.3: Stellar birthrates in the $L_{H\alpha} - M_B$ plane. Data from three different sources are plotted as indicated in the figure. Galactic, but no internal extinction corrections have been applied to either $L_{H\alpha}$ or M_B . Rather the internal extinction corrections have been incorporated into the models (red lines). Linear fits (solid black, blue and gray lines) to the each of the individual datasets are carried out in the range that is commonly well-sampled ($-18 \lesssim M_B \lesssim -14$). The red dashed lines indicate $b=0.7$ based on the models computed in this work, for Chabrier, Salpeter and Kennicutt IMFs from top to bottom. The red solid lines show the median birthrate calculated using the 11HUGS $H\alpha$ fluxes and compiled M_B s, which is 0.34 for a Chabrier IMF, 0.42 for a Salpeter IMF, and 0.51 for a Kennicutt IMF. The right axis shows the corresponding SFR scale, based on the solar metallicity Kennicutt 1998 conversion, for approximate reference.

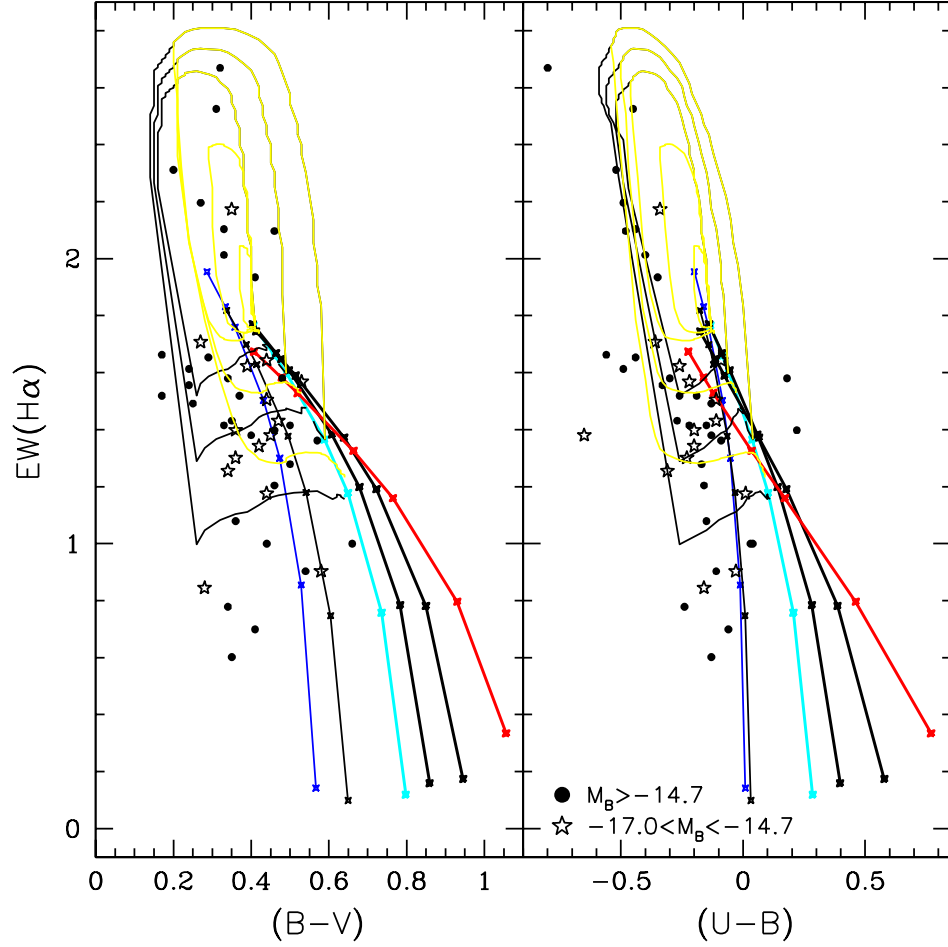


Figure 6.4: Burst models in the $H\alpha$ EW-Color plane. Similar to Figure 6.2, but with eight selected $Z_{\odot}/5$ burst models overplotted. The yellow and black loops represent bursts of 10^7 and 10^8 yr durations respectively. All bursts are added to 10 Gyr old continuous SFR models. As the burst evolves, the colors and EWs move around the loops in the counter-clockwise direction. The height of the loop is controlled by the amplitude of the burst and the SFH of the underlying population, while the width is controlled by both the burst duration and amplitude. The three innermost yellow loops are $b=2$, $b=5$ and $b=10$ bursts superimposed on a constant SFR model, while the two outermost black loops represent $b=10$ bursts superimposed on $\tau=8$ Gyr and $\tau=4$ Gyr models.

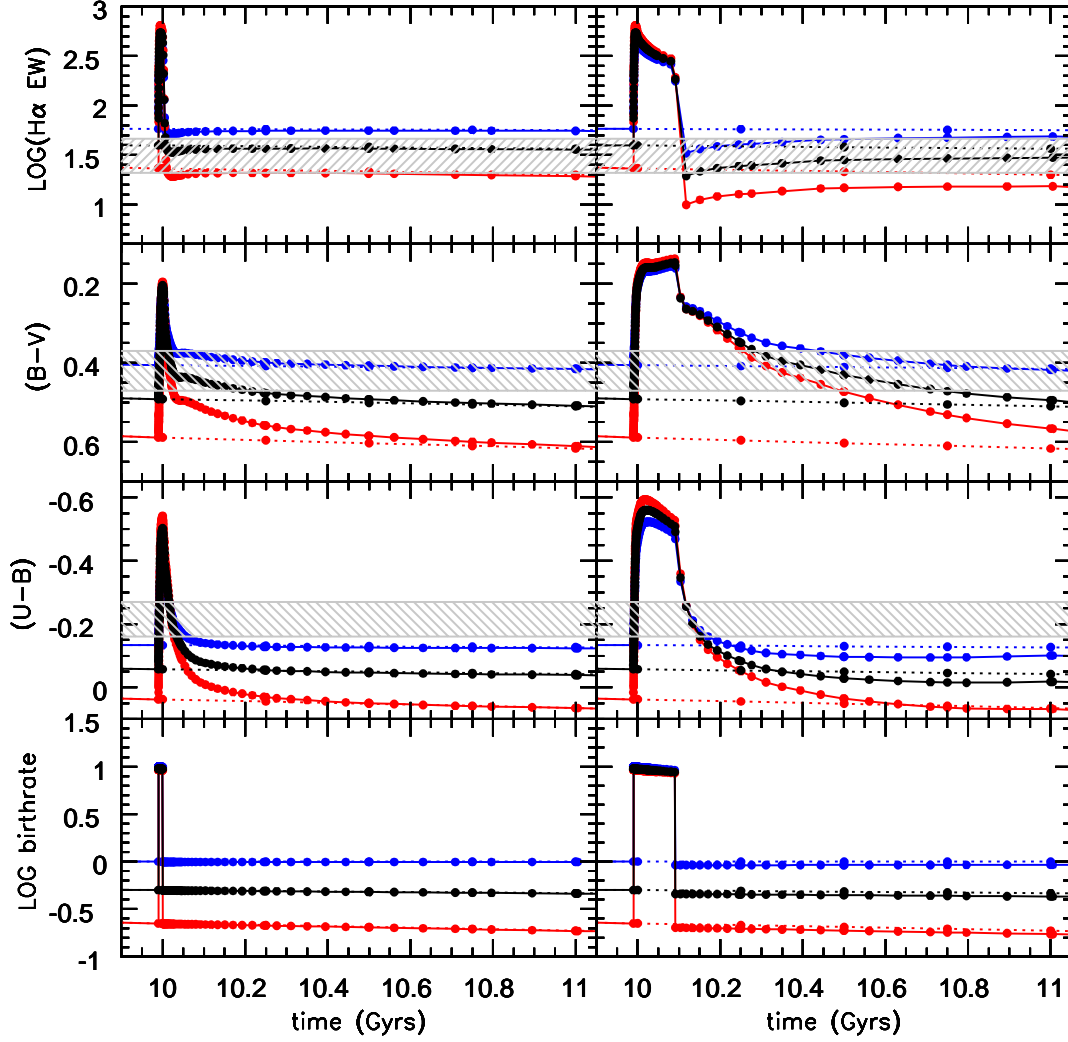


Figure 6.5: Time evolution of $U-B$, $B-V$ and $H\alpha$ EW following the onset of a burst. $Z_{\odot}/5$, Salpeter IMF burst models with $b=10$ amplitudes are shown. 10^7 yr duration bursts are shown in the left panels, while longer 10^8 yr duration bursts are shown in the right panels. The bursts are added to $\tau = 4$ Gyr (red), $\tau = 8$ Gyr (black), and constant SFR (blue) populations at an age of 10 Gyrs. The evolution of the models which have not been through a burst are also plotted (dotted lines). The gray hatched areas represent the ranges where the majority of the observations lie. For the $H\alpha$ EW, the area corresponds to the $\pm 1\sigma$ range as determined from the 11HUGS sample. The gray areas in the $U-B$ and $B-V$ plots are based on the median, and upper and lower quartile values from van Zee's (2001) study of isolated dwarf irregular galaxies.

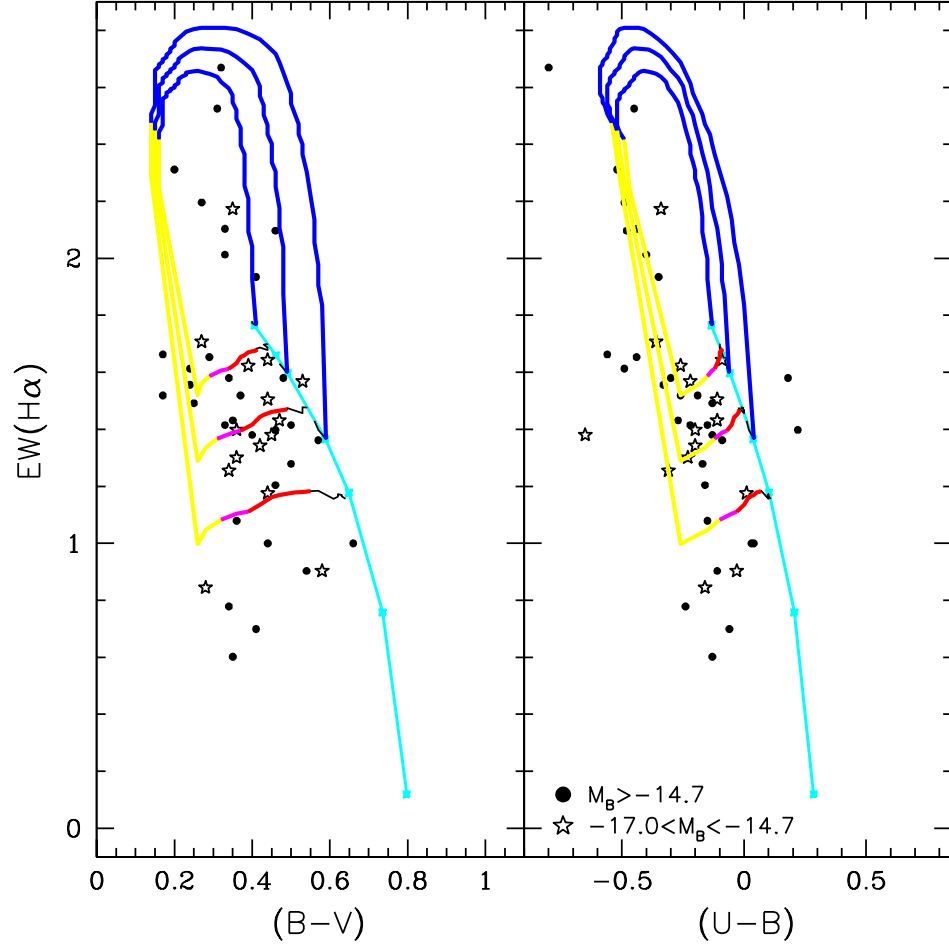


Figure 6.6: Time evolution of burst models in the H α EW-Color plane. Similar to Figure 6.4, but now only showing the 10^8 yr duration burst models. The blue, yellow and pink portions of the tracks each indicate 10^8 yr periods. The red curve indicates a 7×10^8 yr period, from 3×10^8 yrs to 1 Gyr following the initiation of the burst.

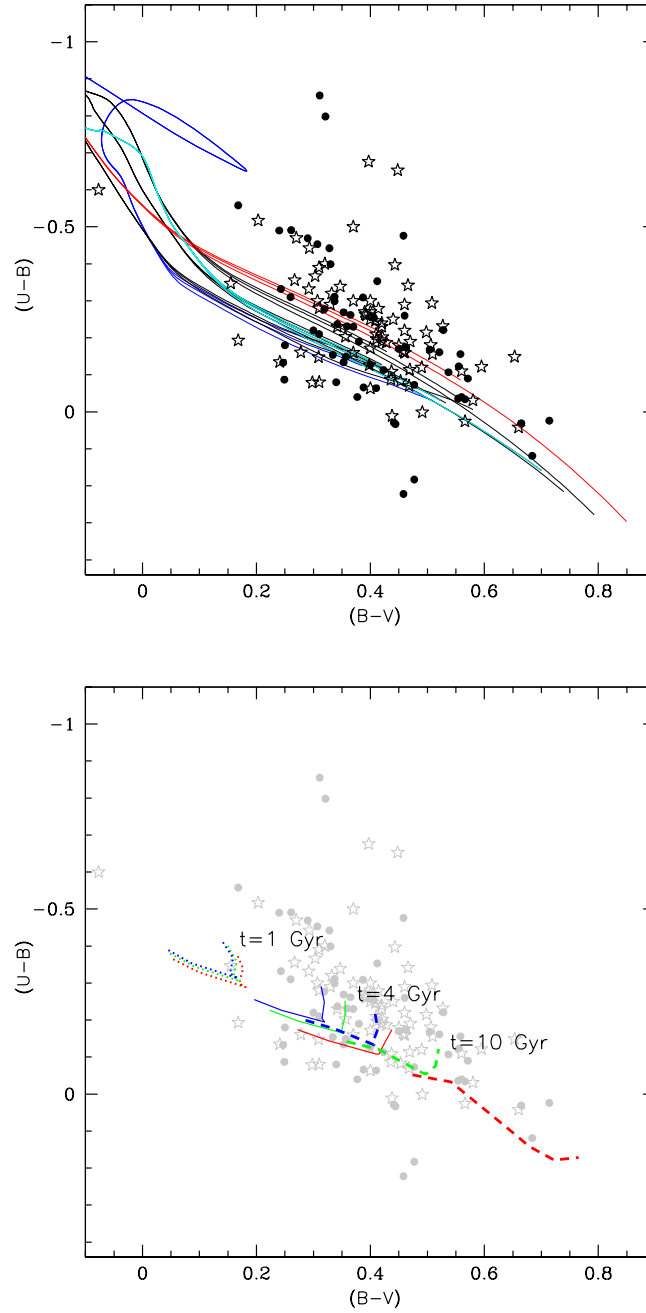


Figure 6.7: Evolutionary tracks of τ models in the UB plane. (*Top panel*) As in the previous figures, the red and blue curves respectively represent the highest ($2.5 Z_{\odot}$) and lowest ($Z_{\odot}/200$) metallicity models, and the light blue curves show the models which best match the metallicities of the dIrrs considered here ($Z_{\odot}/5$). The data again are taken from Hunter & Elmegreen (2006) and (van Zee 2001). (*Bottom panel*) Positions of the tracks at three different ages. Here the red, green and blue curves represent $\tau = 3$, $\tau = 8$, and constant SFR models.

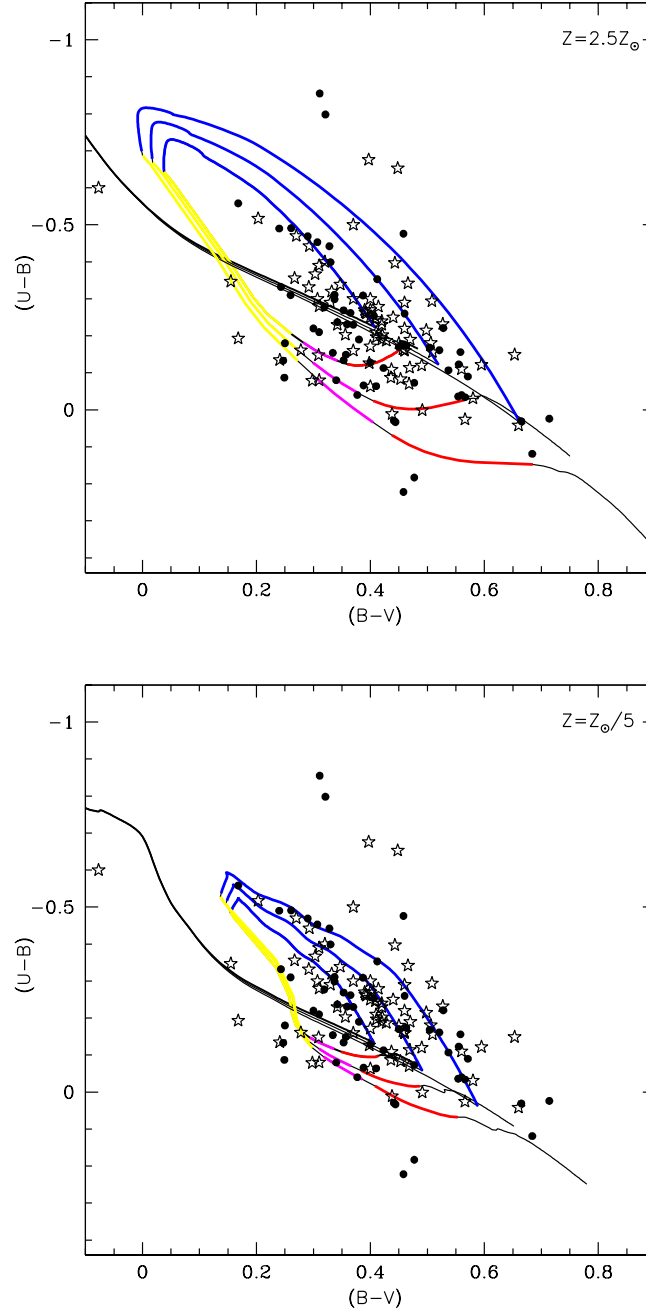


Figure 6.8: Evolutionary tracks of burst models in the UBV plane. The top panel shows the 10^8 duration, $b = 10$ bursts in the $2.5 Z_{\odot}$ models, while the bottom panel shows those in the $Z_{\odot}/5$ models. The bursts are added to $\tau = 4$ Gyr (outermost loop), $\tau = 8$ Gyr (middle loop), and constant SFR (innermost loop) populations at an age of 10 Gyrs. As in Figure 6.6, the tracks have been color-coded to indicate increments of 10^8 yr of time (blue, yellow and pink) and 7×10^8 yrs (red).

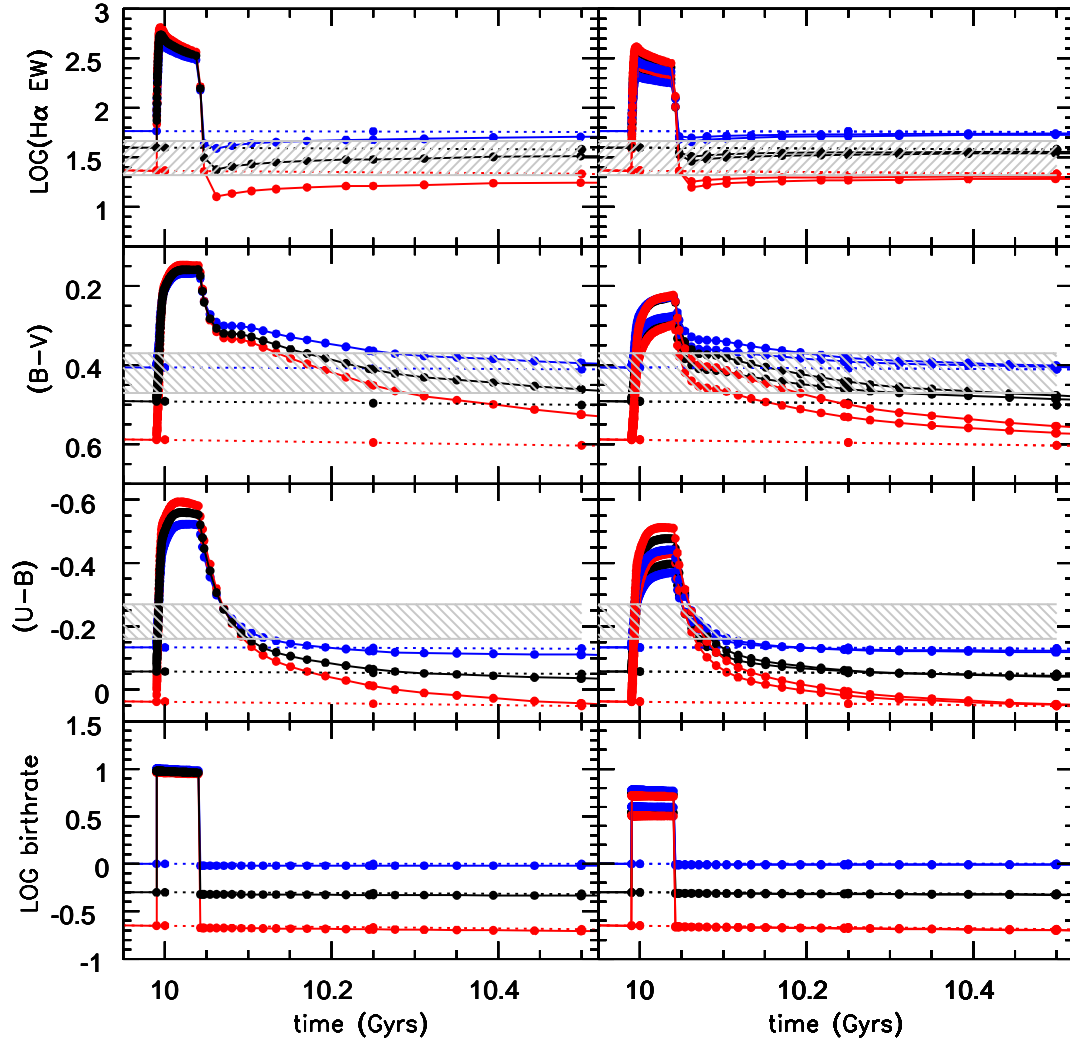


Figure 6.9: Same as Figure 6.5, but now showing 50 Myr duration bursts. The left panels show the decay of a $b = 10$ episode, while the right panels compares the decays of $b = 4$ and $b = 6$ episodes.

APPENDIX A

EMISSION-LINE FLUX CALIBRATION

The method that we have used to calculate physical emission-line fluxes from the observed narrow-band count rates is documented here. Our observations have been taken through intermediate-bandpass (65 – 75 Å) filters, so our “narrow-band” observations generally include flux from $H\alpha$ as well as the $[NII]_{\lambda\lambda 6548,6583}$ emission lines. This changes the effective transmission from what would be expected for a single emission-line in the bandpass, and we explicitly account for this effect as described below. Also, we have used a broadband R filter for the continuum measurement, and our reduction incorporates corrections for emission-line contamination of the R image and the bandpass shift between the $H\alpha$ and R filters.

A.1 Unit Response

To derive a physical flux, our first step is to calculate the unit response of the detector-filter-telescope combination; that is, we compute the ratio of the observed count rate, CR [counts s^{-1}], to the mean source flux density, f_{λ} [erg s^{-1} cm^{-2} Å $^{-1}$]. To do this, we first note that for a given observation, the instrumental magnitude m_{inst} is related to the calibrated magnitude m through the basic equation

$$m = m_{inst} - \kappa \sec(z) + ZP , \quad (A.1)$$

$$= -2.5 \log CR - \kappa \sec(z) + ZP . \quad (A.2)$$

Here, the zero point ZP is based on observations of spectrophotometric stan-

dards (see also discussion in Section 2.3.5), and the extinction coefficient κ is assumed to be 0.08.

Using the absolute Hayes & Latham (1975) based calibration from Massey et al. (1988), we also have that the monochromatic magnitude m_ν is given by

$$m_\nu = -2.5 \log f_\nu - 48.59 . \quad (\text{A.3})$$

To express this in terms of f_λ , we require the relation $f_\nu = \frac{\lambda^2}{c} f_\lambda$, so that

$$m_\nu = -2.5 \log(\lambda^2 f_\lambda) - 2.397 . \quad (\text{A.4})$$

Combining Eqs. A.2 and A.4 yields the unit response for the image:

$$U \left[\frac{\text{counts s}^{-1}}{\text{erg s}^{-1} \text{ cm}^{-2} \text{ \AA}^{-1}} \right] \equiv \frac{f_\lambda}{\text{CR}} = \lambda^{-2} 10^{-0.4(ZP+2.397-\kappa \sec(z))} . \quad (\text{A.5})$$

A.2 Transmission Corrections

Our second step is to compute $T(\lambda)$, the effective transmission of the filter at the wavelength of the redshifted $\text{H}\alpha$ + $[\text{NII}]$ lines. This corrects for differential transmission across the filters – the decrease in transmission that occurs when the $\text{H}\alpha$ and $[\text{NII}]$ emission lines are not at a filter’s peak transmission wavelength (approximately the central wavelength).

Let us first say that the total emission line flux, f_{tot} , as observed at the top of the Earth’s atmosphere is

$$f_{tot}(\text{H}\alpha+[\text{NII}]) = \frac{f_{cal}(\text{H}\alpha+[\text{NII}])}{T(\lambda)} , \quad (\text{A.6})$$

so that f_{cal} represents a calibrated, but transmission *uncorrected* line flux as measured from the continuum subtracted narrowband image.

To produce images where only $H\alpha+[NII]$ emission is present, the R -band image is scaled and subtracted from the narrow-band image as described in 2.3.2. However, emission-line flux is also contained within the bandpass of the R filter, so in this process of continuum removal, a small fraction of the true $H\alpha+[NII]$ flux is lost from the narrow-band image. We can recover this flux, and compute $T(\lambda)$ along the way, by expressing the image subtraction procedure algebraically:

$$f_{tot}(H\alpha+[NII]) \frac{T_{NB}(\lambda)}{t_{NB}} - f_{tot}(H\alpha+[NII]) \frac{T_R(\lambda)}{t_R} F^{-1} = f_{cal}(H\alpha+[NII]) \frac{t_{NB}}{t_{NB}} , \quad (A.7)$$

where $T_R(\lambda)$ and $T_{NB}(\lambda)$ are the normalized filter transmission, as described at the end of this section, t_R and t_{NB} are the exposure times, and F is the factor used to scale down the R -band surface brightness to match the continuum level in the narrow-band image for the purposes of continuum subtraction.

Solving for $f_{tot}(H\alpha+[NII])$ results in an expression that incorporates corrections for both the presence of the $H\alpha+[NII]$ in the R -band filter, and the differential transmission across both R and narrow-band filters:

$$f_{tot}(H\alpha+[NII]) = f_{cal}(H\alpha+[NII]) \left[T_{NB}(\lambda) - T_R(\lambda) \frac{t_R}{t_{NB}} \frac{1}{F} \right]^{-1} . \quad (A.8)$$

Comparing this with Eq. A.6 we see that

$$T_\lambda = T_{NB}(\lambda) - T_R(\lambda) \frac{t_R}{t_{NB}} \frac{1}{F} . \quad (A.9)$$

The second term in this equation describes the line flux that is lost during the subtraction of the continuum, and amounts to an effective reduction in the line transmission by 4%. This is shown in the bottom two panels of Figure A.1, using

the KPNO filters as an example, where the curve which describes the final transmission correction, T_λ (solid line), is depressed relative to $T_{NB}(\lambda)$ (open circles). The size of the effect corresponds to the ratio of the integrated throughputs between the narrow and R -band filters, and is also approximately equivalent to the ratio of the bandwidths.

Finally, we need T_R and T_{NB} , which are *not* simply the normalized transmissions at the wavelength of the redshifted $H\alpha$ line. Since the narrowband filters used are ~ 70 Å wide, emission from $[\text{NII}]\lambda\lambda 6548, 6583$ is also present in the images, and these flanking lines generally will not be attenuated by the same factor as the $H\alpha$ flux. To account for this, the transmissions at the redshifted wavelengths for all three lines are computed, and the average of these, weighted by the relative fluxes of the lines, is taken. The $[\text{NII}]/H\alpha$ ratios that we have used are given in Table 2.4 and a method for estimating them when spectral measurements are not available is described in Appendix B.1.

We compare the effect of using a flux-weighted transmission correction with one that is simply read off from the normalized filter tracing at the position of $H\alpha$ in Figure A.1. Naturally, the disparity between the two transmissions will increase as the target galaxy's $[\text{NII}]/H\alpha$ line ratio increases. We illustrate the largest disparity possible with $[\text{NII}]\lambda 6584/H\alpha = 0.54$.

In Figure A.1, the wavelength range over which $H\alpha$ is shifted for the recessional velocities spanned by the galaxies in the 11HUGS sample is marked by the solid red and blue lines. The corresponding positions of the $[\text{NII}]\lambda\lambda 6548, 6583$ lines are also drawn in the middle panel. In the R -band (upper panel) the difference between these two transmissions are negligible (0.2%) since the throughput is essentially constant over the relevant wavelength range. However, there are differences of a few percent in the narrowband (middle panel) that vary accord-

ing to the redshift of the target. The residual from the “native” transmission of the narrowband filter at the shifted wavelength of $H\alpha$ is shown in the bottom panel.

A.3 The Final Calibrated Emission Line Flux

We now combine the results from the last two sections to arrive at a final expression for f_{tot} . The calibrated flux f_{cal} (prior to corrections for differential transmission) can be computed by summing the unit response U over the filter bandpass and then multiplying by the measured emission-line CR from the continuum-subtracted narrow-band image:

$$f_{cal}(H\alpha+[NII]) = U \cdot \text{FWHM}_{NB} \cdot \text{CR}(H\alpha+[NII]) . \quad (\text{A.10})$$

Finally, the transmission correction T_λ is applied through the combination of Equations A.6 and A.10, and U is written out explicitly using Equation A.5. This yields:

$$f_{tot}(H\alpha+[NII]) = U \cdot \text{FWHM}_{NB} \cdot \text{CR}(H\alpha+[NII]) \left[T_{NB}(\lambda) - T_R(\lambda) \frac{t_R}{t_{NB}} \frac{1}{F} \right]^{-1}, \quad (\text{A.11})$$

$$= \lambda^{-2} 10^{-0.4(ZP+2.397-\kappa \sec(z))} \text{FWHM}_{NB} \text{CR}(H\alpha+[NII]) \left[T_{NB}(\lambda) - T_R(\lambda) \frac{t_R}{t_{NB}} \frac{1}{F} \right]^{-1} \quad (\text{A.12})$$

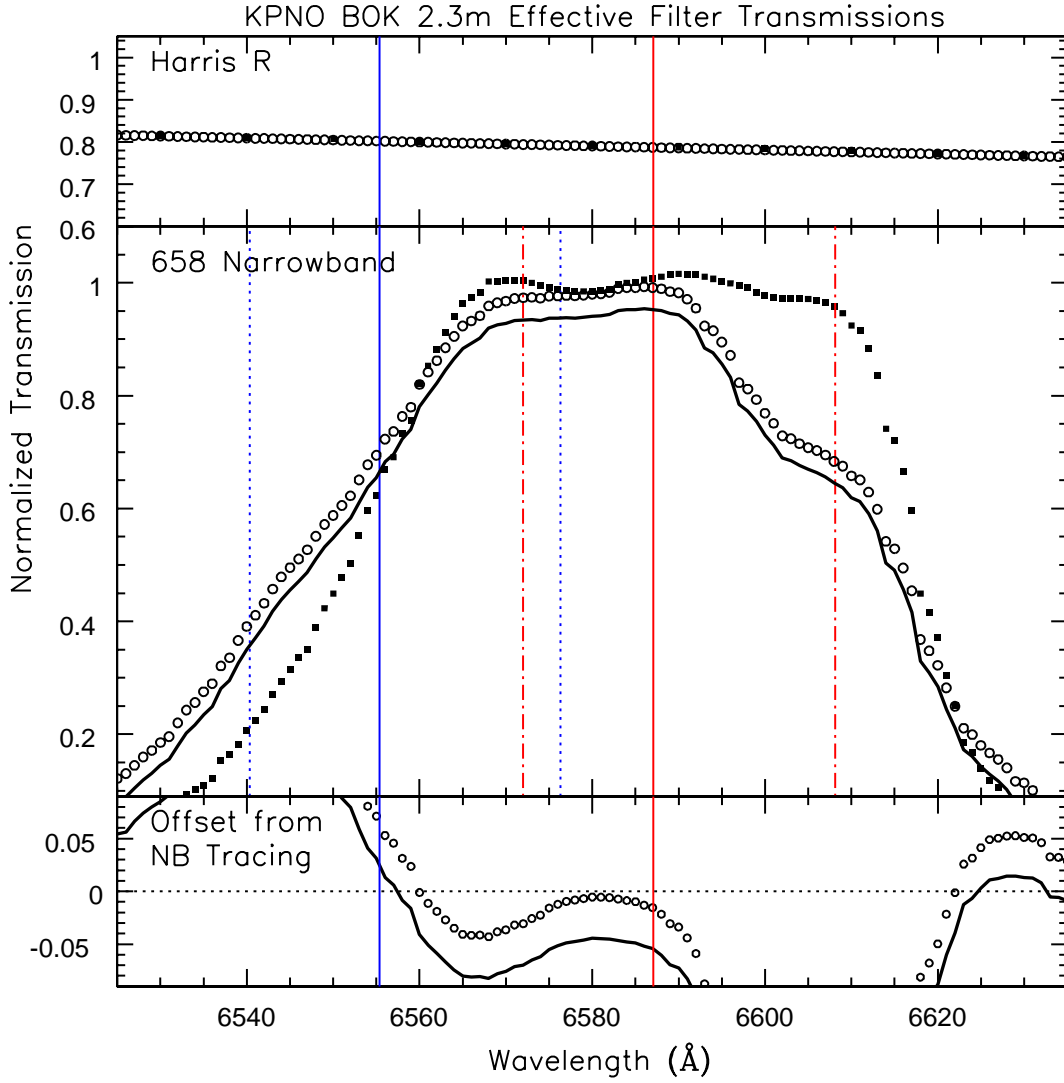


Figure A.1: Normalized response functions for the R -band filter used at the Bok telescope (top panel), and for the Andover 3-cavity interference “658” filter acquired for the 11HUGS survey (bottom panel). The native transmission of the filters are traced by the solid squares. The open circles represent the $[\text{NII}] + \text{H}\alpha$ flux-weighted transmission, assuming the maximum $[\text{NII}]\lambda 6583/\text{H}\alpha$ ratio of 0.54 for star-forming galaxies (see Appendix B.2). The solid curve describes the final effective 658 transmission which has further been corrected for the loss of emission-line flux during continuum subtraction. The extents of these corrections are illustrated with the residual plot in the bottom panel. The solid red and blue lines mark the wavelength range over which $\text{H}\alpha$ is shifted for the recessional velocities spanned by the galaxies in the 11HUGS sample. The corresponding positions of the $[\text{NII}]\lambda\lambda 6548, 6583$ lines are also indicated in the middle panel.

APPENDIX B

CORRECTIONS TO THE OBSERVED $H\alpha$ + [NII] FLUXES AND EW'S

B.1 [NII]/ $H\alpha$ Estimation

The [NII]/ $H\alpha$ flux ratio of a galaxy can be coarsely predicted from its blue absolute magnitude M_B using a correlation between the two which we have derived based on data from the Moustakas & Kennicutt (2006; MK06) integrated spectrophotometric atlas of nearby galaxies. This data set consists of spectra obtained by drift-scanning the spectrograph slit over as much of the optical extents of the galaxies as practically possible. Thus, spectral measurements extracted from this dataset represent the averaged, integrated properties of the galaxies, rather than local ones derived from the more usual single-position spectral observations of individual HII regions or the nuclear regions of galaxies.

Figure B.1 shows the scaling between [NII] λ 6584/ $H\alpha$ and M_B . The absolute magnitudes plotted have been corrected for foreground extinction (but not for internal extinction) as in Moustakas, Kennicutt & Tremonti 2006, and are scaled to $H_0 = 75 \text{ km s}^{-1} \text{ Mpc}^{-1}$. Filled points represent galaxies whose line emission is due to star formation, while open triangles are those in which the ionization is non-thermal and due to the presence of an AGN. Open squares show galaxies with ambiguous classifications. The determinations in MK06 are based on the standard $\text{LOG}([\text{OIII}]\lambda 5007/H\beta)$ vs. $\text{LOG}([\text{NII}]\lambda 6583/H\alpha)$ diagnostic diagram (Baldwin, Phillips & Terlevich 1981). An ordinary least squares bisector fit is performed, excluding galaxies with AGN. The adopted relationship is based on this fit of 267 star forming galaxies. We impose the additional constraint that the

value of $[\text{N II}] \lambda 6584 / \text{H}\alpha$ not exceed 0.54. That is:

$$\begin{aligned} \log([\text{NII}]\lambda 6584 / \text{H}\alpha) &= (-0.173 \pm 0.007) M_B - (3.903 \pm 0.137) \quad \text{if } M_B > -21 \\ [\text{NII}]\lambda 6584 / \text{H}\alpha &= 0.54 \quad \text{if } M_B \leq -21 \end{aligned} \quad (\text{B.1})$$

The $1\text{-}\sigma$ scatter in the ordinate is 0.26 dex, indicating that the estimates based on this correlation are good to a factor of about two.

We use this scaling relationship to estimate the $[\text{NII}]/\text{H}\alpha$ ratio whenever actual spectral measurements are not available from MK06, the Nearby Field Galaxies Survey (Jansen et al. 2000), or the various dwarf galaxy datasets of van Zee (van Zee & Haynes 2006 and references therein). The $[\text{NII}]/\text{H}\alpha$ values that we have adopted are listed in Table 2.4. They are used to compute flux-weighted $\text{H}\alpha + [\text{NII}]$ filter transmissions (Appendix A.2) and to correct the measured fluxes for $[\text{NII}]$ contamination, which are essential for ultimately deriving SFRs.

B.2 Estimation of the Extinction in the $\text{H}\alpha$ Flux and EW

We coarsely estimate the average attenuation of the global $\text{H}\alpha$ flux $A_{\text{H}\alpha}$ by using the observed correlation between $A_{\text{H}\alpha}$ and the blue absolute magnitude M_B . The correlation is again based on measurements from the drift-scan spectra of MK06, from which the Balmer decrement is used to calculate the reddening. The validity of using the Balmer decrement to infer the average amount of nebular extinction in galaxies is supported by studies which have shown that the agreement between IR-based SFRs and $\text{H}\alpha$ -based SFRs is improved when the $\text{H}\alpha$ luminosity is corrected for extinction in this way (Dopita et al. 2002; Rosa-Gonzalez et al. 2002; Kewley et al. 2002; Moustakas et al. 2006). Using the Cardelli, Clayton & Mathis (1989) extinction law, with a ratio of selective to total absorption R_V of 3.3 (appropriate for the LMC), and the assumption of an intrinsic case B recombin-

tion $H\alpha/H\beta$ value of 2.86, $A_{H\alpha}$ can be expressed in terms of the observed $H\alpha/H\beta$ ratio:

$$A_{H\alpha} = 6.20 \log \frac{f_{H\alpha}}{f_{H\beta}} - 2.83. \quad (\text{B.2})$$

In Figure B.2, $A_{H\alpha}$ is plotted against M_B , the absolute magnitudes shown have been corrected for foreground extinction (but not for internal extinction) as in Moustakas et al. 2006, and are scaled to $H_0 = 75 \text{ km s}^{-1} \text{ Mpc}^{-1}$. The data exhibit the well-known trend that the more luminous objects are more heavily obscured. We fit a piecewise function to the data which is a constant at the lowest luminosities and a second order polynomial for $M_B < -15.0$. Objects that have $A_{H\alpha} < 0$, a signal-to-noise less than 10 in the $H\beta$ line, or contain AGN are excluded from the fit. The adopted scaling relation is:

$$A_{H\alpha} = \begin{cases} 0.14 & \text{if } M_B \geq -15.0 \\ 1.971 + 0.323 M_B + 0.0134 M_B^2 & \text{if } M_B < -15.0 \end{cases} \quad (\text{B.3})$$

Of course, there is a great deal of scatter from this average relationship which becomes more severe with increasing luminosity. There is a 50% scatter for galaxies with $M_B < -18$. However, for the dwarf galaxies of primary interest in this thesis, the scatter is much more manageable: for $-14.7 < M_B < -18$ it is 20% and for the lowest luminosity galaxies, where we have assumed a constant average correction, it is 8%.

To correct the EW for internal extinction, the differential reddening between the gas and stars must be considered. The fractional decrease of the EW should be lower than the that of the nebular emission alone since the continuum flux will also be attenuated. However, the effect on the continuum will be less severe than it is on the $H\alpha$ emission since the older stellar populations, which are primarily responsible for the continuum flux, are expected to be less enshrouded by dust

than the more recently formed stars.

To roughly account for differential attenuation, we follow the prescription given by Calzetti 2001 which estimates that the reddening experienced by stellar continuum is about half of that experienced by the ionized gas. This results in Equation 16 in Calzetti 2001:

$$\log [\text{EW}(\text{H}\alpha)_{\text{atten}} / \text{EW}(\text{H}\alpha)_{\text{true}}] = -0.40 E(B - V)_{\text{gas}}. \quad (\text{B.4})$$

This can be re-written in terms of $A_{\text{H}\alpha}$, again using the Cardelli et al. (1989) extinction law:

$$\log [\text{EW}(\text{H}\alpha)_{\text{atten}} / \text{EW}(\text{H}\alpha)_{\text{true}}] = -0.14 A_{\text{H}\alpha}. \quad (\text{B.5})$$

If individual measurements of the $\text{H}\alpha/\text{H}\beta$ ratio are available from the integrated spectra of MK06 or the NFGS, we use them to compute the internal extinction. Otherwise, the scaling relationships given above are used to estimate the correction.

B.3 Comments on the Resultant Correction

Since the [NII] and internal extinction corrections work in opposite senses, such that one will tend to cancel the other, it is interesting to examine their combined effect as a function of M_B . In the top panel of Figure B.3, the $\text{H}\alpha$ extinction factor is plotted in gray while the fractional flux contribution from [NII] is plotted in black for galaxies in MK06. In the middle panel, the combined [NII] and internal extinction flux correction factors are shown. The negative adjustment for the [NII] is smaller than the positive adjustment for the extinction, so the resultant correction increases the value of the observed flux. However, the opposite tends to be true for the EW, as a consequence of the differential attenuation between

the nebular emission and the continuum light, so the corrected $H\alpha$ EWs are on average smaller than the observed quantities (bottom panel).

The fact that the two corrections offset each other leads to an interesting advantage in using $H\alpha$ measurements which include $[NII]\lambda\lambda 6548,84$. Although the correction for nebular internal extinction alone spans a factor of ~ 6 range (top panel, gray points), combining the $[NII]$ and extinction corrections for the flux reduces this range by 30% (middle panel). The $EW(H\alpha + [NII])$ is even more robust to variations in the extinction than the flux, as there is some cancelation in the ratio; the range in the top panel is reduced by a factor 3 as shown in the bottom panel.

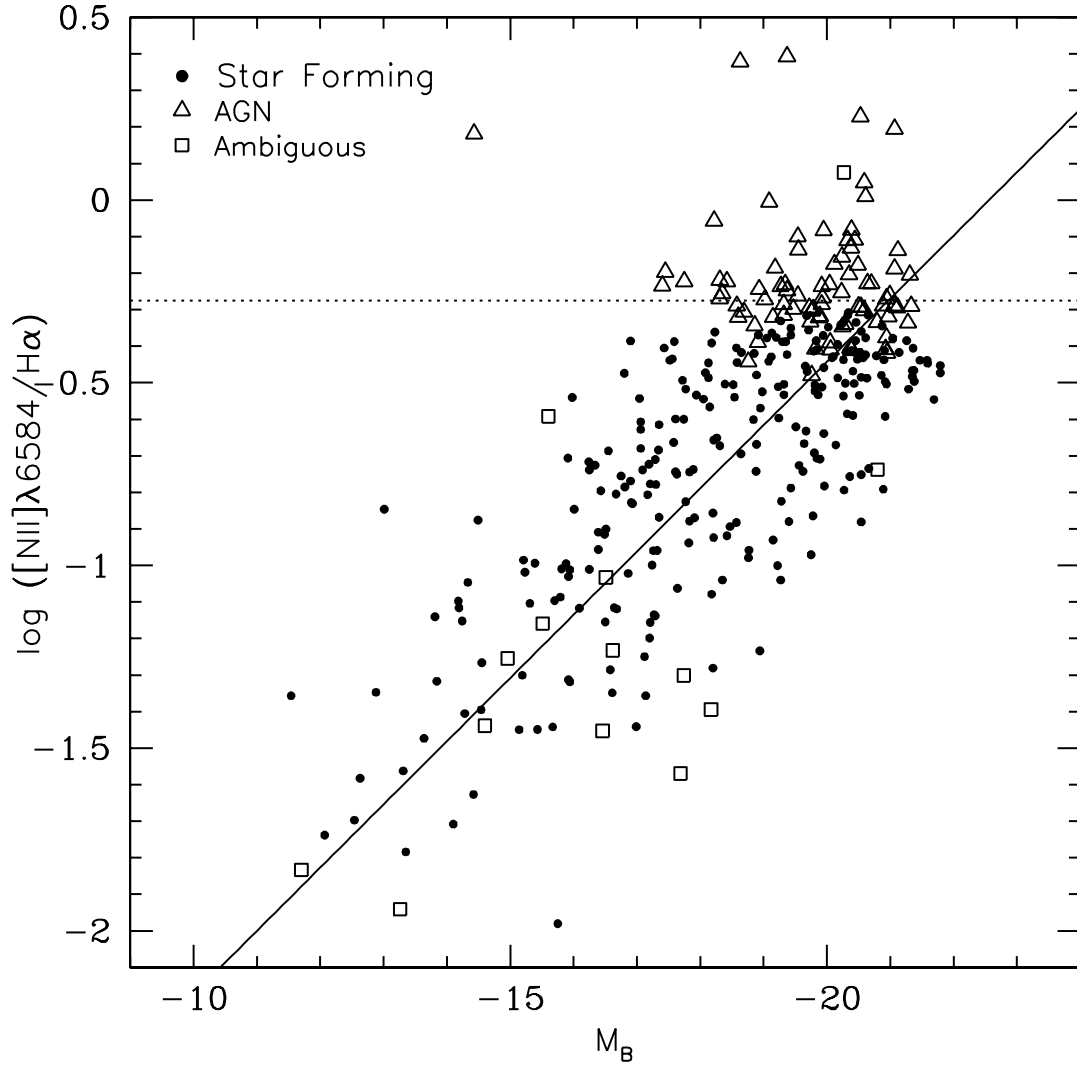


Figure B.1: The [NII] λ 6583/H α ratio plotted against M_B for galaxies in the MK06 integrated spectral atlas. Points represent star-forming galaxies while triangles denote galaxies with AGN. Squares represent galaxies with ambiguous classifications. The solid line shows the best fit line, excluding those galaxies with AGN. The fit is used to correct the observed fluxes for [NII] contamination when individual estimates of the [NII]/H α ratio from the integrated spectra of MK06 and the NFGS, or the various spectral datasets of van Zee et al. (van Zee & Haynes 2006 and references therein) are not available.

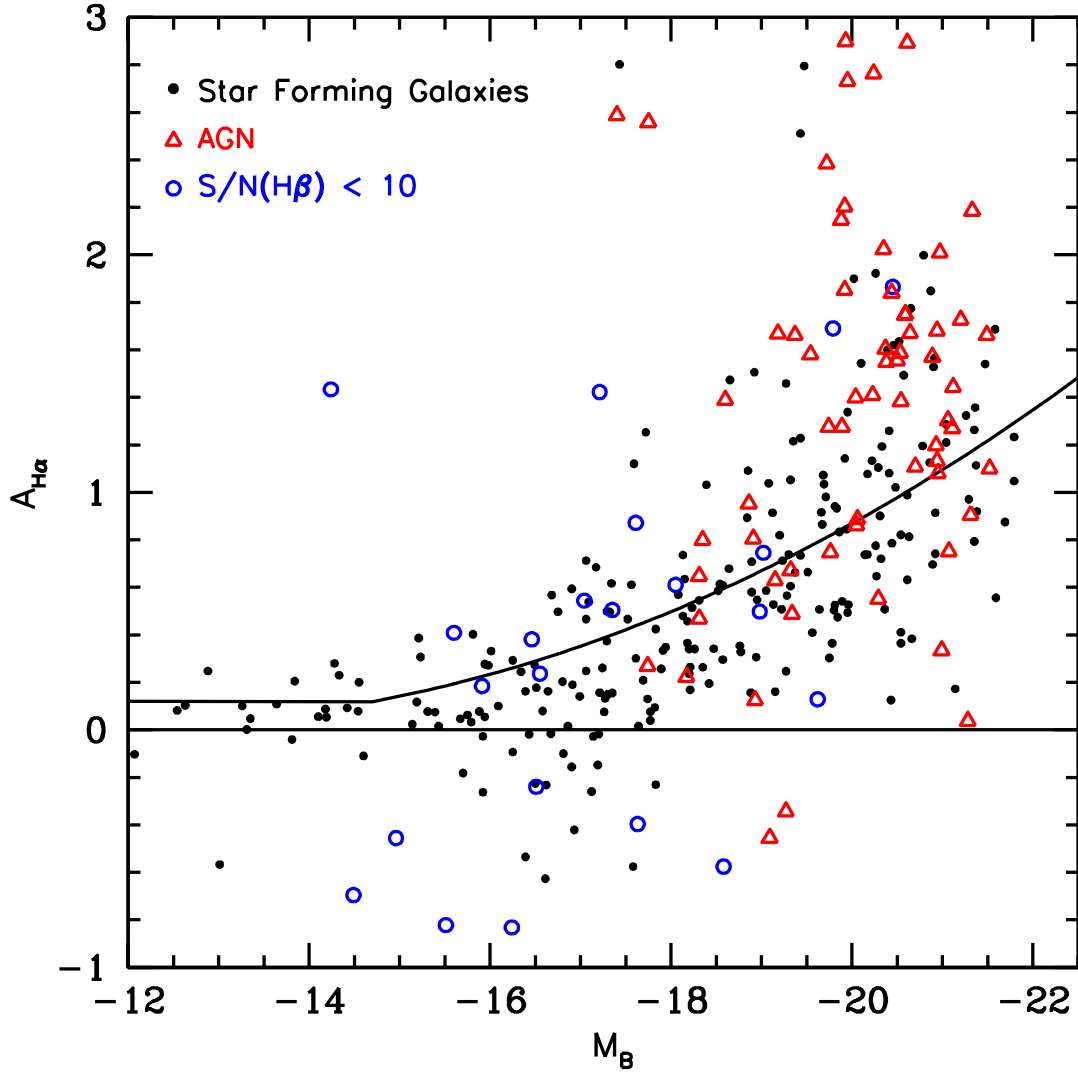


Figure B.2: $A_{H\alpha}$, the nebular dust attenuation at $H\alpha$ in magnitudes, against M_B for galaxies in MK06. Galaxies with AGN spectral signatures (open triangles) or low S/N in $H\beta$ (open circles) are not included in the fit (solid curve). The fit is used to correct $L_{H\alpha}$ for internal extinction when individual estimates of $A_{H\alpha}$ from the integrated spectra of MK06 and the NFGS are not available.

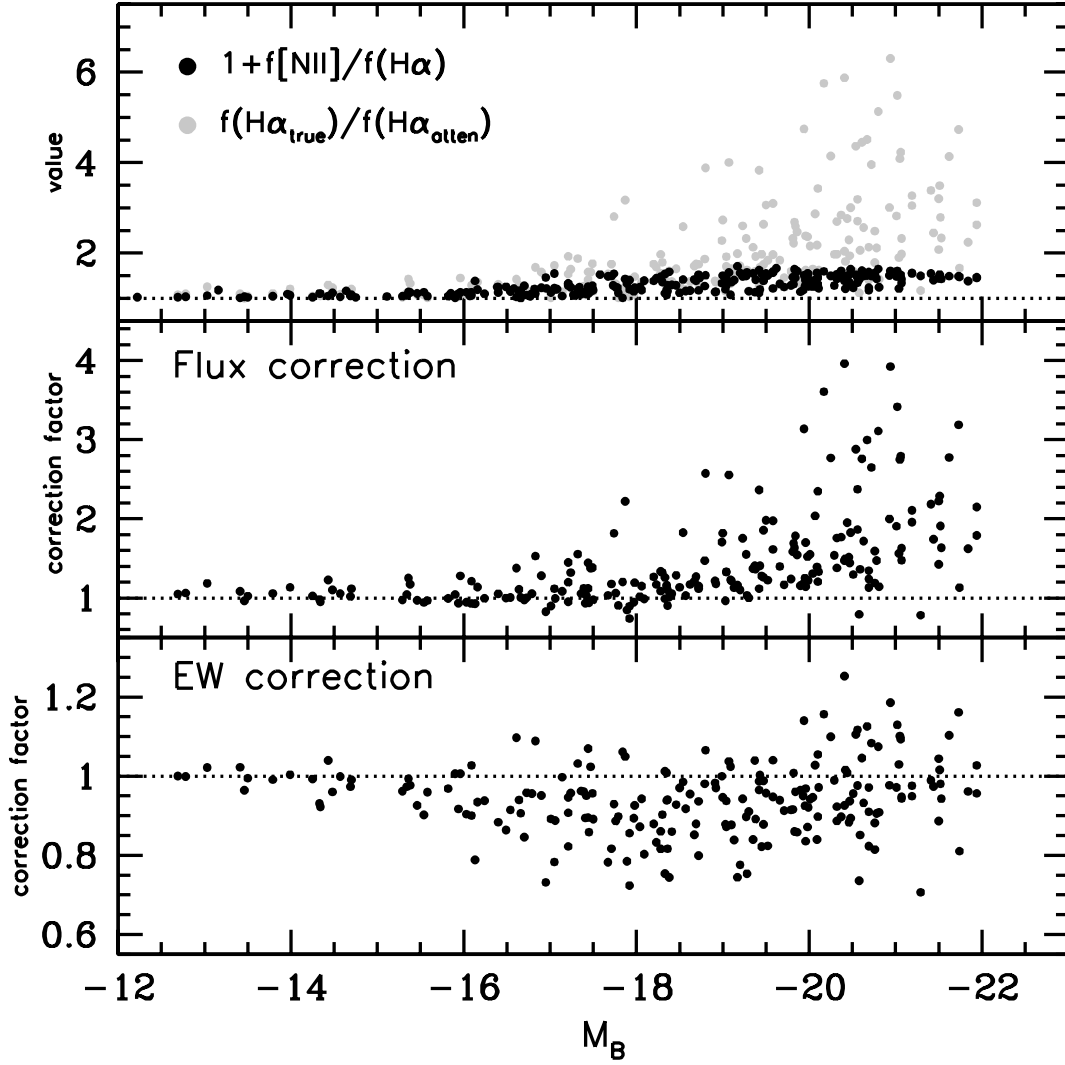


Figure B.3: Effects of the Combined [NII] and Internal Extinction Correction. *Top panel*– The factor by which the $\text{H}\alpha$ flux is extinguished is plotted in gray while the fractional flux contribution from [NII] is plotted in black for galaxies in MK06. *Middle panel*– The combined [NII] and internal extinction flux correction factors are shown. The negative adjustment for the [NII] is smaller than the positive adjustment for the extinction, so the resultant correction increases the value of the observed flux. *Bottom panel*– However, the opposite tends to be true for the EW, as a consequence of the differential attenuation between the nebular emission and the continuum light, so the corrected $\text{H}\alpha$ EWs are on average smaller than the observed quantities.

REFERENCES

- Annibali, F., Greggio, L., Tosi, M., Aloisi, A., & Leitherer, C. 2003, *AJ*, 126, 2752
- Aparicio, A., Gallart, G., & Bertelli, G. 1997a, *AJ*, 114, 669
- Aparicio, A., Tikhonov, N. & Karachentsev, I. 2000, *AJ*, 119, 177
- Bell, E.F. & de Jong, R.S. 2001, *ApJ*, 550, 212
- Belokurov, V. et al. 2006, *ApJL*, 647, 111
- Bergvall, N. et al. 2006, *A&A*, 448, 513
- Blanton, M.R., Eisenstein, D., Hogg, D.W., Schlegel, D.J. & Brinkmann, J. 2005, *ApJ*, 629, 143
- Bohuski, T.J., Fairall, A.P. & Weedman, D.W., 1978, *ApJ*, 221, 776
- Brinchmann, J. et al. 2004, *MNRAS*, 351, 1151
- Bruzual, G. & Charlot, S. 2003, *MNRAS*, 344, 1000
- Burstein, D. & Heiles, C. 1978, *ApJ*, 225, 40
- Calzetti, D. 2001, 113, 1449
- Chabrier, G. 2003b, *PASP*, 115, 763
- Charlot, S., Worthey, G., & Bressan, A., 1996, *ApJ*, 457, 625
- Dekel, A. & Silk, J., 1986, *ApJ*, 303, 39
- Dekel, A. & Woo, J., 2003, *MNRAS*, 344, 1131

- da Costa et al. 1998, AJ, 116, 1
- de Vaucouleurs, et al. 1991, "Third Reference Catalogue of Bright Galaxies"
(Berlin, Heidelberg & New York: Springer-Verlag)
- Dolphin, A.E., Weisz, D.R., Skillman, E.D. & Holtzman, J.A. 2006, in "Resolved
Stellar Populations," eds. D. Valls-Gabaud & M. Chavez, (San Francisco: ASP)
- Dohm-Palmer, R. C. et al. 1998, AJ, 116, 1227
- Dong, S., Lin, D.N.C. & Murray, S.D., 2003, ApJ, 596, 930
- Dopita, M.A., Periera, L., Kewley, L.J. & Capacciolo, M. 2002, ApJS, 143, 47
- Doyle, M.T. et al. 2005, MNRAS, 361, 34
- Elmegreen, B.G. 2006, ApJ, 648, 572
- Elmegreen, B.G. & Scalo, J. 2006, ApJ, 636, 149
- Ferrarese, L., et al. 2000b, ApJS, 128, 431
- Fingerhut, R.L. et al. 2003, ApJ, 587, 672
- Freedman, W.L. et al. 2001, ApJ, 553, 47
- Freeman, K.C. et al. 1977, A&A, 55, 445
- Gallagher, J.S. & Hunter, D.A. 1984, ARA&A, 22, 37
- Gallagher, J.S., Hunter, D.A., & Tutukov, A.V. 1984, ApJ, 284, 544
- Gallagher, J.S. 1998, AJ, 115, 1869
- Gallagher, J.S. 2005, in "Starbursts: From 30 Doradus to Lyman Break Galaxies"
ed. R. de Grijs & R. Gonzalez Delgado (Dordrecht: Springer), 11

- Garnett, D. 2002, ApJ, 581, 1019
- Gavazzi, G., Boselli, A., Pedotti, P., Gallazzi, A. & Carrasco, L. 2002, 2002, A&A, 386, 114
- Gerola, H., Seiden, P. E. & Schulman, L. S. 1980, ApJ, 242, 517
- Gil de Paz, A., Madore, B. F. & Pevunova, O. 2003, ApJS, 147, 29
- Greggio, L., Marconi, G., Tosi, M. & Focardi, P. 1993, AJ, 105, 894
- Hamuy, M. et al. 1992, PASP, 104, 533
- Hamuy, M. et al. 1994, PASP, 106, 566
- Haro, G. 1956, Bol. Obs. Tonantzintla Tacubaya, 2, 8
- Hayes, D.S. & Latham, D.W. 1975, ApJ, 197, 593
- Haynes, M. P., & Giovanelli, R. 1984, AJ, 89, 758
- Heckman, T.M. 2005, in “Starbursts: From 30 Doradus to Lyman Break Galaxies,” ed. R. de Grijs & R. Gonzalez Delgado (Dordrecht: Springer), 3
- Huchra, J.P. 1977a, ApJS, 35, 171
- Huchra, J.P. 1977b, ApJ, 217, 928
- Hunter, D.A., Gallagher, J.S. & Rautenkranz, D. 1982, ApJS, 49, 53
- Hunter, D.A. & Gallagher, J.S., 1985, ApJS, 58, 533
- Hunter, D.A. & Gallagher, J.S., 1986, PASP, 98, 599
- Hunter, D.A. & Elmegreen, B.G, 2004, AJ, 128, 2170

- Hunter, D.A. & Elmegreen, B.G. 2006, ApJS, 162, 49
- James, P.A. et al. 2004, A&A, 414, 23
- Jansen, R.A., Franx, M., Fabricant, D. & Caldwell, N. 2000, ApJS, 126, 271
- Kannappan, S.J. 2004, ApJ, 611, L89
- Karachentsev, I.D., Kajsin, S.S., Tsvetanov, Z. & Ford, H. 2005, A&A, 434, 935
- Kennicutt, R.C. 1983, ApJ, 272, 54
- Kennicutt, R.C., Tamblyn, P. & Congdon, C.E. 1994, ApJ, 435, 22
- Kennicutt, R.C. 1998a, ARA&A, 36, 189
- Kennicutt, R.C. 1998b, ApJ, 498, 541
- Kennicutt, R.C., Lee, J.C., Funes, J.G., Sakai, S. & Akiyama, S. 2005, in "Starbursts: From 30 Doradus to Lyman Break Galaxies," ed. R. de Grijs & R. Gonzalez Delgado (Dordrecht: Springer), 187
- Kewley, L.J., Geller, M.J., Jansen, R.A. & Dopita, M.A. 2002, AJ, 124, 3135
- Karachentsev, I.D., Karachentseva, V.E., Huchtmeier, W.K. & Makarov, D.I. 2004, AJ, 127, 2031
- Kauffmann, G. et al. 2003a, MNRAS, 341, 33
- Kauffmann, G. et al. 2003b, MNRAS, 341, 54
- Kroupa, P. & Weidner, C 2003, ApJ, 598, 1076
- Larson, R.B. & Tinsley, B.M. 1978, ApJ, 219, 46
- Lasker, B.M. et al. 1990, AJ, 99, 2019

- Lee, J.C., Salzer, J.J., Impey, C., Thuan, T. X. & Gronwall, C. 2002, *AJ*, 124, 3088
- Lee, J.C., Salzer, J.J. & Melbourne, J. 2004, *ApJ*, 616, 752
- Leitherer, C., & Heckman, T. M. 1995, *ApJS*, 96, 9
- Leitherer, C., et al. 1999, *ApJS*, 123, 3
- Leonard, D.C. et al. 2002, *PASP*, 114, 35
- Longair, M.S. et al. 1998, "Galaxy Formation" (Berlin: Springer-Verlag)
- Mac Low, M.-M. & Ferrara, A. 1999, *ApJ*, 513, 142
- McGaugh, S.S. 2005, *ApJ*, 632, 859
- Marconi, G., Tosi, M., Greggio, L. & Focardi, P. 1995, *AJ*, 109, 173
- Marlowe, A.T., Heckman, T.M., Wyse, R.F.G. & Schommer, R. 1995, *ApJ*, 438, 563
- Markarian, B.E. 1967, *Astrofizika*, 3, 55
- Martin, C.L. 1999, *ApJ*, 513, 156
- Marzke, R.O. et al. 1998, *ApJ*, 503, 617
- Massey, P., Strobel, K., Barnes, J.V. & Anderson, E. 1988, *ApJ*, 328, 315
- Massey, P., & Olsen, K. A. G. 2003, *AJ*, 126, 2867
- Meyer, M.J. et al. 2004, *MNRAS*, 350, 1195
- Miller, B.W. & Hodge, P. 1994, *ApJ*, 427, 656
- Mould, J.R. et al. 2000, *ApJ*, 529, 786
- Mould, J.R. et al. 2005, *AJ*, 129, 698

- Moustakas, J. & Kennicutt, R.C. 2006, ApJS, 164, 81
- Moustakas, J., Kennicutt, R.C. & Tremonti, C.A. 2006, ApJ, 642, 775
- Nilson, P. 1973, Uppsala General Catalogue of Galaxies (Uppsala: Uppsala Astron. Obs.)
- Oke, J. B. 1990, AJ, 99, 1621
- Origlia, L., Goldader, J. D., Leitherer, C., Schaerer, D., & Oliva, E. 1999, ApJ, 514, 96
- Osterbrock, D. 1989, "Astrophysics of Gaseous Nebulae and Active Galactic Nuclei" (Mill Valley: University Science Books)
- Papaderos, P., Loose, H.-H., Fricke, K. J., & Thuan, T. X. 1996a, A&A, 314, 59
- Papaderos, P., Loose, H.-H., Fricke, K. J., & Thuan, T. X. 1996b, A&A, 120, 207
- Parodi, B. R., Barazza, F. D. & Binggeli, B. 2002, A&A, 388, 29
- Paturel, G. et al. 2003, A&A, 412, 57
- Pogge, R.W. & Eskridge, P.B. 1987, AJ, 93, 291
- Pogge, R.W. & Eskridge, P.B. 1987, AJ, 106, 1405
- Rosa-Gonzalez, D., Terlevich, E. & Terlevich, R. 2002, MNRAS, 332, 283
- Rauzy, S. 2001, MNRAS, 324, 51
- Rhoads, J.E. 2000, PASP, 112, 703
- Richer, M. G., & McCall, M. L. 1995, ApJ, 445, 642
- Richer, M.G. et al. 2001, A&A, 370, 34

- Roberts, M.S. & Haynes, M. P. 1994, ARA&A, 32, 115
- Rosenberg, J.L. & Schneider, S.E. 2002, ApJ, 567, 247
- Salpeter, E.E. 1955, ApJ, 121, 161
- Salzer, J.J. 1989, ApJ, 347, 152
- Salzer, J.J. et al. 2000, AJ, 120, 80
- Salzer, J.J. et al. 2001, AJ, 121, 66
- Sargent, W.L.W. 1972, ApJ, 173, 7
- Sargent, W.L.W. & Searle, L. 1970, ApJ, 162, 155
- Schaller, G., Schaerer, D., Meynet, G. & Maeder, A. 1992, A&AS, 96, 269
- Schlegel, D.J., Finkbeiner, D.P. & Davis, M. 1998, ApJ, 500, 525
- Schmidt, M. 1968, ApJ, 151, 393
- Searle, L. & Sargent, W.L.W., 1972, ApJ, 173, 25
- Searle, L., Sargent, W.L.W. & Bagnuolo, W.G. 1973, ApJ, 179, 427
- Shaya, E.J., Tully, R.B. & Pierce, M.J. 1992, ApJ, 391, 16
- Skillman, E. D., Kennicutt, R. C. & Hodge, P. W. 1989, ApJ, 347, 875
- Skillman, E.D. & Bender, R., 1995, RMxAC, 3, 25
- Skillman, E.D. 1996, in "The Minnesota Lectures on Extragalactic Neutral Hydrogen," e.d. Skillman, E.D. (San Francisco: ASP), 106
- Springob, C.M., Haynes, M.P., Giovanelli, R. & Kent, B. 2005, ApJS, 160, 149

- Thuan, T.X. & Martin, G.E. 1981, ApJ, 247, 823
- Thuan, T.X. 1983, ApJ, 268, 667
- Tinsley, B.M. 1968, ApJ, 151, 547
- Tinsley, B.M. 1972, A&A, 20, 383
- Tonry, J.L. 2001, ApJ, 546, 681
- Tosi, M., Greggio, L., Marconi, G. & Focardi, P. 1991, AJ, 102, 951
- Tremonti, C.A. et al. 2004, ApJ, 613, 898
- Trentham, N. & Tully, R. B. 2002, MNRAS, 335, 712
- Tully, R.B. & Shaya, E.J. 1984, ApJ, 281, 31
- Tully, R.B. 1988a, "Nearby Galaxies Catalog" (Cambridge & New York: Cambridge University Press)
- Tully, R.B. 1988c, AJ, 96, 73
- Tully, R.B., Verheijen, M.A.W., Pierce, M.J., Huang, J.-S. & Wainscoat, R.J. 1996, AJ, 112, 2471
- Tully, R.B. & Pierce, M.J. 2000, ApJ, 533, 744
- Vader, J.P. 1986, ApJ, 305, 669
- van den Bergh, S., 1961, Zeitschrift fur Astrophysik, 53, 219
- van Zee, L. Haynes, M.P. & Salzer, J.J. 1997, AJ, 114, 2479
- van Zee, L, Skillman, E.D., & Haynes, M.P. 1998, AJ 116, 1186

- van Zee, L. 2000, AJ, 119, 2757
- van Zee, L. 2001, AJ, 121, 2003
- Vazquez, G. A., & Leitherer, C. 2005, ApJ, 621, 695
- Walter, F. & Brinks, E. 1999, AJ, 118, 273
- Weidner, C. & Kroupa, P. 2005, ApJ, 625, 754
- Weidner, C. & Kroupa, P. 2006, MNRAS, 365, 1333
- Yahil, A., Tammann, G. A. & Sandage, A. 1977, 217, 903
- Zamorano, J. et al. 1994, ApJS, 95, 387
- Zhang, Q. & Fall, S.M. 1999, ApJL, 527, 81
- Zwaan, M.A., Briggs, F.H., Sprayberry, D. & Sorar, E. 1997, ApJ, 490, 173
- Zucker, D.B. et al. 2006, ApJL, 643, 103
- Zwaan, M.A. et al. 2003, AJ, 125, 2842
- Zwicky, F., Herzog, E., Kowal, C.T., Wild, P. & Karpowicz, M. 1961-1968, Catalogue of Galaxies and of Clusters of Galaxies (Pasadena: Caltech)